DOKUZ EYLÜL UNIVERSITY
GRADUATE SCHOOL OF NATURAL AND APPLIED SCIENCES

AN INVESTIGATION OF THE BEHAVIOR OF FIBER REINFORCED CONCRETE PILES UNDER LATERAL LOADING

by
Cihan Taylan AKDAĞ

February, 2011
İZMİR

AN INVESTIGATION OF THE BEHAVIOR OF FIBER REINFORCED CONCRETE PILES UNDER LATERAL LOADING

A Thesis Submitted to the
Graduate School of Natural and Applied Sciences of Dokuz Eylül University
In Partial Fulfillment of the Requirements for the Degree of Doctor of Philosophy in Civil Engineering, Geotechnical Engineering Program

by
Cihan Taylan AKDAĞ

February, 2011
İZMİR

Ph.D. THESIS EXAMINATION RESULT FORM

We have read the thesis entitled **"AN INVESTIGATION OF THE BEHAVIOR OF FIBER REINFORCED CONCRETE PILES UNDER LATERAL LOADING"** completed by **CİHAN TAYLAN AKDAĞ** under supervision of **ASSOC. PROF. DR. GÜRKAN ÖZDEN** and we certify that in our opinion it is fully adequate, in scope and in quality, as a thesis for the degree of Doctor of Philosophy.

Assoc. Prof. Dr. Gürkan Özden

Supervisor

Prof. Dr. Arif Şengün Kayalar

Thesis Committee Member

Prof. Dr. Necdet Türk

Thesis Committee Member

Prof. Dr. Feyza Çinicioğlu

Examining Committee Member

Assoc. Prof. Dr. Özgür Yaman

Examining Committee Member

Prof.Dr. Mustafa SABUNCU
Director
Graduate School of Natural and Applied Sciences

ACKNOWLEDGMENTS

I am heartily thankful to my supervisor, Assoc. Prof. Dr. Gürkan Özden, whose encouragement, guidance and support from the initial to the final level enabled me to develop an understanding of the subject. I am deeply indebted to my committee members Prof. Dr. Arif Şengün Kayalar and Prof. Dr. Necdet Türk.

Support of this research was provided by the Scientific Research Project, Dokuz Eylül University office of BAP (Project No: 2007.KB.FEN.13) and The Scientific and Technological Research Council of Turkey, TÜBİTAK (Project No: 109M389), which is gratefully acknowledged.

I would like to thank *Taykon Steel Ltd* and construction technician Fatih Adil for their help in the design and construction of the steel test container.

I am grateful to Dokuz Eylül University Torbalı Vocational School. This study would not have been possible without Structural Mechanics and Structural Materials Laboratory of the Civil Engineering Department, and Mechanical Laboratory of the Metallurgical-Material Engineering Department.

I want to express my gratitude to my colleagues and friends Hakan Elçi and Özgür Bozdağ for their help whenever I needed. Thank you to those who helped the project as laboratory staff: Hasan Özdemir and Faruk Tunay. I would like to acknowledge the students: Ersin Eren, Mehmet Mete, Fulya Elmasoğlu, H. Eren Kuşçu, Güzide Koçak, Kaan Güncan, and Ercan Bayık who helped with the instrumentation and test preparation. I would like to thank the students: Ezgi Aytaç and Cihangir Çorbacıoğlu who helped during concrete casting.

A special acknowledgement goes to Juliane Stopper for her amazing support and patient. I am deeply and forever indebted to my father Gazi Akdağ and my mother Nazife Akdağ for their love, support and encouragement throughout my entire life.

AN INVESTIGATION OF THE BEHAVIOR OF FIBER REINFORCED CONCRETE PILES UNDER LATERAL LOADING

ABSTRACT

In this study, the influence of nonlinear behavior of reinforced concrete (RC) piles on soil-pile interaction was investigated. Primary goal of the model test program was to investigate the hypothesis that nonlinear pile material behavior might play an important role on soil-pile interaction (SPI), an aspect of SPI which was not studied extensively for RC piles.

A comprehensive testing program is planned and pursued in order to account for the influence of pile bending stiffness on soil-pile interaction (SPI), loading rate and axial load effects on lateral pile response. Prior to the model pile tests, bending tests were made on beam specimens to obtain the moment-curvature relationship of piles. Five types of model piles were tested under lateral loading and lateral-axial loading. Tests involved testing of model piles with and without bending reinforcement. The steel fiber ratio by volume is decided as 1% for the bending reinforced model pile with fibers and steel fiber reinforced concrete model piles.

Test results such as hinge formation, head displacement, moment distribution and soil surface movement around the pile were assessed and the performances of the piles were evaluated. Experimentally derived p-y curves are compared with the currently available industry standard API (American Petroleum Institute) recommended p-y curves. Effects of nonlinear behavior of steel fiber reinforced concrete and reinforced concrete pile on soil-pile interaction were investigated. A new methodology to improve the industry standard API procedure is suggested to incorporate pile flexibility parameters into the p-y curve formulation.

Keywords: Model piles, steel fiber reinforced concrete, lateral load, soil-structure interaction, p-y curves

ÇELİK LİFLİ BETON KAZIKLARIN YATAY YÜK ALTINDAKİ DAVRANIŞININ İNCELENMESİ

ÖZ

Bu çalışmada betonarme kazıkların doğrusal olmayan davranışının zemin-kazık etkileşimi üzerindeki etkisi incelenmiştir. Betonarme kazıkların davranışı zemin-kazık etkileşimi açısından henüz geniş anlamda araştırılmamıştır. Bu nedenle, model test programının öncelikli hedefi, doğrusal olmayan kazık malzemesi davranışının zemin-kazık etkileşimi üzerinde önemli bir rolünün olduğu hipotezinin doğruluğunu araştırmaktır.

Bu çalışmada, kazık eğilme rijitliğinin, zemin-kazık etkileşimi üzerindeki etkisinin dikkate alındığı kapsamlı bir deney programı planlanmıştır. Yükleme hızı ve düşey yükün yatay yükler altındaki kazığın davranışına etkileri de araştırılmıştır. Model kazık deneyleri öncesinde kazığın moment-eğrilik ilişkisini elde etmek amacıyla kiriş elemanlar üzerinde eğilme deneyleri yapılmıştır. Model deneyleri beş tür kazık üzerinde yatay yükle birlikte sabit düşey yük ve sadece yatay yük koşullarında gerçekleştirilmiştir. Deney kazıkları eğilme donatılı ve eğilme donatısız kazıklardan oluşmaktadır. Çelik lifli beton ve çelik lifli betonarme kazıklarda lif içeriği hacimsel olarak %1 oranında uygulanmıştır.

Kazık performansları mafsal oluşumu, kazık başı deplasmanları, kazık boyunca moment dağılımı ve zemin yüzeyinde oluşan deformasyonlar açısından karşılaştırılmıştır. Deneysel olarak elde edilen p-y eğrileri ile uygulamada standart olarak kullanılan API (Amerikan Petrol Enstitüsü) p-y eğrileri karşılaştırılmış;. betonarme ve çelik lifli betonarme kazıkların zemin-kazık etkileşimi üzerindeki etkileri araştırılmıştır. Uygulamada standart olarak kullanılan API prosedürü kazığın esneklik parametreleri ile birleştirilerek p-y eğrilerinin oluşturulmasında yeni bir yöntem önerisi sunulmuştur.

Anahtar sözcükler: Model kazıklar, çelik lifli beton, yatay yük, zemin-yapı etkileşimi, p-y eğrileri

CONTENTS

Page

CHAPTER ONE
INTRODUCTION

Piles are foundation elements that can transfer heavy structural loads to deeper soil layers with higher capacity. Most structures are subject to large lateral loads due to the action of wind, earthquake, impact, waves, or lateral earth pressure. In many cases lateral loads govern the design of the pile foundation system. Knowledge accumulated during model and field test studies have played an important role in the development of new analysis tools for piles under lateral loads. (Abendroth & Greimann, 1990; Dickin & Nazir, 1999; Patra & Pise, 2001) Majority of the model pile studies were performed on steel piles and nonlinear behavior of the surrounding soil and its effects on soil-pile interaction were accounted. However, piles are often constructed as reinforced concrete (RC) in practice and one should expect that RC piles would behave differently.

Reinforced concrete piles exhibit nonlinear response after the occurrence of first crack on the pile. Nonlinear analysis of reinforced concrete piles can be carried out using moment-curvature relation. The pile behaves linearly during initial loading stage at the end of which first crack takes place. The cracking of the concrete occurs early in the loading with a considerable reduction in pile stiffness, EI. The variation of EI has a significant effect on soil-pile interaction. Furthermore, loading rate and axial load alter the soil-pile response.

The reduction of EI along the deflected portion of the pile is a reflection of the combined effect of pile and soil properties. In *rc* piles, tensile cracks occur easily under flexural loading due to brittle nature of cement-based materials. It has long been known that the major benefit achieved by using fiber reinforcement in concrete is the improvement of the material from brittle to more ductile behavior. Short and randomly distributed fibers can solve out the problems of cracking and low energy absorption capacity of brittle materials. Significant improvement in energy absorption capacity, possible increase of ultimate tensile strength and well crack-width control mechanism are the essential advantages of adding fibers in concrete.

Experimental studies have shown that concrete with steel fibers in adequate quantities improves the shear resistance as a result of delaying the formation and development of cracks; acting directly across the cracks, implying greater effectiveness in the crack-arresting mechanism.

The objective of this model study is to investigate nonlinear behavior of laterally loaded conventional reinforced concrete piles and piles with steel fiber reinforcement in cohesionless soils. Emphasis was given to the understanding of the interaction between cohesionless soil and pile.

This dissertation provided insight regarding influence of nonlinear behavior of reinforced concrete piles on soil-pile interaction. Bending resistance to the concrete piles was provided by the conventional rebars and steel fibers. Unreinforced concrete piles were also tested in order to obtain reference test data. Primary goal of the model test program was to investigate the hypothesis that nonlinear pile material behavior might play an important role on soil-pile interaction (SPI), an aspect of SPI which was not studied extensively for RC piles. Majority of the previous research was devoted on the effect of soil nonlinearity and pile geometry on SPI.

The second chapter of the thesis is devoted to the literature review. The fundamental aspects of steel fiber influence on soil-pile interaction are discussed for steel fiber reinforced concrete and plain concrete piles in the third chapter where the factors to be considered in the planning and design of a model test study on reinforced concrete piles are presented. The testing system and testing materials are introduced in the fourth chapter. Test results are presented and discussed in chapter five, which includes laboratory concrete and beam bending test findings in addition to the model pile test results. The sixth chapter covers lateral load-deformation (p-y) curves, discussions on SPI aspects of the dissertation and a new proposed p-y curve establishment methodology for RC piles in medium dense sands. The thesis ends with the conclusions.

CHAPTER TWO
LITERATURE REVIEW

2.1. Fiber Reinforced Concrete (FRC)

The addition of fibers in brittle materials can be traced back to prehistoric times. Straw and horsehair were used to reinforce sun-baked bricks and plaster, respectively. In modern times, however, fibers have been utilized in a wide range of engineering materials including ceramics, plastics, cement, and gypsum products to enhance their engineering characteristics. Such characteristics include tensile strength, crack resistance, crack control, durability, fatigue life, resistance to impact and abrasion, shrinkage, expansion, thermal characteristics, and fire resistance (ACI, 1996).

Tensile cracks that take place under flexural loading and action of environmental conditions occurred due to brittle nature of cement-based materials. It has long been known that the major benefit achieved by using fiber reinforcement in portland cement concrete is the conversion of the material from brittle to more ductile behavior. Short and randomly distributed fibers can overcome the problems of cracking and low toughness of brittle materials. Significant improvement in energy absorption capacity, possible increase of ultimate tensile strength and well crack-width control mechanism are the essential advantages of adding fibers into brittle matrix.

Reinforcement of cementitious materials with discrete fibers has been successfully applied nearly more than four decades (Soranakom & Mobasher, 2008). Numerous research studies have been done during the last two decades on a variety of discrete fiber systems, including Steel Fiber Reinforced Concrete (SFRC) (Ashour, Wafa, & Kamal, 2000; Barros & Figueiras, 1999) and Glass Fiber Reinforced Concrete (GFRC) (ACI, 1996), Slurry Infiltrated Mat Concrete (SIMCON) (Bayasi & Zeng, 1997), Engineered Cementitious Composites (ECC: PVA-ECC: reinforced with polyvinyl alcohol fibers; PE-ECC: reinforced with high modulus polyethylene fibers) (Fischer & Li, 2002; Li, Wang & Wu, 2001; E.H., Yang, Wang, Y.Yang, & Li, 2008). The terminology “fiber reinforced concrete

(FRC)” can be used to globally define concrete materials including either steel or petroleum based fibers. FRC is now being used in growing amounts in structures such as highway overlays, airport pavements, bridge decks and machine foundations (Zhang, Stang, & Li, 1999).

2.1.1 Industrial Applications of Fiber Reinforced Concrete

Fibers have been utilized in many applications, including repair/ rehabilitation of damaged structures, impact-resistant structures, and tunnel linings (Oh, Park, Kim, & Choi, (2005). Number of structural applications of FRCs are growing steadily. Victor Li (2002) stated that in the near future ultra-high performance FRC will be commercially valued in various engineering structural applications.

In recent years, the demand for high strength concrete has been growing at an ever-increasing rate, and many new structures have been built using concrete with a compressive strength as high as 100 MPa. Recent studies have, however, shown increasing evidence that the brittle nature of high strength concrete can be overcome by addition of discrete fibers of short length and small diameter in the concrete mix. Adding fibers improve some mechanical properties of high-strength concrete such as tensile strength and flexural energy absorption capability (Mansur, Chin, & Wee, 1999; Rossi, 2000; Eren & Celik, 1997; Banthia, Yan, & Bindiganavile, 2000; Krumbach, Seyfarth, Erfurt, & Friedmann, 1998). A case history for the application of high-strength fiber reinforced concrete includes a repair project of a parking garage in Vancouver (Banthia et al., 2000). Another application of steel fibers in high-strength concrete is the construction of two highway bridges on the Bourg lés Valence bypass in Drome Region of France (Simon, Hazar, Lecointre, & Petitjean, 2002).

Some current industrial applications of FRC are summarized by Li (2002). This documentary study demonstrates wide-range applications in different parts of the world. Some of such applications can be mentioned as repair airfield runway patch (steel fiber-US), industrial floor restoration (metglas® fiber- France), pavement overlay 75 mm to 175 mm thick (steel fiber- Canada), and wall panels (carbon fiber-Japan) to illustrate the wide range of fiber utilization. However, most of these sample applications are semi-structural. Additional experimental studies are needed in order to establish design methods and specifications for the use of FRC as structural elements.

In this respect, this thesis study on the steel fiber reinforced concrete (RC-with fibers) piles may be considered as a contribution to the literature in terms of the application of SFRC in a major foundation element. The literature review on steel fiber reinforced concrete is pursued in the following paragraphs from this point of view.

2.2 Steel Fiber Reinforced Concrete (SFRC)

Experimental studies involving the use of discontinuous steel reinforcing elements to improve the properties of the concrete date from 1910. It was stated that during the early 1960s the first major investigation was made to evaluate the potential of steel fibers as reinforcement for concrete (Romualdi & Batson, 1963). Naaman (2003) notes that cementitious matrices such as concrete have low tensile strength and they fail in a brittle manner. Flexural strength, fatigue strength, tensile strength and the ability to resist cracking are enhanced with the use of steel fibers (Nataraja et al., 1999).

Barros & Figueiras (1999) highlighted that when steel fibers are added to a concrete mixture, they are randomly distributed and act as crack arrestors. Pulling fibers out of the concrete require more energy, giving a substantial increase in toughness. In tension, SFRC fails ultimately only after the steel fiber breaks or is pulled out of the cement matrix.

Steel fibers have a relatively high strength and modulus of elasticity. They are protected from corrosion by the alkaline environment of the cementitious matrix, and their bond to the matrix can be enhanced by mechanical anchorage or surface roughness. Most common steel fibers are circular in cross-section, with a diameter ranging from 0.4 to 0.8 mm, and a length in the range of 25~60 mm. Their aspect ratio, that is, the ratio of length to diameter or equivalent diameter, is generally less than 100. Aspect ratio is an essential parameter for fibers to be uniformly dispersed in an unhardened concrete mixture. The commonly observed ratio of 40 to 60 is sufficient for such a distribution following usual mixing procedures.

The uniaxial compression test results of fiber reinforced concrete have revealed a slight increase in the compression strength, stiffness, and strain at peak load and a substantial increase in the post peak energy absorption capacity (Fanella & Naaman, 1985; Ezeldin & Balaguru, 1992). In compression, the ultimate strength is only slightly affected by the presence of fibers with a volume fraction of approximately 1.5%. Uniaxial compression strength is reported to increase as high as 15% (ACI 544.1R-96).

2.2.1 Flexural Behavior of SFRC and RC-with steel fiber

Flexural response of the pile material is a fundamental aspect of laterally loaded pile foundations. The primary advantage in using SFRC is its good flexural performance. The most significant improvement by adding fibers to concrete is the substantial increase in the energy absorption capacity (Choi & Lee, 2002; Barros & Figueiras, 1999; Mailhot, Bissonnete, & Pigeon, 2001; Dry & Corsaw, 2003). Steel fibers increase the deformation capacity of concrete. In most cases, steel fibers are pulled out as a result of debonding rather than being ruptured under tensile stress. The comparison of failure pattern of beams with and without fibers was presented by Johnston (1994) as shown in Figure 2.1. If the element is loaded, the stress is absorbed as a result of the bridging fibers and the bending moments are redistributed. The concrete element does not fail spontaneously when the matrix cracks down. Steel fibers enhance the energy absorption and the ductility of the concrete under tensile stress not only in the post-cracking stage, but also before the peak load. The studies demonstrate that the flexural strength of SFRC is about 50 to 70 percent more than that of the unreinforced concrete matrix in the traditional third-point bending test (Shah & Rangan, 1971; Johnston, 1974).

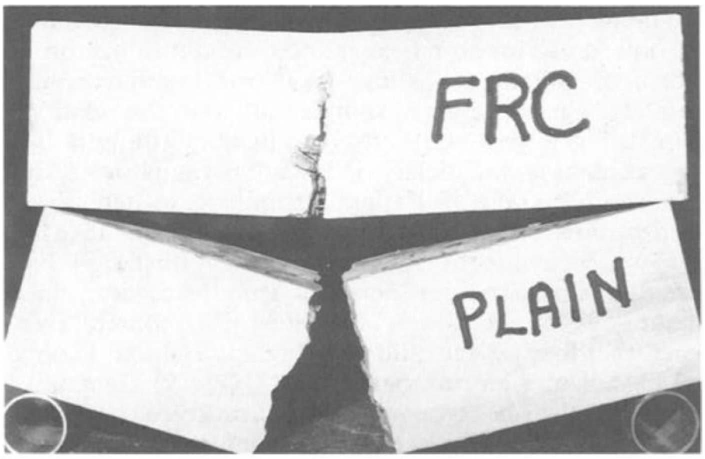

Figure 2.1 Energy absorption of FRC in flexure compared with plain concrete (Johnston, 1994)

Several research studies have examined the effect of fiber reinforcement on the flexural response of beams with and without steel reinforcement bars. Flexural beams were frequently tested to assess the performance of SFRC according to ASTM C 1018. This test method involves a third-point loading configuration in order to develop uniform moment distribution in the central portion of the test beam (Figure 2.2). Stress-strain relationships, load-mid span deflections, first crack strength, post-cracking behavior, stress-crack width relations of flexural members were investigated through the experiments.

Researchers (Robins, Austin, Chandler, & Jones, 2001) investigated the fracture of SFRC under flexural loading in order to come up with an approach that can predict flexural behavior of steel fiber reinforced concrete in the form of a load-deflection response. Relationship between the third stages of crack propagation and the flexural load-deflection response of a steel-fiber reinforced concrete beam is presented in that study (Figure 2.3). Stage 1, 2, 3, and 4 represents uncracked, microcracked, macrocracked, and macrocrack with fibers being pulled forms of the test material, respectively. In the post-crack, response is activated fiber bridging.

Fibers bridge the cracks and increase the ductility of the member. Crack propagation diagram of Stage 4 is illustrated in the study (Figure 2.4).

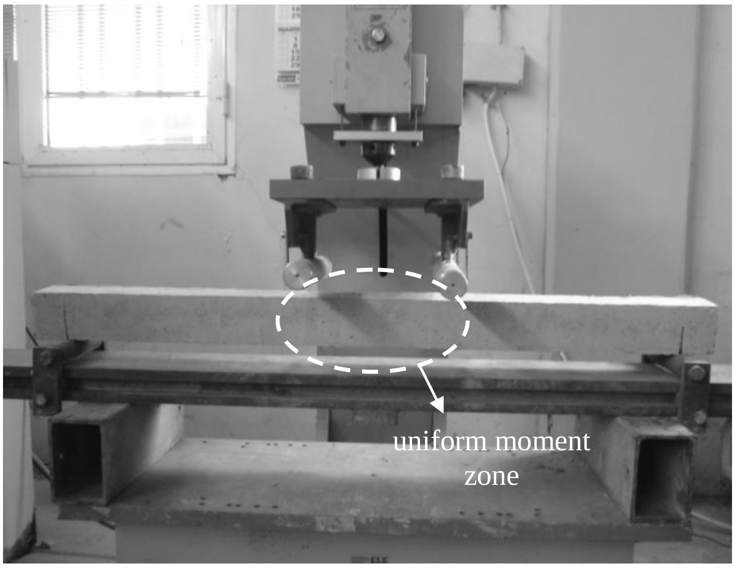

Figure 2.2 Third-point bending test system

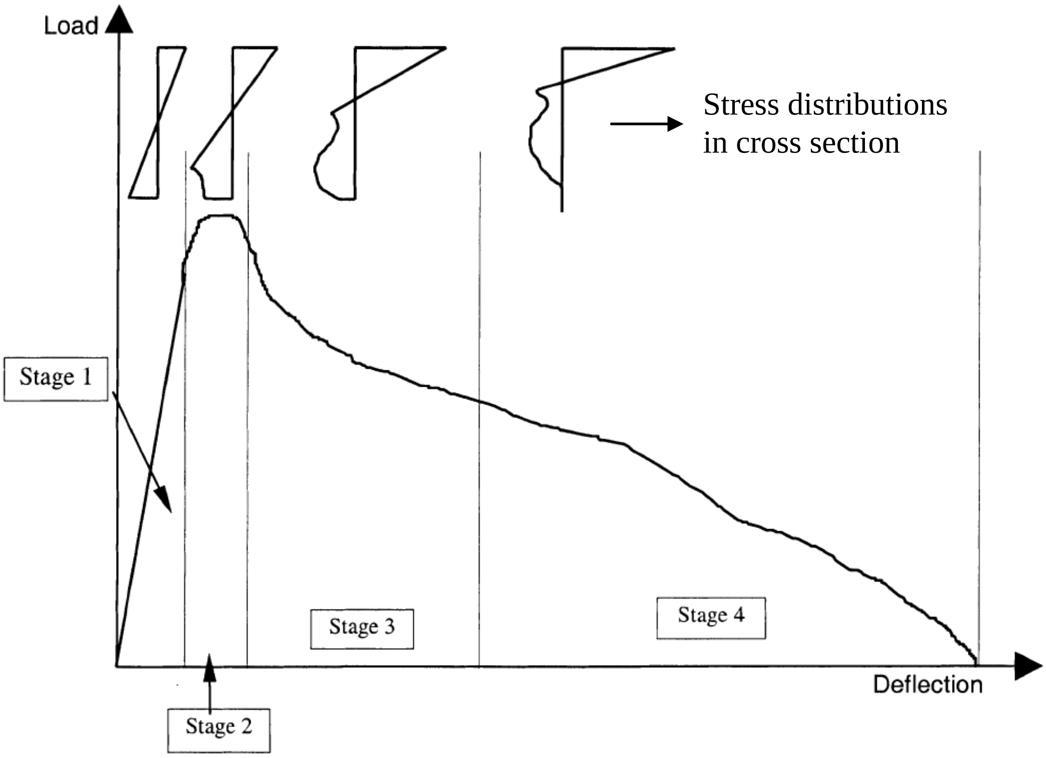

Figure 2.3 A typical load-deflection curve of SFRC (Robins et al., 2001)

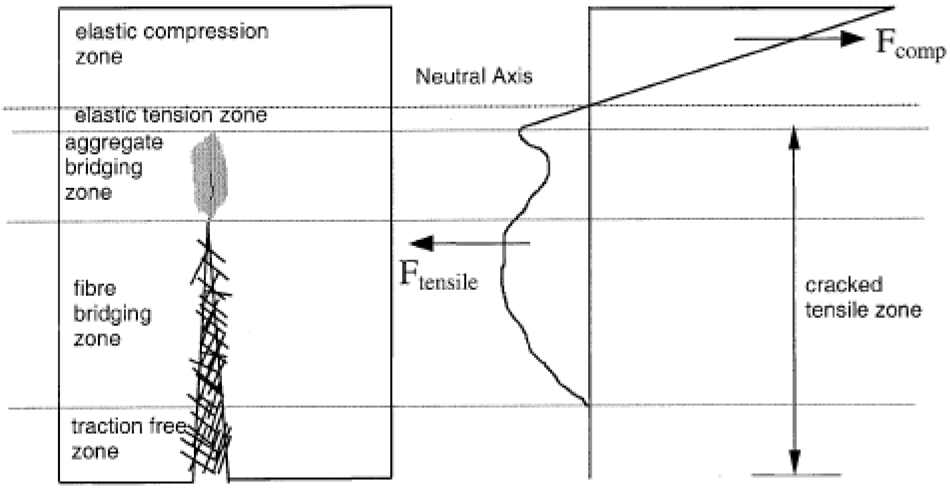

Figure 2.4 Fiber bridging response of SFRC beam under flexural loading-Stage 4 (Robins et al. 2001)

A similar load-deflection behavior can be seen from the flexural tests result of other researchers (Barros & Figueiras, 1999) as shown in Figure 2.5. Tests were performed on beams to simulate post-cracking behavior and to assess the fracture energy of SFRC with steel fiber content 0 to 60 kg/m^3.

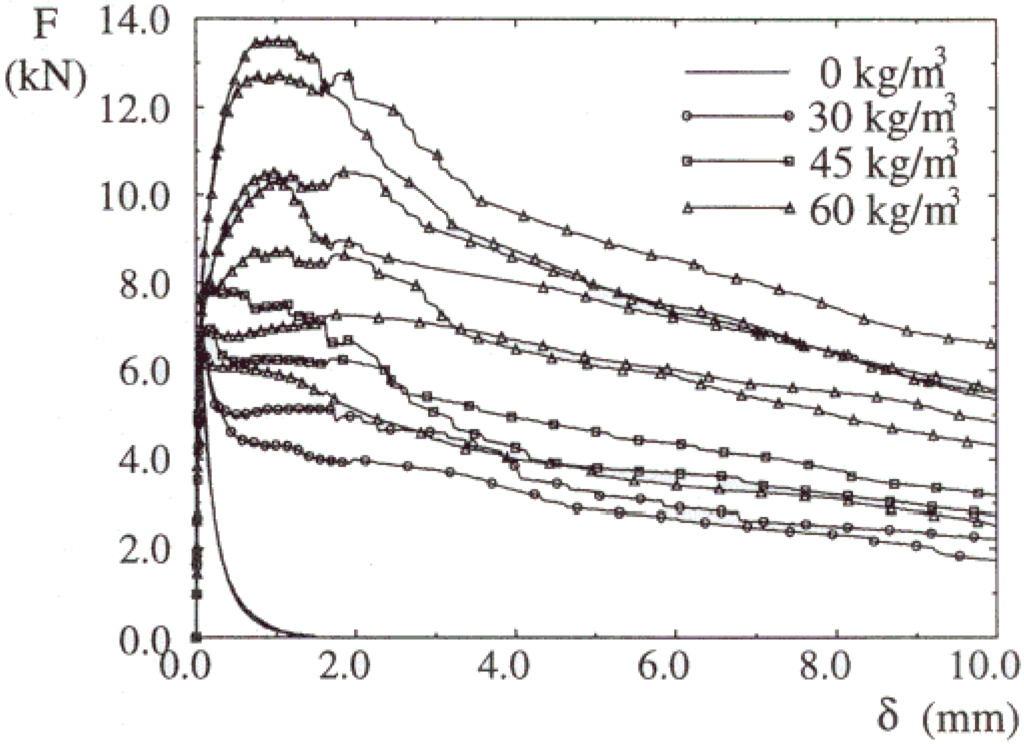

Figure 2.5 Load-deflection relationships (Barros & Figueiras, 1999)

Semi-analytical method is developed to predict fatigue behavior of fiber reinforced concrete under flexural loading based on force in critical cracked section (Zhang, et al., 1999). Researchers obtained experimental monotonic flexural stress-crack mouth opening displacement (CMOD) curves and compared them with the theoretical expected behavior (Figure 2.6 and Figure 2.7). The result shows that steel fiber reinforced concrete continues to carry flexural loading with the increase of deformation in contrast with the plain concrete undergoing a decrease in flexural stress.

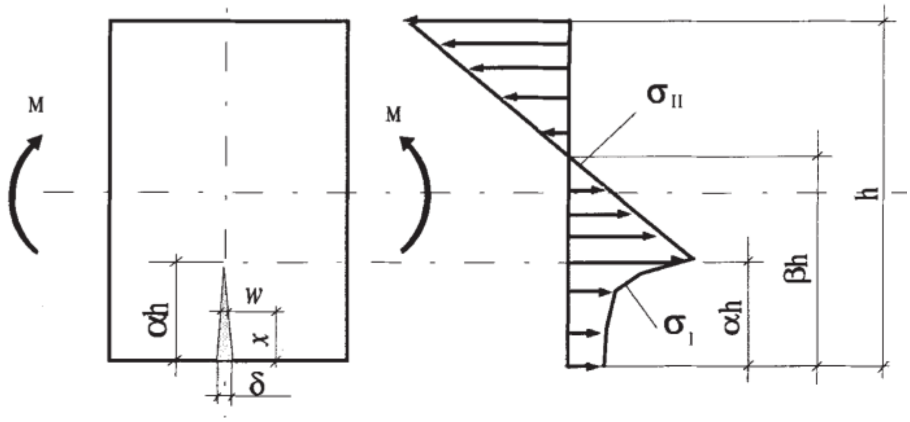

Figure 2.6 In the second stage, the crack length (αh), α[0,1], CMOD (δ) and external moment (M) (Zhang et al., 1999)

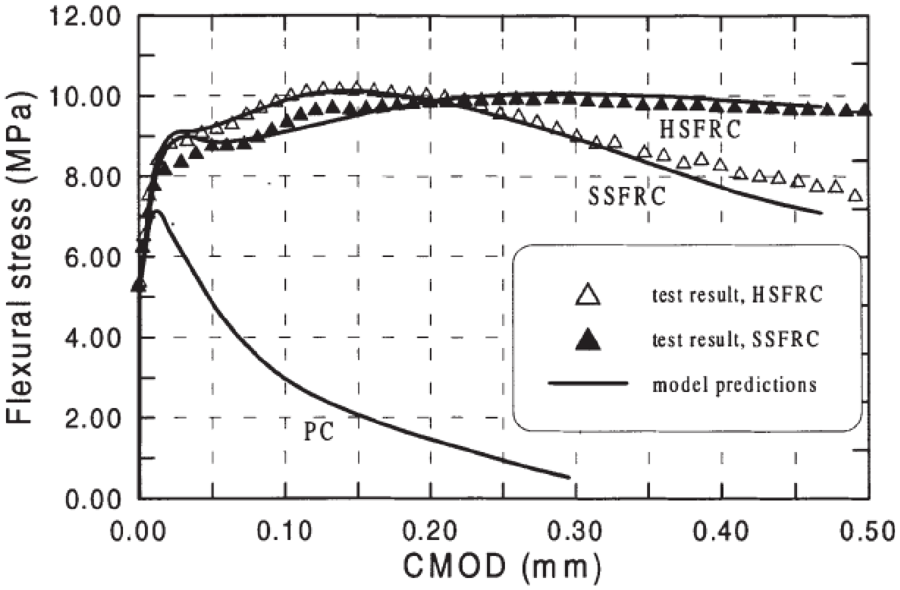

Figure 2.7 Flexural stress versus crack mouth opening displacement. SSFRC: smooth steel fiber concrete and HSFRC: hooked steel fiber concrete (Zhang et al., 1999)

The flexural behavior of steel fiber reinforced concrete with longitudinal tensile reinforcement (*RC-with steel fiber*) has been researched with a rising trend in the last decade. Dancygier & Savir (2006) performed flexural experiments on high strength steel-fiber reinforced concrete (HSFRC) elements with a minimum amount of reinforcement (Figure 2.8). In the referred study, researchers compared the flexural response of high strength concrete (HSC- with and without fibers) beams with reinforcement ratio 0.28% (H4-H5), 0.56% (H8) and control normal strength concrete (NSC- without fibers) beams. A constant volumetric ratio of hooked end steel fibers 0.75% and same stirrup reinforcement were utilized in all of the beams. Moment-mid span deflection results can be seen in Figure 2.9. Researchers found that higher structural ductility was obtained in beam specimens with fibers, in which the amount of flexural reinforcement was increased (H8-F2-1_35 and H8-F2-1_60 with reinforcement ratio 0.56%).

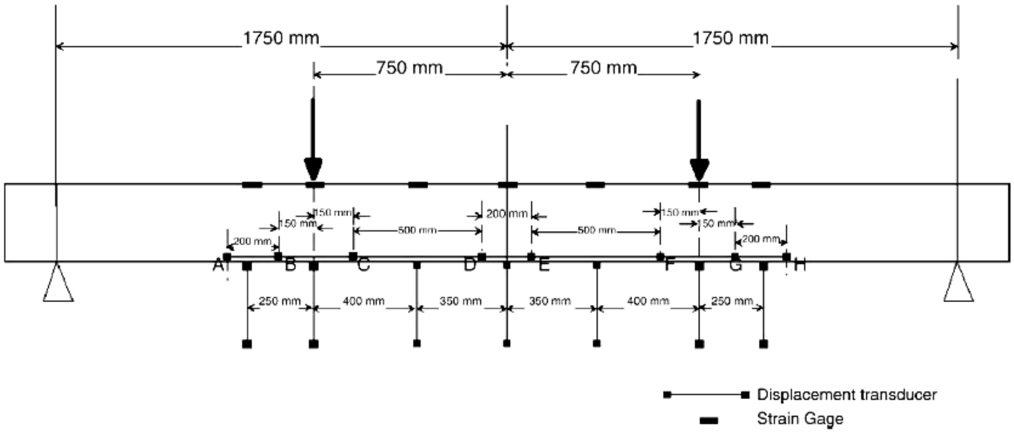

Figure 2.8 Flexural test set-up (Dancier & Savir, 2006)

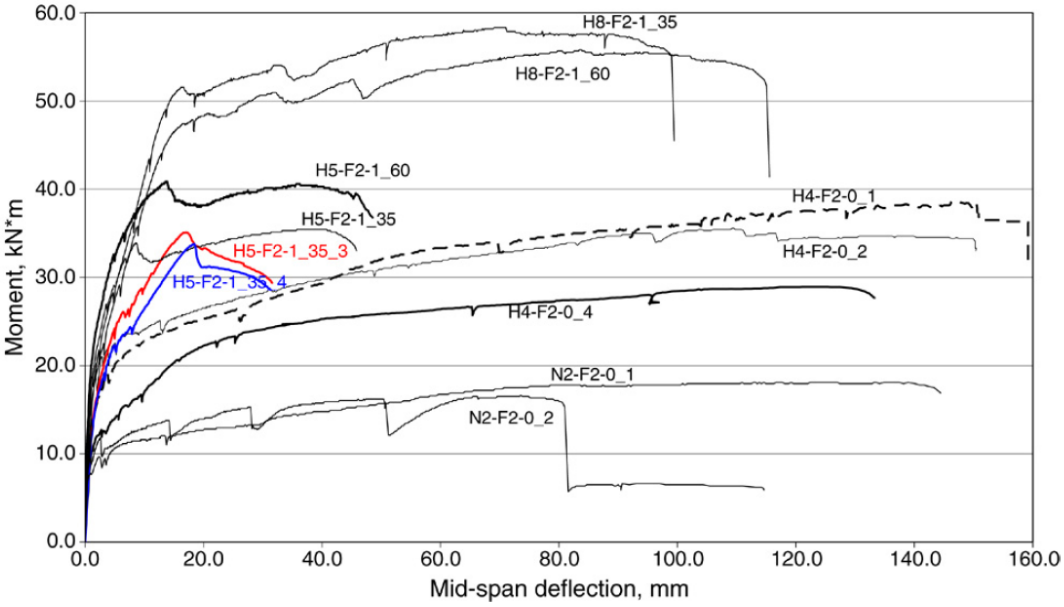

Figure 2.9 Moment-deflection curves In the figure: H8-F2-1_35; H8-F2-1_60; H5-F2-1_60; H5-F2-1_35; H5-F2-1_35_3; H5-F2-1_35_4 (*HSFRC-with steel fiber*), H4-F2-0_1; H4-F2-0_2; H4-F2-0_4 (*HSFRC-without steel fiber*), N2-F2-0_1; N2-F2-0_2 (*NSC-without steel fiber*) (Dancier & Savir, 2006);

Another important study was made by Chunxiang & Patnaikuni (1999). In that research, high-strength reinforced concrete beams and steel fiber-reinforced high strength concrete beams with steel fiber content of 1% by volume were tested. Three types of fibers (Type I, II and III) were used in different sizes. The reinforcement design and test configuration are shown in Figure 2.10. The load-displacement curve (Figure 2.10 c) of concrete beams without steel fibers falls much faster with the increase in displacement, which express that beams with steel fibers exhibited higher ductility.

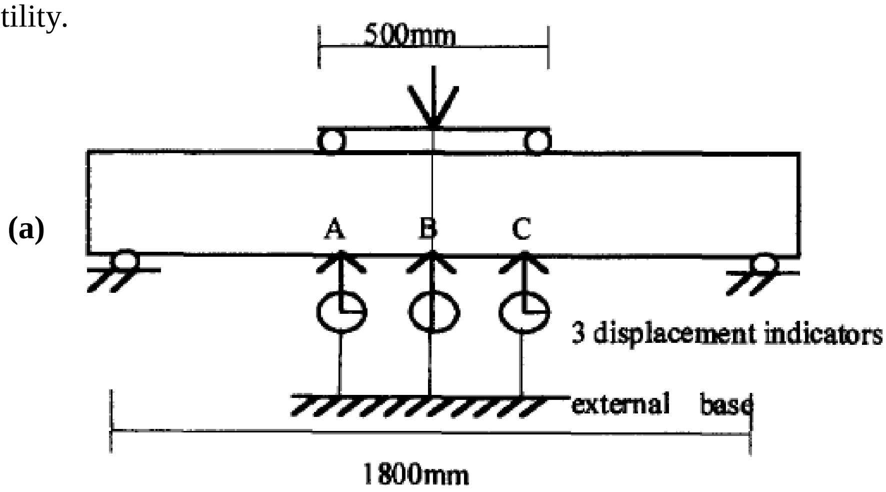

Figure 2.10 (a) (Please note the following for further information!)

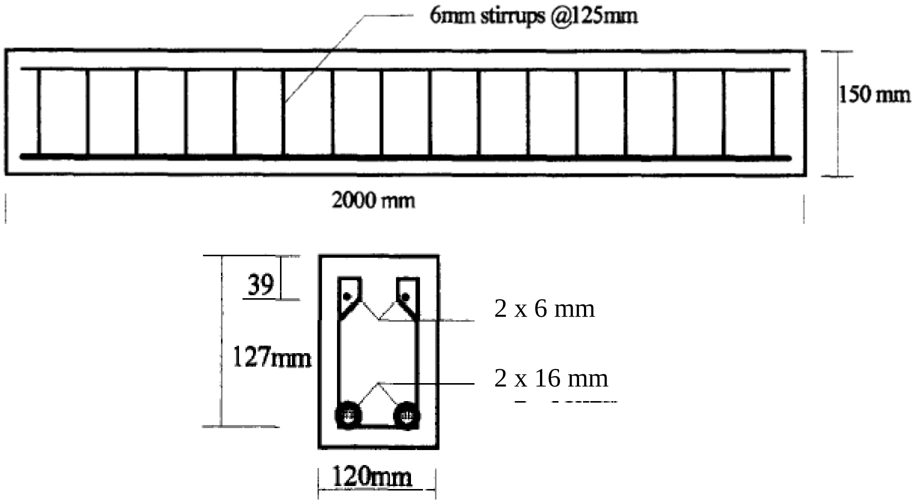

(b)

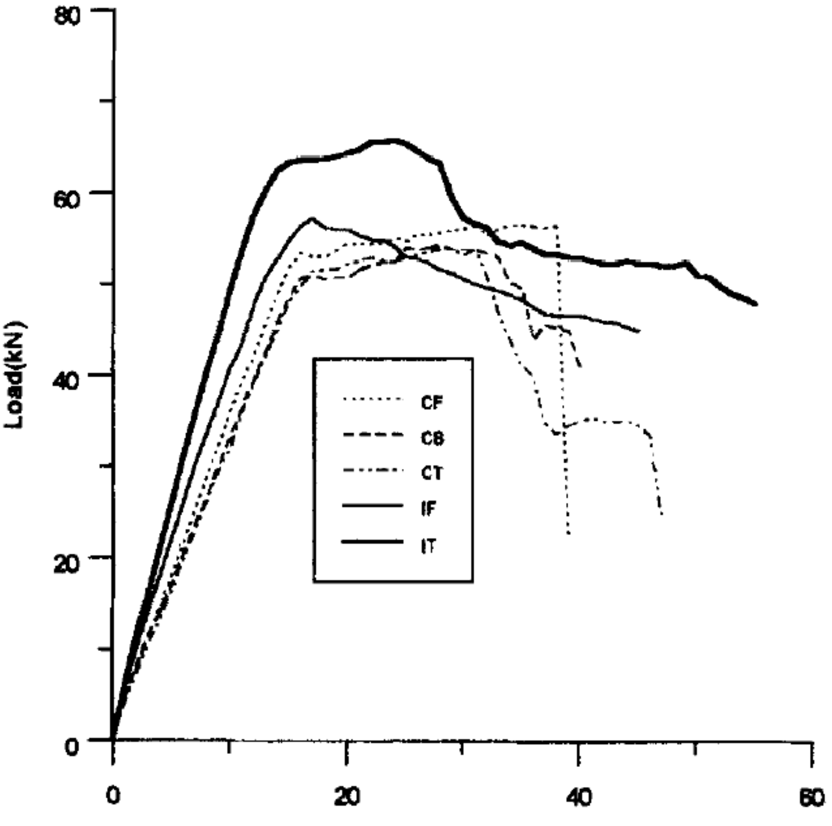

(c)

Figure 2.10 (a) Test configuration (b) Details of test beams (c) Comparison of load-central displacement curves of concrete beams with (IF and IT - Type I: 18 x 0.4 x 0.3 mm) and without (CF, CS and CT) steel fibers (Chunxiang & Patnaikuni,1998)

The effect of concrete compressive strength and tensile reinforcement ratio on the flexural behavior of fibrous concrete beams was discussed by Ashour (2000) and Ashour et al. (2000). Variation of modulus of rupture with respect to steel fiber content and compressive strength of concrete is given in Figure 2.11. It is underlined in this study that generally researchers paid less attention to the flexural rigidity of FRC. According to the article, flexural rigidity increases as the concrete compressive strength and steel fiber content increases. It is stated that the inclusion of steel fibers in high-strength concrete beams improves the arresting mechanism of crack propagation and consequently enhances the effective moment of inertia. Addition of steel fibers reduced the crack width, increased the number of cracks, enhanced the ductility and delayed the final crushing of the concrete.

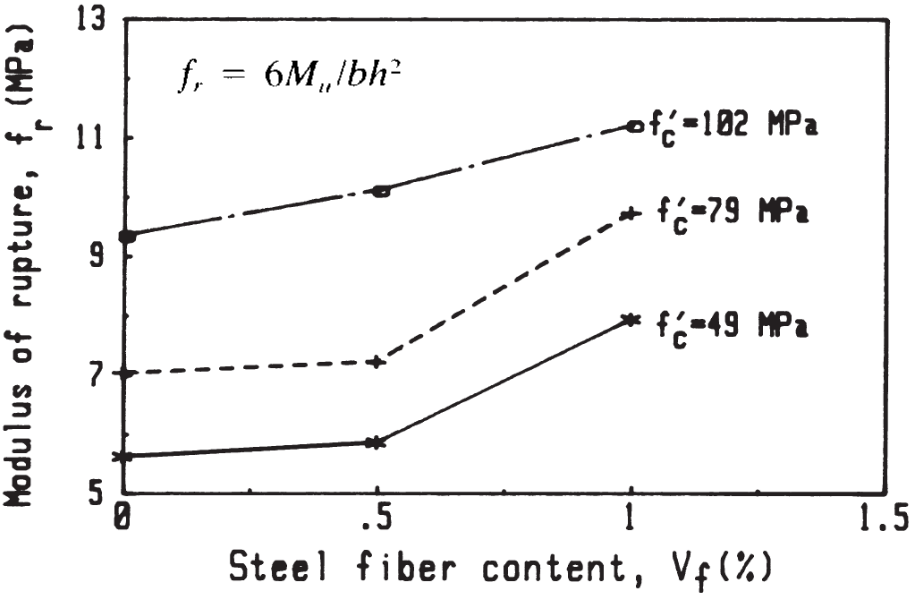

Figure 2.11 Effect of fiber content on modulus of rupture (Ashour et al., 2000)

An experimental and analytical study on steel fiber reinforced high-strength concrete in fully prestressed and partially prestressed (Figure 2.12 and Figure 2.13) beam specimens is an interesting example (Padmarajaiah & Ramaswamy, 2004). Tests were performed on beams with half depth and full depth steel fiber content 0.5%, 1.0% and 1.5% by volume. Results were evaluated in respect to ductility and energy absorption capacity of tested beams. Ductility of the elements was assessed by using ductility factor. Ductility factor is indicated as, $\delta_1/\ \delta_2$ where δ_1 is deflection of the first crack and δ_2 is the deflection at 90% for fully pre-stressed and 80% for partially pre-stressed of the peak load, beyond the peak load. Energy absorption was described as the area under the load-deflection curves. The results of the research showed that presence of fibers in the fully and partially pre-stressed beams enhanced cracking and ultimate flexural strength of the beams. Maximum increase in flexural strength in fully pre-stressed beams were obtained 8%, 16% and 21% because of inclusion of 0.5%, 1.0% and 1.5% fibers by volume fraction, respectively. It was indicated that addition of fibers increased the energy absorption capacity and ductility. Increase of ductility was 18%, 45% and 68% and increase of energy absorption was 25%, 78% and 88% for the fully pre-stressed with full depth fiber content 0.5%, 1.0% and 1.5% by volume. Detailed information the other beam cast as partially pre-stressed can be found from the referred text.

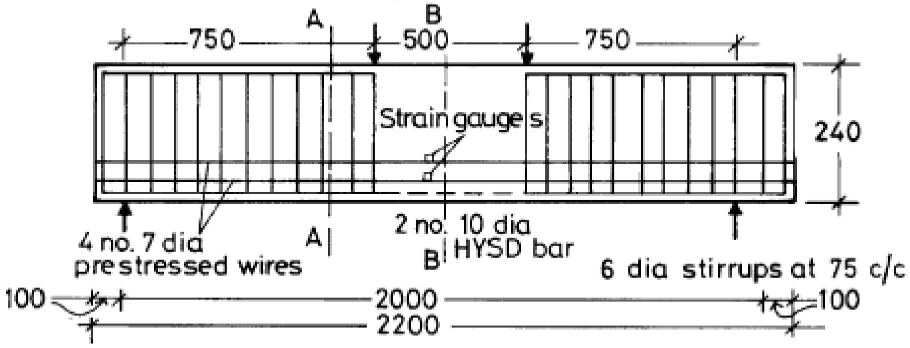

Figure 2.12 Experimental set–up beam specimens under flexural loading (Padmarajaiah & Ramaswamy, 2004)

All of the above-mentioned researches on fiber reinforced concrete with longitudinal tensile reinforcement (RC-with steel fiber) are related to high-strength concrete (HSC). There are also recent studies on normal strength concrete (NSC) with longitudinal reinforcement and fiber content (Özcan, Bayraktar, Şahin, Haktanır, & Türker, 2008; Campione & Mangiavillano, 2008). According to conventional third-point bending experimental results, the ultimate load capacity of steel fiber added reinforced concrete was obtained 18% larger than ordinary RC beams for concrete class C20 (Özcan et al.,2008).

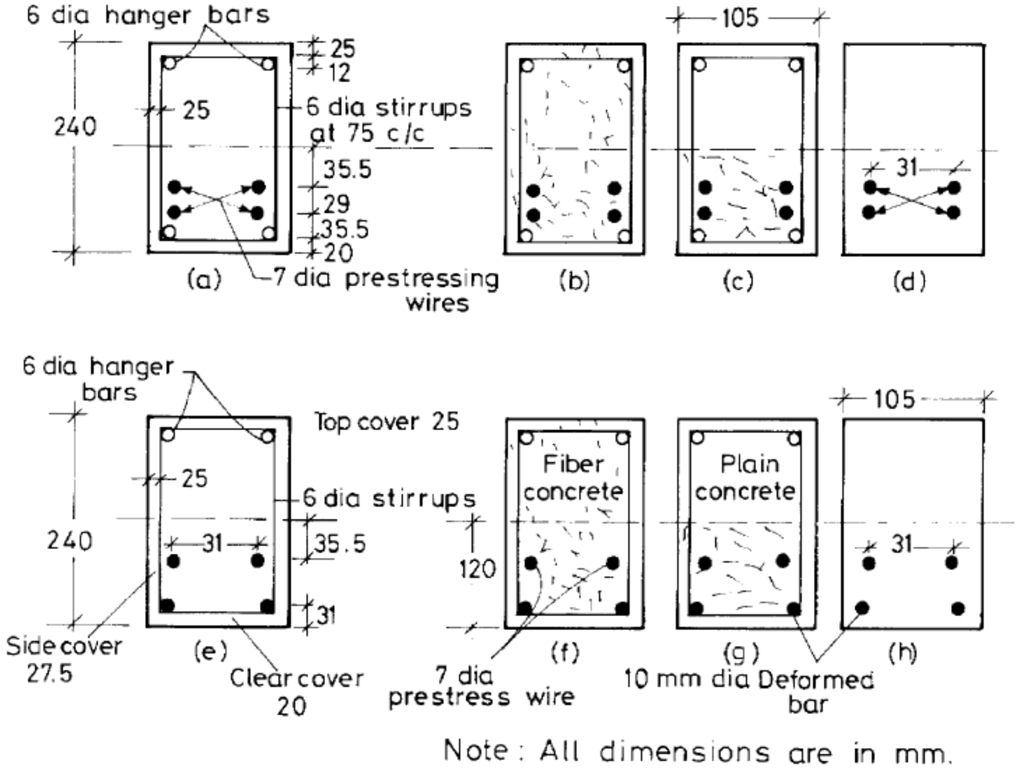

Figure 2.13 Cross sectional details of specimens (a) fully pre-stressed plain concrete (b) full depth fiber-reinforced pre-stressed concrete (c) fully pre-stressed beam specimens with half depth fiber (d) having partial depth fiber in shear span only (e) partially pre-stressed plain concrete specimen (f) full depth fiber-reinforced concrete partially pre-stressed beam specimens (g) half depth fiber-reinforced partially pre-stressed beam specimen (h) partially pre-stressed beam specimen having partial depth fiber in shear span only (Padmarajaiah & Ramaswamy, 2004)

Campione & Mangiavillano (2008), focused on the flexural behavior of plain concrete with 30 MPa cylindrical strength and fibrous reinforced concrete with hooked end steel fibers at a volume percentage of 1% in beams under monotonic and cyclic loading. Stress strain curves of concrete and SFRC in compression are presented in Figure 2.14. Reinforcement detail of the test beams are shown in Figure 2.15. Flexural loading results as load-deflection curves of *RC* and *RC-with steel fibers* for the monotonic loading can be seen in Figure 2.16. It can be seen in the figure that brittle flexure failure occurs without bending reinforcement. It is emphasized that because of fibers bridging capacity across the cracks, the shear strength of the beams increases and failure is ductile. The results were interpreted by the researchers that fibrous beams exhibited ductile.

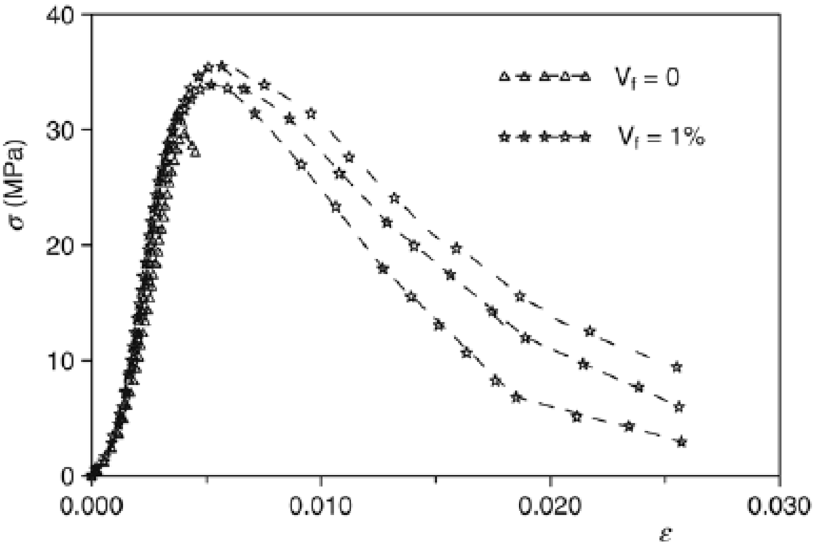

Figure 2.14 Stress-strain relation of plain and steel fiber concrete (Campione & Mangiavillano, 2008)

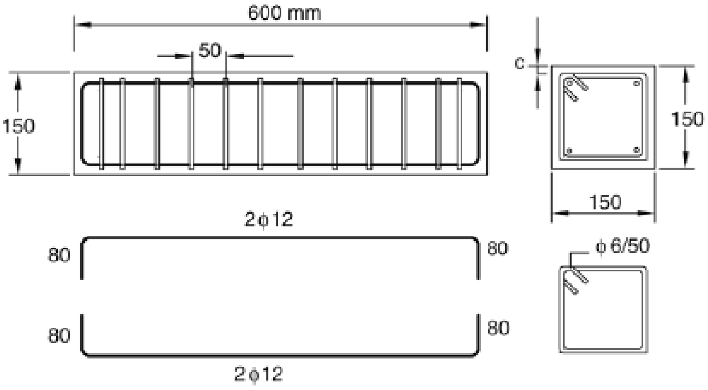

Figure 2.15 Reinforcement details and geometry of beams (Campione & Mangiavillano, 2008)

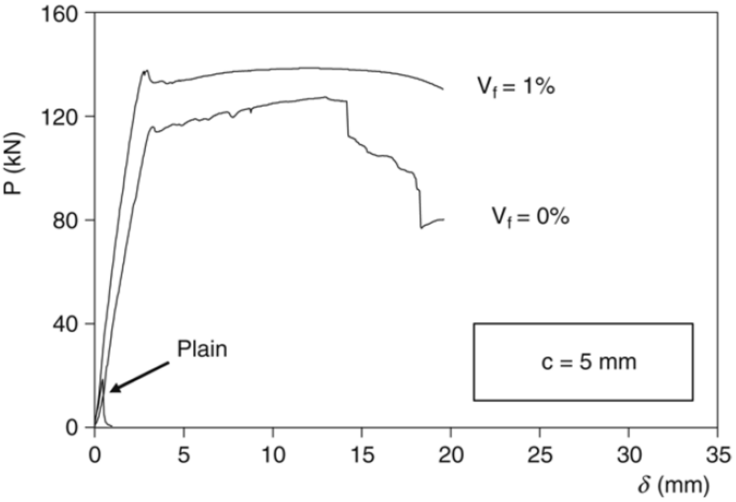

Figure 2.16 Monotonic load-deflection curves in flexure (Campione & Mangiavillano, 2008)

2.2.2 Shear Strength of Steel Fiber Reinforced Concrete Beams

The effect of steel fibers on shear strength with and without stirrups has been studied by several authors. Lots of researches, published nearly past three decades, have taken into consideration of the possibility of utilizing steel fibers as shear reinforcement (Li, Ward, & Hamza, 1992; İmam, Vandewalle, Mortelmans, & Van Gemert, 1997; Kwak, Eberhard, Woo-Suk Kim, & Jubum Kim, 2002; Ahiary & Mutsuyoshi, 2006; Barakat & Altoubat, 2010).

Experimental studies have shown that concrete with steel fibers, using adequate quantities, improves the shear resistance in consequence of delaying the formation and development of cracks; acting directly to the diagonal cracks and smaller distance between the fibers with respect to that between the stirrups, implying greater effectiveness in the crack-arresting mechanism (Cuccihara, Mendola, & Rapia, 2004). The possibility of substituting transverse reinforcement (stirrups) for steel fibers in concrete with bending reinforcement may significantly reduce the production cost. Another advantage is saving in laboring costs by avoiding the need for shaping the reinforcing bars and tying them in the form-work.

Shear strength of steel fiber-reinforcement concrete beams without shear stirrups were experimentally studied and prediction of ultimate shear strength was proposed by Kwak et al., (2003) and Li et al. (1992). Tests were examined on several beams with bending rebars. In the study of Li et al. (1993) the effect of shear-span effective depth ratios a/d ranging from 1.0 to 4.25, bending reinforcement ratio, ρ, and beam depth, d, and beam width, b, were investigated under center point bending condition (Figure 2.17). Test results of shear strength-reinforcement ratio relationship including different kind of fibers as aramid (Kevlar), polyethylene (Spectra), and steel with a %1 volume fraction are shown in Figure 2.18. It can be seen in the figures that shear strength increases in the range of 100 and 200 percent with the addition of fibers. In addition, it was concluded that both first shear crack stress and ultimate shear strength increased with the reinforcement ratio.

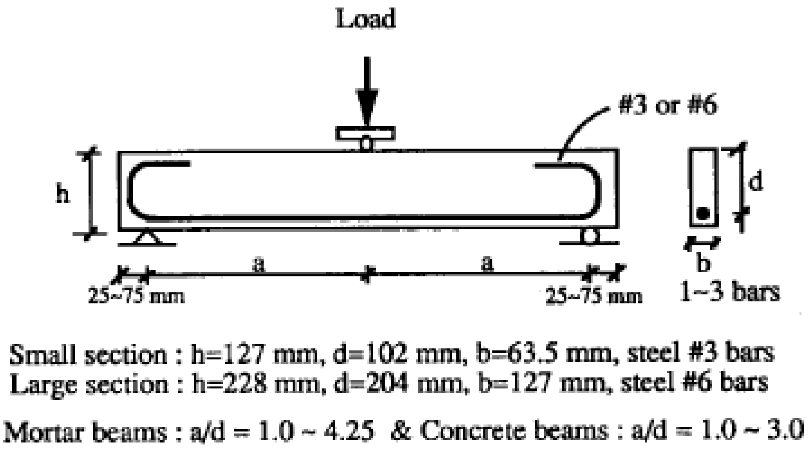

Figure 2.17 Center point bending test system (Li et al., 1993)

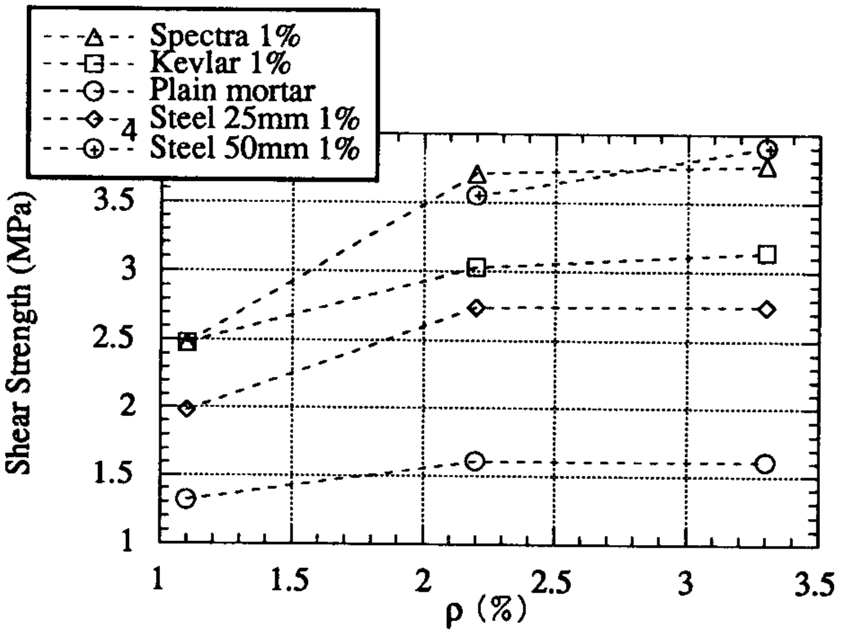

Figure 2.18 Shear strength- reinforcement relations (ρ: reinforcement ratio), Spectra (polyethylene fiber, 12.7 mm length, Kevlar (Aramid, 6.4 mm length) (Li et al., 1992)

Twelve beam tests (Figure 2.19) were conducted on reinforced beams with three steel fiber volume fractions (0, 0.5 and 0.75%) and three shear-span/depths ratio (a/d=2, 3, and 4) and two concrete classes (31 and 65 MPa) by Kwak et. al. (2002). According to the study, increasing of fiber content changed failure mode of the beams from shear to flexure.

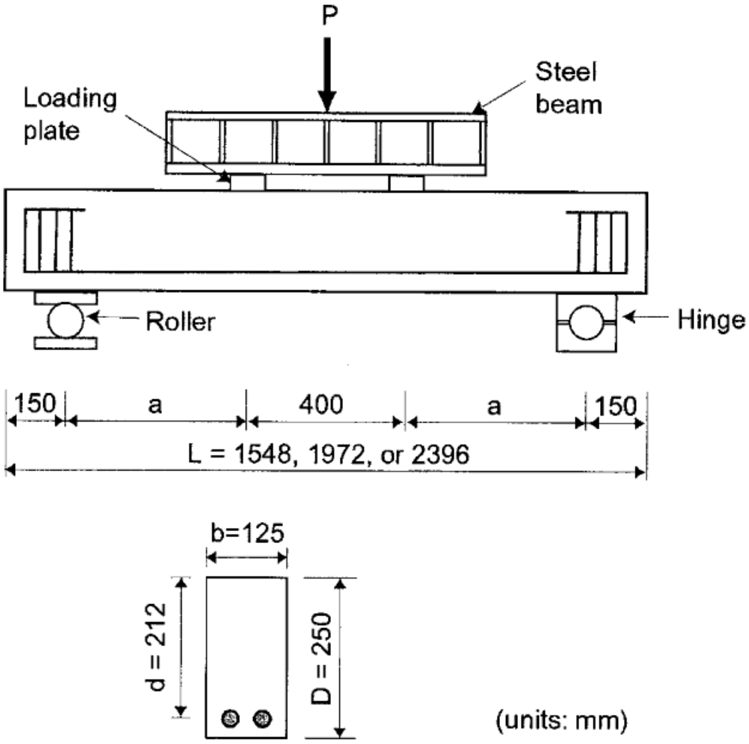

Figure 2.19 Details of test beams tested without and with steel fibers (Kwak et al., 2002)

Shear behavior of beams with bending cast reinforcement with and without steel fibers were compared in the above mentioned researches. Some investigations were also made on high strength steel fiber reinforcement concrete (HSFRC) with stirrups and without stirrups (Junior & Hanai, 1997; Junior & Hanai, 1999; Meda, Minelli, Plizzari, & Riva, 2005). These studies contain tests on pre-stressed elements. The experimental results of full scale pre-stressed beams show that the shear behavior of fiber reinforced concrete beams without conventional reinforcement is similar to, or even better than that of beams with stirrups Meda et al. (2005). Furthermore, shear strength behavior of beams with both stirrups and steel fibers was significantly improved. The research results of Junior & Hanai, (1999) indicate that both fibers and pre-stressing increase shear strength.

Tests were performed by Lim & Oh (1999) on normal strength concrete in order to investigate the influence of fiber reinforcement on the mechanical behavior of reinforced concrete beams in shear. Test variables were the volume fraction of steel fibers and ratio of stirrup rebars. Cracking shear strength with respect to fiber contents is presented in Figure 2.20. It is observed from the tests that through the addition of steel fiber the shear cracking strength of fiber reinforced concrete is higher than that of conventional reinforced concrete. It was suggested that combined use of steel fibers by 1% volume fraction and stirrups would improve cracking shear strength.

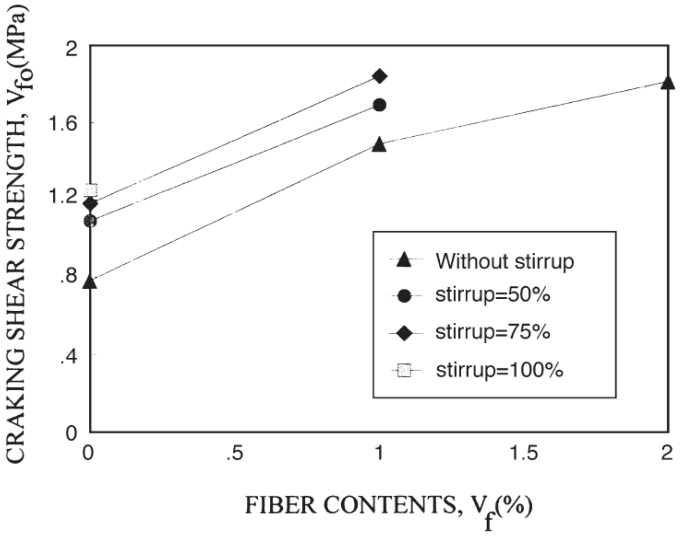

Figure 2.20 Variation of cracking shear strength-with fiber content test results (Lim & Oh, 1999)

2.2.3 Moment-Curvature Relation of Steel Fiber Reinforced Concrete

The laterally loaded pile exhibits linear response during the initial stages of the loading and its bending stiffness (EI) is constant. During subsequent loading effective pile cross section gets reduced due to crack formation resulting in a decrease in bending stiffness. The variation in the value of EI is expected to have a significant effect on the soil-pile interaction. The reduction of EI along the deflected portion of the pile is a reflection of the combined effect of pile and soil properties as well as the moment-curvature (M-Φ) relationship at any level of loading.

Nonlinear analysis of reinforced concrete (RC) beams can be carried out based on moment-curvature relation. In this approach, stiffness (EI), where E is elasticity modulus of concrete and I is moment of inertia, can be determined as the slope of the moment-curvature relation.

During the last decade, some analytical and a few experimental studies were done in order to get moment-curvature response of fiber reinforced concrete (FRC) (Soranakom & Mobasher, 2007; Padmarajaiah & Ramaswamy, 2004). Soranakom & Mobasher (2007) listed their goal as; (1) to develop a procedure to obtain moment-curvature relationships in closed form for operation in structural and finite element analyses; (2) to develop the closed-form load-deflection relationships for nonlinear materials under typical loading conditions and; (3) to develop a procedure for back-calculation of material properties from flexural load-deflection tests. Padmarajaiah & Ramaswamy (2004) proposed two analytical models to account for fully and partially pre-stressed steel fiber reinforced concrete. Cross sectional details of test elements were presented in Figure 2.13 *Section 2.2.1*. Moment-curvature relation for the tests and model analyses in that study are presented in Figure 2.21. The researchers reported that the curvatures were considerably reduced with fiber addition. From the beginning of the test up to the failure, the stiffness of the pre-stressed beams increased for fiber content by volume %1.5. It was claimed that larger fiber content has a greater influence in improving structural performance.

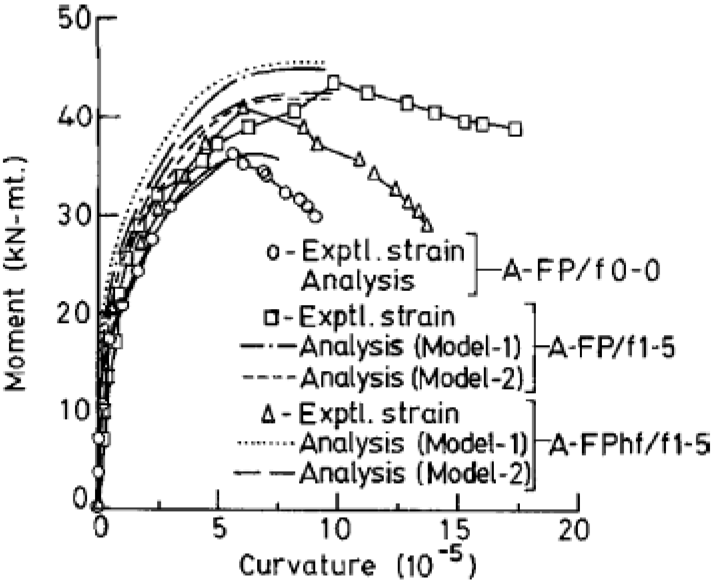

Figure 2.21 Moment-curvature behavior of fully pre-stressed steel fiber reinforced concrete (A-FP/f-0.0: concrete without fiber; A-FP/f-1.5 pre-stressed concrete with full depth %1.5 fiber content by volume; A-FPhf/f-1.5 pre-stressed concrete with half depth %1.5 fiber content by volume (Padmarajaiah & Ramaswamy, 2004)

2.2.4 Steel Fiber Reinforced Concrete Piles

The ductility and energy absorption capacity of piles are the essential factors while designing earthquake resistant pile foundations. In this respect steel fiber is considered as an advantageous material that can add considerable ductility and energy absorption capacity to RC piles. As noted many times in the literature, steel fiber inclusion to the concrete matrix may reduce transverse reinforcement ratio. There is considerable amount of research on the behavior of steel fiber reinforced RC structural elements such as beams and columns. However, studies on SFRC piles are scarce in the literature. In a relatively recent study Bodin & Madhkan (2002), tested four large scale SFRC piles in order to understand their dynamic behavior. It is reported in this study that SFRC piles exhibit higher ductility and a better energy dissipation capacity than conventional reinforced concrete piles. However, piles were dynamically loaded by means of a conventional bending test set-up with mid-span and axial loading. Therefore, test program of Bodin & Madkhan provided structural response data. Behavior of laterally loaded SFRC piles in a subgrade soil was not investigated. Bodin & Madkhan stated that dynamic lateral SFRC pile response would not be superior to that of the regular RC piles if they were not loaded axially at the same time.

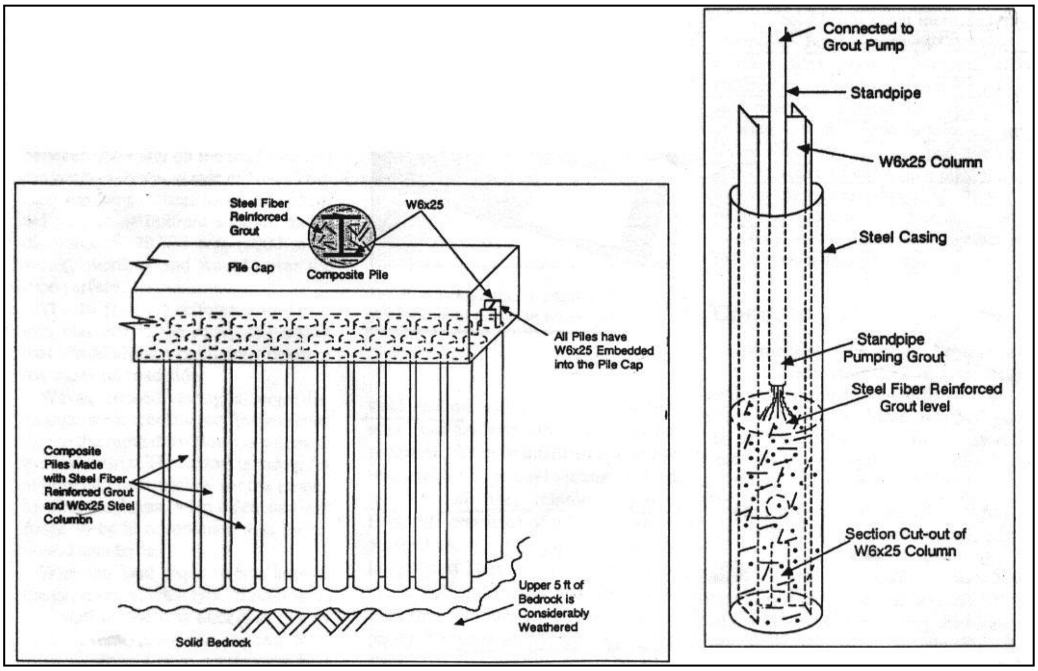

Figure 2.22 Piling arrangement and manufacturing procedure in Mesa Dam project (Bayasi & Downey, 1995)

A well documented use of SFRC piles has taken place in the construction of a flood protection wall for the lower access road leading to the power generation house of Horse Mesa Dam located in 100 km northeast of Phoenix Arizona (Bayasi & Downey, 1995). It was determined that the sides of the access road would be incapable of withstanding a large discharge. The road was washed out six times since February 1968. Pile wall construction was proposed to prevent the road. The engineers decided to construct composite piles consisting of wide flange steel section encased within steel fiber reinforced grout. After the boring was made steel member was placed in the hole followed by the placement of steel fiber reinforced grout into the casing. Pile manufacturing procedure of this project is shown in Figure 2.22. According to Bayasi & Downey use of steel fiber reinforced concrete perhaps made this project possible. They noted as “Steel fibers confine plain concrete and enhance its integrity and crack resistance. Steel fiber grout encasing the steel beam members of the Dam adequate protection was achieved”. Bayasi & Downey (1995), noted that conventional grout was deemed inadequate especially under impact loads from water carried debris. Steel fiber reinforced grout was necessary for adequate impact resistance and toughness.

2.3 Laterally Loaded Pile Foundations

Piles have long been used with the aim of supporting lateral and axial loads for a variety of structures comprising high rise buildings, bridge abutment, offshore platforms, transmission lines, power stations, and highway structures. Piles are foundation elements that can transfer heavy loads from the superstructure to deeper soil layers with higher shear strength and less compressibility. Most structures are subjected to lateral loads due the action of wind, earthquake, impact, blast, waves, and lateral earth pressures.

In many cases, lateral loads govern the design of the pile foundation system. Several theoretical and experimental studies were done with the purpose of establishment of a design method for piles under lateral loading.

In the theoretical studies, analytical results were compared with the test data (Khoadir & Hassiotis, 2005). In the study of Zhang (2009), a method was proposed for non-linear analysis of laterally loaded rigid piles in cohesionless soil. It assumes in the method that both the ultimate soil resistance and the modulus of horizontal subgrade reaction increase linearly with depth. Centrifugal test results and three-dimensional finite element analyses were compared. The system equations were derived for a rigid pile under a lateral eccentric load by considering the force and moment equilibrium. An iteration scheme containing three main steps is then proposed to solve the system equations to obtain the behavior of the pile (Figure 2.23). The degradation of the modulus of horizontal subgrade reaction with pile displacement at ground surface was also considered. The developed method is validated by comparing its results with those of centrifugal tests and three-dimensional finite element analysis. It was reported that the developed method showed good agreement with the experimental results. However, in that study, method was developed in order to understand the response of the rigid steel piles.

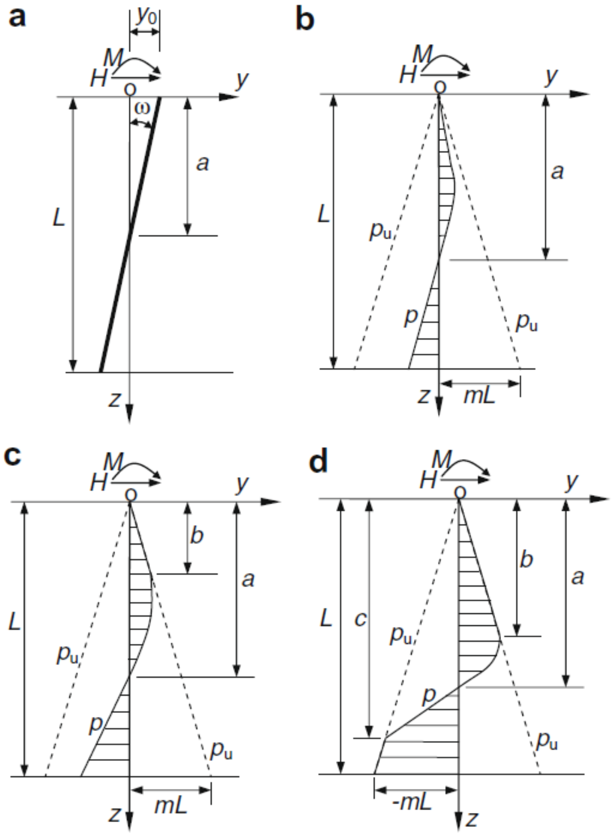

Figure 2.23 (a) A laterally loaded rigid pile; (b) soil reaction distribution with no yielding; (c) soil reaction distribution with yielding only in a region above the rotation point and (d) soil reaction distribution with yielding in regions both above and below the rotation point. (Zhang, 2009)

In experimental studies, various lateral loading test methods were utilized. Laterally loaded pile tests can be classified as centrifugal tests (Gerolymos, Escoffier, Gazetas, & Garnier, 2009), full scale tests under cyclic and static loading (Long & Reese, 1984; Rollins, Lane, & Gerber, 2005) and model pile tests under cyclic and static loading (Singh & Prakash, 1971; Peng, Clarke, & Rouainia 2006). Generally, full scale tests were performed on steel pipe piles (Seed & Reese, 1955; Brown, Morrison, & Reese, 1989). In addition, a few full scale lateral loading tests were made to understand the behavior of reinforced concrete piles (Janoyan, 2001; Hutchinson, Chai, & Boulanger, 2005; Juirnarongrit & Ashford, 2003). Model pile tests were made of usually flexible materials such as aluminum alloy tubes (Patra & Pise, 2001). Zhang, Silva and Grismala, (2005) proposed a method for ultimate lateral resistance calculation to piles in cohesionless soil. The authors evaluated the method results with that obtained centrifugal tests of flexible (aluminum tubes) model piles.

The nonlinear characteristics of model pile as reinforced concrete must be considered for the analysis of soil-pile interaction. It reveals that pile tests and subsequent analyses performed within the scope of this dissertation have a special position when the model pile material (reinforced concrete) is taken into consideration. In the subsequent sections a review of laterally loaded piles are presented.

2.3.1 Available Methods for the Analysis of Soil-Pile Interaction

Laterally loaded pile is a soil-pile interaction (SPI) problem solution of which requires adequate understanding of soil and pile behavior. Researchers have been working on the subject for more than four decades. Some methods, such as the ultimate load capacity approach (Broms, 1964 a-b), the elastic method (Poulos & Davis, 1980, Poulos,1971 a-b), finite element method (Brown, Shie & Kumar, 1989, Ellis & Springman, 2001, Fan & Long, 2005), and the p-y curve approach (Matlock, 1970, Reese, 1977, Murchison & O’Neill, 1984) were developed for the analysis of laterally loaded pile response.

The ultimate lateral load capacity approach is also as called “limit state method”. In this method, ultimate load expresses the failure state: the passive soil failure around the pile or failure of the pile (Fan & Long, 2005). The dimensions of piles are determined in such a manner that it is capable to withstand ultimate lateral soil pressure, p_u, which depends on ultimate strength parameters of the soil. The reaction against the pile is associated with Mohr-Coulomb strength parameters. The approach by Brinch Hansen (1961) is applicable to short piles whereas Brom’s method (1964 a and b) may be used for both rigid and flexible piles. The limit state approach however, does not account for nonlinear soil-pile interaction.

In the elastic method, pile is considered as a structure in a homogeneous linear and isotropic elastic medium (Poulos & Davis, 1980). The relation between soil reaction force per unit length (*p*) and pile deflection at the same depth (*y*) is supposed to be linear. This method is limited to the elastic range.

Currently, finite element method (FEM) is more widely utilized because of its potential to cover a variety of soil-pile interaction problems. Soil resistance and pile deflection relations, (p-y curves) were derived from computed bending moments of a pile in a three-dimensional (3D) finite element model (Brown et. al., 1989). Pile elements were modeled as linearly elastic in this study. The soil response to piles under lateral loads in sand was investigated using non-linear finite element approach by Fan & Long, (2005). A parametric study was performed in order to find the effects of pile properties (stiffness and diameter) and soil properties, (coefficient of horizontal earth pressure and soil dilatancy) on SPI. The sand was modelled using an elastic-plastic constitutive model whereas the piles were modelled as linear elastic materials in this research. It was mentioned in the referred study that the effect of pile stiffness on p-y response was not significant; ultimate soil resistance had a non-linear relationship with pile diameter; ultimate soil resistance increased with coefficient of horizontal earth pressure. Bransby, (1999) performed two-dimensional finite element analyses to find load transfer relationship of laterally loaded piles.

In some studies full-scale and model pile test data were compared with the finite element analyses results. Geotechnical centrifuge tests were performed in order to understand the response of piled bridge abutments on soft clay and plane strain finite element analyses were reported (Ellis & Springman, 2001). Numerical analyses were compared with the test data. It can be noticed from the above mentioned studies that nearly all of the FEM analyses the piles were modeled as elastic structural members. Nonlinearity of the pile was not fully taken into consideration.

The p-y method is commonly used for the analyses of the soil-pile response and more popular among these methods. It is an extension of subgrade reaction method. Laterally loaded pile is often solved as a beam on an elastic foundation (BEF) involving nonlinear modelling of the soil-pile interaction response (p-y curve) (Figure 2.24 and Figure 2.25). The traditional p-y curve models developed by Matlock, (1970) and Reese, Cox, & Koop, (1974) are semi-empirical models where soil response is characterized as independent nonlinear springs (Winkler springs) at discrete locations (Figure 2.25).

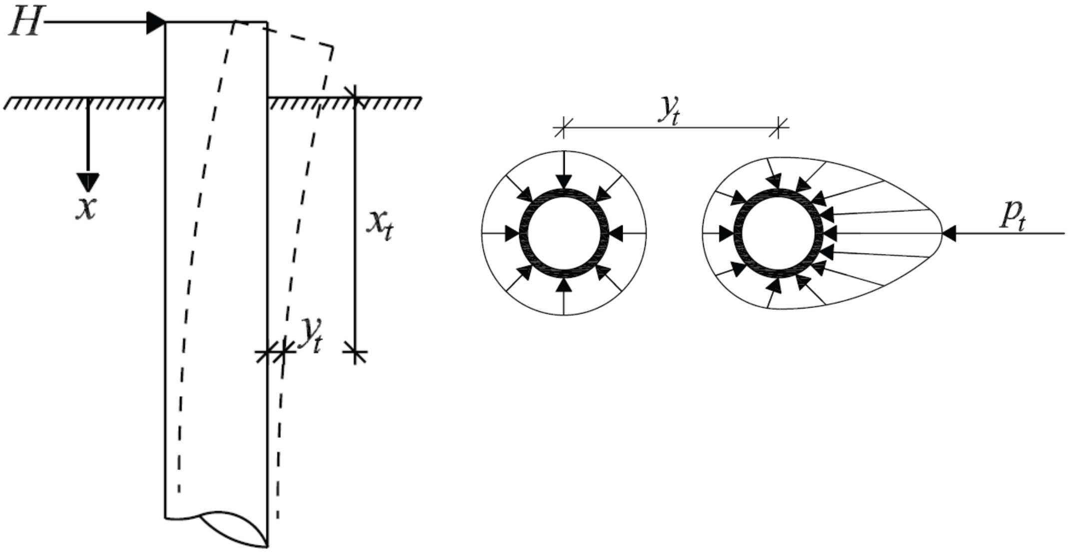

(a) (b)

Figure 2.24 (a) Pile bending under lateral loading (b) Stresses on a vertical pile before and during lateral loading (Reese & Van Impe, 2001)

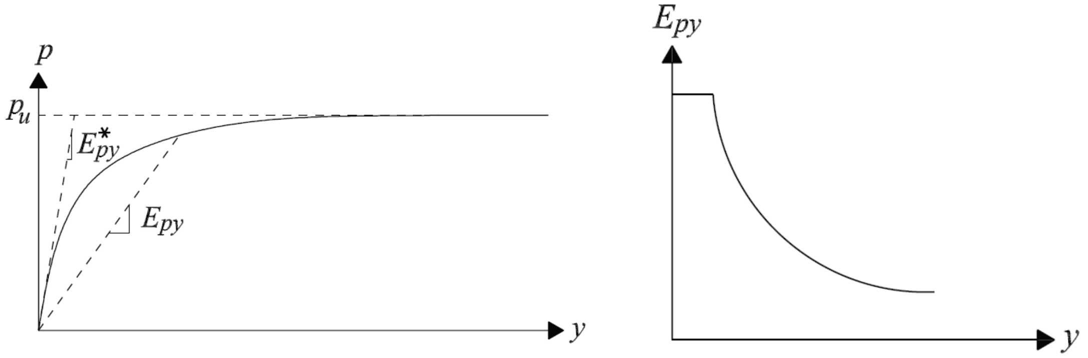

(a) (b)

Figure 2.25 (a) p-y curve and (b) Variation of modulus of subgrade reaction (Reese & Van Impe, 2001)

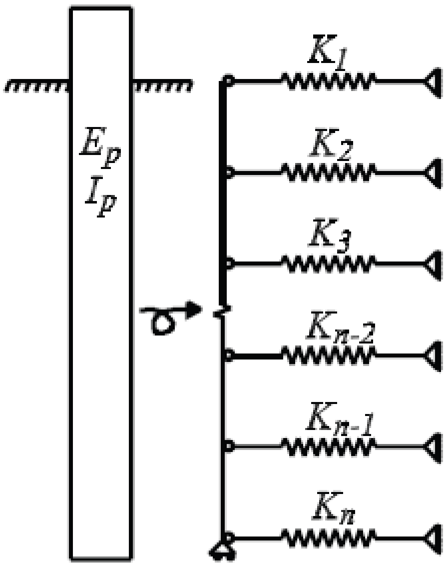

Figure 2.26 The Winkler approach with the pile modelled as an elastic beam element supported by non-linear springs. (Brodbaek, Moller, Sorensen, & Augustesen, 2009)

Typical soil resistance (p: *force per unit length, F/m*) and pile deflection (y: *m*) curve is shown in Figure 2.25 where p_u is ultimate soil resistance and E_{py} (p/y: F/m^2) is modulus of subgrade reaction. Because of the complex stress conditions developed in the soil during pile installation and subsequent loading, Murchison & O'Neill

(1984), stated that complete and comprehensive theoretical derivations of p-y curves have not been developed yet. Ashour & Norris (2000), discussed reliability, another word such as “potential” of the traditional p-y curves in representing true SPI. They paid attention to the fact that currently employed p-y curve models were developed based on the results of field tests in uniform soils such as Mustang Island (Cox, Reese, & Grubbs, 1974), Sabine River (Matlock, 1970) and Houston (Reese & Welch, 1975) tests and that they were adjusted mathematically using empirical parameters to extrapolate beyond specific field test conditions

The formulations for currently available p-y curve models do not directly account for a change in pile’s bending stiffness, EI. Ashour, Norris, & Pilling, (2002) noticed that considering some factors while neglecting the other in the traditional p-y method limits its application. The only pile parameter that is included in the traditional p-y curve formulation is the pile width. The stiffness of the pile and its variation with pile deflection are only represented empirically, a fact resulting in extrapolation of available p-y models to different soil-pile conditions such as p-y curves obtained on steel pipe piles to RC piles and vice versa. Ashour & Norris (2000) considered additional effects such as pile bending stiffness, pile cross-sectional shape, pile-head fixity, and pile-head embedment. The researchers recommended strain wedge (SW) model formulations in order to take such effects into consideration (Ashour & Norris, 1998).

2.3.2 Effect of Pile Bending Stiffness (EI) on Lateral Load-Deformation Curves

Steel fiber addition to concrete alters bending stiffness (EI) of the material. Recent studies demonstrated that effect of pile stiffness on p-y curve is significant as shown in Figure 2.27 and Figure 2.28 (Ashour et al., 2002, Ashour & Norris, 2000). It was stated in the studies by Ashour that the influence of pile properties such as pile bending stiffness on the nature of the p-y curve might be demonstrated via the SW model approach.

Reinforced concrete piles exhibit linear response up to first crack occurrence on the pile. During that stage, stiffness stays constant or varies slightly. Further loadings causes crack development around the hinge location. Bending stiffness reduces suddenly at first crack and then keeps decreasing along the pile by subsequent loadings. The variation in the value of EI has a significant effect on the p-y curve. Ashour, Norris & Shamsabadi (2001) improved SW model in order to predict nonlinear material modeling. It should be note that the effect of bending stiffness on p-y curve was investigated by parametric studies. This is the disadvantage of SW model.

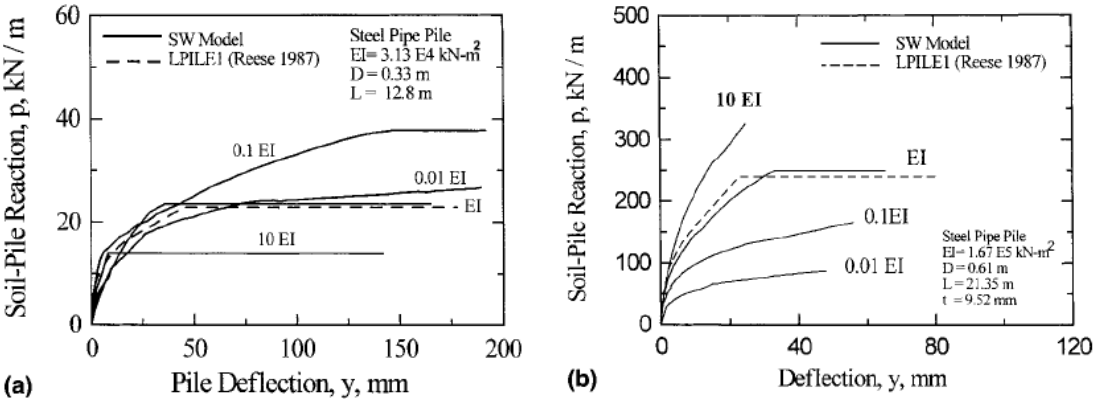

Figure 2.27 Effect of bending stiffness on p-y curve (a) 0.915-m depth at Sabine River test site, clay (b) 1.83-m depth at Mustang Island test site, sand (Ashour & Norris, 2000)

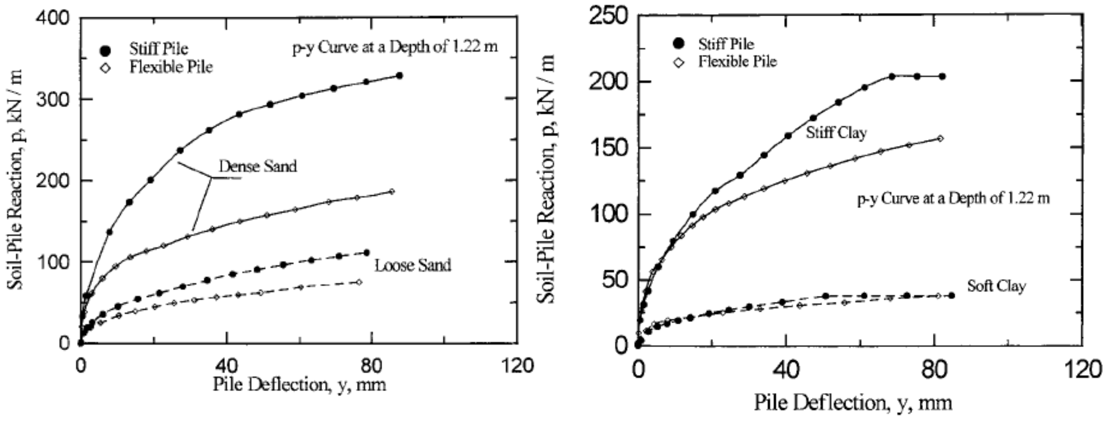

Figure 2.28 Effect of bending stiffness on p-y curve (a) in sand (b) in clay (Ashour & Norris, 2000)

The strain wedge (SW) model analyzes the response of laterally loaded piles based on a representative soil-pile interaction methodology that incorporates pile and soil properties. The SW parameters are related to predicted 3D passive wedge of soil developing in front of the pile. It is explained that the basic purpose of the SW model is to relate stress-strain-strength behavior of the layered soil in the wedge to 1D beam on an elastic foundation (BEF) parameters. The SW model is able to provide a theoretical link between 3D soil-pile interaction and 1D BEF characterization. One obtains corresponding BEF parameters by linking the SW model to BEF analysis through iterative solution of the following governing differential equation:

$$EI\left(\frac{d^4y}{dx^4}\right)+E_s(x)y=0 \qquad (2.1)$$

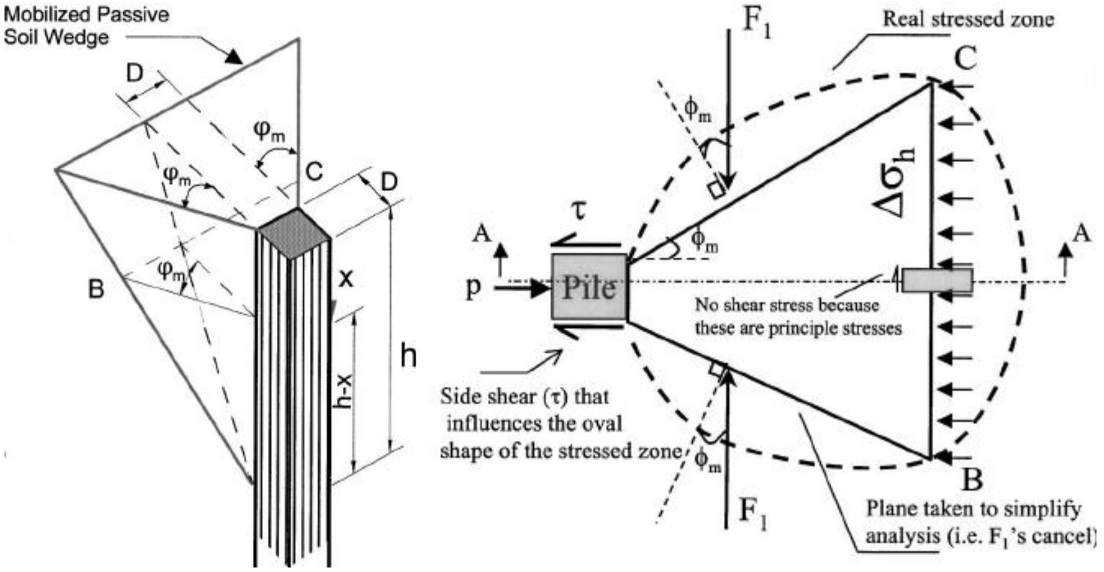

(a) Basic strain wedge (SW) model (b) Force equilibrium in a slice of the wedge at depth x

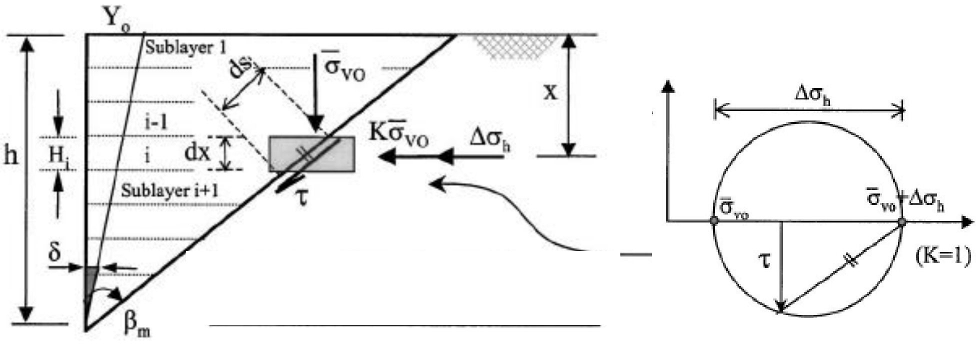

(c) Forces at the face of the soil passive wedge (section elevation A-A)

Figure 2.29 Characterization and equilibrium of strain wedge model (Ashour, Pilling, & Norris, 2004)

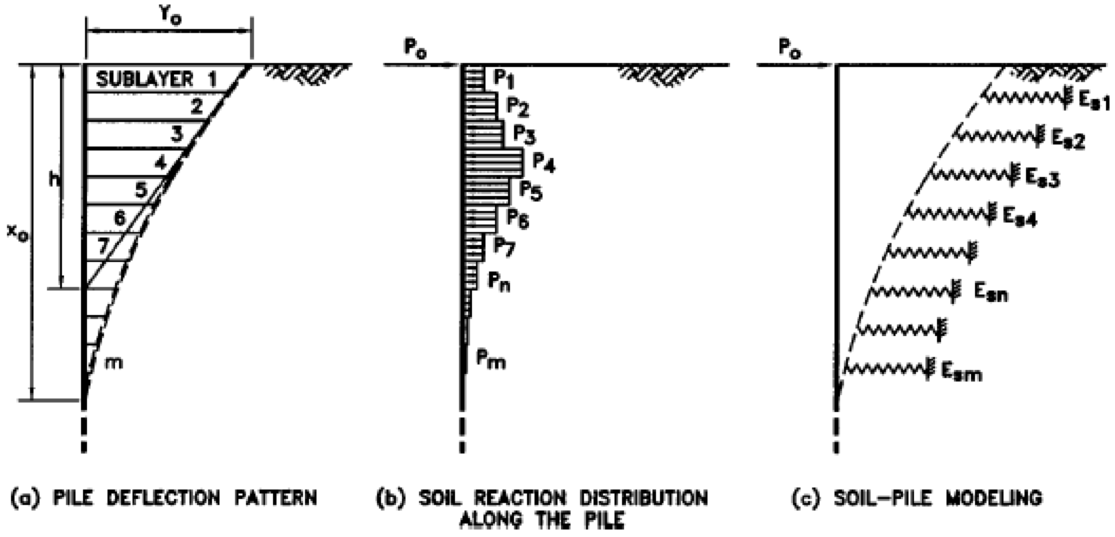

(a) PILE DEFLECTION PATTERN (b) SOIL REACTION DISTRIBUTION ALONG THE PILE (c) SOIL–PILE MODELING

Figure 2.30 Distribution of soil-pile reaction along deflected pile (Ashour, Pilling, and Norris, 2004)

Basic configuration of SW model and distribution of soil-pile reaction along the deflected pile are shown in the Figure 2.29 and Figure 2.30. Mobilized passive wedge in front of the pile is characterized by base passive wedge depth, h; the mobilized friction angle, ϕ_m , angles $\theta_m = 45 - \phi_m/2$ and $\beta_m = \theta_m + 90$. Multi sublayer technique is used for application of the SW model to divide the soil profile and the loaded pile into sublayers and segments of constant thickness (Figure 2.29 c).

In the literature some researchers have emphasized the effect of nonlinear moment-curvature relationship on reinforced concrete pile behavior. The cracking of the concrete occurs early in the loading with a considerable reduction in pile bending stiffness, EI. Further reductions take place as bending moment increases. Test data on moment-EI relationship of reinforced concrete piles and the effect of axial load (P) on this relation are shown in Figure 2.31 (Reese & Van Impe, 2001).

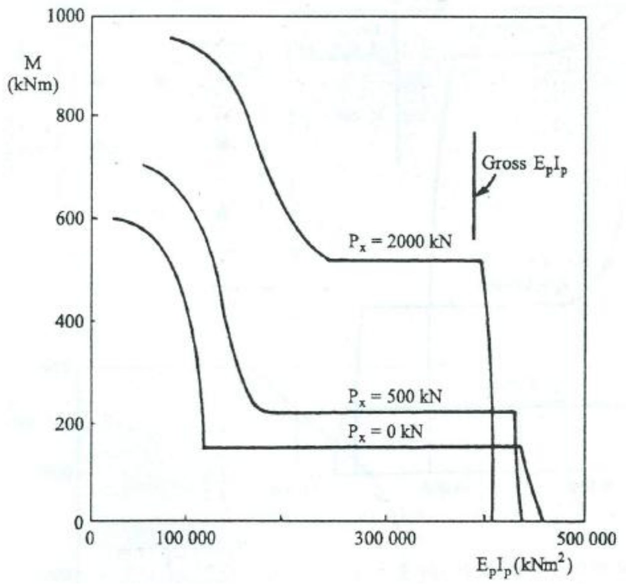

Figure 2.31 Moment- E_pI_p relationship of a tested reinforced concrete pile (Reese & Van Impe, 2001)

Investigations have been done to characterize the nonlinear lateral load response of bored piles, drilled earth retaining wall (Wang, 1986; Janoyan, 2001; Hutchinson, Chai, Boulanger, & Idriss, 2004; Juirnarongrit & Ashford, 2005; Limkatanyu, Kuntiyawichai, Spacone, & Kwan, 2008). Janoyan (2001) indicated that researchers generally use constant EI values for soil-pile reaction and pile deflection (p-y) analysis of reinforced concrete. In that study, Janoyan performed full-scale field tests on large diameter shaft with a 1.8 m in a stiff clay. Pile was instrumented with strain gauges in order to get bending moments. Curvature was calculated from the gauge records. The p-y curves were developed based on curvature measurements of the pile using bilinear moment-curvature relationship. An investigation was done to understand the effect of nonlinear variation of EI along a pile on head deflection of pile and maximum bending moment development by Wang (1986). It can be seen in this study that there are significant differences in load-deflection curves (Figure 2.32). In the referred study, the lateral load analyses show that the flexural rigidity changes dramatically with moment along the pile (Figure 2.33).

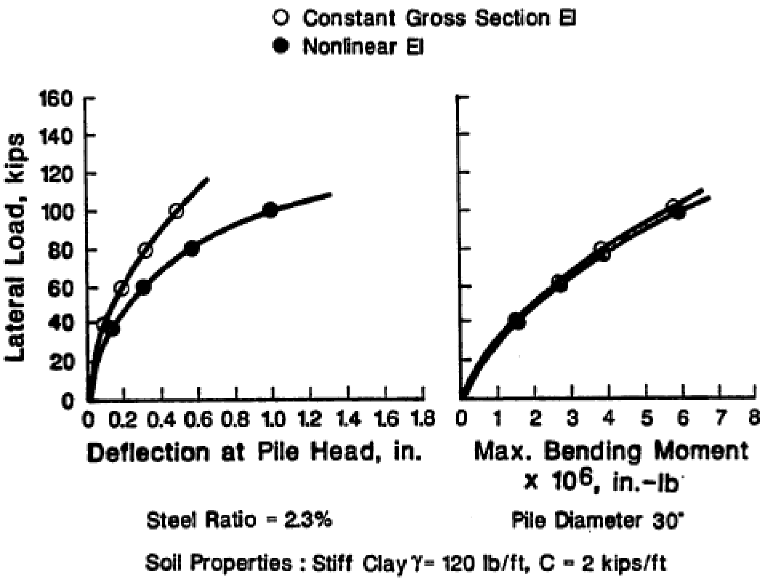

Figure 2.32 Influence of EI on pile head deflection (Wang, 1986)

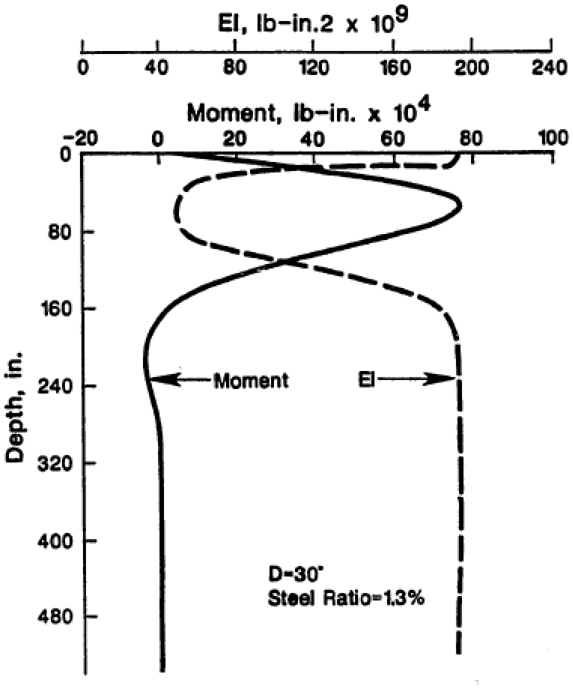

Figure 2.33 Bending moment and EI along the pile under lateral loading (Wang, 1986)

Nip & Ng (2004), introduced a method of back-analysis for long piles using inclinometer data and assuming fourth-order polynomial to represent the variation soil reaction along the pile. Tests were performed on concrete piles 28.0 m and 29.5 m long and 1.5 m in diameter. The nonlinear concrete response was considered in this study by adjusting EI along the length of the pile based on relationship of flexural stiffness and bending moment shown in Figure 2.34.

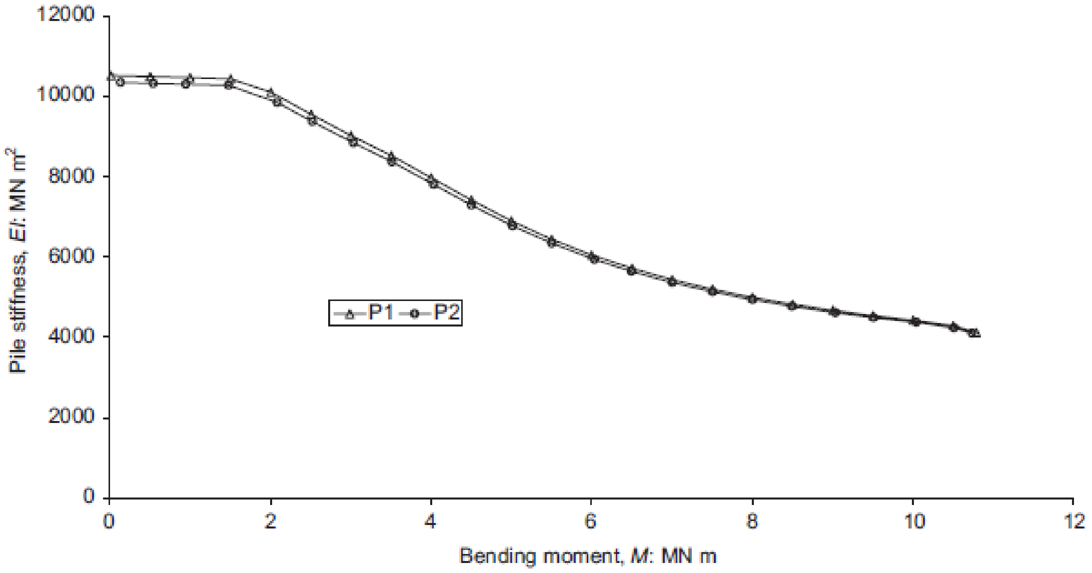

Figure 2.34 Computed relationship between pile flexural stiffness and bending moment; P1-pile 1 and P2- pile 2 (Nip and Ng, 2004)

Four full scale reinforced concrete piles were tested in two different soil conditions: loose dry sand and dense dry sand (Chai & Hutchinson, 2002). The pile with a diameter of 0.406 m and tested length of 5.48 m, was embedded in a large soil container 6.71 m in diameter and 5.49 m in length (Figure 2.35and Figure 2.36). The axial load was applied with two high-strength steel tie-down rods and cyclic lateral load was applied. Particular interests of the research are the lateral strength and stiffness of the pile-soil system, maximum moment depth, and plastic hinge depth in the pile. Researchers indicated that the local deformation can be characterized in terms of the curvature distribution along the pile. Measured-curvature distribution is shown in Figure 2.37. It is concluded that curvature in loose sand spread larger than that of tested pile in dense sand.

Figure 2.35 Soil-reinforced concrete pile test set up
(Chai & Hutchinson, 2002)

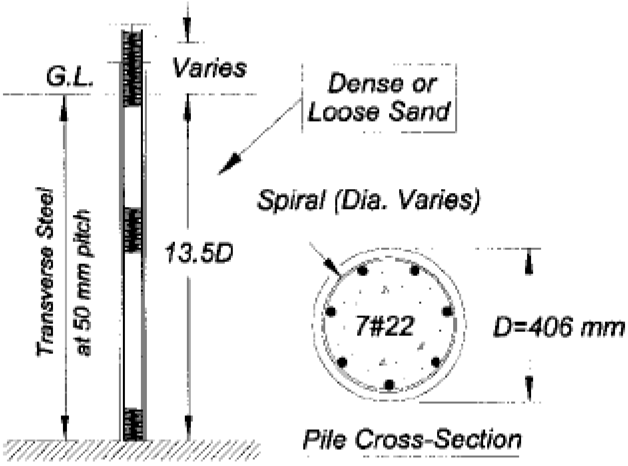

Figure 2.36 Reinforcement details of the test pile
(Chai & Hutchinson, 2002)

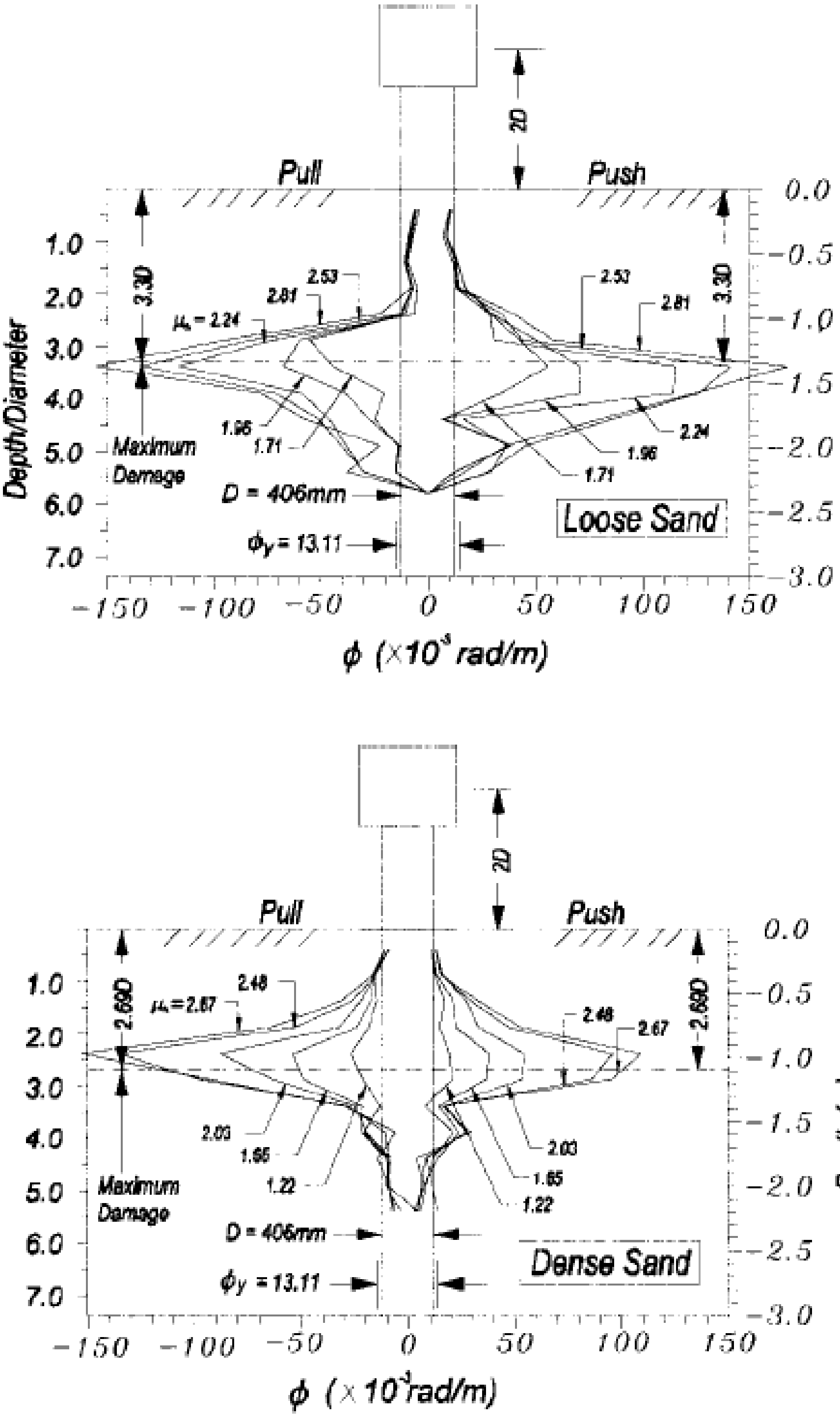

Figure 2.37 Curvature distributions of tested piles (Chai & Hutchinson, 2002)

CHAPTER III
INFLUENCE of STEEL FIBERS on SOIL-PILE INTERACTION

3.1 Introduction

It has been noticed in the past that piles have faced damage under major lateral loads (Mizuno, 1987; Fujii, Cubrinovski, Tokimatsu, & Hayashi, 1998). It has been demonstrated by previous observations that increasing pile dimensions or reinforcement may not be adequate for satisfactory pile design that are resistant to heavy lateral loads. This fact has triggered intensive research in the last two decades and resulted in better understanding of lateral load carrying mechanisms of pile foundations. Major improvements to design and analysis methods have been made in the past (Kagawa & Kraft, 1981; Tao, Kagawa, Minowa, & Abe, 1998; Mylonakis, Nikolaou, Gazetas, Tazoh, 1997; Nikolaou, Mylonakis, Gazetas, Tazoh, 2001). Knowledge accumulated during model and field test studies have played an important role in the development of new analysis methods (Abendroth & Greimann, 1990; Dickin & Nazir, 1999; Patra & Pise, 2001). Such research and past experiences revealed that use of more ductile piles have become a necessity since high pile curvatures are unavoidable for most cases. However, allowable inelastic action of such piles and their allowable ductility under lateral loading conditions, on the other hand, has not been fully studied yet and more research effort is needed on this subject (Gazetas & Mylonakis, 1998). Fiber reinforced concrete *sfrc* can be considered as a contemporary material being able to provide desired additional ductility to conventional reinforced concrete *rc* piles.

Influence of steel fibers on soil-pile interaction was investigated using the data of laterally loaded model piles (Akdağ, 2004) in order to gain insight on load-deformation (p-y) curves of steel fiber reinforced concrete, *sfrc,* piles. It was hypothesized that nonlinear pile material behavior might play an important role on soil-pile interaction (SPI). Three different steel fiber ratios by volume were utilized in the production of model piles. Performances of these piles were compared with that of the conventional concrete pile. The goal was to observe the influence of steel fibers on ductile pile behavior by isolating them from other reinforcement components (i.e. bending and shear reinforcement). The experimental p-y curves for *sfrc* and concrete piles in medium dense sand and their comparison with the finite element model analyses and available p-y establishment techniques (Özden & Akdağ, 2009) enabled the design of a more advanced testing system for further model tests on reinforced concrete piles.

3.2 Model Tests of Steel Fiber Reinforced Concrete (SFRC) and Concrete Piles

Concrete and steel fiber reinforced concrete model piles were subject to monotonic lateral load tests in a testing pool housing the subgrade materials (i.e. medium dense sand and gravel) and the testing piles. Three types of materials including steel fibers, concrete, sand and gravel were utilized throughout the study. Hooked-end steel fibers were used in the production of *sfrc* piles. Length, diameter and aspect ratio of the hooked-end steel fibers were set as 30 mm, 0.55 mm and 55. Respective values of the water/cement ratio and cement content of the conventional concrete and *sfrc* batches were set as 0.45 and 495 kg per cubic meter. The designed compressive strength is equal to 40 MPa.

The overall testing system consists of the testing pool, the testing frame, model test pile, and a loading mechanism including a loading reel, a steel rope and a metal load transfer fastener. The cross-section of the concrete pool, model pile and the loading mechanism are illustrated in Figure 3.1 where dimensions are in centimeters. Plan dimensions of the pool were established as 150 cm x 130 cm the longer side being in the loading direction. Diameter and length of the model piles were set as 7 cm and 105 cm. The soil surrounding the pile was artificially prepared in two layers. Layers were compacted by dry tamping method. The upper layer consisted of medium dense uniform silty sand whereas the underlying gravel layer was well-graded. The soil layers were in dry condition throughout the testing program. The sand layer served as the main subgrade material whereas the bottom gravel layer functioned as the dense soil providing necessary soil support to the pile so that the pile would not exhibit rigid body motion and occurrence of at least one plastic hinge was ensured while the piles were loaded to failure.

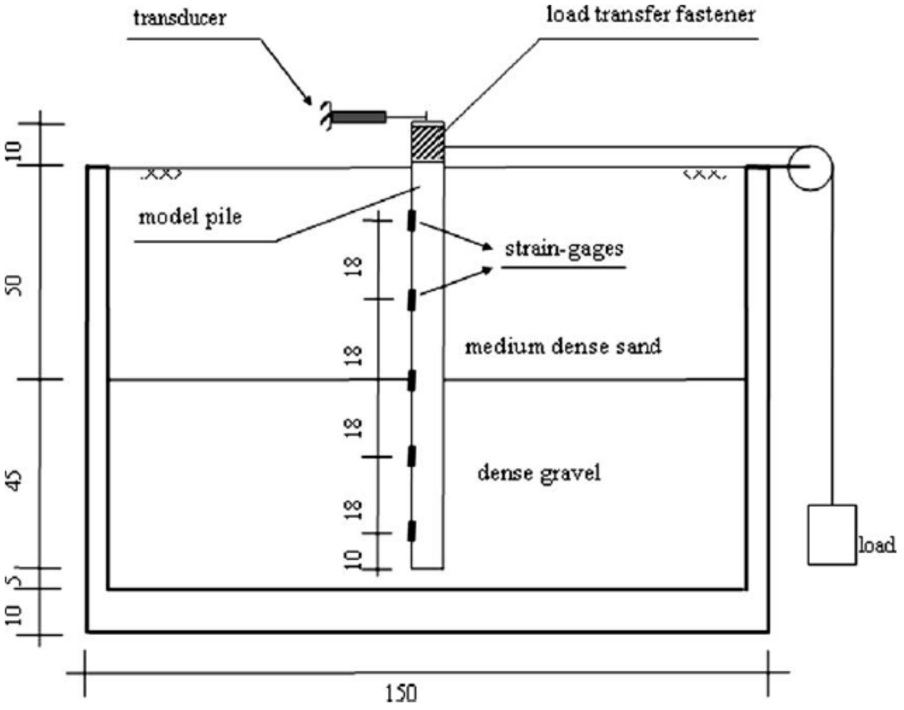

Figure 3.1 Soil-pile model testing system.

Number of piles that could be accommodated in the pool during the testing program was decided following three dimensional finite element analyses where the entire testing system was modeled. The FEM analyses revealed that the optimum number of piles to be placed in the pool would be two since interference took place among the wedges when there were more than two piles. One may notice this fact in Figure 3.2 a and b. The interference between the piles is obvious through plastic points reminding that the sand surrounding the neighboring pile would be distorted when the pile next to it is loaded for the three piles case (Figure 3.2 b). The loaded pile in the two piles case, on the other hand, does not generate such a negative effect on its neighbor (Figure 3.2 a). Therefore, the test series were pursued placing two piles in the pool and loading one pile at a time for each test. Instrumentation of the testing system involved installation of strain-gages, pile head transducers (Figure 3.3) and a data-conditioning set-up.

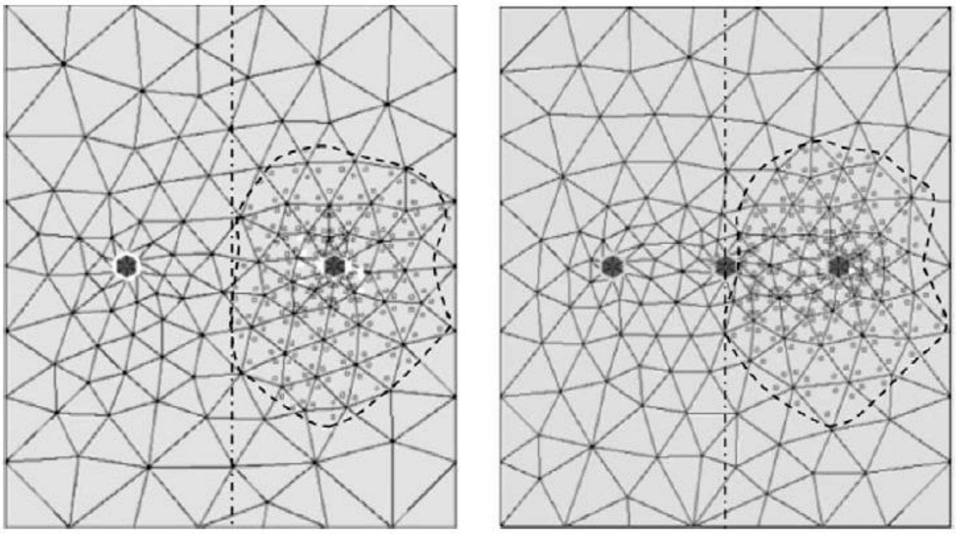

Figure 3.2 Finite element models: (a) with two piles; (b) with three piles.

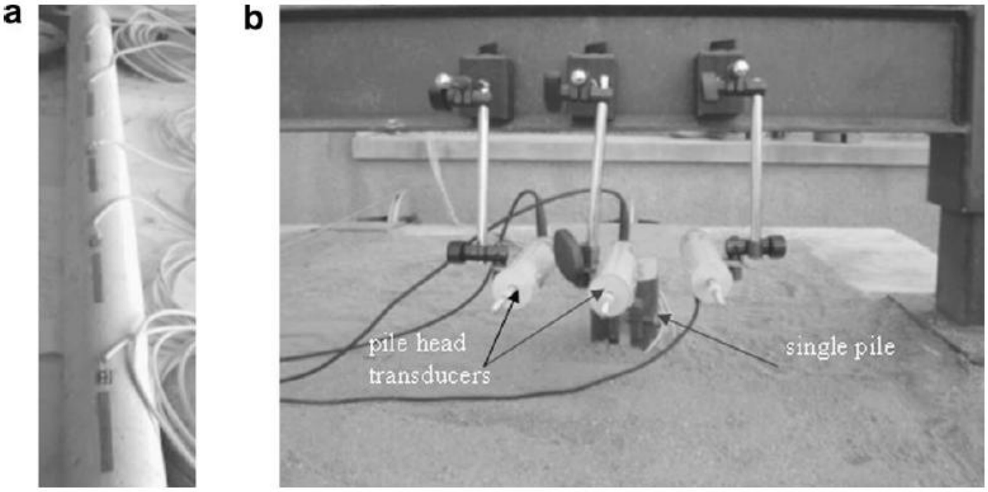

Figure 3.3 Instrumentation of the testing system: (a) strain-gages bonded on the model pile; (b) model pile head displacement transducers.

3.3 Results and Discussions of Model Pile Tests on SFRC and Concrete Piles

Lateral load tests involved testing of model *sfrc* and concrete piles. Steel fiber reinforced concrete, *sfrc* piles with only hooked-end fibers were produced at fiber contents of 0.75% (Test-d), 1% (Test-c) and 1.5% (Test-b) by volume. The test performed on the concrete pile was named as Test-a. All tests were load controlled and conducted monotonically with equal load increments. Corresponding pile head displacements and bending moment variations along the pile length were measured and recorded at each load increment step. All model piles of the testing program failed developing plastic hinges. The number and location of these hinges, however, varied depending on the pile material. The piles in Test a and Test d developed single hinge whereas piles Test b and Test c failed with double hinges (Figure 3.4).

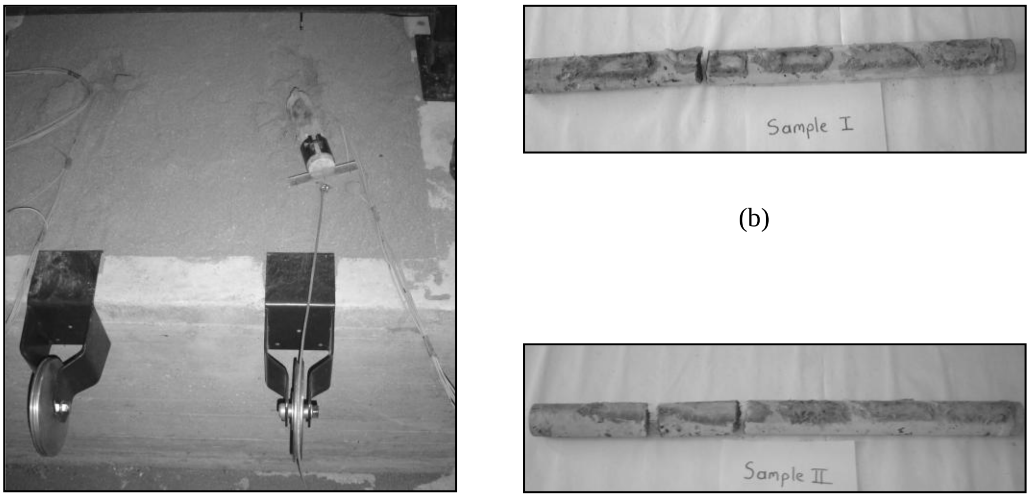

(b)

(a)

(c)

Figure 3.4 Failure patterns of model piles (a) Pull-out behavior (b) damaged concrete pile (c) damaged *sfrc* pile with 1.5% steel fiber.

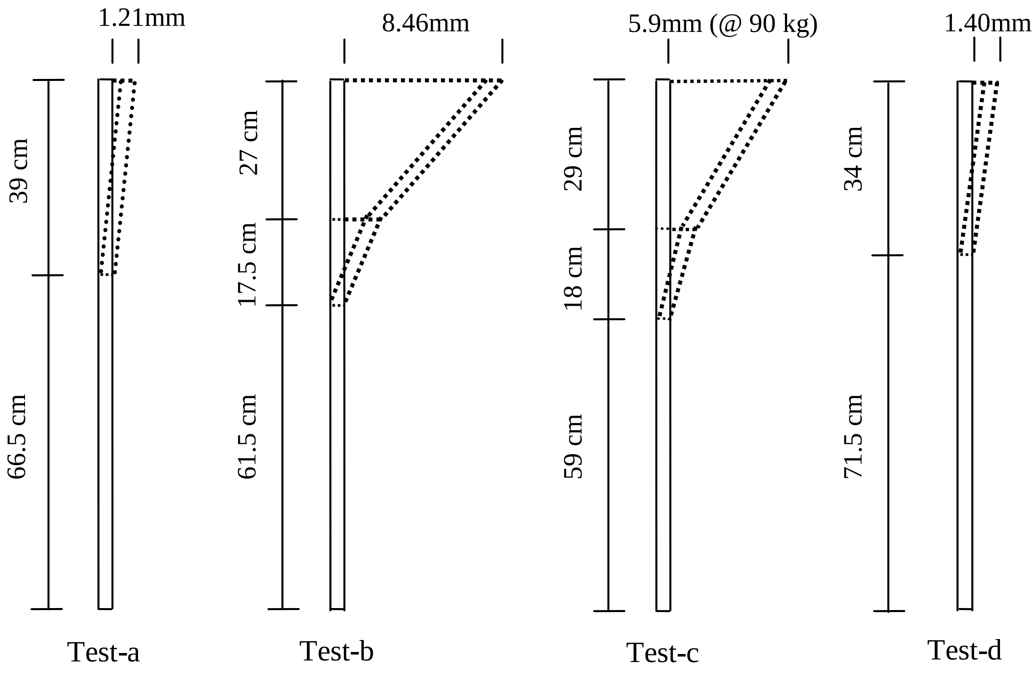

Figure 3.5 Failure locations and final head displacements of model piles.

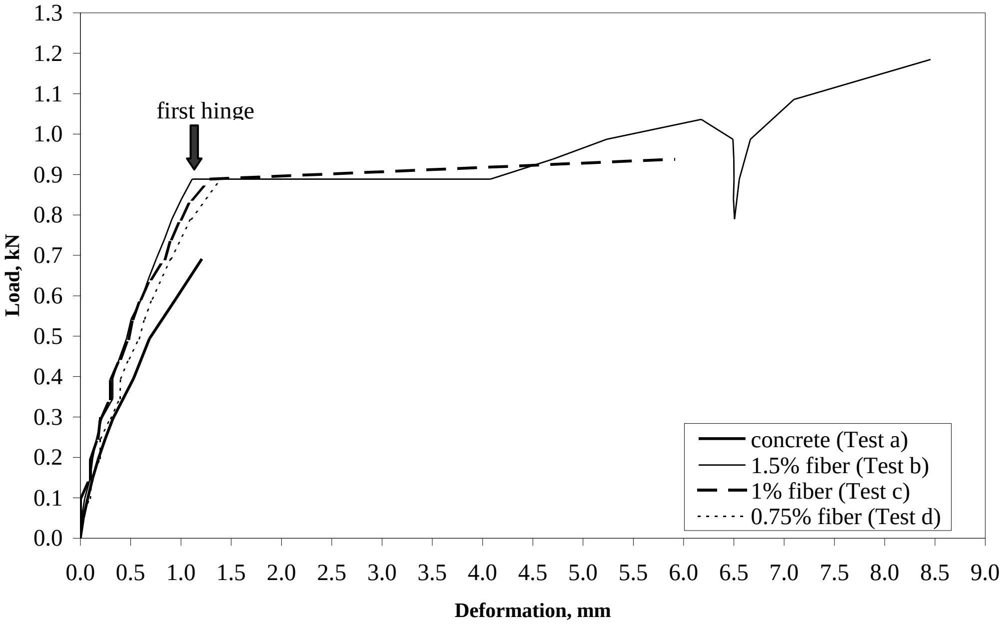

Figure 3.6 Load-pile head displacement relationship (Özden & Akdağ, 2009)

Damage patterns of the piles along with their final head displacements are illustrated in Figure 3.5. One should note in this figure that deformation readings could not be recorded in Test-c beyond 5.9 mm until complete failure took place since enough travel space for the displacement gage has not been left accidentally during its installation before the test. The *sfrc* piles with 1.0% and 1.5% steel fiber (Test-c and Test-b) experienced a sudden head displacement increase at the moment the first hinge has developed (Figure 3.6). The pile of Test-b, however, was able to carry additional load increments after excess deformations under constant load due to steel fiber pull-out mechanism gradually ceased after 4.0 mm of pile head displacement. The upper portion of the pile above the first hinge sustained imposed lateral loads until complete failure took place with the development of the second hinge. It is evident in Figure 3.6 that no head displacement recovery took place when the pile was unloaded at 6.5 mm of head displacement indicating plastic deformations on the pile. Variations of recorded bending moments along the pile length are given in Figures 3.7 a and b where they were grouped with respect to the number of hinges developed in the tests. The failure moments in Test-a and Test-d were almost equal to each other as shown in Figure 3.7 a. However, maximum lateral load at which the pile in Test-d failed was 28% larger than that in Test-a. The fact that recorded bending moments were less in Test-d for a certain lateral load level such as H=0.69 kN is an indication to a more flexible response when compared with the concrete pile of Test-a. A similar comparison of the *sfrc* piles (Test-b and Test-c) revealed that the pile with 1% steel fiber generated the smallest bending moment at the same lateral load (H=0.88 kN) where the initial hinge took place (Figure 3.7 b).

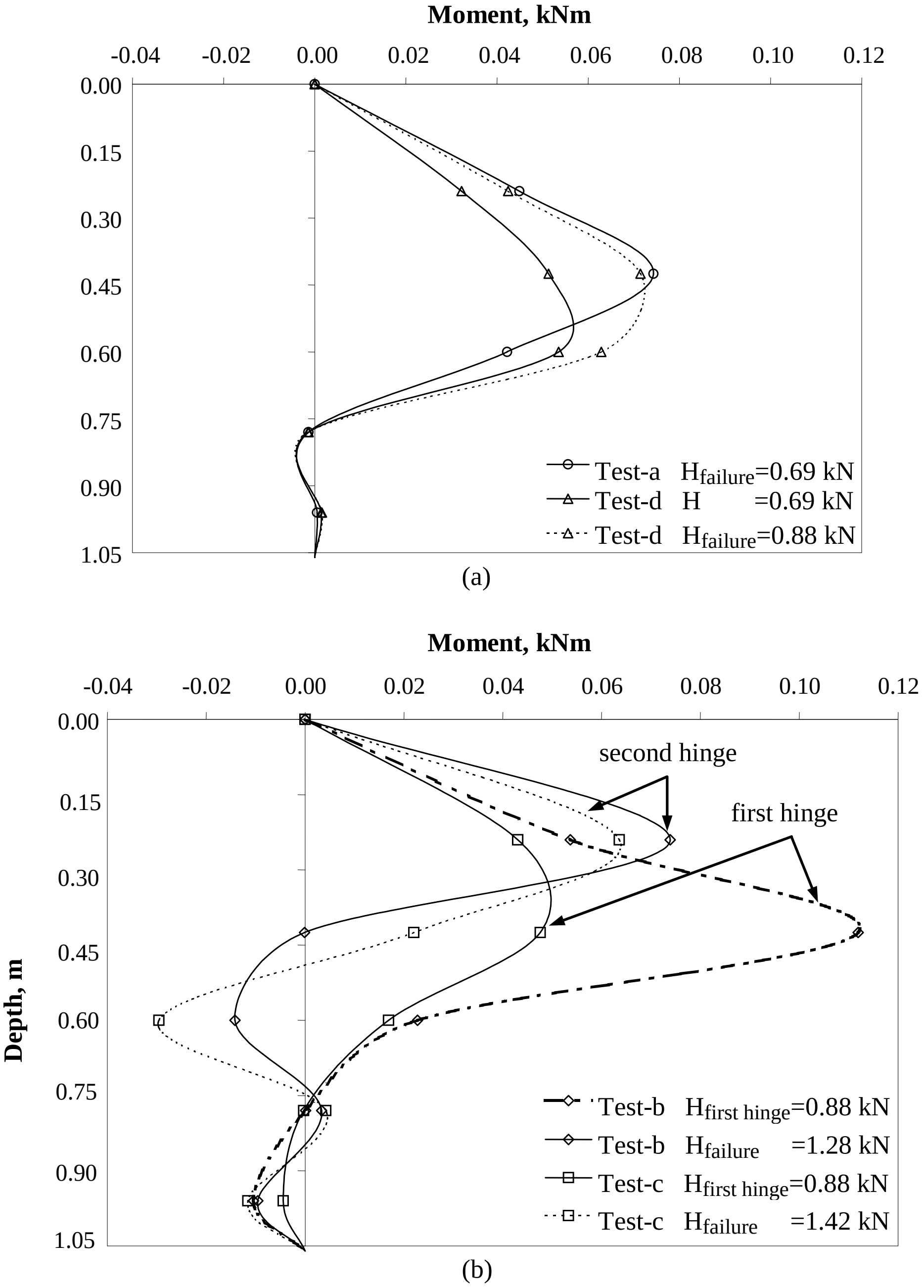

Figure 3.7 Comparison of bending moment distributions (a) Test-a and Test-d (b) Test-b and Test-c (Akdağ, 2004)

3.4 Soil-Structure Interaction Aspects of SFRC Piles

The complete pile failure in model tests was observed as the pull-out of the pile from the surrounding soil. The pull-out failure as used here for *sfrc* piles describes the failure mechanism where bonding between steel fibers and the concrete matrix cannot sustain generated stresses and the portion of the pile above the plastic hinge is pulled out of the sand. As mentioned above, number of plastic hinges was not the same for Test-b, Test-c, and Test-d. Following the development of the first hinge in Test-b and Test-c, the piles were not pulled out of the surrounding soil as opposed to Test-d. The portion of the pile between the lower and upper hinges stayed in the subgrade sand as shown in Figure 3.8. It is thought that steel fibers at the location of the first hinge in Test-b and Test-c were able to hold the pile inside the sand due to the reestablished interlock with the concrete matrix after a certain amount of sliding took place following the occurrence of the first hinge. The occurrence of single hinge in model concrete pile (Test-a) can be explained by generation of tensile stresses that are higher than the tensile strength of the concrete.

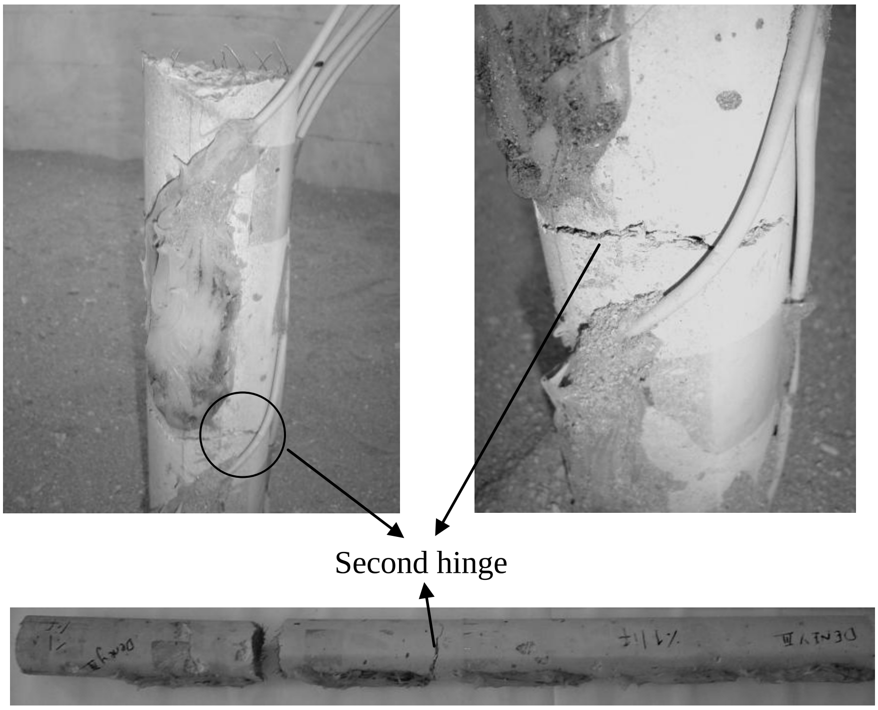

Figure 3.8 Damaged *sfrc* pile with 1% steel fiber, Test-c (Özden & Akdağ, 2009)

The mechanism that is effective on the behavior of *sfrc* piles towards failure can be explained by means of the interplay between soil and pile and number of fibers per section. The lower portions of the piles below the first hinge remained in place as a result of the confinement effect of the surrounding soil in Test-b and Test-c. The downward side friction acting along the pile surface reduces pull-out stresses on the steel-fibers at the first hinge location. This mechanism is illustrated in Figure 3.9. The number of fibers per section was less in Test-d (with 0.75% steel fiber) and has resulted in lower pull-out strength. This has avoided development of double plastic hinges in Test-d.

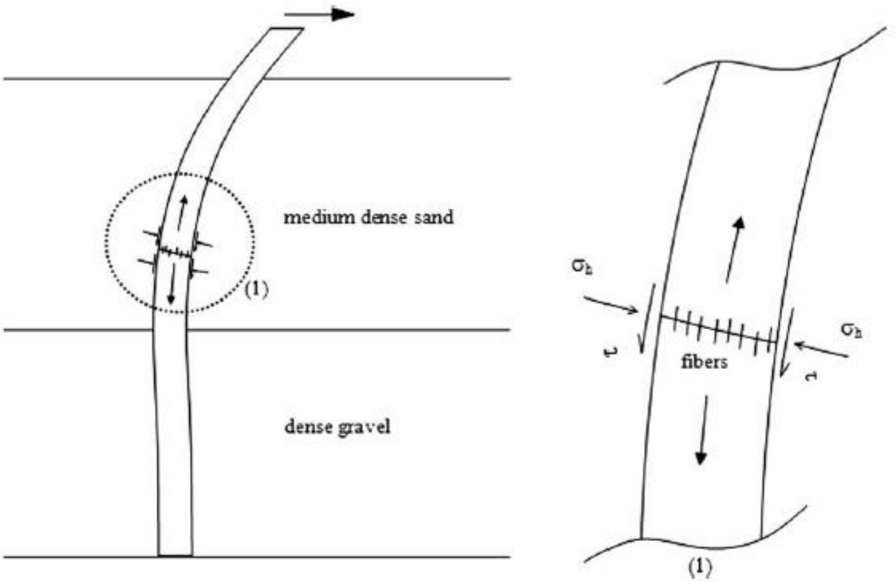

Figure 3.9 Fiber pull-out mechanism in surrounding soil (Özden & Akdağ, 2009)

The soil-pile interaction could be expressed by means of nonlinear load-deformation relationships (p-y curves). These curves were derived using the data of the second strain gage mounted at 23 cm below the pile head until the first hinge occurred. The gages close to and below the first hinge location generated low and somehow fuzzy excitations. The load transfer to the lower portions of the model piles and recorded data was probably influenced by discontinuities nearby the plastic hinge.

Distribution of shear, soil resistance, and pile deformation with depth, however, were obtained by successive integration and differentiation of the recorded bending moment data using cubic spline interpolation. Bending stiffness values of the test piles were adjusted during iterations so that measured pile head displacements were matched during double integration. This has been necessary in order to account for the nonlinear response of the pile material to lateral loading (Reese & Van Impe, 2001).

The p-y curves based on test data are given and compared with the curves based on hyperbolic p-y curve model (Murchison & O’Neill, 1984), a technique later adapted by the American Petroleum Institute (API) as the standard procedure, finite element analysis and Strain Wedge analysis of the model tests (Figure 3.10.). It should be noticed that the ultimate soil resistance utilized by the hyperbolic p-y curve model is significantly less than maximum soil resistance values based on model test data. This may be attributed to the fact that the ultimate soil resistance as used in the industry standard p-y models American Petroleum Institute (API, 2000) is based on limited field data where steel pipe piles were tested in saturated dense sand (Cox, Reese, and Grubbs, 1974). Similar findings were also reported in the past on laterally loaded model piles where API based p-y curves yielded soil resistance values that were significantly smaller than those of the experimental curves (Yan & Bryne, 1992). Analyses of field lateral load tests on a variety of piles (pre-stressed concrete, steel and timber) also showed that API based p-y curves underestimated experimentally derived soil resistances (Prakash & Kumar, 1996). There have been several research studies in order to overcome the drawbacks of the above mentioned p-y models. The strain wedge model of Ashour and Norris is an approximation in modeling soil-pile interaction since it was possible to take the influence of pile stiffness on p-y curves into consideration (Ashour & Norris, 1998; Ashour & Norris, 2000). The p-y curve developed for the concrete pile (Test-a) using the strain wedge model simulated the experimentally derived curves more realistically in terms of both stiffness and ultimate strength characteristics (Figure 3.10). This may be attributed to the fact that soil deformation and pile stiffness characteristics are considered in a more systematic fashion in the strain wedge model (Ashour et al., 2002). However, SW model isn't based on experimental studies. It is necessary to verify or improve the strain wedge model with the data obtained in a more comprehensive testing program of reinforced concrete model piles.

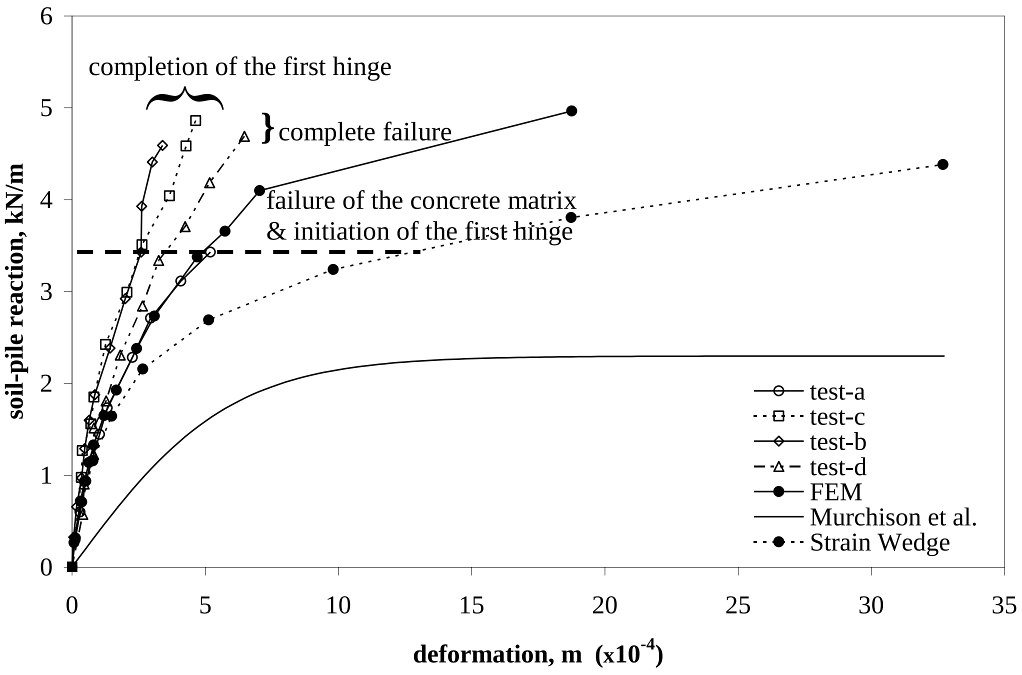

Figure 3.10 Soil-pile reaction versus deformation curves 13 cm below the soil surface (Özden & Akdağ, 2009)

Load-deformation curve obtained by means of 3D finite element analyses of the model tests, however, was found to be in good agreement with experimental p-y curves (Figure 3.10). Soil-pile interaction at the pile surface was taken into consideration using interface elements where strength reduction factor was assigned as 0.77 in the FEM models. The Mohr-Coulomb material model was utilized as the soil model. The angle of internal friction values were assigned as 35.7° and 42° for the sand and gravel layers in the Mohr-Coulomb model, respectively. The elasticity module of the upper sand and underlying gravel layers were assumed to vary linearly with respective module definitions of E_S=0.154z and E_S=7.54+1.936z where z is the depth parameter. This assumption was based on the evaluation of the secant soil-pile module determined through the back analyses of the model test data. The Poisson's ratio for the pile material was assumed as 0.15 and 0.30 for soil materials.

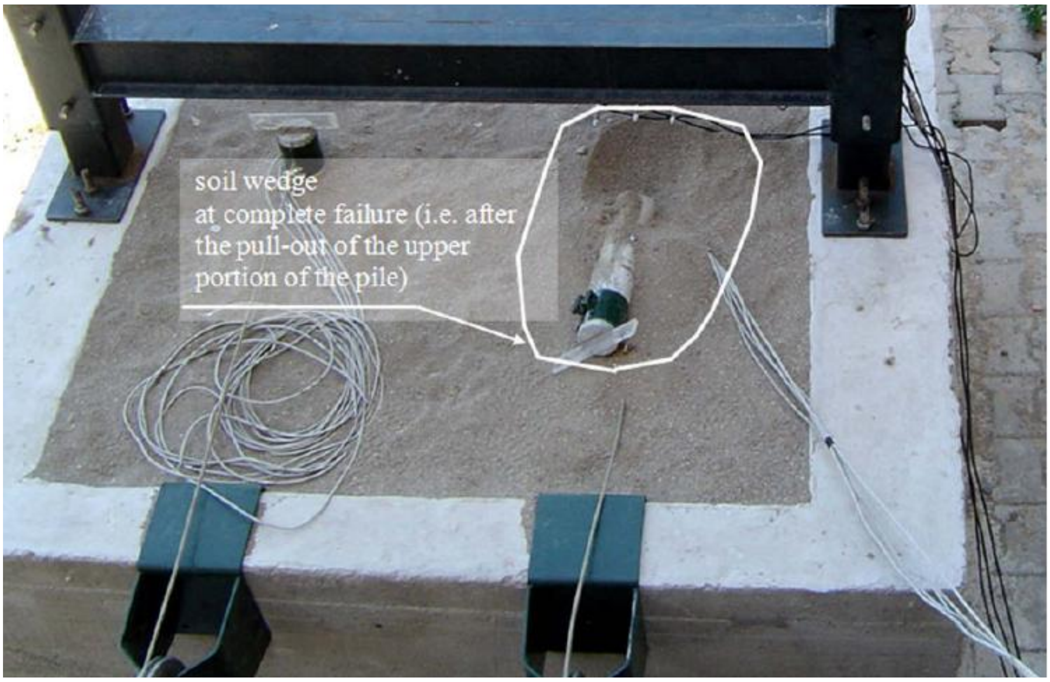

Figure 3.11 Condition of the sand surface around the test pile (Özden &Akdağ, 2009)

This study provided insight regarding lateral load carrying mechanism and interaction of *sfrc* piles with cohesionless soils. Addition of steel fiber increased lateral load capacity of model piles as much as 28% compared with the concrete model pile. This fact can be attributed to the stress distribution and absorption capacity of *sfrc* due to fiber bridging, interfacial de-bonding and sliding mechanisms (Li, F., & Li, Z. 2001).

The soil–pile interaction especially affected *sfrc* model pile response by means of side friction stresses acting along the pile surface thereby reducing pull-out stresses on steel fibers. Positive influence of soil side friction on fiber pull-out stresses has resulted in the occurrence of a second hinge on the remaining portion of the pile above the first hinge for piles with steel fiber ratio higher than 0.75%. Comparison of experimental load–deformation curves (p–y curves) with those from available analytical models and FEM analyses revealed that the first hinge has been initiated in the model piles just before the soil has reached its ultimate resistance as shown in 3.10. This stage is represented by a dashed line in the figure. It can be noticed that the slope of the experimental p–y curves above this line remarkably increased indicating rigid pile behavior. The soil wedge observed during model tests occurred as the upper portions of the piles were pulled out of the surrounding soil (Figure 3.11). There were no significant deformations on the sand surface before the pull-out failure. It was possible to obtain experimental p-y curves until the completion of the first hinge for Test-b and Test-c (i.e. piles with 1.5% and 1% steel fibers) beyond which strain gage readings reversed their sign due to the rigid motion of the pile in the soil after it has reached its ultimate resistance.

The preceding discussion about model pile tests on *sfrc* and concrete piles, experimental p-y curves and finite element analyses revealed that steel fiber could improve lateral pile behavior. However, *sfrc* piles still behave rigidly without bending reinforcement and further tests are necessary to investigate the response of reinforced concrete piles with added steel fibers. API based p-y curves and contemporary strain wedge model failed to completely trace the experimental p-y curves. A similar trend was also observed in FEM analysis although it provided a better fit p-y curve to the experimental one. It appears that decrease of pile bending stiffness (EI) has a major influence on soil-pile interaction (SPI). This aspect of SPI has only been taken into consideration indirectly in currently available models. It is considered that realistic p-y curve establishment would not be possible for reinforced concrete piles without incorporating nonlinear pile material behavior into the current p-y establishment procedures. The model tests were performed under pure monotonic loading conditions and expected positive contribution of steel fibers to pile response under faster loading rates could not be observed. Axial load was not applied during the tests necessitating consideration of this factor in future tests.

A more comprehensive testing program is planned and pursued in order to account for the above mentioned factors (i.e. influence of pile bending stiffness on SPI, loading rate and axial load effects on lateral pile response). The steel fiber ratio by volume is decided as 1% since the model pile tests analyzed herein showed this ratio as the most efficient one. Details of this testing program and discussions of the test data are presented in the following chapters.

CHAPTER FOUR

TESTING SYSTEM AND TESTING MATERIALS

4.1 Introduction

The objective of this research is to study the effects of nonlinear behaviour of concrete with bending reinforcement and steel fibers pile (*ws-sfrc*) and conventional reinforced concrete piles (*rc*) on the SSI. Therefore, it has been necessary to establish a small-scale testing system to compare test performance of the model piles. The second issue is to set up a bending test system to get the moment-curvature relationship of the model piles by testing flexural elements. The effect of the pile stiffness, EI, on soil-structure interaction (p-y response) was investigated with considering nonlinear moment-curvature relationship of flexural elements. In the following sections, model pile and test container dimension determination criteria are described. Soil-pile interaction model test system, concrete mix design, characteristics of model pile materials, preparation of model piles and subgrade material properties are expressed. Model pile instrumentation and testing procedure is explained. Description of bending test system and calibration studies of model piles are presented in this section.

4.2 Model Pile and Test Container

The dimensions of the model pile and the test container were determined according to geotechnical scaling laws (Wood, 2004) and overall boundary effect considerations. Mix design rules for concrete with steel fiber are also explained for when deciding about the pile section.

4.2.1 Scaling of the Model Pile

When the stiffness of the soil surrounding the pile in the test container and in the field (i.e. prototype pile) is identical, Equation 4.1 in the following is recommended;

$$E_m I_m = \frac{1}{n^4} E_p I_p \qquad 4.1$$

where, $E_m I_m$ = *rigidity of model pile*

$E_p I_p$= *rigidity of prototype pile*

n= *scale factor*

Same Young's modulus were selected for both prototype and model pile corresponding to the compressive strength 30 MPa. Considering Wood's recommendations, model piles dimensions with 7.0x7.0 cm square section and 160 cm length was decided. Prototype dimensions of that model pile were calculated with 40x40 cm square and 9.25 m in length. Scale factor, *n* was obtained as 5.75, nearly 6.

An essential factor that would affect the maximum aggregate size in the mix is considered as the size of the element since too small molds with respect to the maximum aggregate would result in the formation of gaps and honeycomb voids at the surface of the element. A general criterion in order to avoid such disturbances is stated as the maximum size of aggregate particles generally should not exceed one-fifth the narrowest dimension of the concrete member or three-fourths the clear spacing between reinforcing bars (Kosmatka & Panarese, 1994). Selecting model pile width as 7.0 cm in square is compatible with minimum element width requirement of five times the maximum aggregate size, 8 mm, in the mix (B pile=70 mm > 5x8 = 40 mm).

Hooked-end straight steel fiber ZP30/0.5 with an aspect ratio L/d=60 was used L and d being the length (30 mm) and width (0.5 mm) of the fiber, respectively (Figure 4.1. The manufacturer reported the specific gravity of the fiber as 7.80 kg/dm^3. This type of steel fiber is the smallest hooked-end fiber to be used in the mix and readily available in the Turkish market. Besides short fibers with an aspect ratio less than 50 are reported to be not able to interlock and can easily be dispersed by vibration (ACI, 96). The steel fiber dictated the maximum size of the aggregate in the mix since fiber length, *l* should be at least 1.5 to 2 times the diameter of the maximum aggregate (DSİ, 1999). The maximum aggregate size has been decided as 8 mm to comply with this requirement (*l*-fiber=30>2x8=16mm).

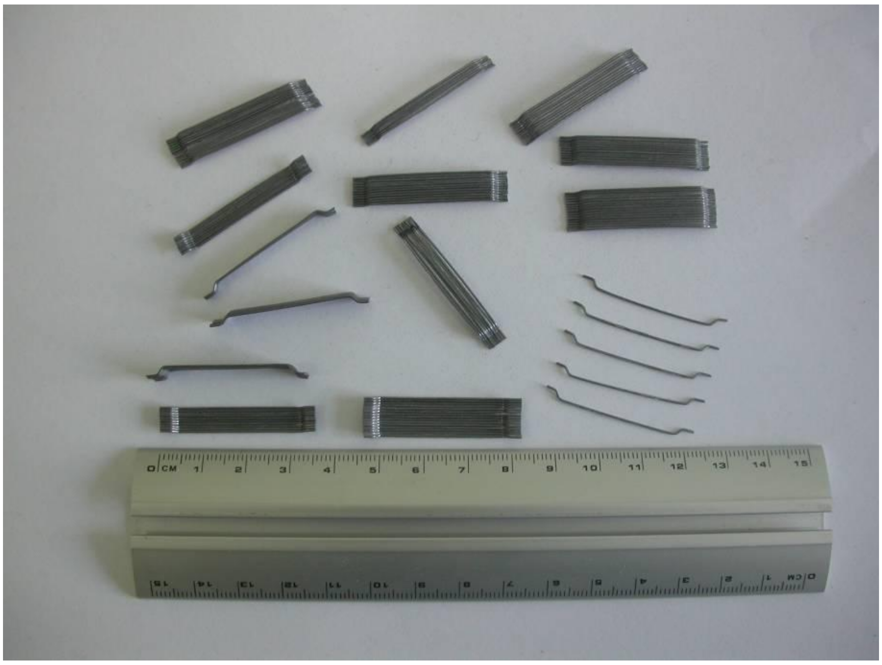

Figure 4.1 Steel fibers used in *sfrc* mix design

The length of the model pile has been set as 1.60 m in order to keep 1.50 m of the length inside the medium dense sand layer. The important point was to avoid the rigid motion of the pile in sand layer. This was deemed essential for all types of the piles since it was desired to continue lateral loading until failure. Previous p-y analyses (Reese, 1984) showed that cracks may occur up to a depth of critical depth (x_c), 1.00 m from the soil surface for the conventional reinforced concrete model pile. The embedded pile length into the sand has been decided 1.50 m to ensure fixed support at the bottom of the model pile. The length of the pile embedded in medium dense sand layer became 1.50 m leaving 0.10 m long portion above the sand for lateral load application and pile head displacement transducer deformation readings.

4.2.2 Test Container

Theoretical solutions for a laterally loaded pile showed that induced stresses and deformations are damped with a sufficiently large outside radius of R around the pile (Equation 4.2) (Baguelin et al., 1977). The soil zone that is heavily affected by pile deformation has been reported as two-pile radius and loading influence becomes negligible beyond ten-pile radius. These considerations can be summarized as in Equations 4.2:

$$\sigma_r, u_r \;\approx\; 0 \text{ at } \mathrm{R} \geq 10\mathrm{r} \qquad 4.2$$

where σ_r, u_r, r are radial stress, radial deformation, pile radius, respectively.

The plan dimensions of the test container were determined by considering passive wedge formation in front of the loaded pile. Wedge type failure theory was developed by Reese et al., (1974) to estimate the ultimate soil resistance near the ground surface. It is assumed that as a result of the deformation of laterally loaded pile, a passive wedge occurred at shallow depths above critical depth (x_c) (Figure 4.2).

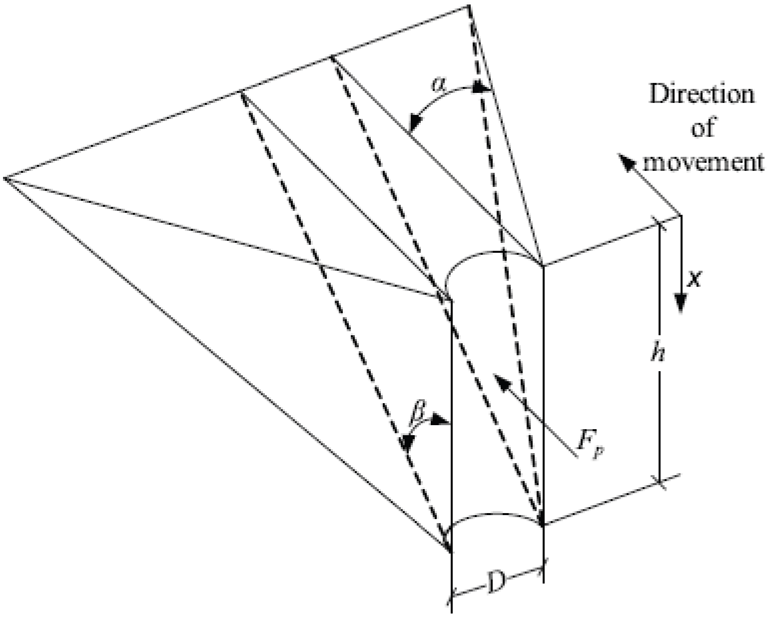

Figure 4.2 Assumed passive wedge failure (Reese et al. 1974)

Preliminary analysis was done on reinforced concrete model pile (rc-pile) by using computer program COM624 (Reese, 1977). Analysis result was assessed by taking into consideration the maximum bending moment depth in order to estimate the passive wedge depth. Moment distribution along the depth demonstrates a rigid behaviour under lateral loading as can be seen in Figure 4.3. Nonlinear behaviour of reinforced concrete pile, in terms of stiffness (EI) reduction with the increase of the lateral load was not taken into account in computer program COM624. The importance of the effect of bending stiffness (EI) on the behaviour of model pile is detailed in *Section 2.3.2*. This analysis was made only to estimate the maximum bending moment depth approximately. Maximum bending moment was estimated at a depth of 66 cm from the pile head according to analysis as can be seen from Figure 4.3.

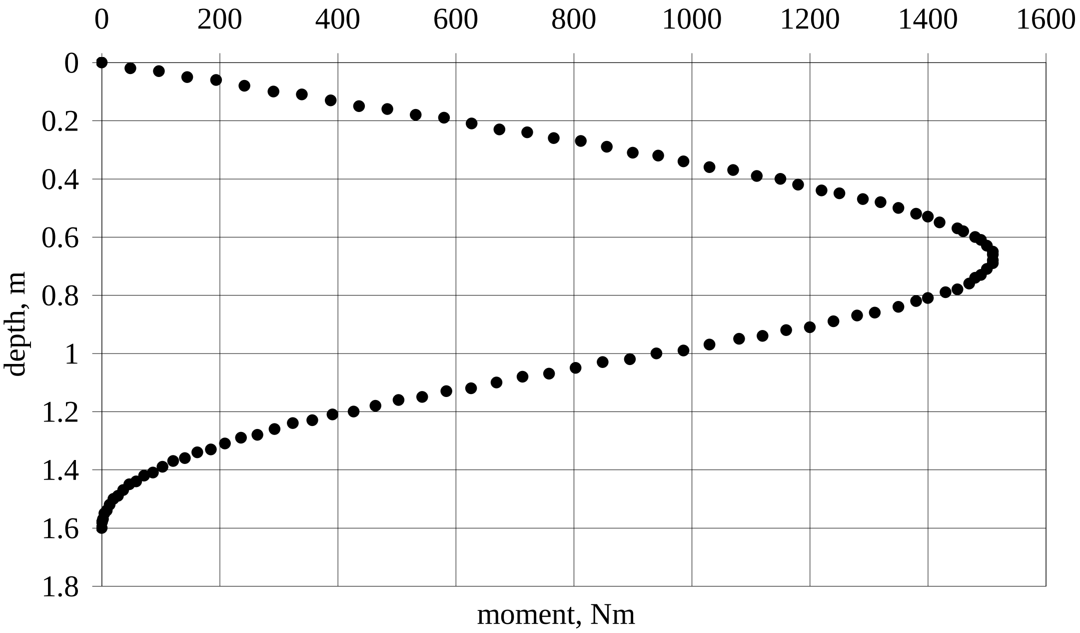

Figure 4.3 Moment distribution result of analysis

When considering the long portion of the pile above the sand is 10 cm, passive wedge depth from the soil surface is estimated as H=56 cm (Figure 4.4). The formation of the passive wedge in front of the pile is obtained as below:

$$AE = GF = H\tan\beta \qquad 4.3a$$

$$\beta = 45 + \frac{\phi}{2} \qquad 4.3b$$

$$\alpha = \phi/2 \qquad 4.3c$$

$$BE = CF = AE\cdot\tan\alpha = H\cdot\tan\beta\cdot\tan\alpha \qquad 4.3d$$

$$AG = EF = D \Rightarrow BC = 2BE + D \qquad 4.3e$$

The angle of internal friction, ϕ=32° (Explained later in this chapter)

Passive wedge depth, H=0.56m

Wedge angle, β=61°

Fanning angle α=16°

D= 7 cm $\Rightarrow AE = GF \cong 100$ cm and BC= 65 cm

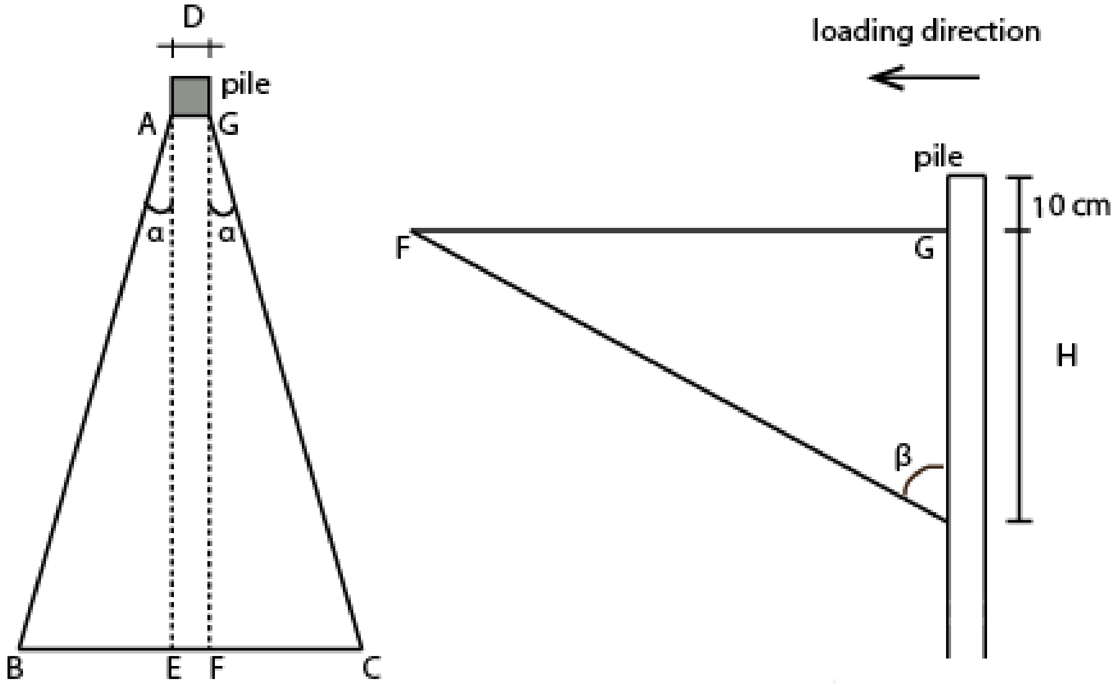

Figure 4.4 Plan and section patterns of passive wedge

The test container was designed to be 150 cm in height and 200 cm by 150 cm in the plan. The overview and the details of the container are presented in Figure 4.5a and 4.5b. As the sand is removed easily following the experiments, two windows were placed on the one of the box walls as can be seen in Figure 4.4. As explained in the above section the width of the model pile has been decided as 7.0 cm. The passive wedge formation and x≥10r lateral loading criteria are provided when the model pile is located at the centre of the testing pool as illustrated in Figure 4.6.

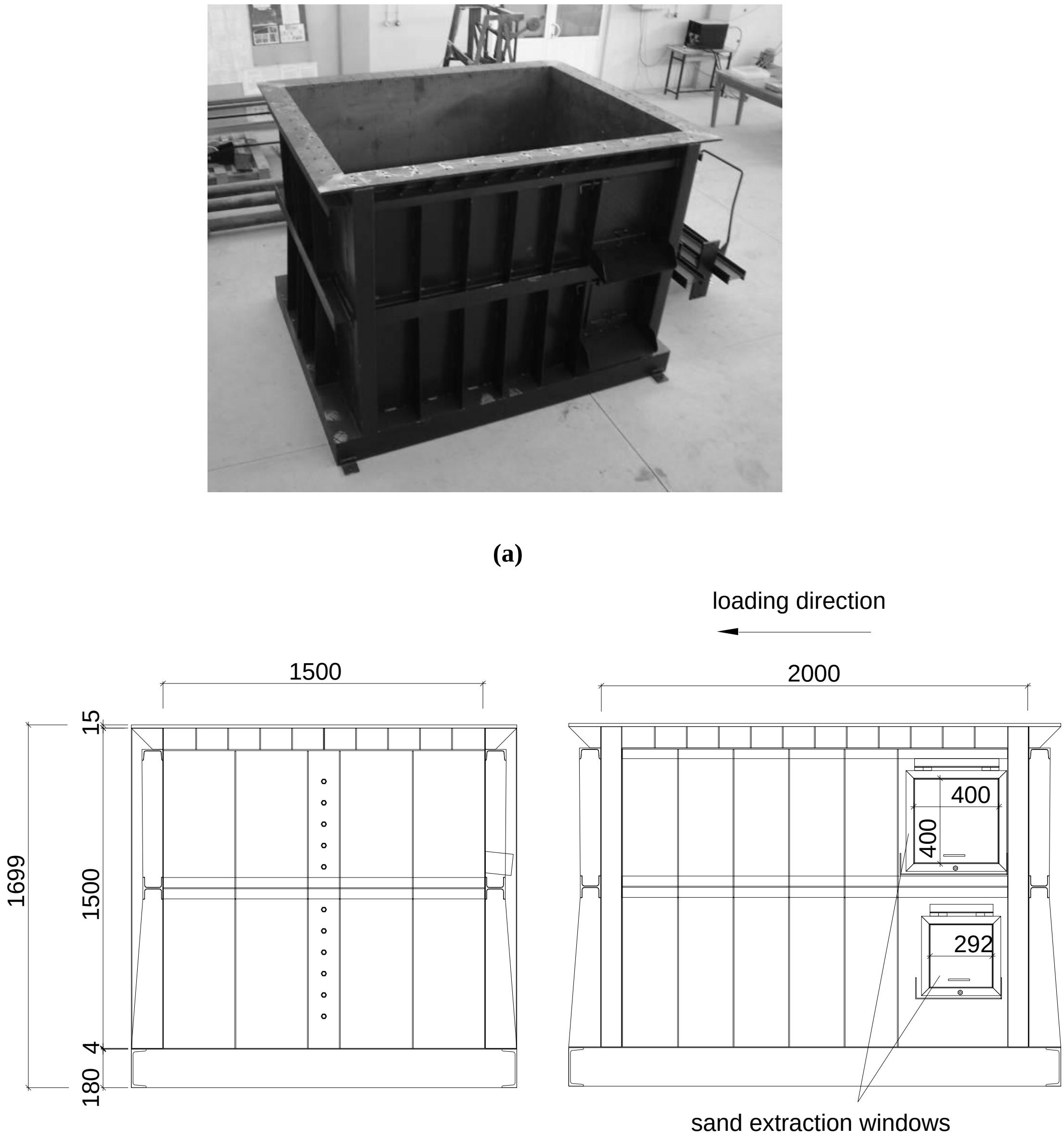

(b)

Figure 4.5 (a) Overview of the test container (b) Side view with dimensions

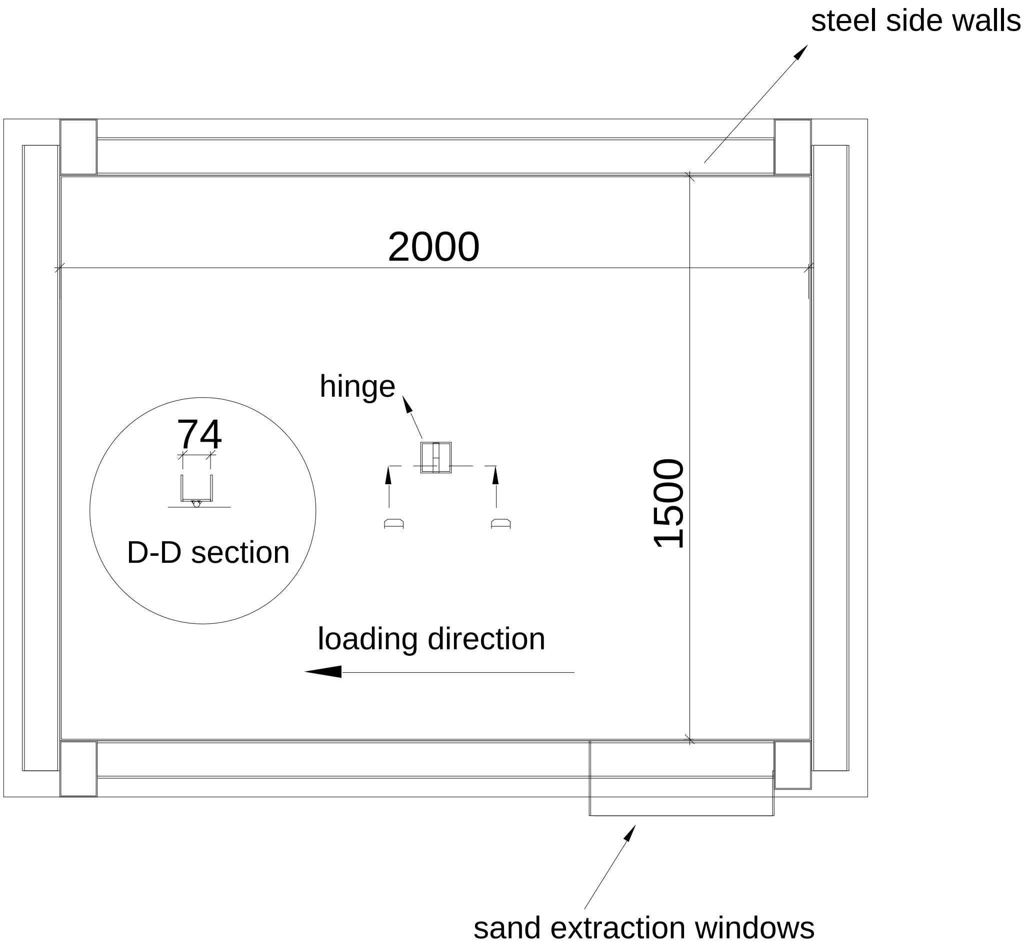

Figure 4.6 Plan dimensions and hinge details of test box

Plan dimensions with hinge details can be seen in Figure 4.6. Hinge was mounted at the middle and the bottom of the test container to control the boundary conditions. It was designed in order to prevent the moment generation at the tip of model pile.

4.3 Testing System

The goal of this study is to investigate static lateral load behaviour of steel fiber reinforced concrete pile, bending reinforced and steel fiber reinforced concrete pile and compare test performance with that of the conventional concrete and conventional reinforced concrete (rc) pile. Appropriate soil-structure interaction model test system was established for this purpose. It was considered that the projected model tests would constitute a firm ground for future in-situ field pile loading tests of rc- steel fiber piles. The cross-section of testing system is illustrated in Figure 4.7. The overall testing system was modelled to consist of the following basic items:

a. Model pile
b. Test container
c. The testing frame
d. Lateral and axial loading mechanism
e. Data acquisition system

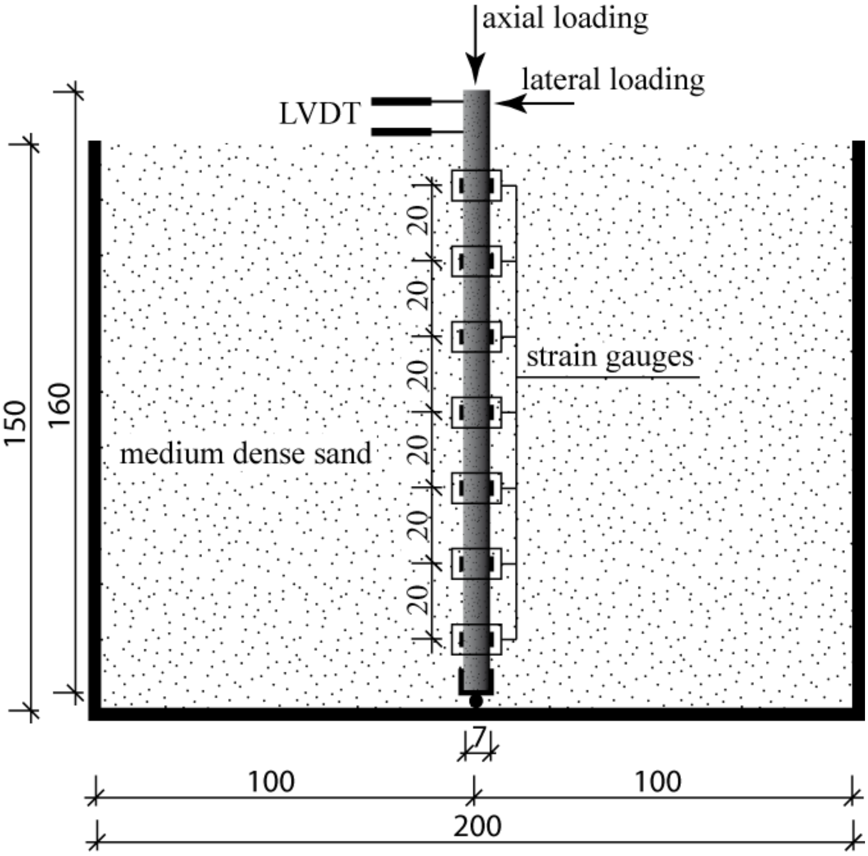

Figure 4.7 Cross-section of the model test system

The system also involves measurement units located along the pile (i.e. strain gages), at the pile head (i.e. displacement transducer), and load cells. A data acquisition system was established to record strain, vertical and lateral load, and pile head displacement during the tests. General view of the overall testing system is given in Figure 4.8. Details of the loading system, instrumentation and data acquisition system are given in subsequent sections.

Figure 4.8 Soil-pile interaction test set-up

4.3.1 Lateral and Axial Loading Mechanism

The test container was equipped with a horizontal loading mechanism with screw stroke 160 mm and 25 kN load capacity (Figure 4.9 and Figure 4.10). The components of the displacement control loading mechanism are;

- Linear movement element: Zimm MSZ-25 KGT standing with screw stroke 160 mm and 25 kN capacity.
- Load transfer rod
- Load cell
- Hinge at pile head: Zimm-MSZ 25 KGK

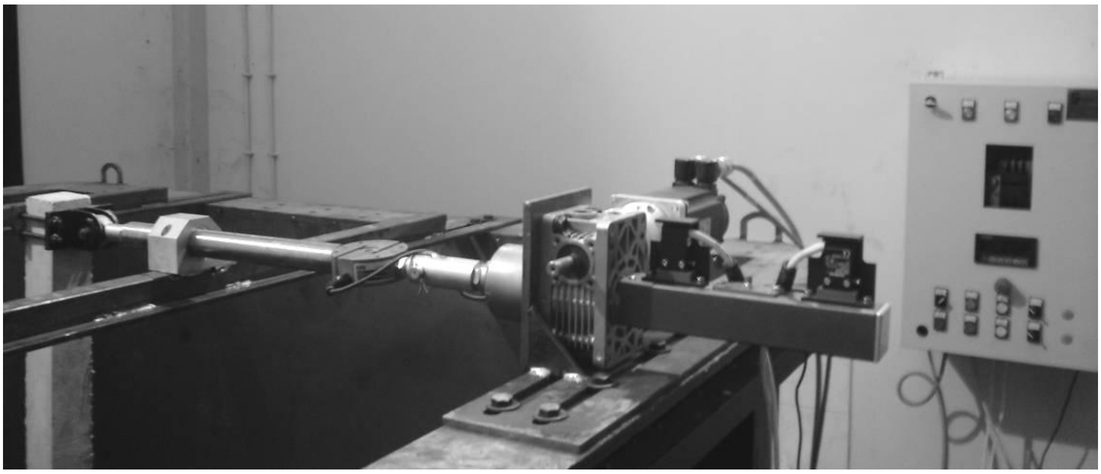

Figure 4.9 Lateral loading mechanism with servo control group

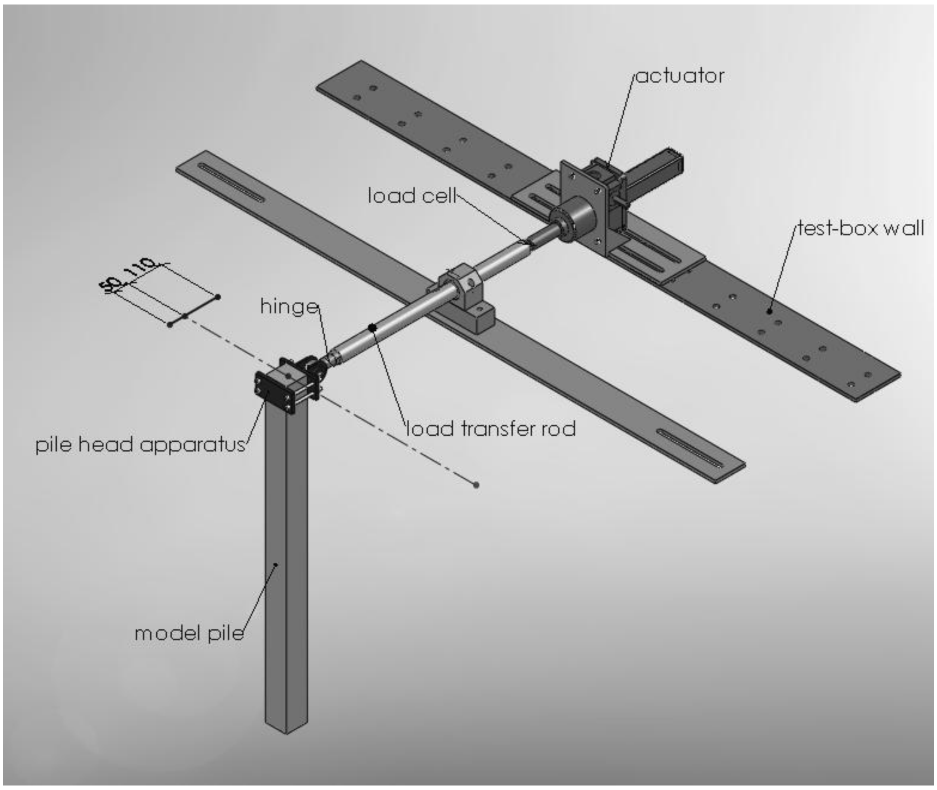

Figure 4.10 Lateral loading mechanism

Vertical loading system was established for the axial and lateral loading test case. General view of the vertical loading mechanism is presented in Figure 4.11. The components of the pile vertical loading system can be listed as testing frame, hydraulic piston, load cell, load transfer rod, and sliding support mechanism.

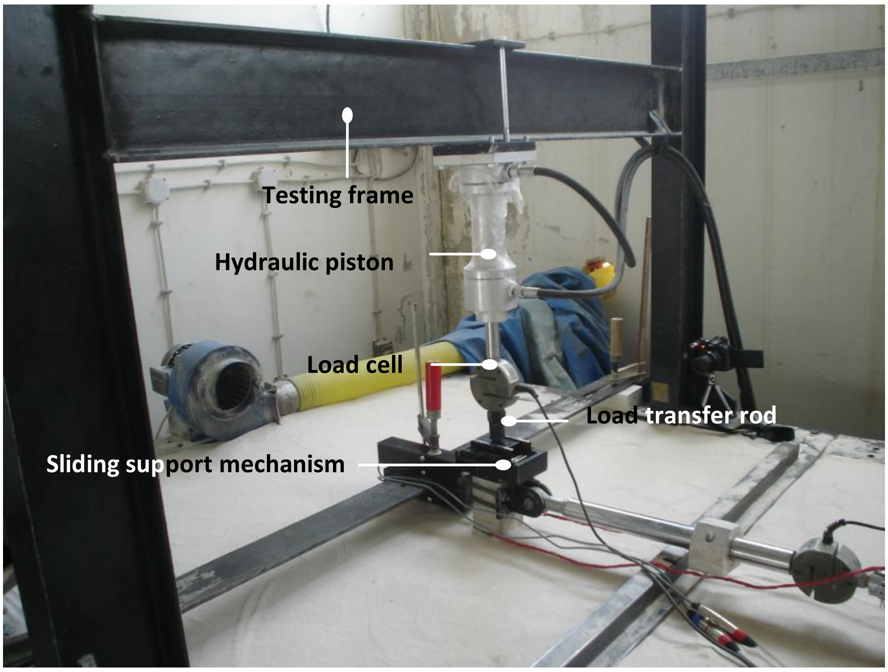

Figure 4.11 Vertical loading mechanism

The detail of the sliding support mechanism which was assembled on the pile head are illustrated in Figure 4.12. In the lateral-axial loading case, deformation-controlled horizontal loading mechanism was used with a constant vertical load. In order to transfer the axial load to the pile a lower plate was settled on the pile head with the intention of maintaining vertical axis of the axial load, an upper plate was positioned between the vertical load transfer rod and lower plate. Rollers were placed between the lower plate and upper plate (Figure 4.13). Thus, lower plate moved with the pile in horizontal direction and upper plate transferred the vertical load on the pile head at the same time. Explained movement can be seen clearly from the photos which were taken prior to the test (Figure 4.14a) and at the end of the test (Figure 4.14b). It is also considered that pile head rotates during the lateral loading. In order to ensure the pile head rotation without restriction, the load transfer rod head was designed in the form of an oval and a slot was opened over the movable plate (upper plate) in order to set a hinge. This oval head was placed in the plate slot as can be seen in Figure 4.14b.

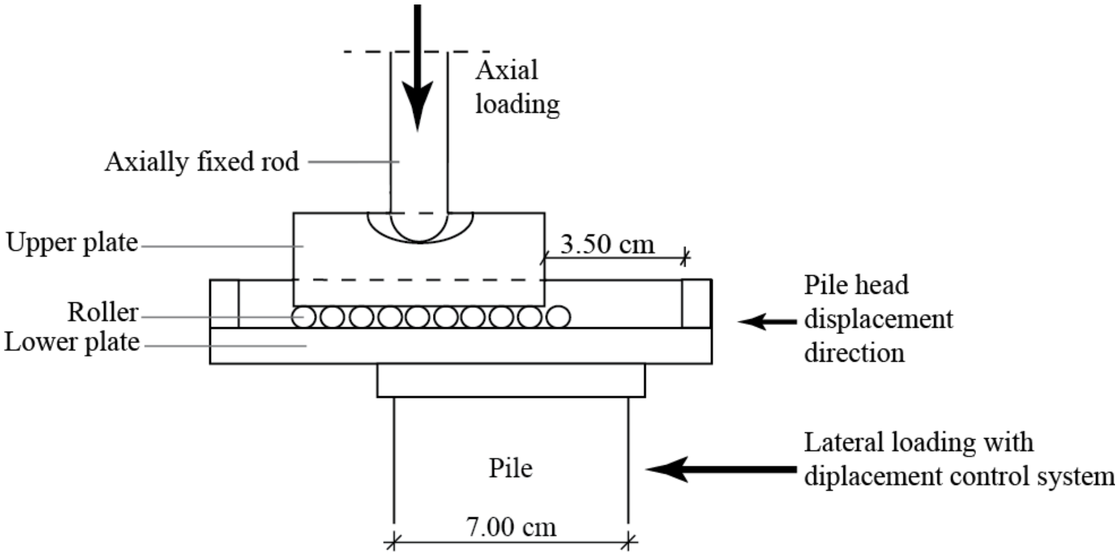

Figure 4.12 Sliding support mechanism illustration at the beginning of the test.

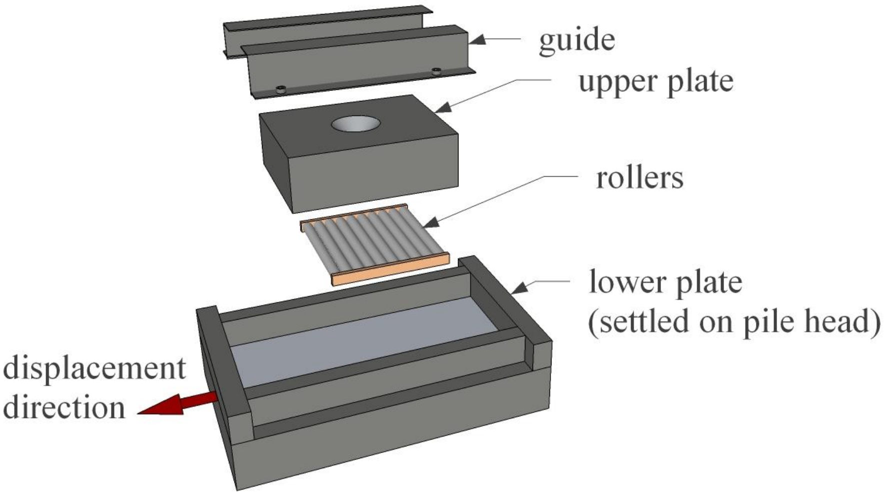

Figure 4.13 Portions of the sliding support system

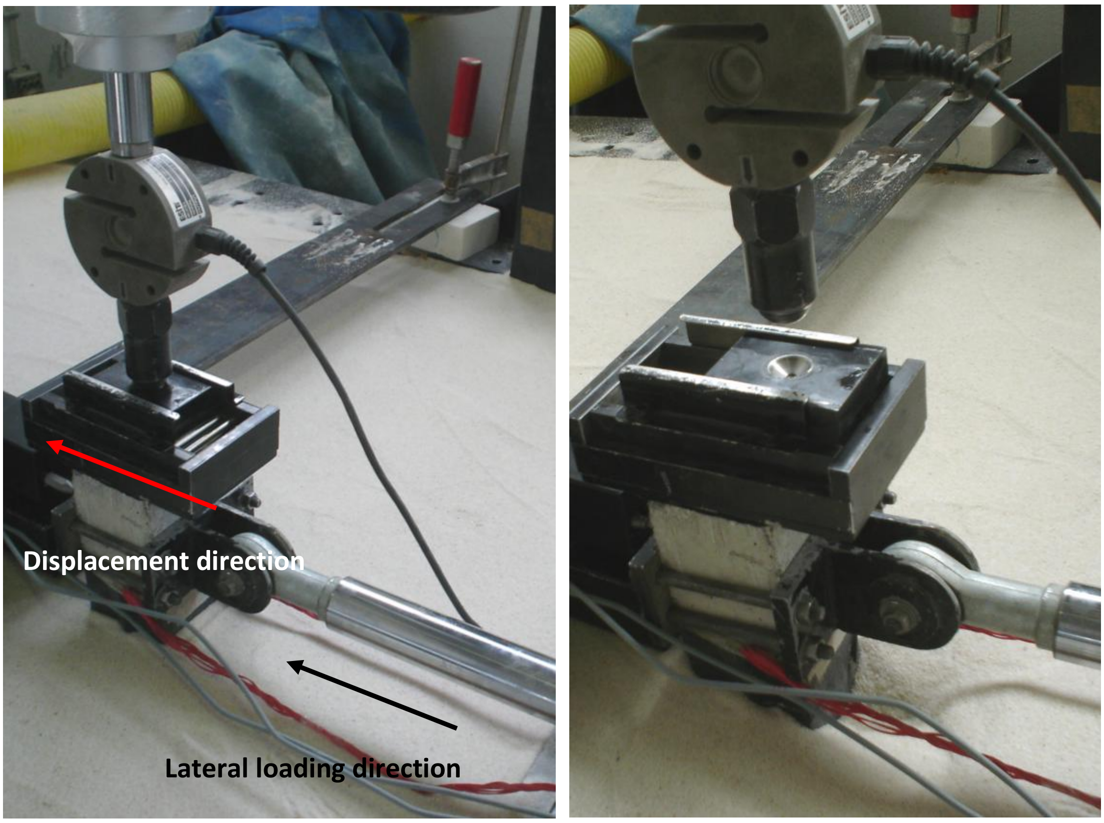

(a) (b)

Figure 4.14 Sliding support mechanism (a) Upper plate position prior the test (b) upper plate position after the test.

4.3.2 Model Pile Instrumentation and Data Acquisition System

Instrumentation of the testing system included installation of strain gauges, pile head displacement transducers, load cells and a data-conditioning set-up. Strain gages, displacement transducers and load cells were conditioned and digitally converted using a data acquisition device. For this purpose PC-based 16-bit resolution data acquisition system (TDG AI8b) was utilized. Data channels are listed as follows:

a. Fourteen channels for strain gauges that are installed on the model pile

b. Two channels for the displacement transducers signals

c. Two channels for the load cell signals

Model piles were equipped using special concrete type strain gauges in order to capture bending moment distribution along the model pile under lateral and lateral-axial loading. These strain gauges were much longer than traditional ones in order to compensate small voids and thin cracks that usually exist on most concrete elements. Strain-gages are made by Tokyo-Sokki with a model number of FLA-30-11. These 30 mm long strain gauges with a gauge resistance of 120.0±0.4Ω and a gage factor of 2.10±1.0% were exited by 5 VDC during the tests. Before adhesive application of the gauges, the surface of the model pile has been sanded using a thin sandpaper to obtain a smooth surface as smooth as possible. Then this surface was washed by means of regular grease and oil solving chemical such as acetone. Gauges were bonded to the model piles using CN-E type adhesive proposed for concrete and mortar. Gauge wires were soldered to the connecting terminal correspondingly to provide a fixed connection. Connecting terminals supply suitable link points to connect strain gauges to instrumentation leads. Signal carrying cable 4m in length which is produced particularly for the strain gauges was soldered to the connecting terminals. Strain gauge installation studies are shown in Figure 4.15.

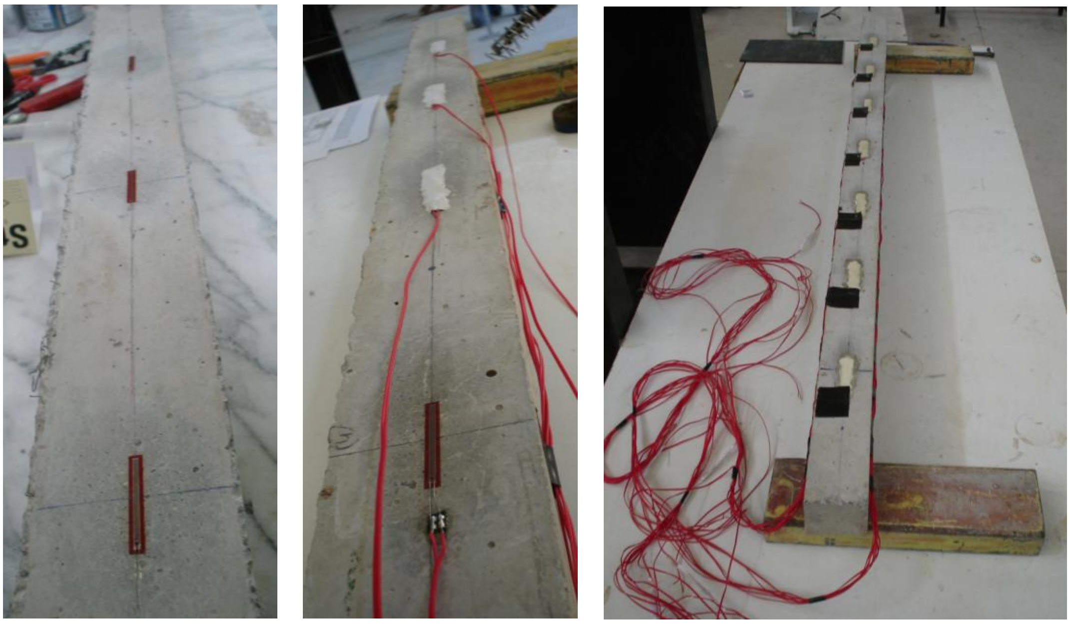

Figure 4.15 Strain gauge installation on the model pile

Once the gauges were bonded to the pile using this adhesive with great care, they were shielded against moisture and accidental mechanical damages. Multi-layer coating method was used for the protection of the strain gauges. For moisture protection SB tape type of coating material was applied over strain gauges and connecting terminals. For the mechanical protection epoxy based material, Araldite, was applied over SB tape. The cross-sectional view of the covered gauge is shown in Figure 4.16.

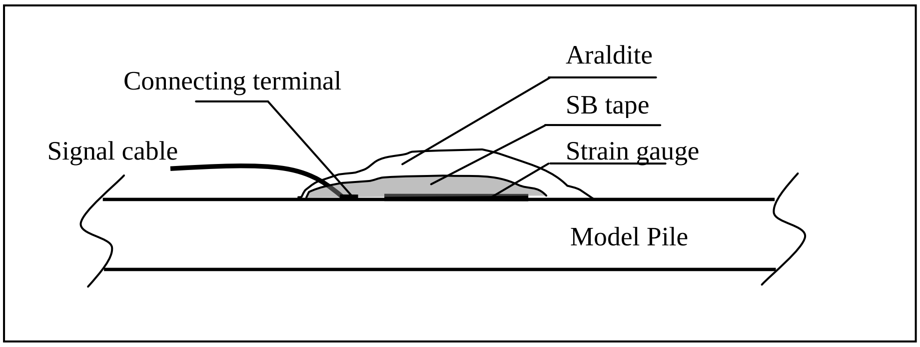

Figure 4.16 Typical strain gauge application with coating materials

Seven strain gauges were installed for one side of each model pile. At every level two strain-gauges were placed longitudinally in opposite directions in order to get the compression and tension strains. The distance between any two gauges were kept equal and set to 20 cm as illustrated in Figure 4.7. Overall instrumentation was so arranged that the strain of the pile during loading would be obtained in satisfactory accuracy.

Pile head load-deflection relationships were obtained by using head deformation transducers and load cells. Two load cells with similar specifications were positioned at the lateral loading and vertical loading mechanism as can be seen in Figure 4.10 and Figure 4.11. Two deformation transducers were positioned on the head of the pile to record the deformation and rotation under two types of loading (Figure 4.17). Distance between the two transducers was measured carefully after setting prior to each test. Transducer properties and calibration procedure is explained in subsequent section 4.3.2.1.

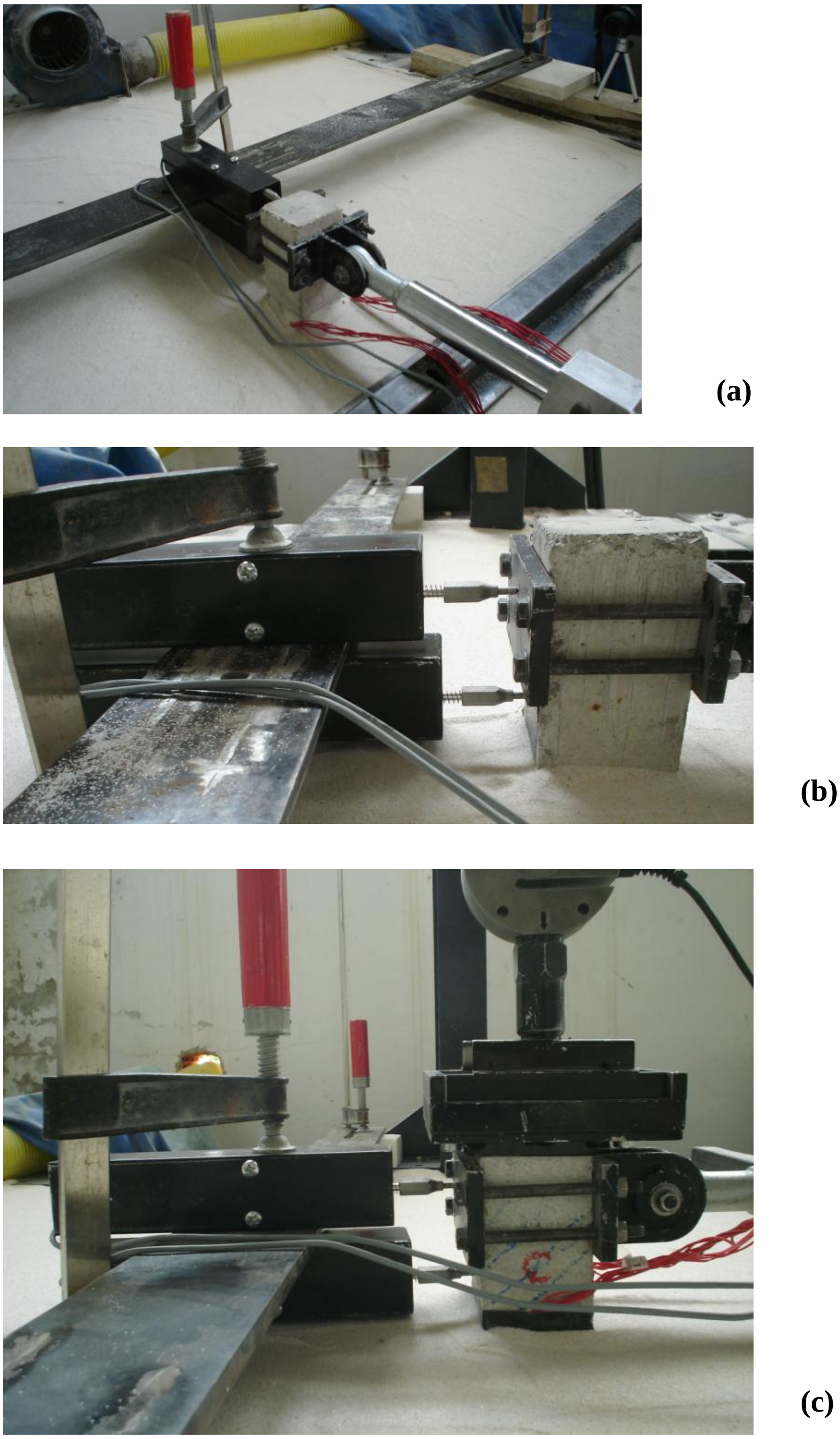

Figure 4.17 Model pile-head displacement transducers (a) general view (b) for lateral loading (c) lateral-axial loading

Data acquisition system included load cells, displacement transducers, strain gauges, analog to digital converter and computer. Transducers at the pile head, strain gauges along the model pile, and load cells in the loading mechanism were used to measure the strain by detecting voltage change. It is known that the changes in resistance caused by the strain are quite small for the strain gauges. Therefore, a bridge circuit is utilized to translate these changes into voltage changes. Wheatstone bridge configuration was necessary as signal conditioner in order to obtain regular voltage readings. A typical Wheatstone bridge consists of four resistive elements. In general single-arm bridges are normally employed for most experimental stress analysis applications. A single active gauge in position R1 with a gauge resistance of 120.0±0.4Ω was employed as illustrated in Figure 4.18. The resistances of R2, R3 and R4 are also equal to 120.0Ω. In this study Wheatstone connecting cables with three (R2, R3 and R4) resistance were used. It is connected properly (Figure 4.18) with the signal carrying cable of strain gauge (R1).

Voltage excitation source was able to supply 10 Volt to transducers, 5 Volt to strain gauges and load cell as shown in the flowchart of overall data acquisition system in Figure 4.19. Strain gauges were connected to the bridge by shielded cable 4 m in length as mentioned above, and the analog signal from bridges was also transferred by means of shielded cables. Total number of reading channels was seventeen for lateral loading case and eighteen for lateral-axial loading case. During lateral loading and lateral-axial loading the pile bent producing analog signal, which was digitized and simultaneously displayed on desktop monitor once it has reached to the computer through USB gateway device with USB connection cable and processed by ADU software called TestLab Basic. As a consequence of this procedure pile head load-displacement, and bending moment distribution along the pile was successfully monitored.

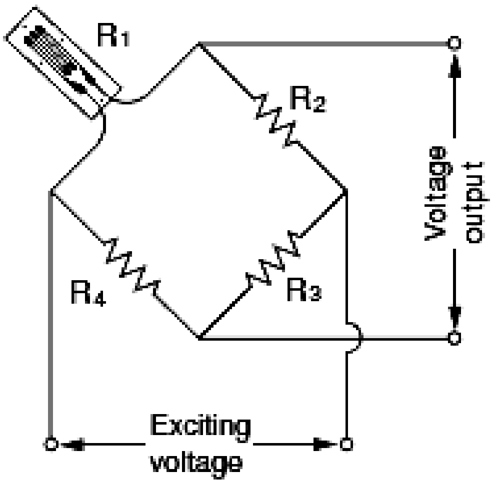

Figure 4.18 A view of quarter bridge
(TML-strain gauges catalog)

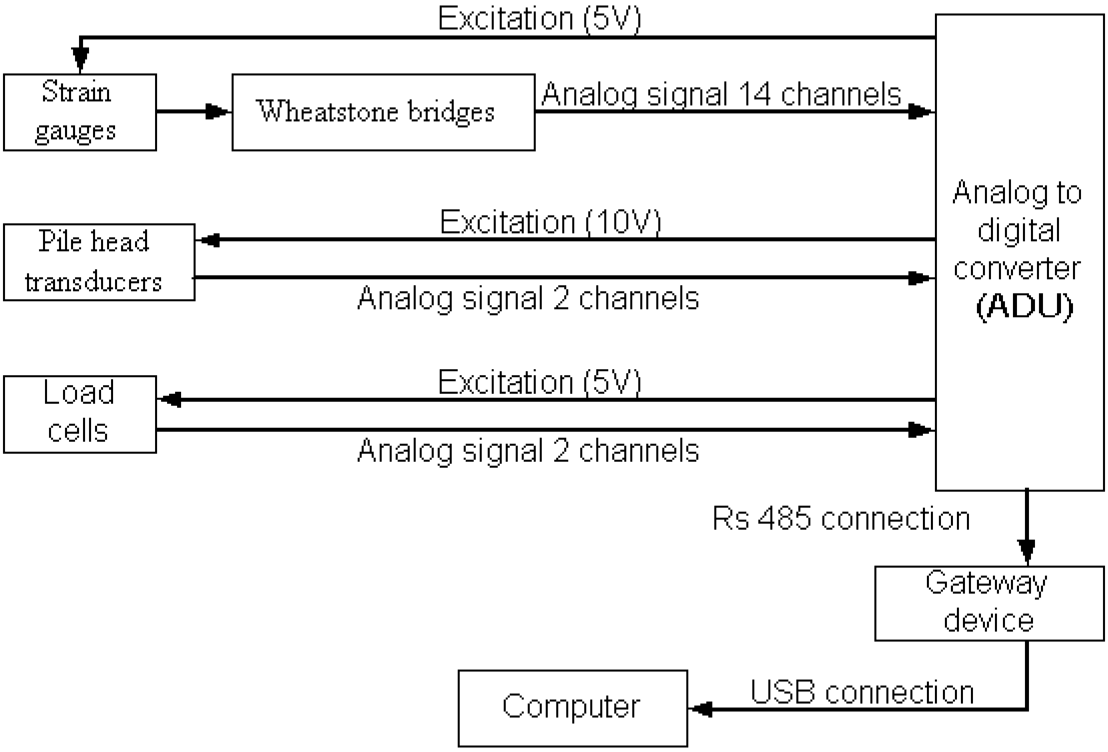

Figure 4.19 Data acquisition system

4.3.2.1 Rectilinear displacement transducers calibration

Rectilinear displacement transducers were utilized with ball tip-PY2 which has a 50 mm stroke, and ± 0.1 % independent linearity as shown in Figure 4.20. Calibration studies of rectilinear displacement transducers were made in Dokuz Eylül University, Metallurgical and Material Engineering Division, Mechanical Laboratory (Figure 4.21). Displacements were applied automatically and counts were recorded by using data acquisition system. Measurement resolution of the data acquisition system is 16-bit, means that the measurement sensitivity of the system is 2^{16}= 65536 count. In full scale (+ /-10V) 65536-count measurement resolution is obtained with 16-Bit CMOS SAR ADC (analog to digital converter). According to the relationship between voltage and count (Figure 4.22), the transfer function of translating the voltage value to count value is shown in equation 4.4. Count value, according to the applied voltage is the production of a digital code between 0-65535. This digital code is used to calibrate the sensors via software. Measured displacement of the linear position transducer as a sensor is proportional to voltage output (Figure 4.23). In total, eight transducers were calibrated. Sample results can be seen in Figure 4.24. The remaining calibration graphs are shown in Appendix-A. Count-displacement relation is obtained linearly as can be seen in the graphics.

Figure 4.20 Displacement transducer

Figure 4.21 Calibration of deformation transducers

$$x = \frac{32768(y+10)}{10} \qquad 4.4$$

Where *x* and *y are* count and voltage respectively.

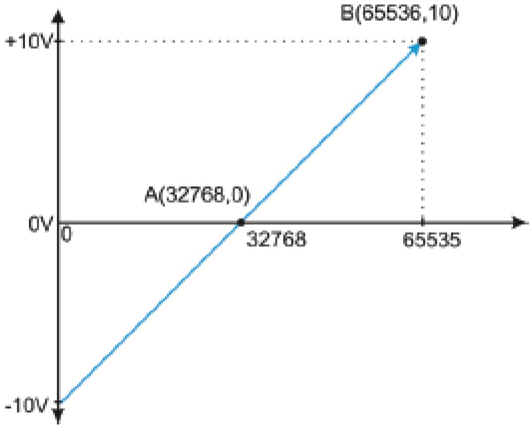

Figure 4.22 Voltage-Count relationship

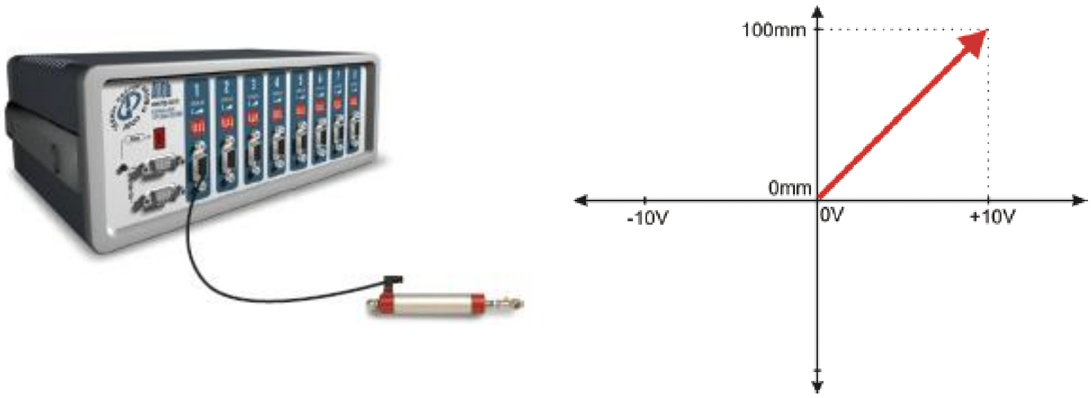

Figure 4.23 Displacement-voltage relation of displacement transducer with 100 mm stroke

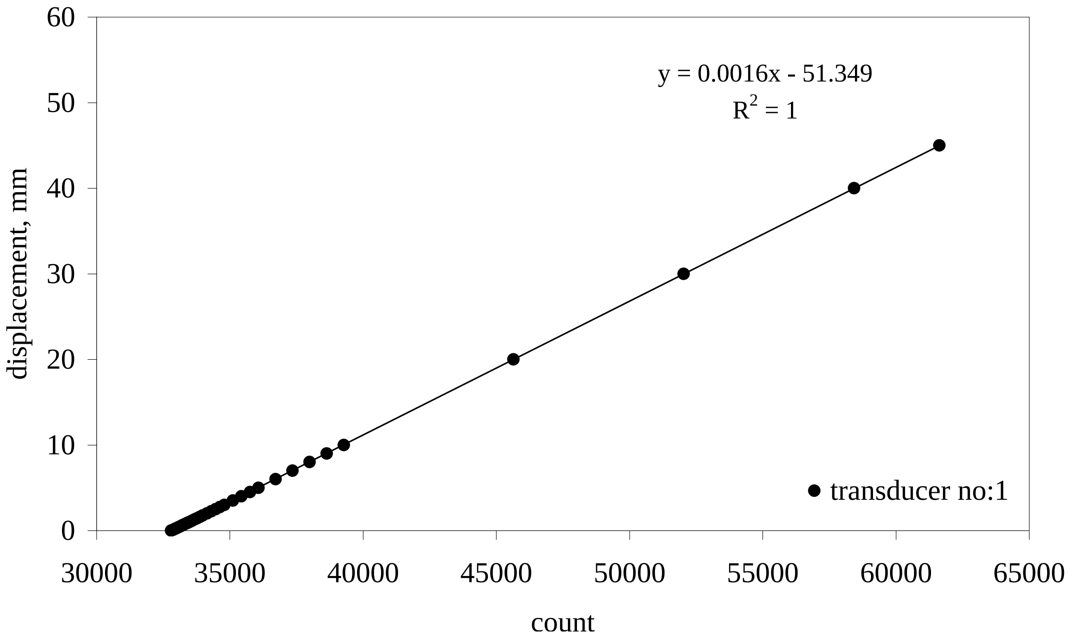

Figure 4.24 Calibration result of transducer no: 1

4.4 Test Materials

4.4.1 Concrete Mix Design and Model Pile Casting

During the course of the study material control tests were planned and performed prior to the casting of the model piles to make sure that consistent concrete production with and without steel fibers could be confidently made. Needless to say it was desirable to obtain notable improvements in the behaviour of the SFRC with respect to the conventional concrete. Experimental work and the design of the concrete mix for both conventional and SFRC cases is briefly explained in the following paragraphs. The preparation of the model piles and flexural elements are also explained.

4.4.1.1 Experimental program

The first step of the design of a concrete mixture is to determine the properties of ingredients, that is cement and aggregates. The properties of the cement, CEM I 42.5 R, was obtained from its manufacturer, whereas the specific gravity, absorption and particle size distribution of the aggregates were determined in laboratory.

After the first step concrete is cast and its fresh and hardened properties were determined. The air content and slump was measured as for the fresh properties whereas the 28 day compressive and flexural strength were determined as for the hardened properties.

4.4.1.2 Characteristics of Materials and Concrete Mix

As explained in *Chapter 4, Section 4.2.1* an 8 mm maximum-size aggregate was selected, as it is less than one fifth of the model pile diameter. Variations of the particle size of the coarse and fine fractions of the aggregate mixture were 5-8 mm and 0-5mm, respectively. Percent absorption test was especially important for the control of net water content of the concrete mix so that determination of correct batch weights would be made. The specific gravity values were used in certain computations for mixture proportioning and control, such as the absolute volume occupied by the aggregate (Table 4.1).

Gradation of aggregates significantly affects concrete mixture proportioning and workability. The grading of aggregates was determined by means of sieve analysis test (Table 4.2). Afterwards, the mixture proportions of the aggregate were decided according to ACI 544.1R-96; (*Table 2.1-Recommended combined aggregate gradations for steel fiber reinforced concrete*). The combined aggregate was obtained by mixing 35% of coarse aggregate with 65% of fine aggregate. This was decided to obtain a better compaction and workability of the concrete mix. The gradation of the combined aggregate, which was generated due to ACI recommendations, is shown in Figure 4.25. As can be noticed in this figure, ACI lower limits nearly follow the decided mixture.

Table 4.1 Characteristics of aggregate fractions

Aggregates (mm)	Absorption (%)	Oven-dry specific gravity	Saturated dry surface specific gravity
5-8	0.44	2.68	2.69
0-5	1.25	2.60	2.64

Table 4.2 Particle size distribution

Sieve size	Aggregate Fraction	
	5-8	0-5
½ in (13mm)	100	100
3/8 in (10mm)	99.86	100
No.4 (5mm)	11.22	97.68
No.8 (2.4mm)	0.36	65.67
No.16 (1.1mm)	0.32	40.03
No.30 (0.60mm)	0.31	23.19
No.50 (0.30mm)	0.30	13.47
No.80 (0.18mm)	0.30	9.32
No.200 (0.075mm)	0.22	5.42

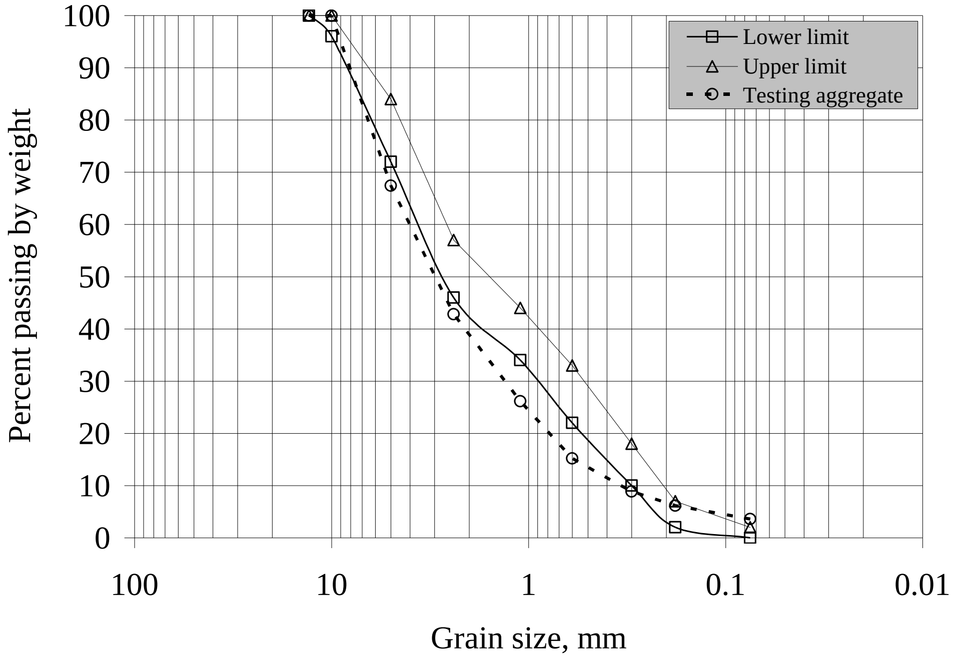

Figure 4.25 Combined aggregate gradations within the ACI recommended limits

Portland cement type CEM I 42.5R was used in concrete mix. The cement manufacturer reported specific gravity of the cement as 3.10. Water cement ratio (w/c) was selected as 0.50.

A slump of approximately 5 in (~13.00mm) was opted to provide good workability for the batch design. Batch characteristics of *sfrc* with respect to the maximum size aggregate are shown in Table 4.4. Having maximum aggregate size equal to 8mm the 3/8″ (10mm) option was chosen to form the basis for *sfrc* design in this study. It should be noted that it was selected 0.50 since lower values would end up producing stiff *sfrc* batches, although upper limit of the water to cement ratio was suggested 0.45 in the Table 4.3. Table 4.4 was used for selecting air content of the batch. Thus, corresponding amounts for water and cement were automatically used in the batch design.

Table 4.3 Range of normal weight SFRC (ACI, 1996)

Mix parameter	**Maximum Size Aggregate**		
	3/8″ (10mm)	**3/4″ (19mm)**	**1.5″ (38mm)**
Cement, kg/m^3	356-593	297-534	279-415
Water-cement ratio, w/c	0.35-0.45	0.35-0.50	0.35-0.55
Percent of fine total aggregate	45-60	45-55	40-55

Table 4.4 Trial mixtures for non-air-entrained concrete of medium consistency Slump: 3″ to 4″-7.62 cm to 10.16 cm, (Kosmatka.and Panarese, 1994)

Water –cement ratio	Maximum size of aggregate	Air content percent	Water lb per cubic yd (kg per cubic meter) of concrete	Cement lb per cubic yd (kg per cubic meter) of concrete
0.50	**3/8 (10mm)**	**3**	**385(228.28)**	**770(456.82)**
	1/2 (13mm)	2.5	365(216.12)	730(433.09)
	3/4 (19mm)	2	340(201.60)	680(403.43)
	1 (25mm)	1.5	325(192.70)	650(385.63)
	1.5 (38mm)	1	300(177.88)	600(355.97)

4.4.1.3 Mixture Proportioning

Proportioning methods have evolved from the arbitrary volumetric method of the early 1900’s to the present day weight and absolute-volume methods were described in the American Concrete Institute’s Committee 211-Standard Practice for Proportioning Concrete Mixes. The volumetric method is said to be more accurate (Kosmatka and Panarese, 1994). Therefore, absolute volumetric method was used in this study. This method can be explained as in the following:

Absolute volume: The volume of freshly mixed concrete is equal to the sum of the absolute volumes of the cement, water (excluding the water present in aggregate voids), aggregate and air. The absolute volume is calculated with the material weight and the specific gravity as follows:

$$Absolute\ volume = \frac{Weight\ of\ material}{Specific\ gravity\ of\ material \cdot Unit\ weight\ of\ water} \qquad 4.5$$

Finally dry-batch weights of conventional concrete and SFRC have the following proportions for one cubic meter of concrete. For SFRC design ZP305 (aspect ratio: 30/0.5), steel fiber was used with a volume ratio of 1% (Table 4.5). Mix characteristics given in Table 4.5 belong to the design concrete mix without moisture correction. This correction, however, is an essential aspect of batch design. The moisture content of aggregate fractions was determined before the trial batch was cast. It should be mentioned that conventional oven was used for moisture content determination since more stable values were obtained. The dry-batch weight of the concrete aggregate therefore has to be adjusted to compensate for any detected moisture variations due to absorbed or surface water of individual grains. The mixing water added to the batch has to be reduced or increased by the amount of moisture change of the aggregate. Such corrections were inevitably made for the batches produced in this study. Trial batches were cast in order to get the fresh concrete properties. As seen from Table 4.5, *sfrc* was used to replace the fine aggregates. For conventional concrete the target slump and air content values are given below:

Target slump : 5 in. (~13.00 cm)

Target air content : 3.0%

Table 4.5 Mixture Proportions

Weight (kg)	Conventional Concrete (kg per cubic meter)	Steel Fiber Reinforced Concrete (SFRC) 1% by volume (kg per cubic meter)
W_{water}	225.00	225.00
W_{cement}	450.00	450.00
$W_{5\text{-}8}$	562.65	562.65
$W_{0\text{-}5}$	1013.73	987.73
Steel Fiber	_	78
ΣW	2251.38	2225.38

4.4.1.4 Properties of Concrete

Compressive strength can be defined as the measured maximum resistance of a concrete specimen to uniaxial compression loading. For conventional concrete and SFRC, 40 dm^3 batches were prepared respectively. First aggregates were mixed for five minutes. Then fibers were added slowly as the mixer was rotating. Finally cement and water were added and mixed until fibers got separated. This took about 4-5 minutes. After the batch was mixed up properly, first slump and air content tests were performed as can be seen in Figure 4.26 a-b-c. The addition of fibers, in general cause a reduction in the consistency of concrete mixtures. This known fact was also observed from the fresh concrete test results and the slump of the mix reduced from 12 to 9 cm. Slump and air content values for the tested samples are revealed in Table 4.6.

Table 4.6 Fresh concrete properties

Concrete	Air content (%)	Density (kg/dm^3)	Slump (cm)
Control concrete	3.1	2.33	12
SFRC (%1)	4.2	2.35	9

In Table 4.7 it can be noticed that target slump and air content values were successfully obtained in laboratory tests indicating satisfactory SFRC and conventional concrete mix designs.

Figure 4.26 (a) Cast of concrete

Figure 4.26 (b) Air content test

Figure 4.26 (c) Slump tests

Compressive strength of *sfrc* and concrete mix was obtained using cubic specimens 15x15x15cm in dimensions shown as in Figure 4.27. Cubic specimens were compacted by rodding method. Specimens were removed from their molds 24 hours later and cured in water at a temperature of 20± 2° C. Tests were performed at 7th and 28th day age. The rate of the test was 6.67kN/sec. For each age and for each type of concrete six specimens were tested and average values of compression test results can be seen in Table 4.7.

Table 4.7 Compressive strength test results

Dimensions 15x15x15	Control concrete (Average)		SFRC ,Fiber: 1% (Average)	
	Compressive strength	Standard deviation value	Compressive strength	Standard deviation value
f_{c-7} (MPa)	33.04	1.85	37.04	0.83
f_{c-28} (MPa)	39.09	2.5	41.19	1.48

4.4.1.5 Reinforcement Details

Both flexural elements and model piles were designed as reinforcement in the same features. Steel bars for the model designing were searched in the market. Some samples were purchased and tested in Metallurgical and Materials Engineering Department. The results were confirmed with the conventional bars used in reinforced concrete design. Stress-strain characteristics of selected bars are presented below (Figure 4.27 and Figure 4.28):

- *Longitudinal reinforcement:* 6 bars of diameter 4 mm for a reinforcement ratio equal to 1.9%. Yield strength, f_{yk}, and Elasticity modulus, $E_{s,}$ were founded 316 MPa and 200760 MPa respectively from the tests
- *Shear reinforcement:* Diameter 2 mm with a spacing equal to 30 mm for reinforced concrete (*rc*) Yield strength, f_{yk}, and Elasticity modulus, $E_{s,}$ were founded 319 MPa and 178000 MPa respectively from the tests

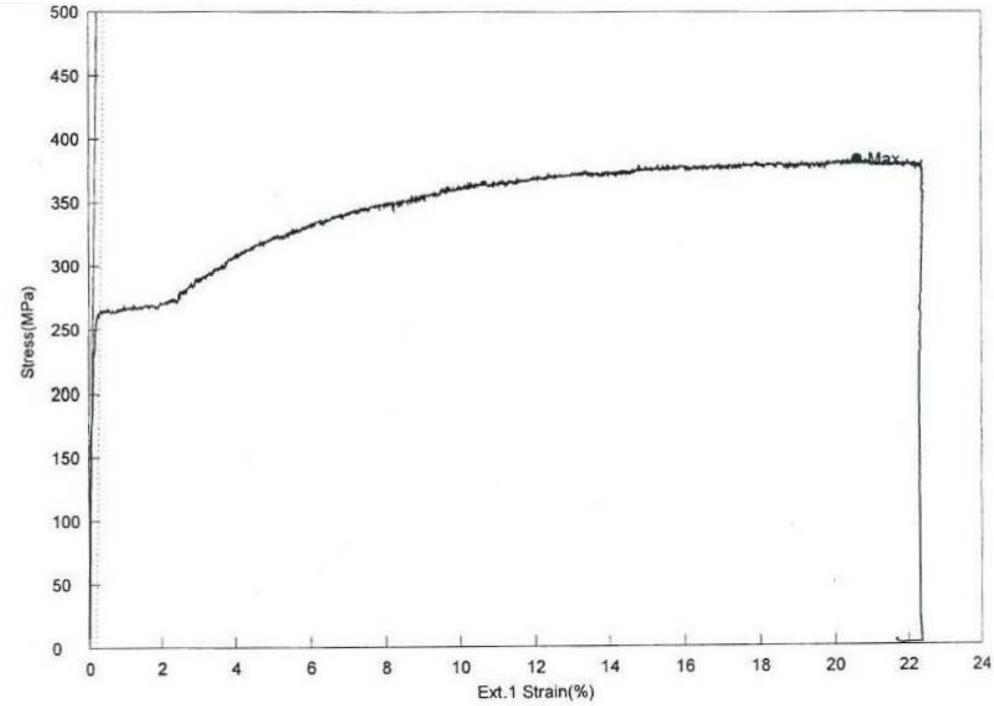

Figure 4.27 Stress-strain relation of longitudinal reinforcement

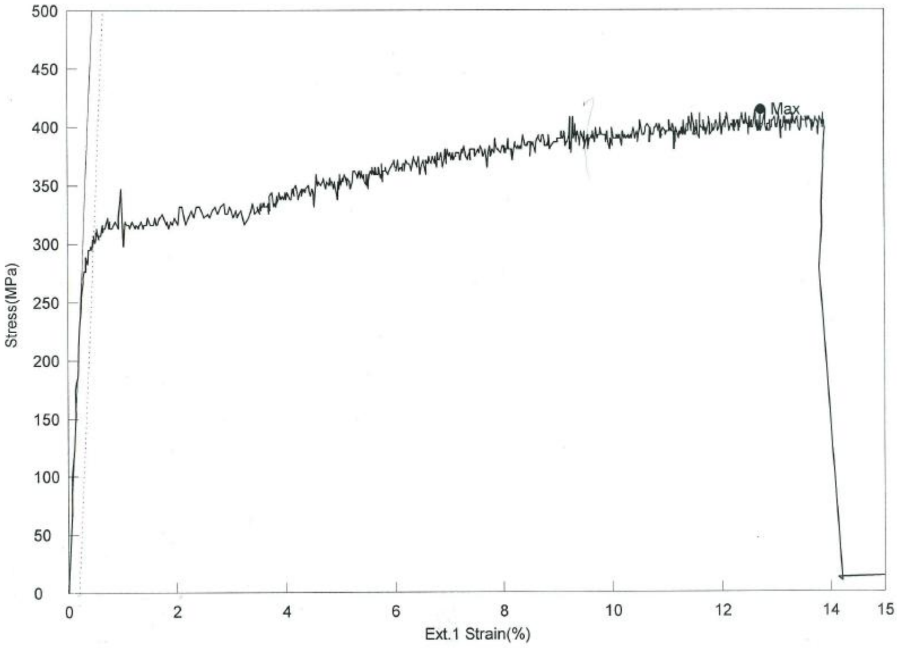

Figure 4.28 Stress-strain relation of shear reinforcement

Cross-sectional reinforcement details of model pile and flexural element is illustrated in Figure 4.29. The details of the shear reinforcement configuration are presented in Figure 4.30 for flexural elements and in Figure 4.31 for model piles. The N-M interaction diagram of the RC section is given in Appendix B. The applied axial load in the lateral-axial loading tests is shown in the N-M diagram which is corresponding to the tension-controlled failure.

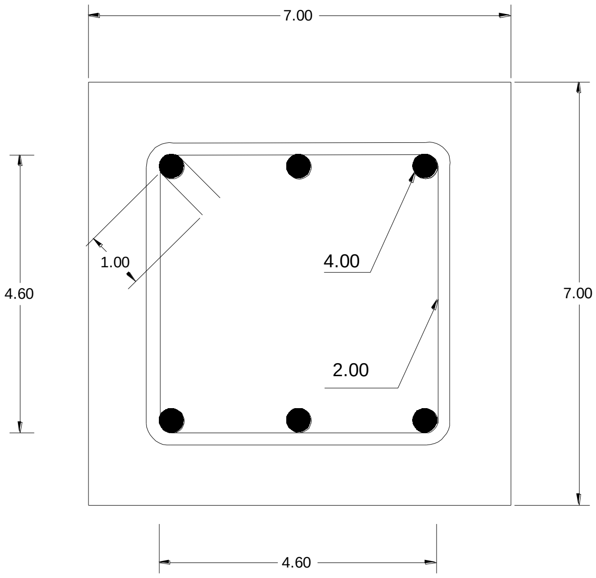

Figure 4.29 Cross section of model piles and flexural elements

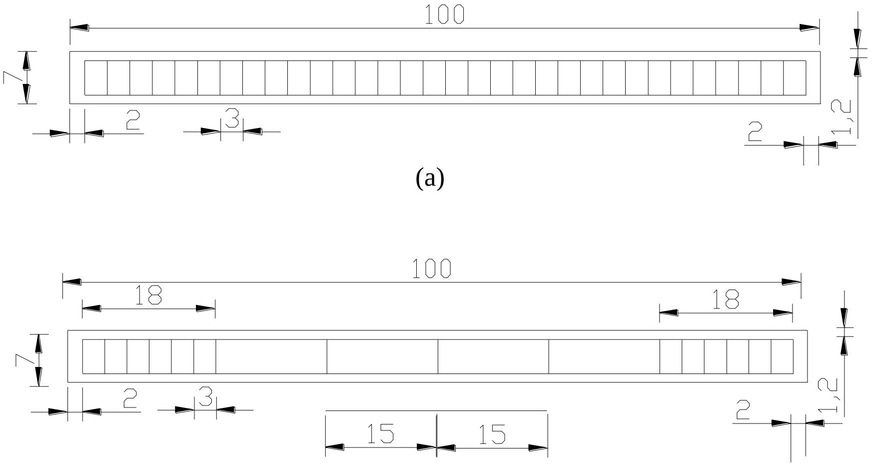

(a)

(b)

Figure 4.30 Reinforcement details (a) reinforced concrete flexural element (b) concrete with only bending reinforcement and concrete with bending reinforcement and steel fiber flexural element

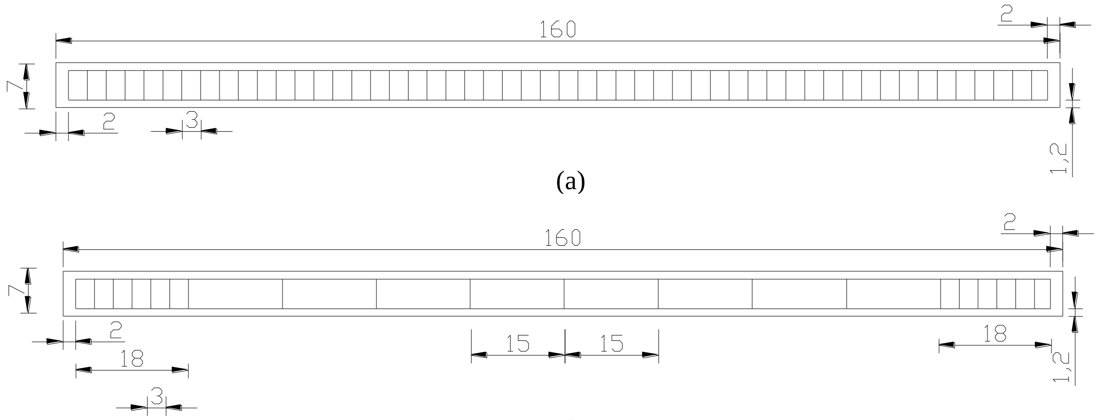

(a)

(b)

Figure 4.31 Reinforcement details (a) reinforced concrete model pile (b) concrete with only bending reinforcement and concrete with bending reinforcement and steel fiber model pile

4.4.1.6 Cast of the Model Piles and the Flexural Elements

The amounts of five types of flexural elements and model piles were casted as shown in Table 4.8. All of the molds were greased before casting. Concrete and steel fiber reinforced concrete *sfrc* of model piles and flexural elements were placed into the steel molds in two layers. They were compacted with rod. Reinforcement was placed 15 cm in length at the head of the concrete and steel fiber reinforced concrete model piles (Figure 4.32). After placing the pile into the test pool, 10 cm of the pile would remain above the soil surface. The aim was to protect this part of the pile from the large shear loads at the interface of soil surface during lateral loading via ring. Reinforced concrete, only bending reinforced concrete, and only bending reinforced *sfrc* was placed into the molds with vibration technique (Figure 4.33 and Figure 4.34). Model piles and flexural specimens were cured 28 days after removing from the molds (Figure 4.35).

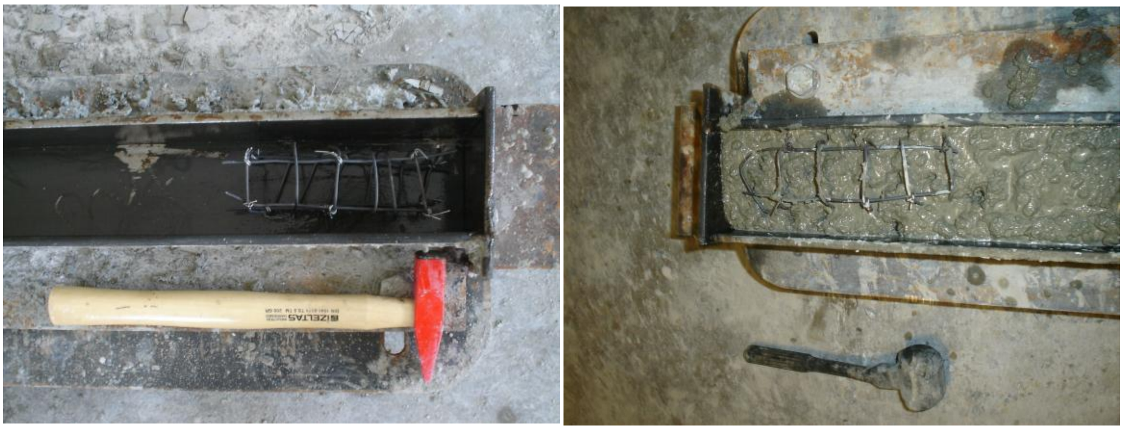

Figure 4.32 Reinforcement at the head of the model pile for conventional concrete (c) and steel fiber reinforced concrete (sfrc)

Table 4.8 Number of cast flexural elements and model piles

Type	Model Pile Dimensions (cm) 7x7x160	Flexural Element Dimensions (cm) 7x7x100
Reinforced concrete **(*rc*)**	5	5
Concrete with bending reinforcement and steel fiber **(*ws-sfrc*)**	5	5
Concrete with only bending reinforcement **(*ws-rc*)**	5	5
Steel fiber reinforced concrete **(*sfrc*)**	10	10
Concrete **(*c*)**	10	10

Flexural strength of *sfrc* and control concrete specimens were determined using third-point bending test technique (Figure 4.36). Testing rate was 0.04 kN/sec and Bending tests were conducted on three specimens for each concrete and *sfrc* flexural element. The average values of flexural strength results are presented in Table 4.9. The testing system was a closed loop servo-hydraulic universal testing machine. The flexural stress σ is the maximum tensile stress at the base of the flexural element as determined at the moment, M , by using simple linear elastic theory:

$$\sigma = \frac{M}{\frac{1}{6}bh^2} \qquad 4.6$$

Where, b and h denote the width and the depth of the flexural element. In Table 4.10 it can be noticed that detected increase of flexural strength for a fiber volume fraction of 1% is 34 % on the average. The result is clearly reflecting the contribution of steel fibers to flexural strength (Figure 4.37).

Figure 4.33 Placement of the reinforcement into the mold

Figure 4.34 Vibration process

Figure 4.35 Cast and cured model piles

Figure 4.36 Flexural tests

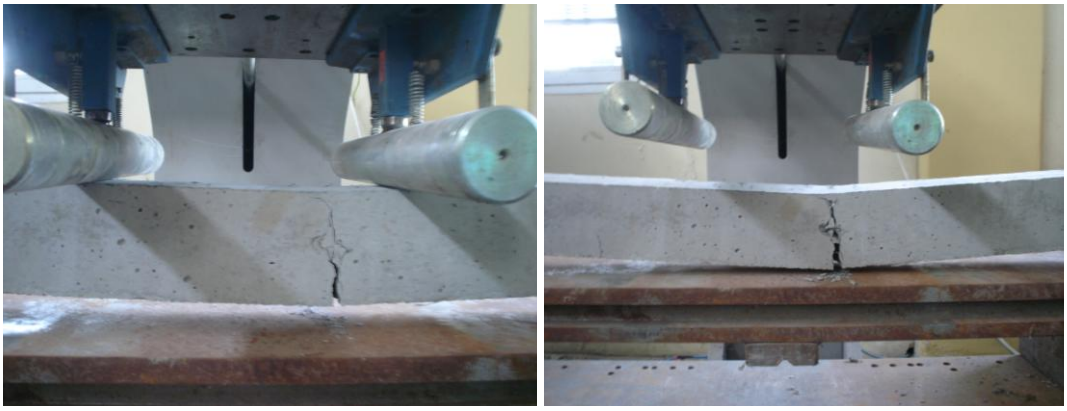

Figure 4.37 Flexural strength test of *sfrc*

Table 4.9 Flexural strength test results

Dimensions 7x7x100	σ_f (MPa)
Control concrete (Average)	4.41
sfrc ,Fiber: 1% (Average)	5.91

4.4.2 Soil Properties

The soil surrounding the pile was a artificially prepared sand layer. The soil layer was in dry condition throughout the testing program. Poorly graded sand (SP) served as subgrade materials to the laterally loaded of model piles. The gradation curve of the medium to fine sand used in this study is shown in Figure 4.38. Grain size and index characteristics of sand are given in Table 4.10. The minimum median diameter (d_{50}) requirement for grain size effect on soil-structure interaction has been described earlier in the literature. Nunez (1988) proposed that the pile diameter should be at least 45 times the median diameter whereas Remaud (1999) suggested same ratio be at least 60. Mean diameter (d_{50}) value of the sand is obtained 0.5 mm matching the above mentioned criteria.

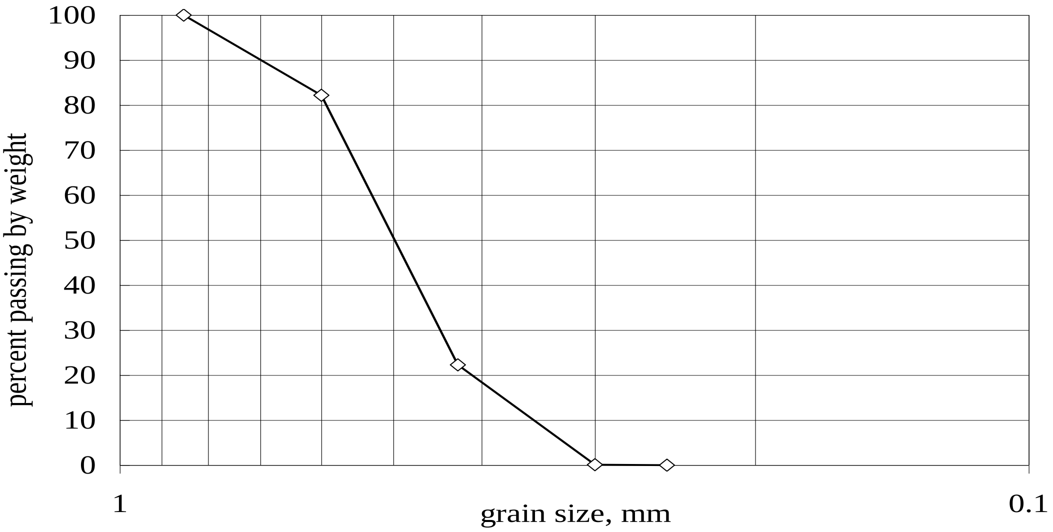

Figure 4.38 Grain size distribution curve

Table 4.10 General soil characteristics

Property	Sand
Mineralogy	Quartz
Specific gravity, G_s	2.65
Maximum dry density, γ_{max} (kN/m^3)	16.06
Minimum dry density, γ_{min} (kN/m^3)	13.13
Maximum void ratio, e_{max}	0.98
Minimum void ratio, e_{min}	0.62
Maximum and minimum particle size,	0.7 – 0.3
Coefficient of uniformity, C_u	1.39
Coefficient of curvature, C_c	1.01
Mean particle size, D_{50} (mm)	0.50
-No. 4	100
-No.200	0
USCS	SP

4.5 Model Pile and Test Soil Placement

According to set up procedure, the instrumented test pile was inserted in the soil container prior to the placement of the test soil. Model pile was positioned at the center of the test container. The pile tip and head was supported by using base hinge and the pile head apparatus of lateral loading mechanism, respectively as shown in Figure 4.39. During the placement works, the perpendicular condition of the model pile was controlled.

Model test soil was transferred into the container by using a conveyor (Figure 4.40). Placement of the sand had a certain procedure. Sand was placed at 50 cm thick layers each compacted by a vibratory compacter to obtain medium dense sand condition (Figure 4.41). Sand was compacted in dry condition three layers in total. In order to set a repeatable compaction procedure the layer is divided into grids in plan. In other words, each layer was divided in 20 equal rectangular segments as illustrated in Figure 4.42. Vibration was applied in one minute for each divided rectangular portion. Total compaction procedure took 60 minutes.

Figure 4.39 Model pile placement into the test container

Figure 4.40 Conveyor for the sand transferring

Figure 4.41 Vibratory compacter and compaction process

The density of the test soil would exert a significant effect on the performance of model piles. Therefore average relative density of the sand which was placed into the test container should be determined with maximum, minimum and test average unit weight of the soil (Equation 4.7). During the preparation of the test sand, it was observed that the same amount of sand was placed successfully into the container for each test. The average unit weight was computed $\gamma = 14.15\ \mathrm{kN/m^3}$. The average relative density, D_r, was found as 40% corresponding to medium dense condition. Direct shear tests were performed on sand specimens prepared at the relative density of the sand in the testing container. The value of angle of internal friction, ϕ, was obtained as 31.5^0 (Figure 4.43). The values of direct shear test and shear stress-strain relationship is given in Appendix C.

$$D_r = \frac{1/\gamma_{\min} - 1/\gamma}{1/\gamma_{\min} - 1/\gamma_{\max}} \qquad 4.7$$

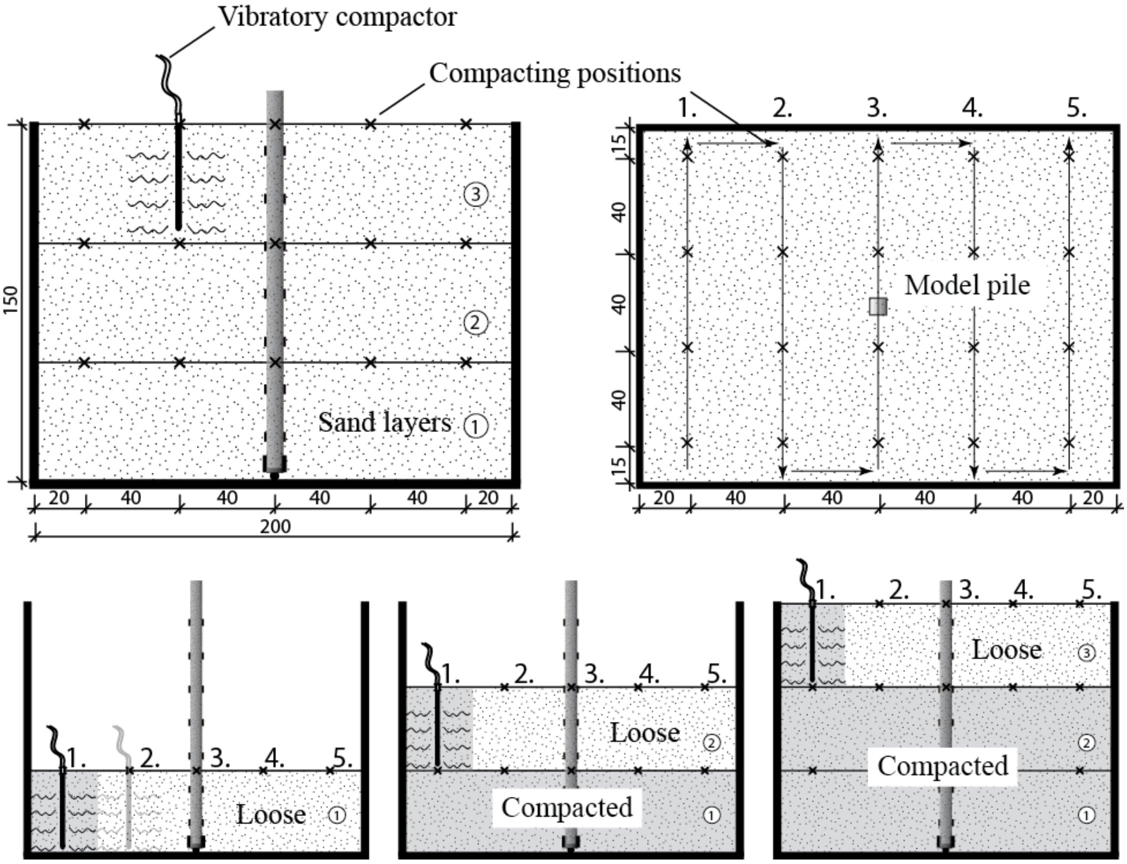

Figure 4.42 Compaction procedure

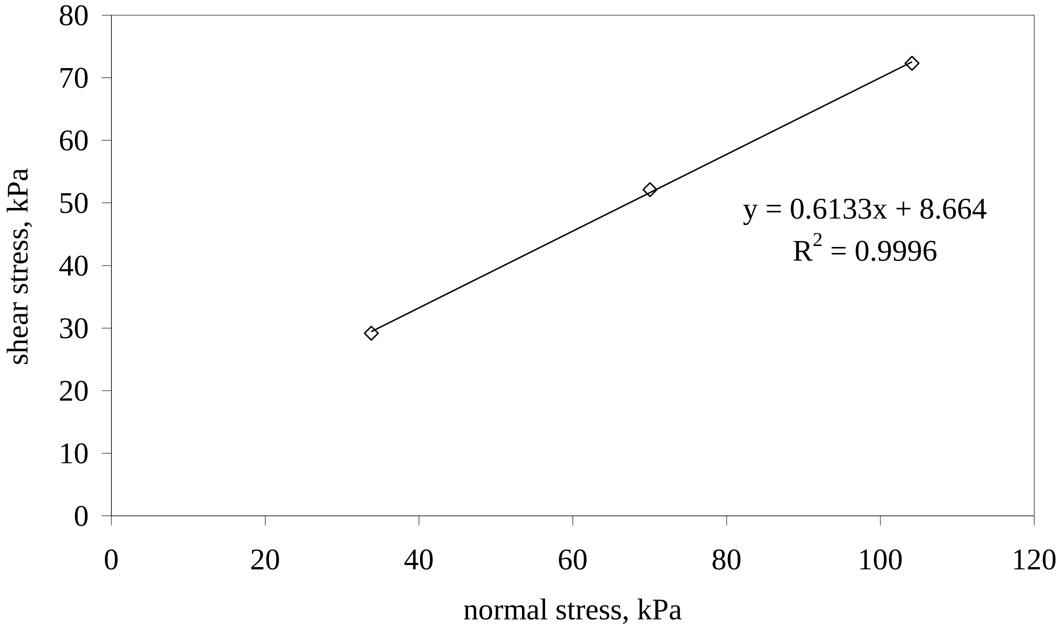

Figure 4.43 Direct shear test result of sand

4.6 Test Set-Up for the Measurement of Moment-Curvature (M-Φ)

As a secondary testing system a test method was considered for bending moment-curvature relationship of the flexural elements under pure bending stress. This system was established in order to obtain the nonlinear behaviour of model piles based on moment-curvature (M-Φ) relationship. Bending test system was also used to perform the calibration of the gauges with respect to the bending moment. Flexural elements were tested for this purpose. The overall bending test system was designed to consist of the following basic items (Figure 4.44).

a. Testing frame
b. Hydraulic piston
c. Load cell
d. Load transfer frame with certain distance from two points
e. Displacement transducer group
f. PC-based data acquisition system

Four point bending test configuration with transducer positions and strain gauges are illustrated in Figure 4.45. The flexural element was simply supported and the vertical loads in the span were set 30 cm apart. Deformation transducers were placed with equal space at constant moment region to get the curvature. In order to acquire a well polynomial, six displacement transducers were positioned along the constant moment region. Therefore, relatively smaller, 196 mm in length and 45 mm in width, displacement transducers were utilized. With the intention of protecting the distance between measurement points and to keep the axis of them during the test, the transducers were placed and fixed with a mechanism as shown in Figure 4.46.

In this experimental study, flexural elements were loaded manually with hydraulic piston and PC-based data acquisition system (TDG AI8b) was used in order to record the induced load and displacements. The details of the data acquisition system were explained in Section 4.3.2.

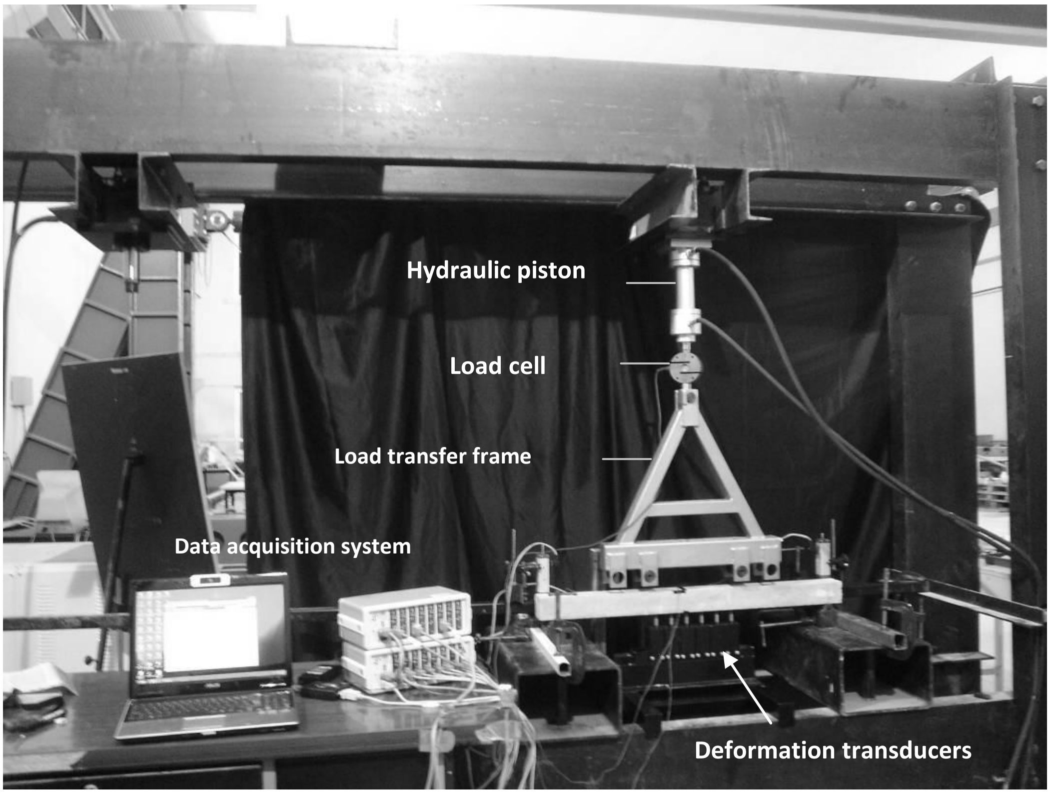

Figure 4.44 Moment-curvature test setup

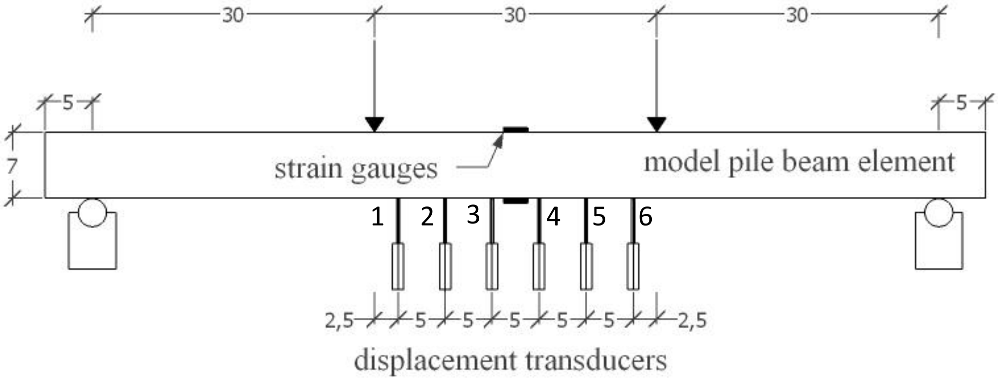

Figure 4.45 Schematic sketch of flexural the test setup

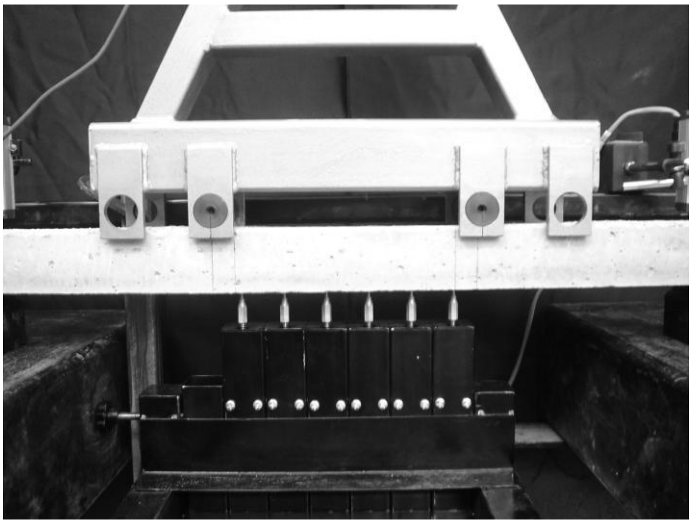

Figure 4.46 Positioned deformation transducers

4.6.1 Bending Test System Checking Studies

A verification test was conducted prior to the moment-curvature tests. For this purpose, a rectangular section steel bar was used for this purpose. In order to get strain readings a strain gage was installed at mid point of the steel bar. Load, deformation and strain were recorded with data acquisition system (Figure 4.47). Using the acquired data, moment-curvature (M-Φ) and stress-strain (σ-ε) relationship were obtained (Figure 4.48 & Figure 4.49). As seen from the figure, the moment of inertia of the bar is $I = 2.813x10^{-9} m^4$. The relations were obtained linearly as it is expected. The slope of the curve of M-Φ means the flexural stiffness (EI) of the steel bar. Elasticity modulus, E, was calculated as $E = 2.11x10^{11}$ N/m^2 according to test result of M-EI and it was accurately well-matched with the steel modulus of elasticity. Stress-strain curve which was gained by using strain gauge and load cell readings also represented the stress-strain behaviour of the steel material. These test results demonstrated that the bending test system was working properly.

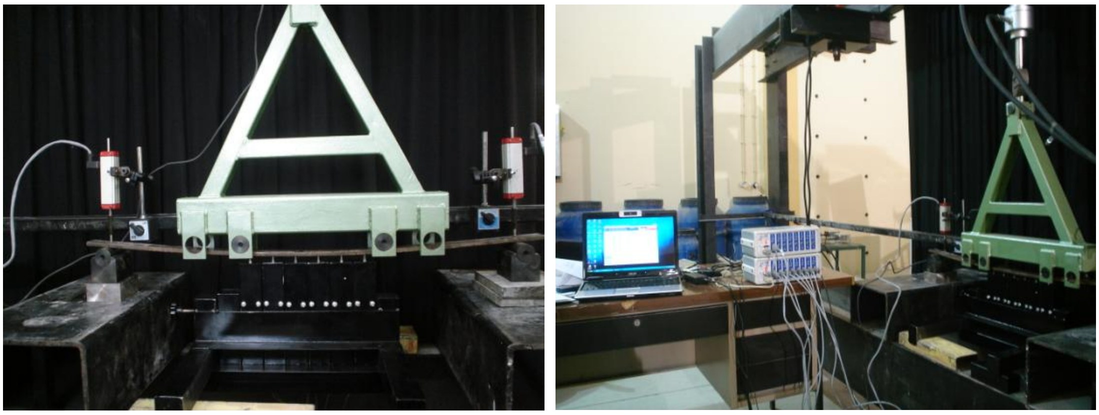

Figure 4.47 Moment-Curvature testing system control studies.

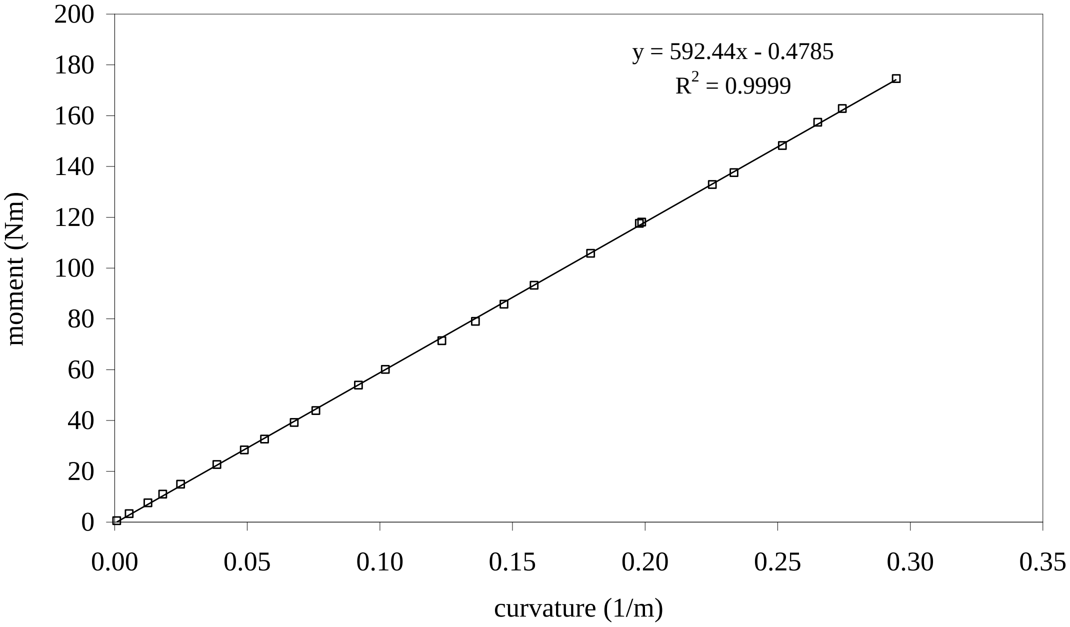

Figure 4.48 Moment- curvature relationship of steel bar

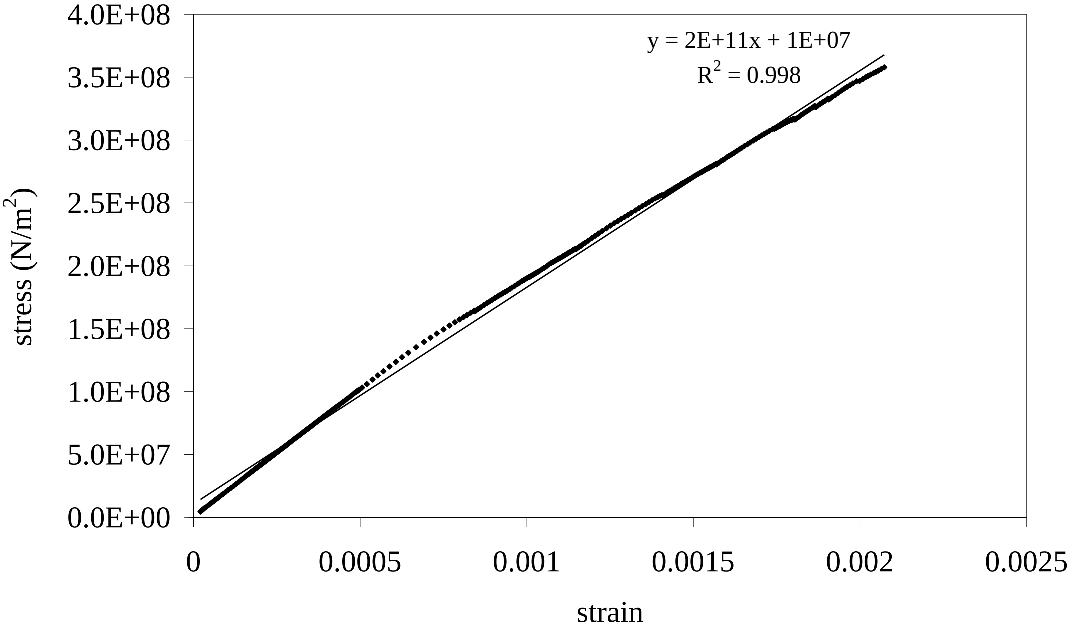

Figure 4.49 Stress-strain relation of steel bar

4.7 Calibration Procedure

A constant moment generation technique similar to the one previously followed by other researchers was used during calibration of the gauges regarding the bending moment (Reese & Van Impe, 2001). The bending test system mentioned above was utilized to develop a relationship for all types of the model piles between measured strain and bending moment. Two strain gauges (Figure 4.45) were instrumented on both compression and tension side of the flexural elements in order to obtain the strains during the loading. The test results of moment-strain relationships for the compression and tension side are presented below from Figure 4.50 to Figure 4.54. Moment graphics along the model pile during the tests were obtained according to these results. Elasticity modulus (E) of concrete and steel fiber reinforced concrete (sfrc) was calculated by using moment calibration relationships (Figure 4.50 & Figure 4.51).

Simple linear elastic theory (Equation 4.6):

$$\sigma = \frac{6 \cdot M}{b \cdot h^2}$$

Hooke's law:

$$\sigma = E.\varepsilon \tag{4.8}$$

From equation 4.6 and 4.8

$$E = \frac{6 \cdot M}{\varepsilon \cdot b \cdot h^2} \tag{4.9}$$

M-ε relation of concrete was obtained:

$$M = 2 \cdot 10^6 \cdot \varepsilon + 9.5064 \tag{4.10}$$

For instance $M = 300Nm$

$$\Rightarrow 300 = 2 \cdot 10^6 \cdot \varepsilon + 9.5064$$
$$\Rightarrow \varepsilon = 1.45 \cdot 10^{-4}$$

The elasticity modulus of the concrete according to Equation 4.9

$$E = \frac{6 \cdot 300}{1.45 \cdot 10^{-4} \cdot 0.07^3}$$
$$\Rightarrow E = 3.613 \cdot 10^{10} N/m^2$$
$$\Rightarrow E = 36130MPa$$

The computed Young's modulus (E) of the concrete according to experiment result was quite-matched with the concrete class (C30) material properties. Computed values of Young's modulus for the concrete and sfrc for the tension and compression side is given in Table 4.11. Results showed that strain corresponding to moment were recorded quite similar on the compression and tension side in the elastic region. In addition, results demonstrated that fiber addition did not influence the modulus of elasticity.

Table 4.11 Modulus of Elasticity

Flexural Element	Modulus of Elasticity, MPa	
	Compression side	Tension side
Concrete (c)	36130	36500
SFRC ,Fiber: 1%	35443	35434

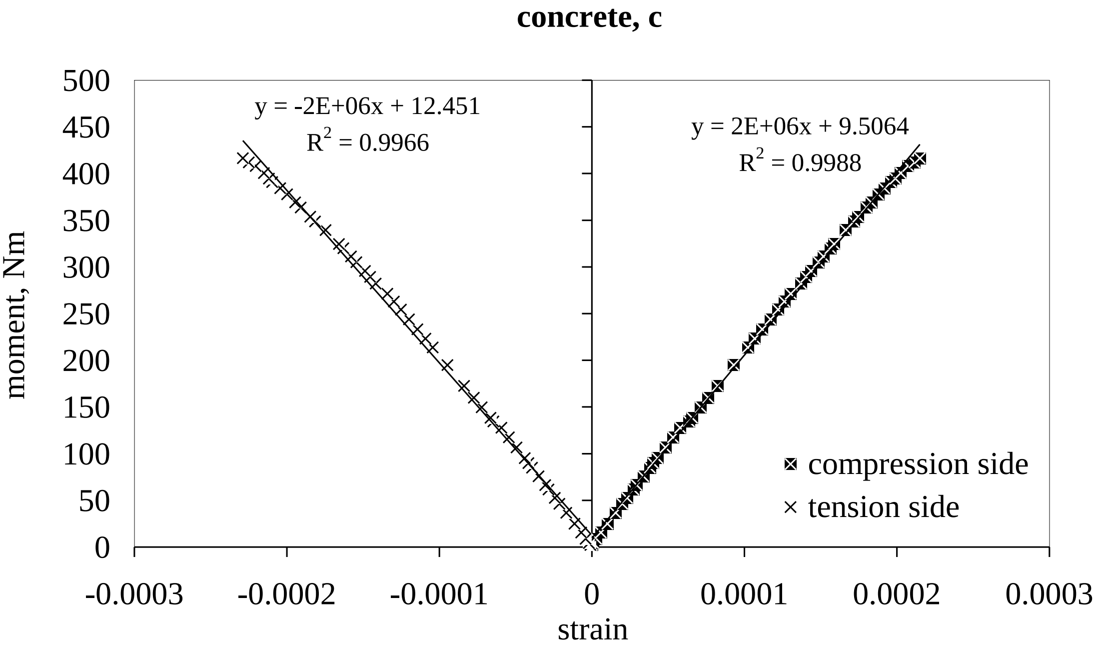

Figure 4.50 Moment calibration of concrete model pile

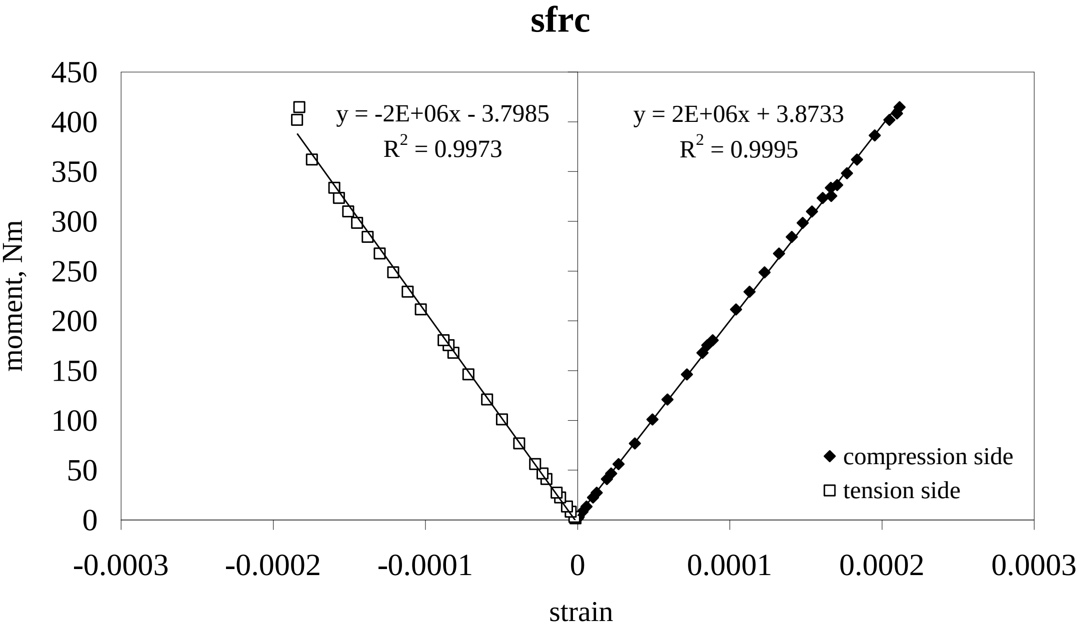

Figure 4.51 Moment calibration of steel fiber reinforced concrete model pile

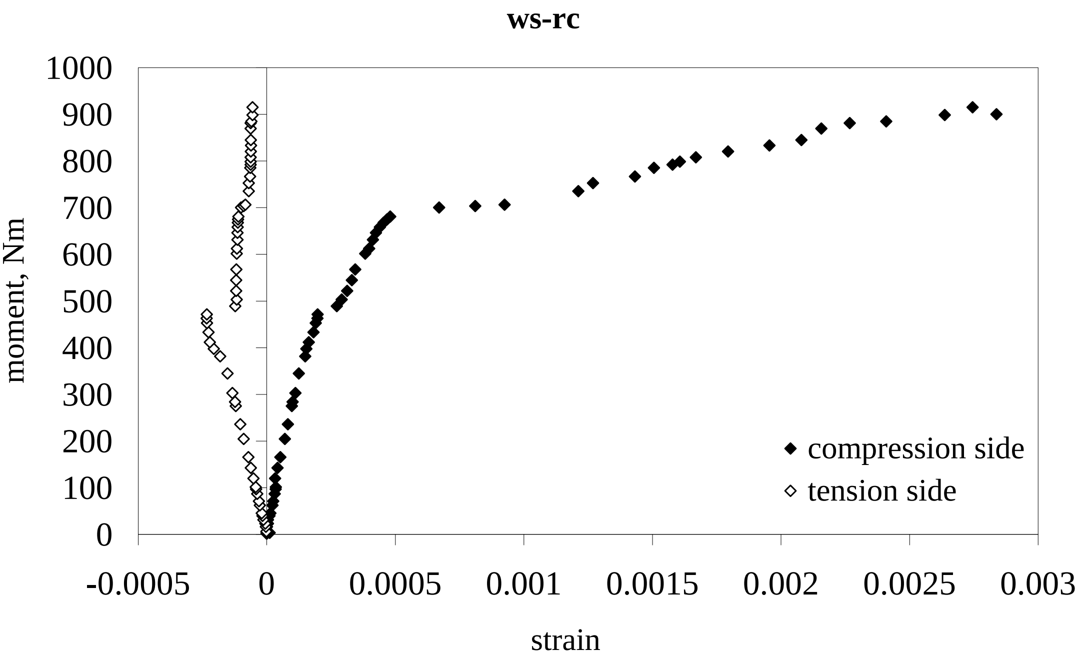

Figure 4.52 Moment calibration of concrete with only bending reinforcement

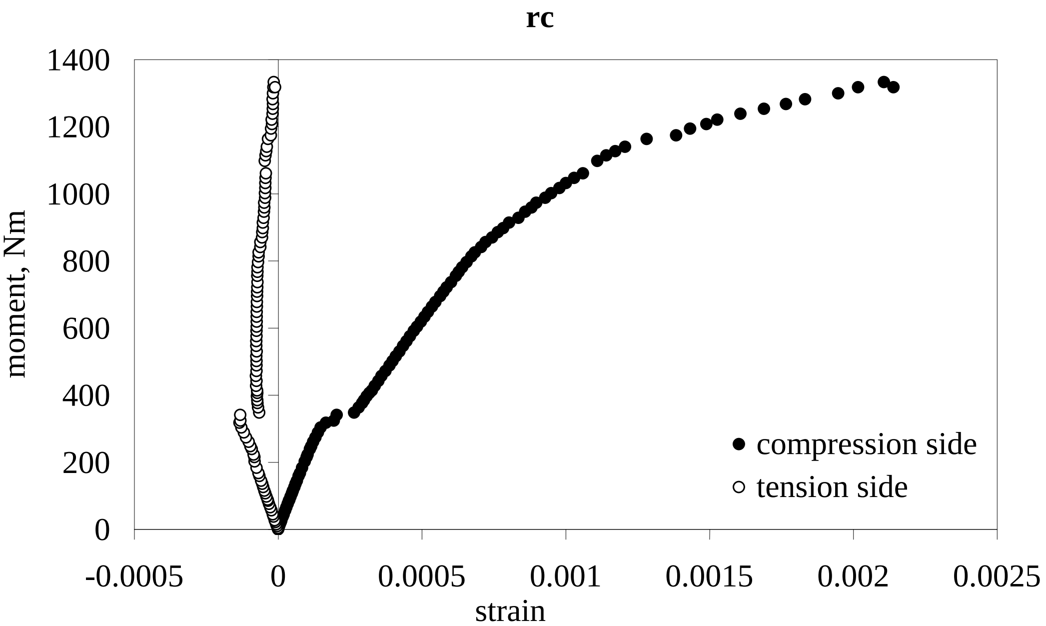

Figure 4.53 Moment calibration of conventional reinforced concrete model pile

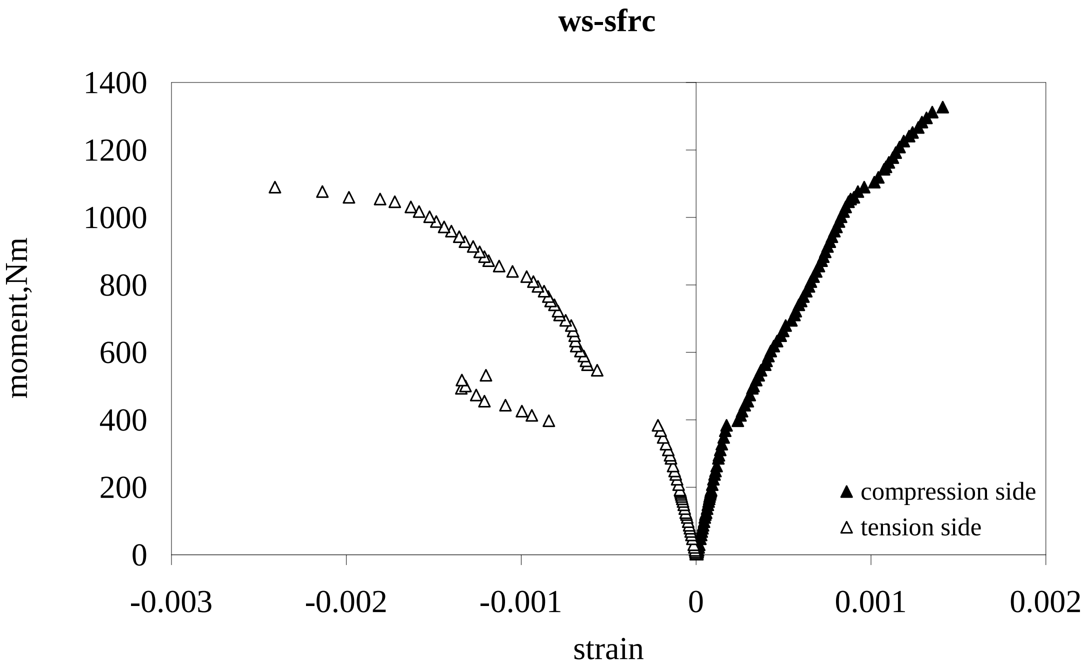

Figure 4.54 Moment calibration of concrete with bending reinforcement and steel fibers

CHAPTER FIVE

TEST RESULTS AND DISCUSSIONS

5.1 Introduction

Five types of model piles were laterally loaded and all tests were performed as deformation controlled. There were two types of loading conditions: (a) only lateral loading and (b) lateral loading while the pile is axially loaded. Thus, the effect of axial loading on the response of laterally loaded piles was investigated. Besides, lateral loads were applied using different loading rates in order to evaluate the influence of loading rate on soil-pile interaction. Pile head displacements and bending moment variations along the pile length were measured and recorded during the tests. The condition of the sand surface around the test pile and cracks along the pile after the tests were also carefully observed and noted. Prior to the model pile tests, bending tests were made on flexural elements to obtain the load-deflection curves and moment-curvature relationship of piles. The test of bending tests and model piles are presented and discussed in detail in the following paragraphs.

5.2 Bending Tests

Bending tests involved testing of flexural elements made of concrete (*c*), steel fiber reinforced concrete (*sfrc*), reinforced concrete (*rc*), concrete with only bending reinforcement (*ws-rc*), and concrete with bending reinforcement and steel fibers (*ws-sfrc*).

5.2.1 Load - Deflection Behavior

Flexural load-deflection curves of midpoint transducers (i.e. #3 & #4) (see Figure 4.45) are shown in Figures 5.1 thru 5.3. It can be seen in Figure 5.1 and Figure 5.2 that deflection readings acquired from the transducer #3 & #4 positioned on the right and left sides of the flexural elements are quite similar. It proves that bending test system is working properly. All flexural elements exhibit linear and fairly similar behavior in the initial loading until first crack occurrence. After initiation of the first crack, however, flexural elements exhibit different post crack behaviors.

Figure 5.3 indicates the comparison between the load-deflection response of plain concrete (*c*) and steel fiber reinforced concrete (*sfrc*) flexural elements. The first crack load and deflection are almost same (Table 5.1). Plain concrete flexural element failed in a brittle manner and load carried was reduced abruptly after the first crack. On the other hand, once the peak strength was reached the load decreased gradually in *sfrc* flexural element meaning that the flexural element exhibited higher energy absorption capacity. Energy absorption capacity can be generally defined as the area under the stress-strain or load-deflection curve. It is found that the energy absorption capacity of the steel fiber reinforced concrete (*sfrc*) flexural element is approximately 2250% larger than that of the concrete flexural element. Failure mode of the *sfrc* flexural element is ductile due to their bridging capacity across the cracks.

A ductility factor was defined in the past in order to numerically express energy absorption capacity of concrete members (Padmarajaiah & Ramaswamy, 2004; Li, 2002). The ductility factor was obtained by dividing the deflection ρ_2 at the load equivalent to the 80% of the peak load to the deflection ρ_1 corresponding to the first crack load. In this study, the load did not drop down 85% of the peak load and forced the author to define the ductility factor by selecting ρ_2 corresponding to 85% of the peak load.

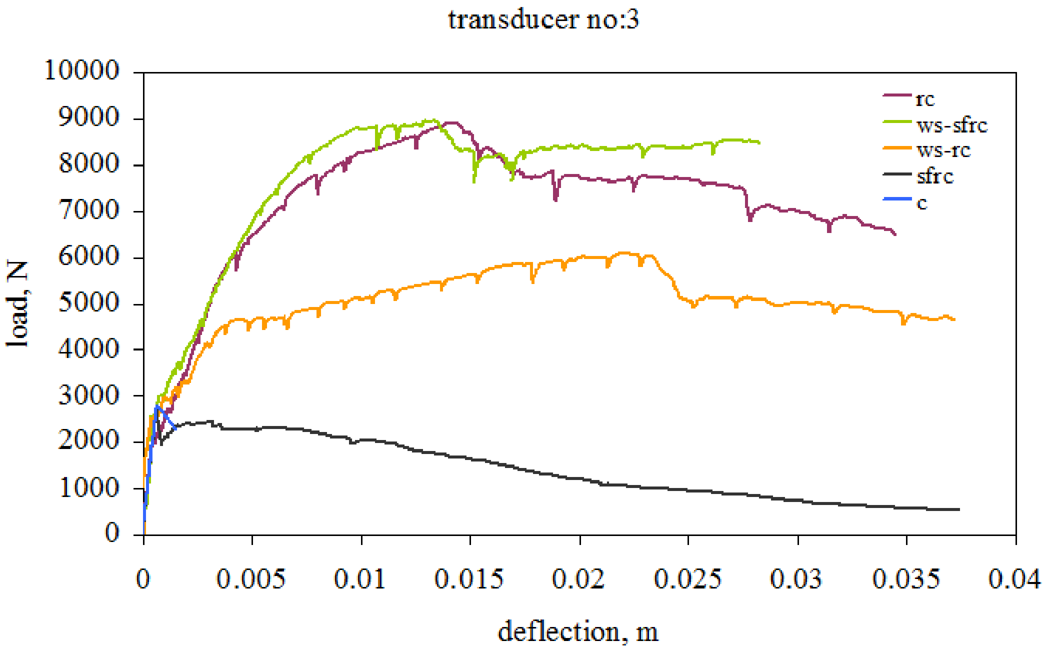

Figure 5.1 Load-deflection curves of transducer #3

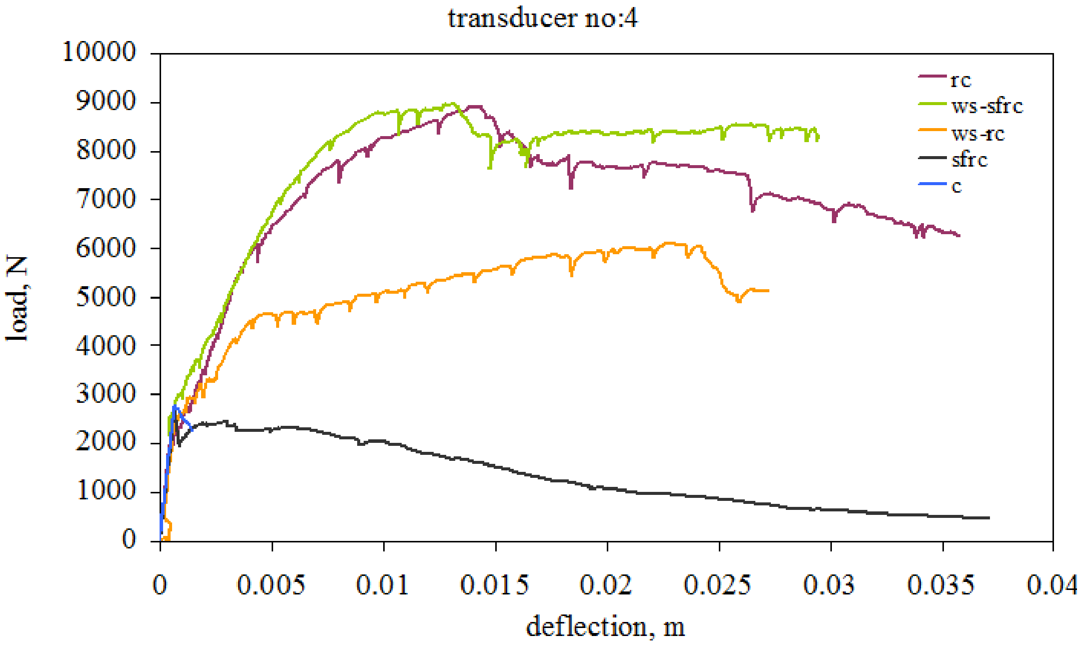

Figure 5.2 Load-deflection curves of transducer #4

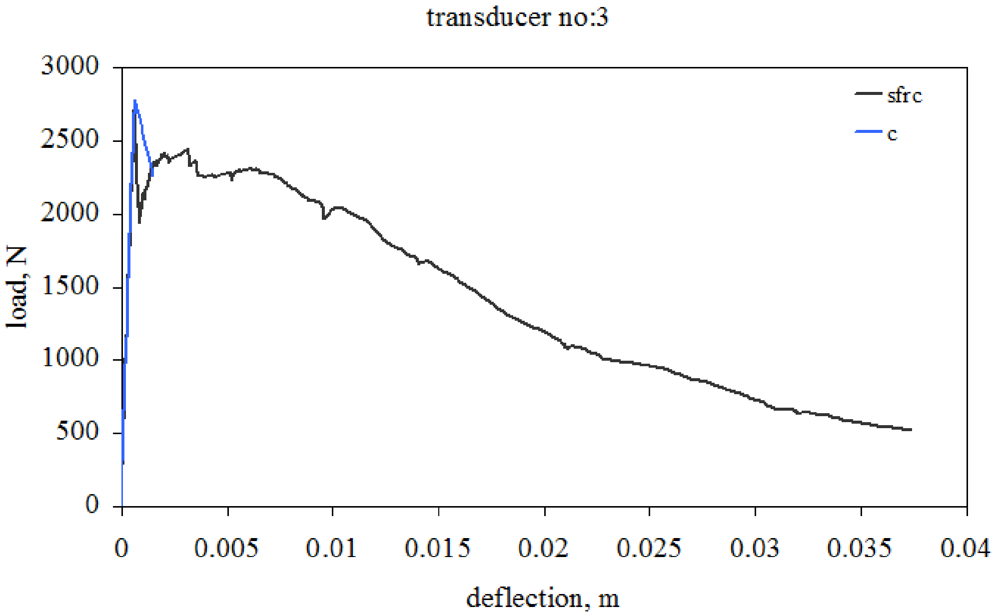

Figure 5.3 Load-deflection curves of concrete (*c*) and steel fiber reinforced concrete (*sfrc*) flexural elements

It was already mentioned in the previous chapter that bending reinforcement ratio was the same in the flexural elements designed as conventionally reinforced (*rc*) and with only bending reinforcement (*ws-rc*). In other words, the *ws-rc* specimen only did not involve shear reinforcement. In the post cracking stage, the behavior of the *rc* and ws-rc flexural element were considerably different (Figure 5.1). One should note in the figure that the response of the *ws-rc* flexural element is governed by the yielding of the bending reinforcement with much smaller peak load (i.e. peak load of the *ws-rc* is 45.6% of the peak load of the *rc*). It can be concluded that shear reinforcement is influential on the flexural behavior of the reinforced concrete flexural elements. Load-deflection behavior of the *ws-sfrc* flexural element, however, happened to be quite similar to that of the rc flexural element both in the initial loading stage and in the post cracking stage. It appears that utilization of 1% steel fiber in *ws-sfrc* generates the effect of shear reinforcement and improves behavior of the flexural element. One should note that flexural behavior of the *ws-sfrc* is superior to the *ws-rc* although there are no stirrups in both flexural elements. Moreover, the first crack load capacity of *ws-sfrc* was 21% higher than that of the *rc*. On the other hand, the ductility factor of *ws-sfrc* was 100% larger than the ductility factor of *rc* (Table 5.1).

Table 5.1 Ductility factors of flexural elements

Flexural element	First crack load (N)	Peak load (N)	ρ_1 (mm)	ρ_2 (mm)	Ductility factor (ρ_2/ρ_1)
rc	2119.80	8887.75	0.514	18.87	36.71
ws-sfrc	2566.02	8940.88	0.414	30.40	73.43
ws-rc	2548.87	6103.49	0.531	24.60	46.33
sfrc	2763.40	2763.40	0.640	3.61	5.64
c	2775.50	2775.50	0.651	1.33	2.04

The flexural test results demonstrated that shear reinforcement ratio in a reinforced concrete flexural element can be considerably reduced by the use of steel fibers. As already stated in the second chapter, recommended steel fiber ratio in volume is 1% and it seems that flexural behavior of laterally loaded piles may be considerably improved by the addition of steel fibers at the recommended volumetric ratio. This may also bring economy since RC piles can be designed without shear reinforcement.

5.2.2 Moment - Curvature Behavior

5.2.2.1 Moment-Curvature Relationship of Reinforced Concrete

Bending stiffness, EI, where E and I represent the modulus of elasticity of the material and the moment of inertia of the cross section, respectively, has a significant role on the behavior of a structural element such as a column, flexural element, or a pile subjected to bending. In some researches, the reduction of the EI with increasing magnitude of bending moment for the reinforced concrete sections was emphasized and taken into consideration (Wang, 1986; Reese & Van Impe, 2001). It was concluded that, the reduction of EI influences the response of soil-pile. Bending stiffness is nearly constant in the initial loading stage up to first crack, which denotes linear behavior of pile. After the crack formation, in the post cracking stage, the behavior of the pile is nonlinear. Bending stiffness, EI, for the initial stage and the post crack stage can be obtained via the slope of the moment-curvature curve.

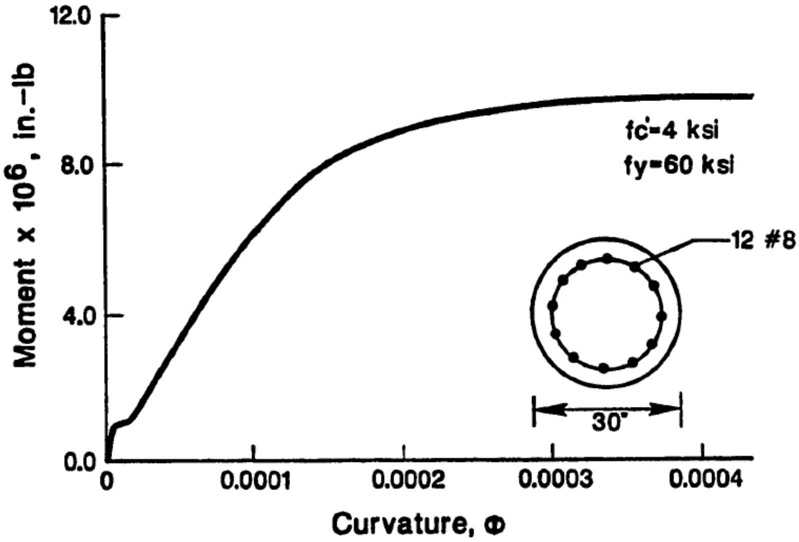

Figure 5.4 Moment-curvature relationship for a circular cross section (Wang, 1986)

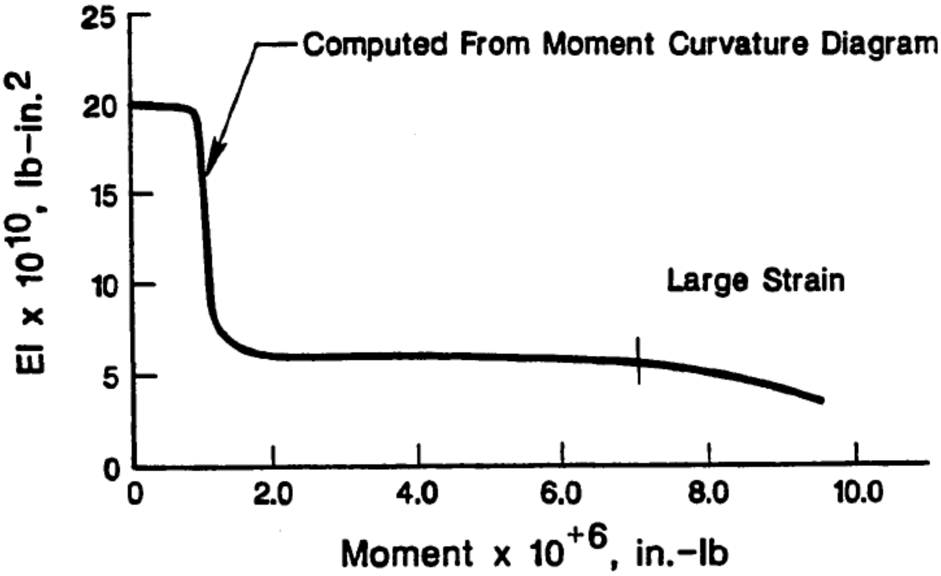

Figure 5.5 Bending moment-bending stiffness relationship for a circular cross section (Wang, 1986)

A relationship of moment-curvature and moment-EI for a reinforced concrete flexural element was presented as an example in the study of Wang, (1986) which is shown in Figure 5.4 and Figure 5.5. The gradually reduction of the EI and nonlinear behavior of moment-curvature can be clearly seen from the related figures. It was noted in that study that most reinforced concrete flexural elements behave nonlinearly even under service-loading conditions due to their linear behavior stage is very small.

Reese & Van Impe, (2001) stated in the case studies as part of their study that three methods were utilized to predict the moment-EI relationship of the tested reinforced concrete piles in San Francisco. Methods involved the analytical method, the approximate (American Concrete Institute–ACI) method, and the experimental method. The curves, which were obtained from the methods, were compared (Figure 5.6). Comparison of the curves demonstrated that an abrupt decrease in EI occurred with increase in bending moment. The scientists noted that analytical method gives the precipitous drop of the curve among the utilized methods. In this PhD thesis, the moment-curvature relationships of the model piles were obtained by experimental study. It should be note that the relation of the moment-curvature depends strongly on the steel ratio, bond characteristics, exact stress-strain curves for the concrete and steel.

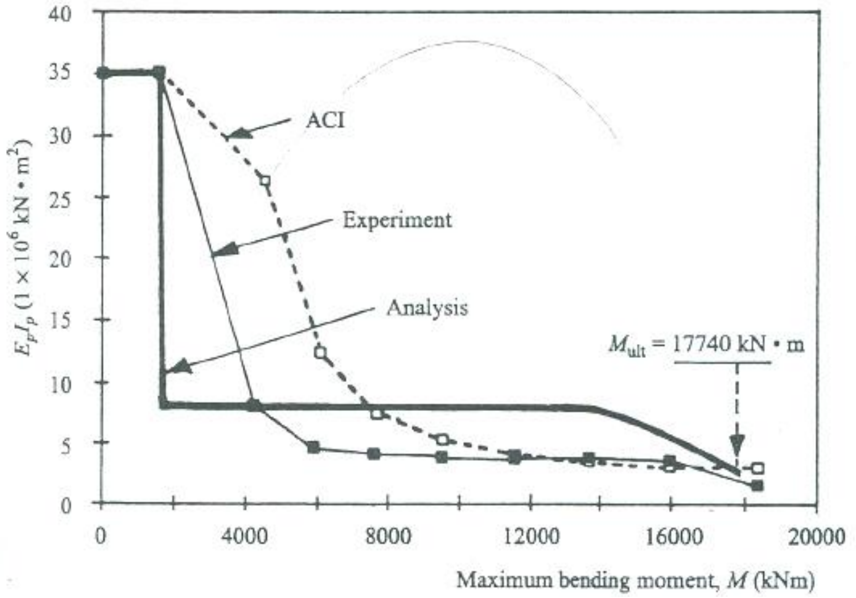

Figure 5.6 Values of bending stiffness as a function of applied moment for the three methods (after Reese, 1997)

Both modulus of elasticity, E, and moment of inertia, I, differ as the stress condition change. The modulus of elasticity changes due to nonlinear behavior of concrete and the moment of inertia decrease, because of the formation of the crack on the tension face of the pile.

The nonlinear analysis of reinforced concrete piles under lateral load can be conducted based on moment-curvature relationship. A portion of flexural element before loading and after bending load is presented in Figure 5.7(I) and Figure 5.7(II) respectively. The shape of the flexural element changed under pure bending. The unit strain, ε, was given by Equation 5.1c where dx= length of the element (Equation 5.1a); and y= distance from neutral axis (Equation 5.1b).

$$\overline{a'b'} = \overline{ab} = dx = \rho \cdot d\theta \tag{5.1a}$$

$$\overline{c'd'} = (\rho + y) \cdot d\theta \tag{5.1b}$$

$$\varepsilon = \frac{\overline{c'd'} - \overline{cd}}{\overline{cd}} = \frac{(\rho + y) \cdot d\theta - \rho \cdot d\theta}{\rho \cdot d\theta} = \frac{y \cdot d\theta}{\rho \cdot d\theta} \Rightarrow \varepsilon = \frac{y}{\rho} \tag{5.1c}$$

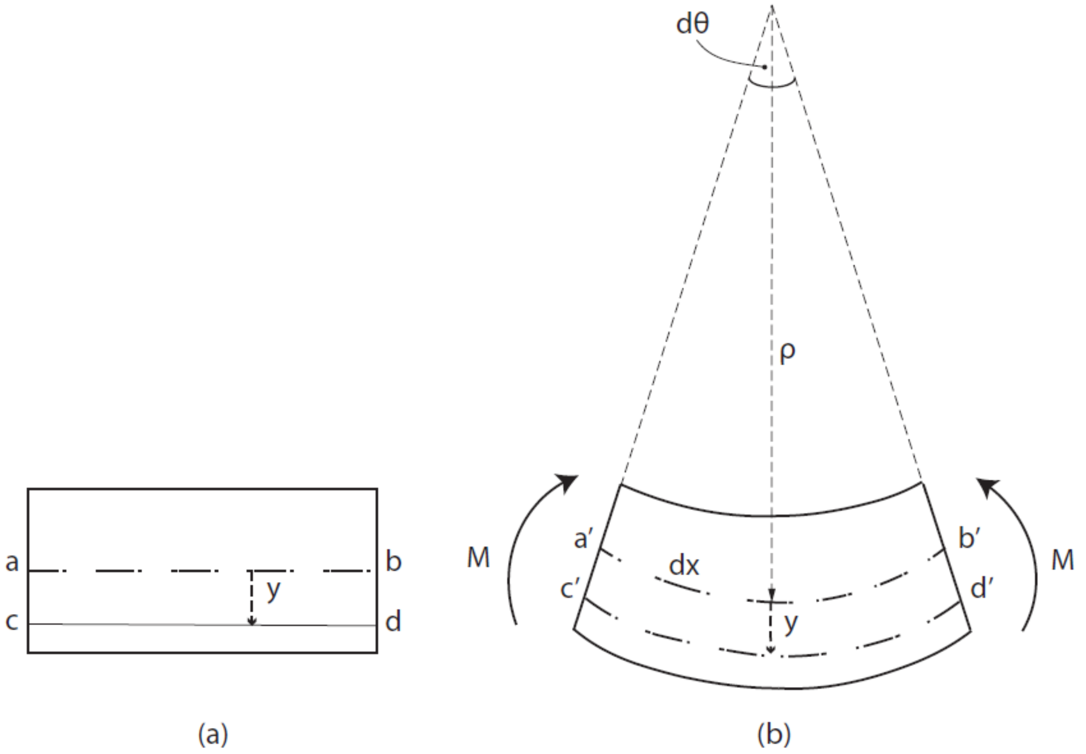

Figure 5.7 Portion of a flexural element (a) before bending (b) subjected to bending (Reese & Van Impe, 2001)

According to Hooke's law and flexural element theory Equations 5.2 and 5.3 are presented below respectively.

$$\sigma = \varepsilon \cdot E \tag{5.2}$$

$$\sigma = \frac{M}{I} y \tag{5.3}$$

Where σ= stress along the flexural element length.

From Equations 5.2 and 5.3

$$\varepsilon \cdot E = \frac{M}{I} y \Rightarrow E \cdot I = M \cdot \frac{y}{\varepsilon} \tag{5.4}$$

From Equations 5.1c and 5.4

$$EI = \frac{M \cdot y}{\frac{y}{\rho}} \tag{5.5}$$

Rewriting Equation 5.5

$$EI = \frac{M}{\left(\frac{1}{\rho}\right)} \tag{5.6}$$

From Equation 5.1a

$$\frac{d\theta}{dx} = \frac{1}{\rho} \tag{5.7}$$

Curvature, $\frac{1}{\rho}$, is described as the angle per unit length at any portion of a flexural element subjected to bending. Therefore, curvature, Φ is given by Equation 5.8.

$$\Phi = \frac{1}{\rho} \qquad 5.8$$

The relation between bending stiffness (EI) and moment (M) and curvature (Φ) is determined from Equations 5.6 and 5.8

$$EI = \frac{M}{\Phi} \qquad 5.9$$

The characteristic moment-curvature relation for a reinforced concrete section was idealized as trilinear relation by Kwak & and Kim, (2002) as shown in Figure 5.8. Moment-curvature behavior was defined in three different stages at that study. The first stage is uncracked stage up to concrete first crack; the second stage is crack-propagation stage up to tension steel yield; and the third stage is up to failure. In Figure 5.8 the point A is corresponding to first crack moment and curvature, M_{cr}-Φ_{cr}, and the point B is corresponding to tension steel yield moment and curvature, M_y-Φ_y.

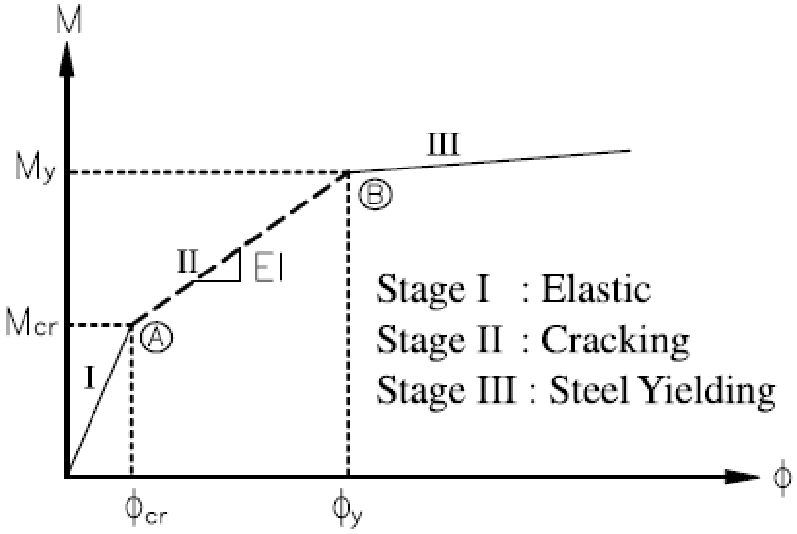

Figure 5.8 Idealized moment-curvature relation of RC (Kwak & and Kim, 2002)

The moment-curvature idealization of the Nilson's (1997) study contains more details in order to express the nonlinear behavior of flexural elements under flexural loading (Figure 5.9). The behavior of flexural element can be expressed as follows:

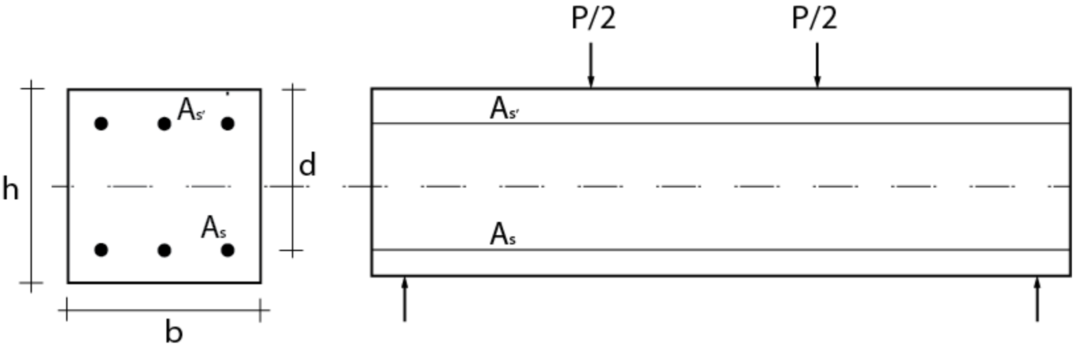

Figure 5.9 Reinforced concrete flexural element under flexural loading

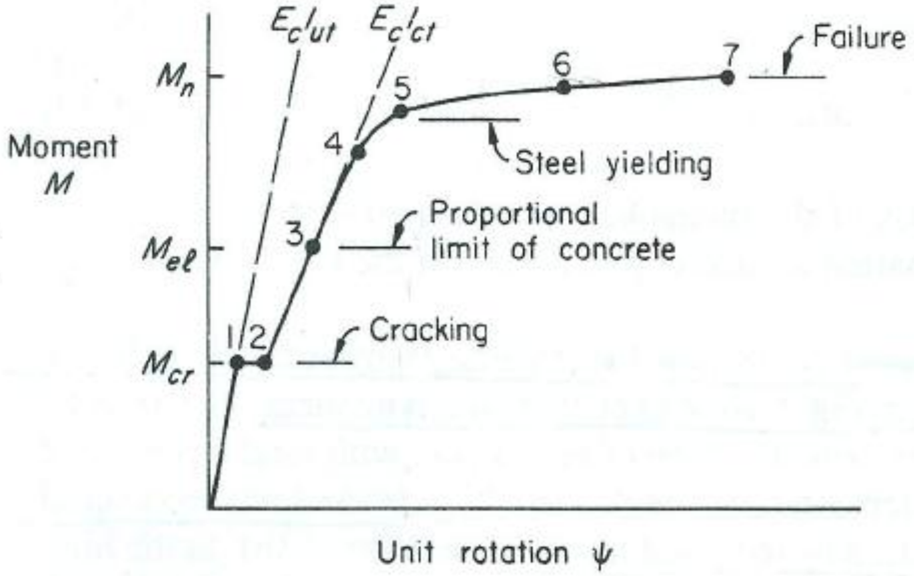

Figure 5.10 Moment-curvature relation of reinforced concrete flexural element (Nilson, 1997)

- Uncracked-elastic stage (up to point 1): In this initial stage moment-curvature diagram is linear and EI is constant. Bending stiffness is defined (E_cI_{ut}) in Figure 5.10, where E_c is modulus of elasticity of concrete and I_{ut} is the moment of inertia of the uncracked section. The entire reinforced concrete section is effective withstanding stress in both side of the neutral axis. Stress-strain relationship of concrete and steel is represented in idealized form in Figure 5.11 to follow the stress-strain development with increasing of load. The distribution of strain and stresses of this stage were illustrated in Figure 5.12a. The steel is well below yield strain $\varepsilon_s<\varepsilon_{sy}$ (ε_s= steel strain; ε_{sy}= yield strain of steel) and concrete strain, ε_c, is below the strain in the elastic limit, ε_{el}, ($\varepsilon_c<\varepsilon_{el}$) in this stage. When the strength is increased up to the tension strength of the concrete (f_{ctk}), first crack develop at the tension side which is illustrated in Figure 5.12b. The moment at the point 1 is called first crack moment or cracking moment $M_{cr.}$

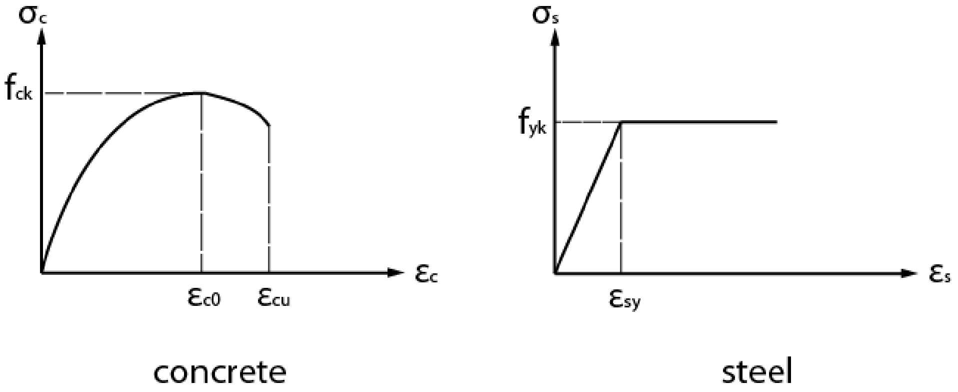

Figure 5.11 Idealized stress-strain curves of concrete and steel

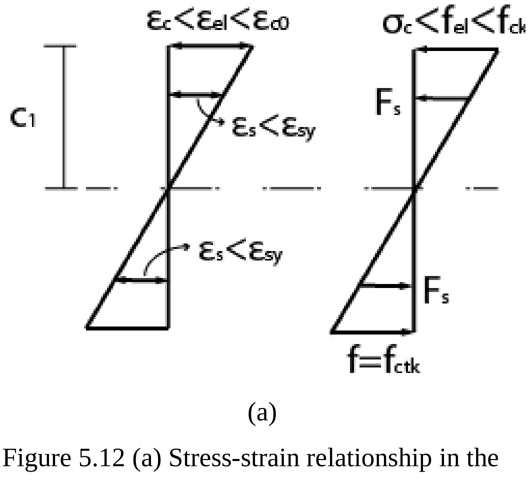

(a)

Figure 5.12 (a) Stress-strain relationship in the uncracked-elastic stage

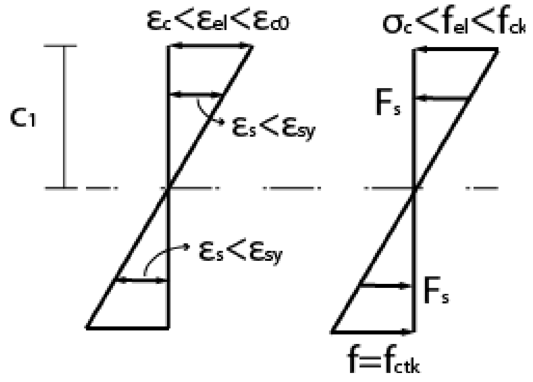

(b)

Figure 5.12 (b) Stress-strain relationship in the uncracked-elastic stage at first crack-point 1 (M_{cr}) *-continued*

- Cracked-elastic stage (from point 1 to point 3): When the first cracking occurs, moment remains constant and curvature increase up to point 2. When the moment is further increased, bending stiffness is noticeably reduced. Bending stiffness is defined (E_cI_{ct}) in Figure 5.10, where I_{ct} is the moment of inertia for the cracked section. In this stage, number of cracks increase along the tension side of the flexural element and cracks penetrates towards the neutral axis. The distribution of these tension cracks is illustrated in Figure 5.14. It should be noted that neutral axis depth decreased with the propagation of cracks. In the limit case, at point 3, the steel strain level is still lower than the yield strain ($\varepsilon_s<\varepsilon_{sy}$) and, the concrete strain reaches elastic limit of it; $\varepsilon_c=\varepsilon_{el}$ (Figure 5.14 a). In this stage stresses and strains are still proportional.

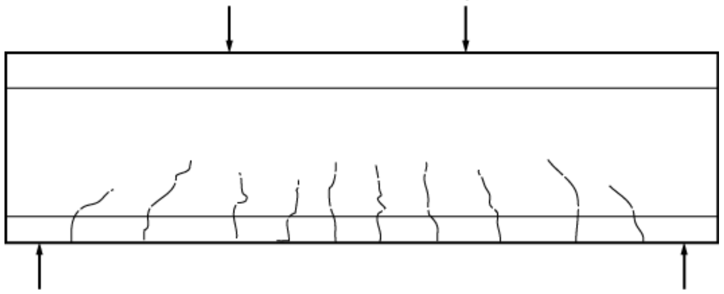

Figure 5.13 Tension crack propagation under increasing load

- Cracked-nonlinear stage (from point 3 to point 7): In this stage concrete is in the nonlinear range and the strain of the concrete is higher than the elastic limit; $\varepsilon_c > \varepsilon_{el}$. Steel is steel below yield strain. Stresses and strains are no longer proportional and neutral axis depth is decreasing. Plastic deformations occur at the upper and lower part of the compression and tension side. EI continue decreasing with the propagation of the cracks. During this stage at point 5, steel reaches yield strain, $\varepsilon_s = \varepsilon_{sy}$, (Figure 5.14 b). After yield moment, M_y, tension cracks extend visibly and propagate upward and the slope of the curve considerably reduced as can be seen in Figure 5.10, the points 5 to 7. After point 5, concrete reaches compression strain, $\varepsilon_{co} = 0.002$ at maximum stress, f_{ck} (Figure 5.14 c). Additional increase in applied moment causes broad nonlinear curvature until the eventually compressive strain limit of the concrete, $\varepsilon_{cu} = 0.003$ is reached at the ultimate curvature Φ_u and ultimate moment M_u or M_n (Figure 5.14 d). At the moment that initiates Φ_u compression side of the concrete fails by crushing.

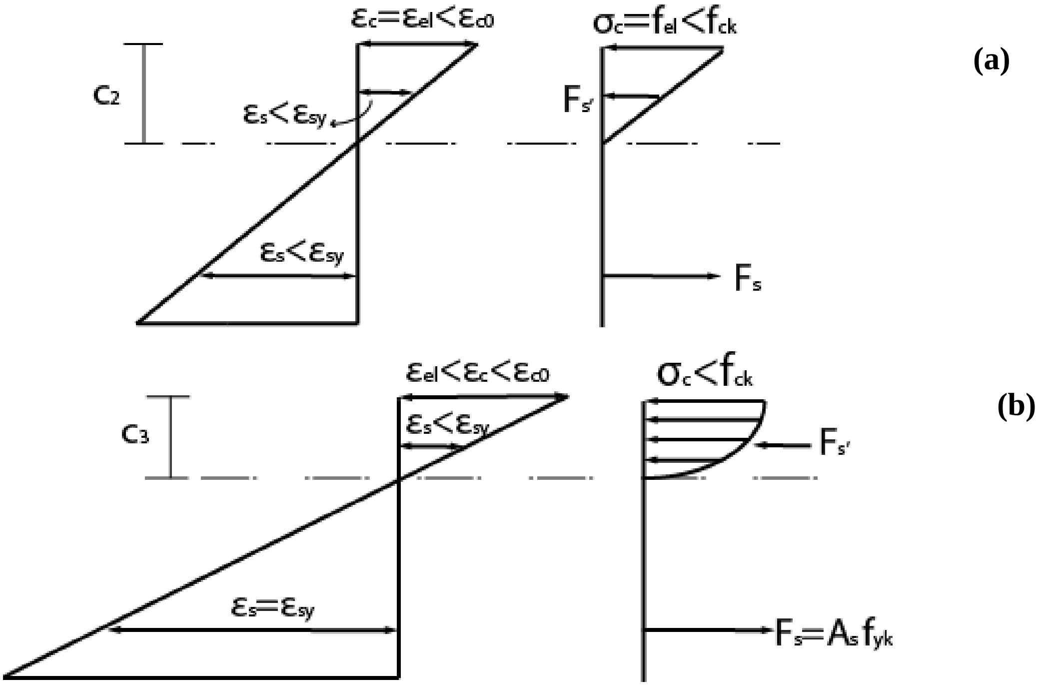

Figure 5.14 (a) Stress-strain relationship in the cracked-elastic stage at point 3 (M_{el})

(b) Stress-strain relationship in the cracked-nonlinear stage at steel yielding- at point 5 (M_y)

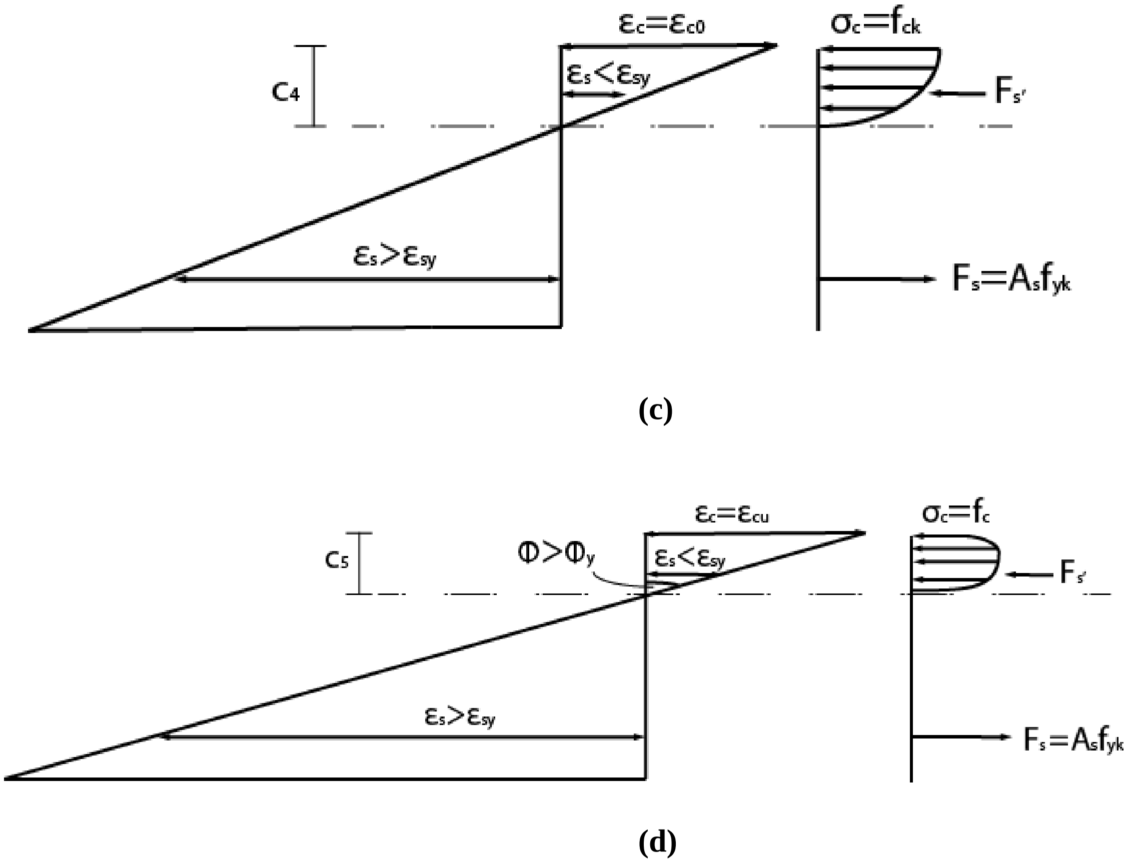

Figure 5.14 (c) Stress-strain relationship in the cracked-nonlinear stage after steel yielding – at point 6 (ε_{c0}) (d) Stress-strain relationship in the cracked-nonlinear stage at concrete crushing– at point 7 (ε_{cu}, M_u or M_n)-*continued*

5.2.2.2 Test Results

Bending test results as moment-curvature curves for all types of the flexural elements are shown in Figure 5.15 and linear stage of moment-curvature relationships are presented in Figure 5.16. The first crack values, nonlinear part of the graph and ultimate values can be clearly seen from the curves. Comparison of moment-curvature behavior of flexural element is presented in the following paragraphs.

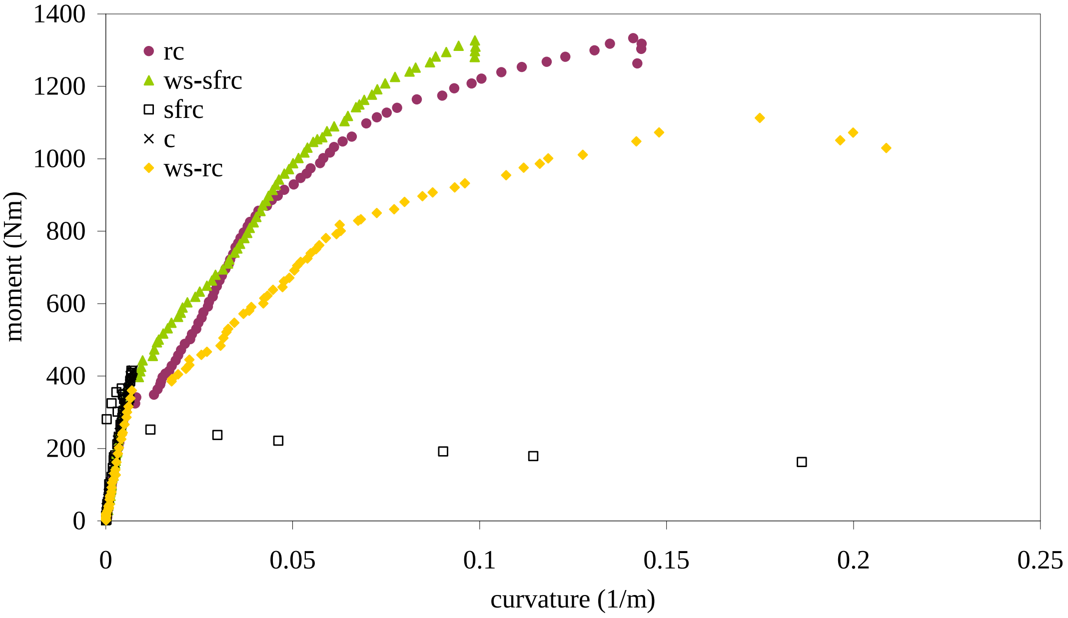

Figure 5.15 Moment-curvature relationship of flexural elements for all types of the model piles

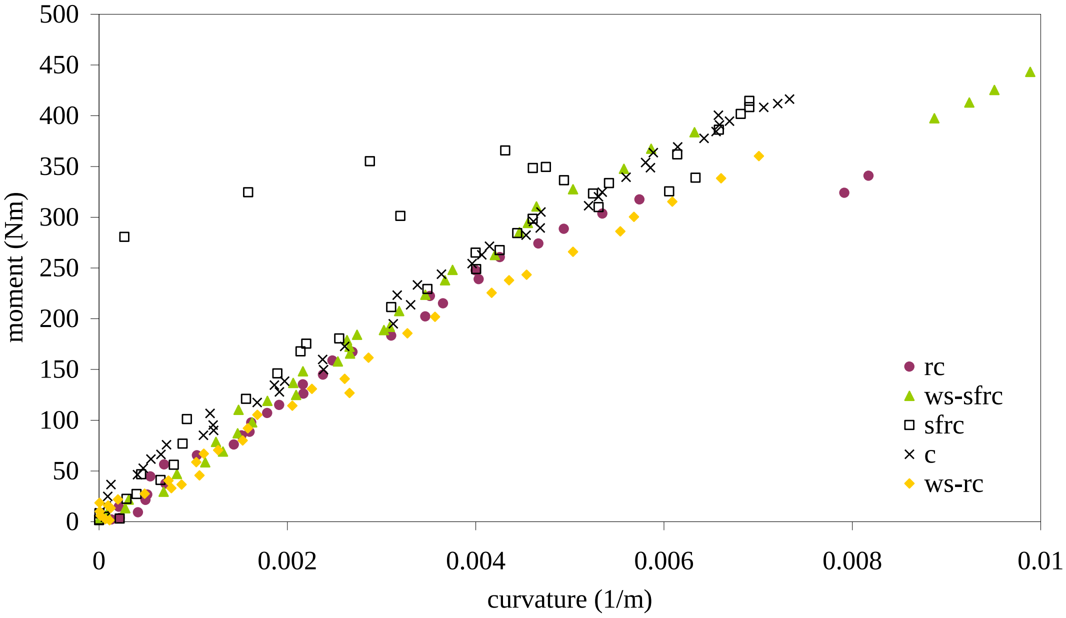

Figure 5.16 Moment-curvature relationship of flexural elements for all types in the linear stage

Quadratic polynomials have been derived from the six displacement transducers along the constant moment region. Curvature corresponding to the moment was determined by double differentiation of quadratic polynomial which is given in Equation 5.10.

$$\Phi = \frac{d^2y}{dx^2} = \frac{M}{EI} \qquad 5.10$$

In order to estimate the yield moment (M_y) some iterative computations were made according to M-Φ and moment-compression strain measurements:

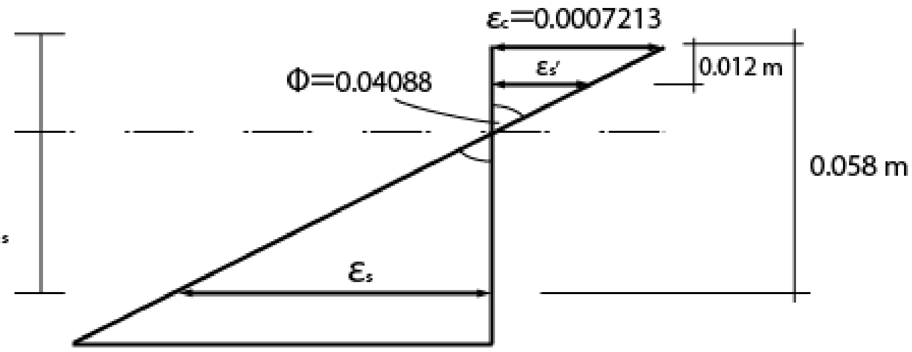

Figure 5.17 Strain distribution at bending moment M= 855.791 Nm

1) When the moment reach M= 855.791 Nm value, curvature and concrete strain on the compression side were recorded; Φ= 0.04088 1/m and, ε_c=0.0007213 respectively. The distribution of the strain along the cross section of the flexural element is illustrated in Figure 5.17.
2) Rewriting Equation 5.1c in order to determine c (y= distance from neutral axis is symbolized by c in the following computations):

$$\frac{1}{\rho} = \Phi = \frac{\varepsilon}{c}$$

$$\Rightarrow c = \frac{\varepsilon}{\Phi}$$

$$\Rightarrow c = \frac{0.0007213}{0.04088} = 0.01764m$$

$$c_s = 0.058 - 0.01764 = 0.04036m$$

The strain of steel

$$\varepsilon_s = c_s \cdot \Phi = 0.0408 \cdot 0.04036 = 0.165\%$$

3) The material characteristics of steel reinforcement are represented in *Chapter 3, section 3.4.1.5* as the yield strength and elasticity modulus of steel bar were

obtained f_{yk}= 265 MPa, E_s=200760 MPa respectively. Thus, the yield strain of the steel on the tension side is determined

$$\varepsilon_{sy} = \frac{E_s}{f_{yk}} \tag{5.11}$$

$$\varepsilon_{s\,y} = \frac{316}{200760} = 0.16\%$$

The computational results show that the strain of the steel, ε_s = 0.165% at specified bending moment reaches the yield strain of the steel ε_{sy}= 0.16%.

Cracking pattern and moment-curvature relationship of conventional reinforced concrete model pile as a reference are presented in the following Figures 5.18 and Figure 5.19.

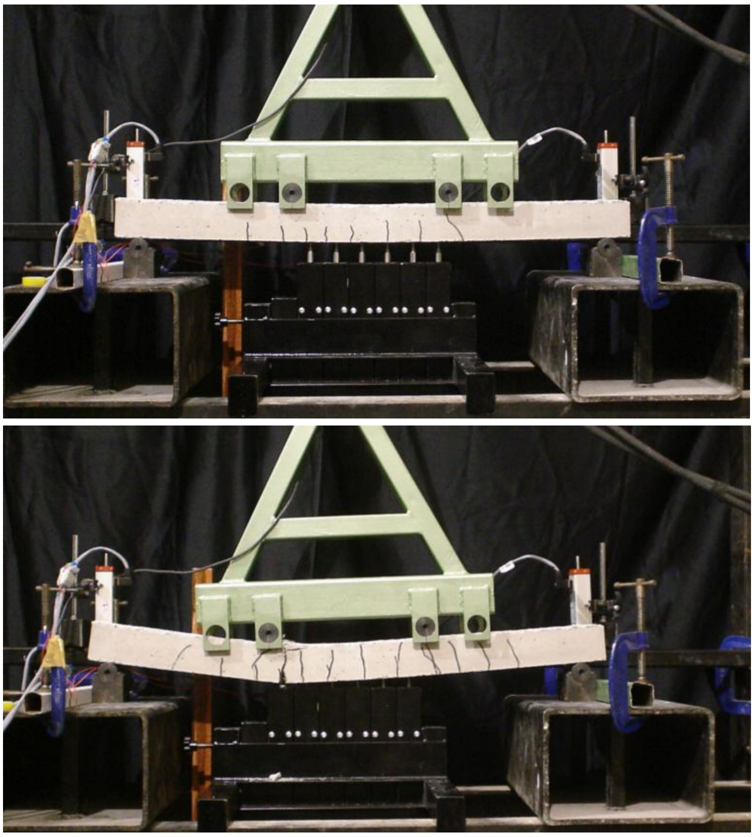

Figure 5.18 Cracking pattern of conventional reinforced concrete flexural element (*rc*) under bending

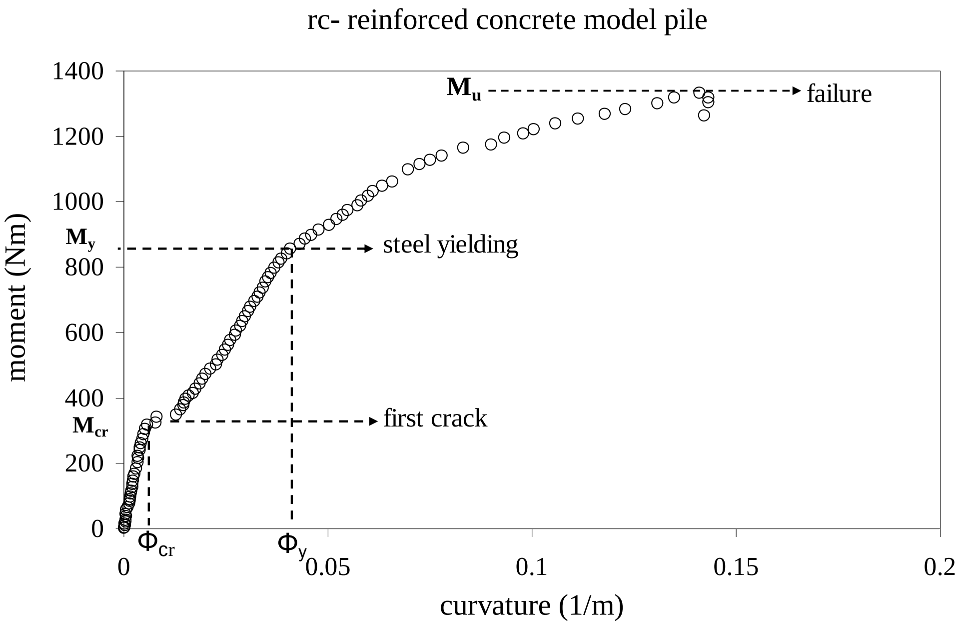

Figure 5.19 Moment-curvature relationship of conventional reinforced concrete flexural element

The cracking patterns of ws-sfrc and *ws-rc* are shown in Figure 5.20 and Figure 5.21.

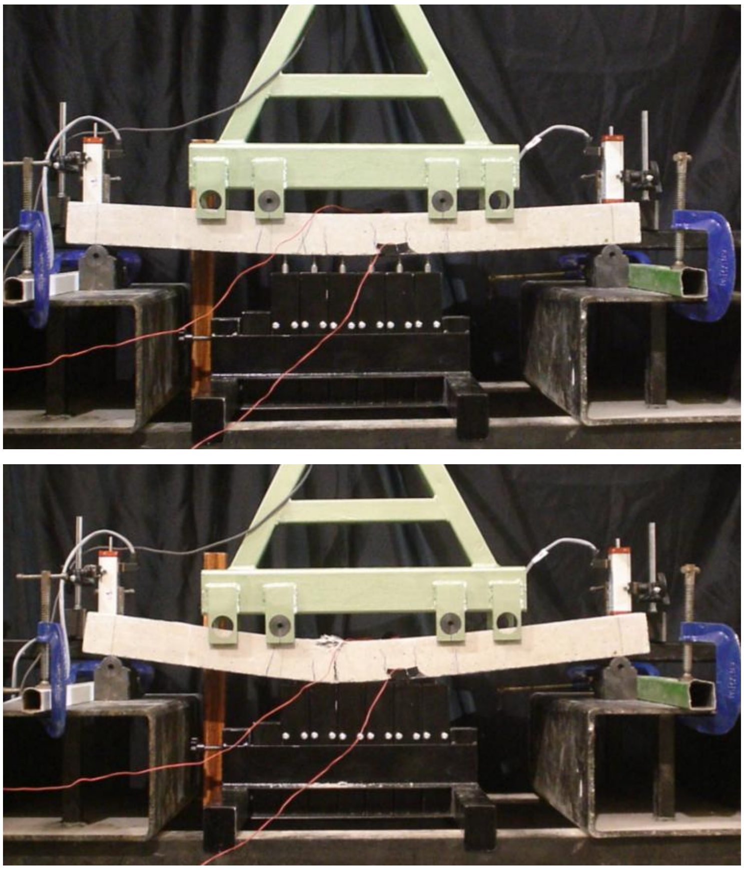

Figure 5.20 Cracking pattern of concrete with bending reinforcement and steel fiber (*ws-sfrc*)

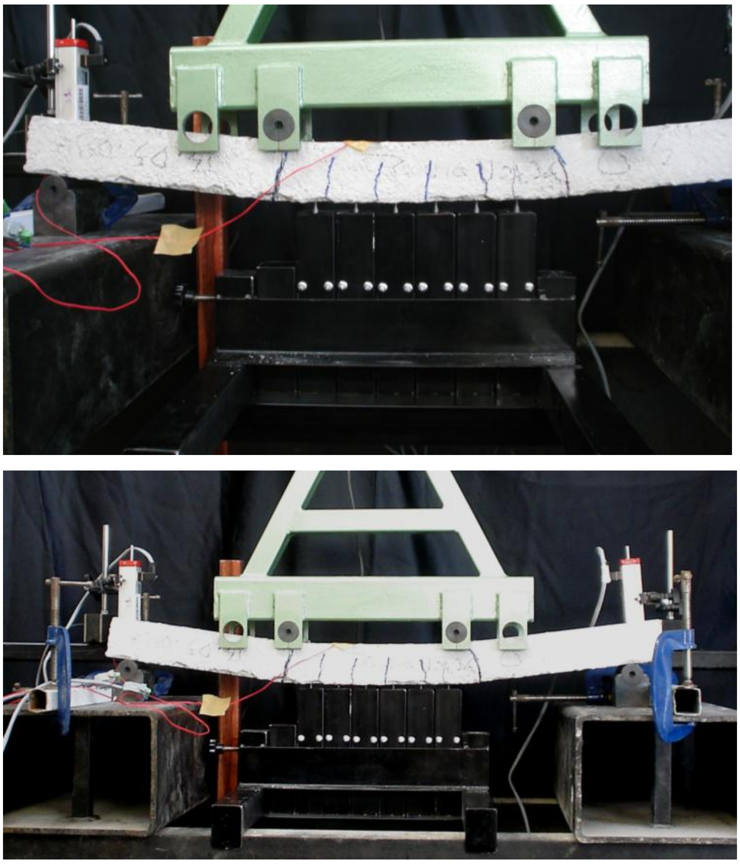

Figure 5.21 Cracking pattern of concrete with only bending reinforcement (ws-rc)

Moment-curvature relation of *rc*, ws-sfrc, and *ws-rc*, are presented from Figure Figure 5.22. In comparison, general moment-curvature behavior of *ws-sfrc* model pile and *rc* model pile were obtained quite similar. On the other hand, the moment curvature relation of *ws-rc* flexural element is noticeably different from the ws-sfrc and *rc* flexural elements. The yield moment and failure moment of *ws-rc* was considerably smaller than the model piles *ws-sfrc* and *rc*.

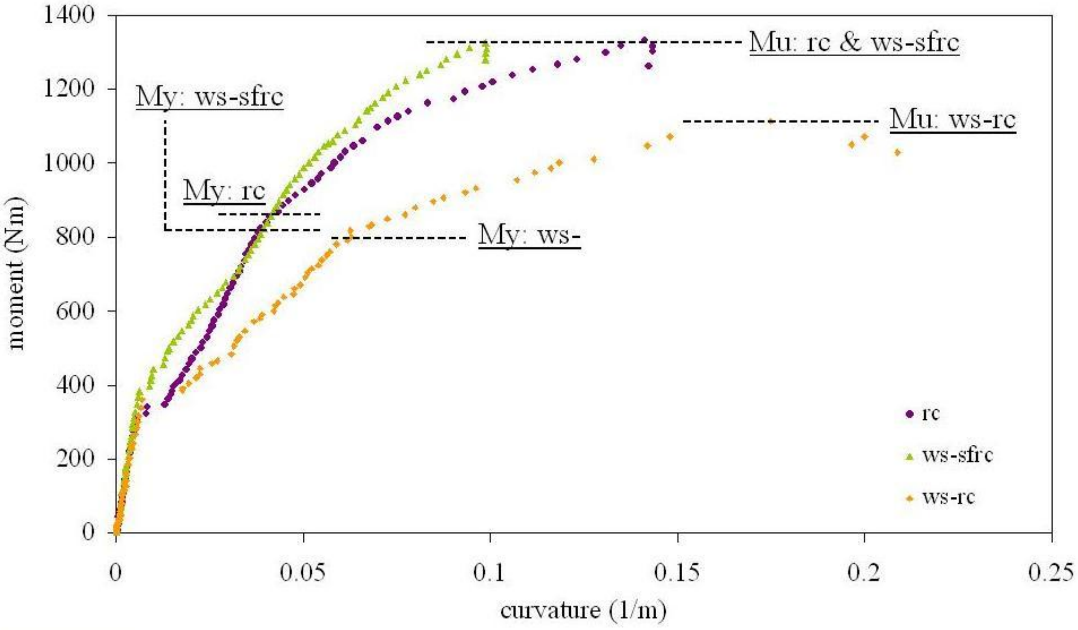

Figure 5.22 Moment-curvature relationship *rc*, *ws-sfrc*, and *ws-rc*

The flexural element, concrete (*c*) failed with single hinge whereas the steel fiber reinforced concrete flexural element failed with two hinges (Figure 5.23). In addition, concrete flexural element cracked immediately just after cracking moment (M_{cr}) level but in the test the steel fiber reinforced concrete flexural element fibers bridge the cracks and moment decrease gradually (Figure 5.24 and Figure 5.25).

Cracking moment and curvature values of all types of model piles under bending are presented in Table 5.2. The experimental based moment-curvature relations of (*rc*) and (*ws-rc*) demonstrate that stirrup has a significant effect on moment-curvature relation. The *rc* flexural element exhibited much better performance than *ws-rc* flexural element. Yield moment (M_y) and ultimate moment (M_u) values for the rc flexural elements were found 8% and 20 % higher than the *ws-rc* flexural element, respectively. It is also seen from the moment-curvature graphics and from the Table 5.2 that presence of steel fiber significantly affected the behavior of flexural elements under bending. The flexural elements *ws-sfrc* exhibited better performance compared to *ws-rc*. In addition, the behavior of rc and *ws-sfrc* were observed to be quite similar. Yield moment (M_y) and ultimate moment (M_u) values were obtained close to each other. Moreover, cracking moment of tested ws-sfrc was obtained 21 % higher that the conventional reinforced concrete.

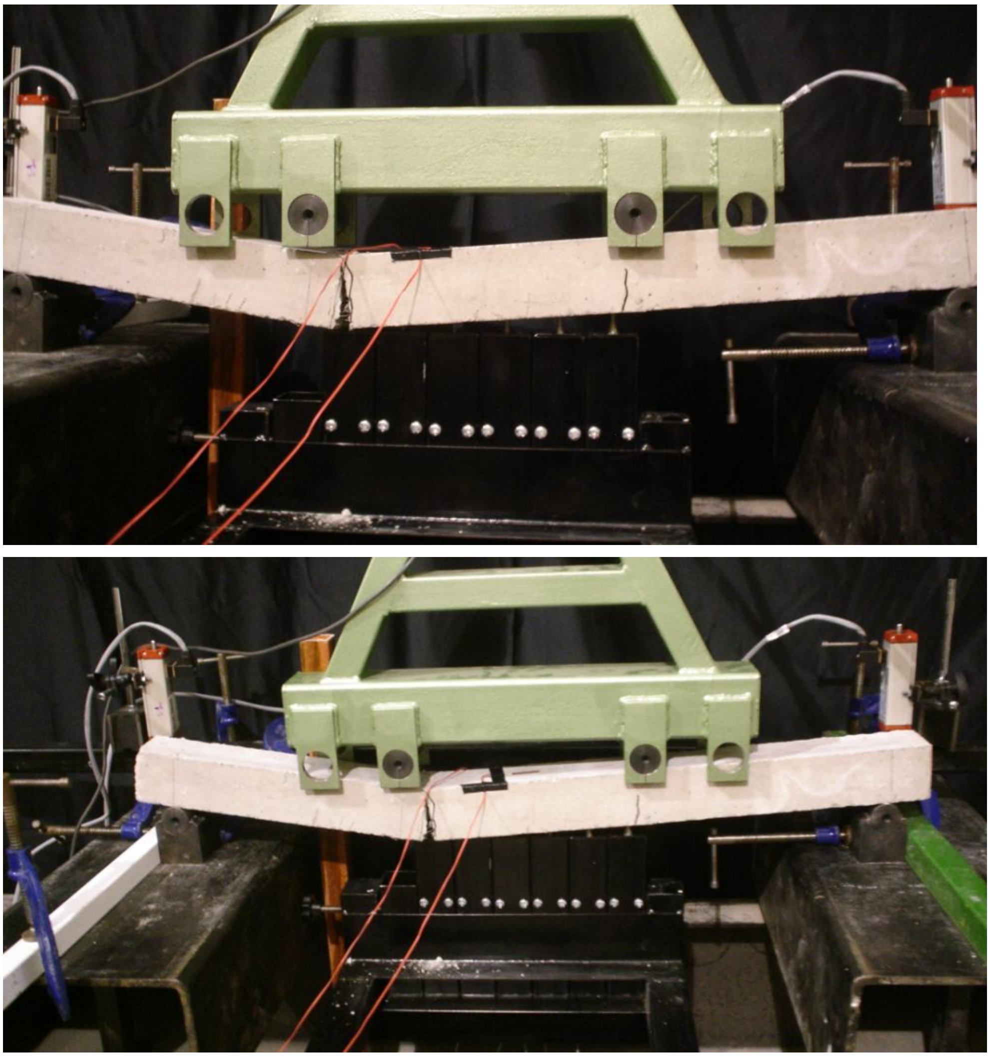

Figure 5.23 Cracking pattern of steel fiber reinforced concrete flexural element (*sfrc*)

Moment (M)-bending stiffness (EI) relations were obtained from moment-curvature test results are shown in Figure 5.26. The results of all flexural elements show that bending stiffness decreases abruptly with increasing moment. Brittle failure occurred in the test of concrete flexural element. Steel fiber addition to concrete prevented the brittle failure of flexural element since fibers absorbed the stress and then bridged the cracks. The initial bending stiffness of *ws-sfrc* flexural element was found 9% higher than rc flexural element. Bending stiffness of ws-sfrc decreased more gradually compare to rc (Figure 5.26). Furthermore, stepwise response occurred in the *ws-sfrc* flexural element tests during subsequent loading.

Gradually decreasing after first crack and stepwise response in the excessive load levels occurred due to steel fiber bridging.

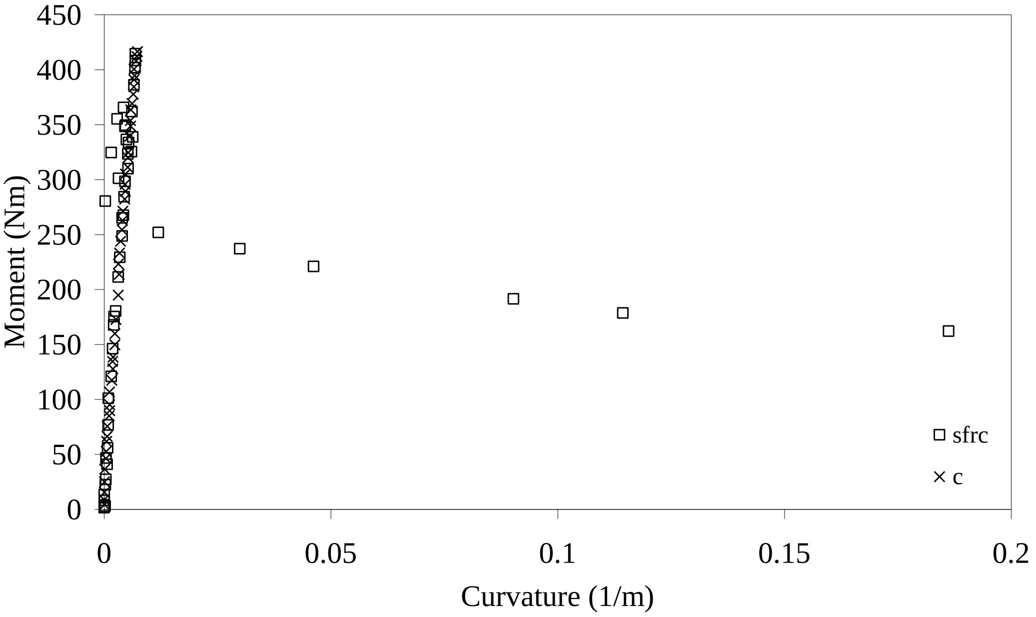

Figure 5.24 Moment-curvature relationship of *c* and *sfrc*

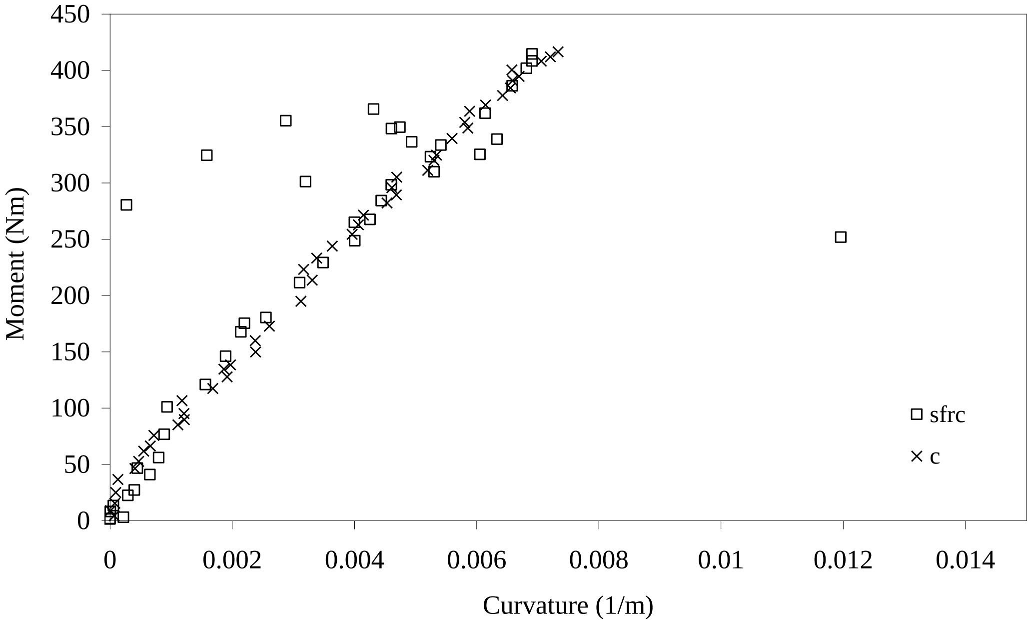

Figure 5.25 Moment-curvature relationship of *c* and *sfrc* up to first crack

Table 5.2 Cracking moment and curvature values of flexural elements

Flexural element	Cracking moment (M_{cr}) Nm	Cracking curvature (Φ_{cr}) 1/m	Yielding moment (M_y) Nm	Yielding curvature (Φ_y) 1/m	Failure moment (M_u) Nm	Failure curvature (Φ_u) 1/m
rc	317.497	0.00574	855.791	0.04088	1332.794	0.1411
ws-sfrc	383.630	0.00632	824.312	0.3956	1326.689	0.09876
ws-rc	360.174	0.00701	791.877	0.06172	1112.553	0.1750
sfrc	414.552	0.00691	-	-	414.552	0.00691
c	416.368	0.00733	-	-	416.368	0.00733

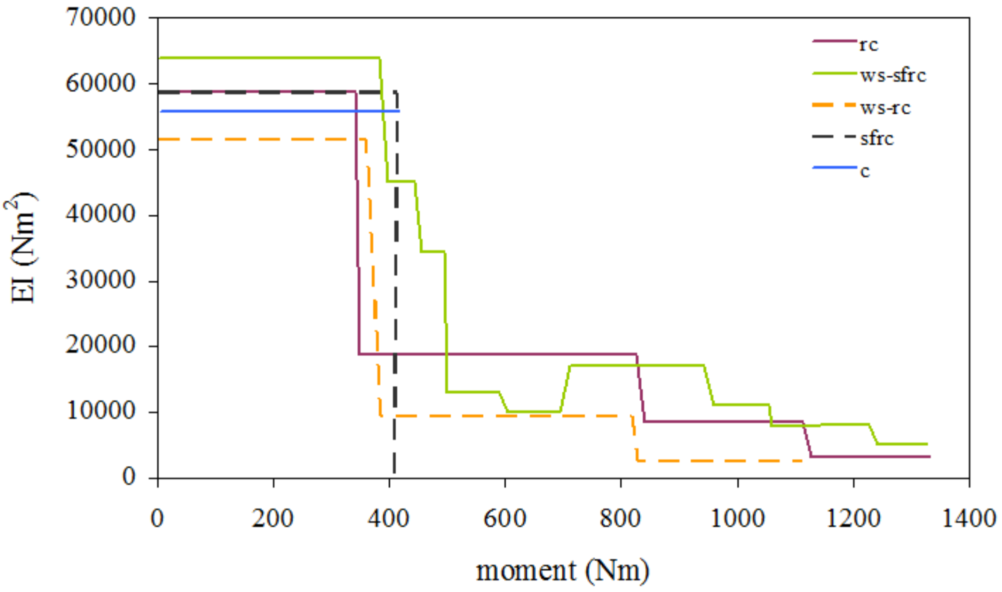

Figure 5.26 Moment-bending stiffness relation of flexural elements

Moment-curvature, moment-EI and, cracking pattern results indicate that steel fiber addition significantly enhance the behavior of flexural elements under flexural loading. The response of bending reinforced flexural elements, *ws-sfrc* and *ws-rc*, are evidently different. The performance of *ws-sfrc* is considerably better than *ws-rc* and quite similar to conventional reinforced concrete. This proves that steel fibers can be an effective replacement for shear reinforcement generally used in reinforced concrete flexural elements (*rc*). It can be concluded that fibers can be utilized structurally with appropriate fiber content to replace, such as stirrups in structural elements to resist bending loading.

5.3 Model Pile Tests

Five types of model piles were tested under lateral loading and lateral-axial loading. All tests were laterally loaded with deformation controlled mechanism and in axial loading case vertical load was applied constant. Tested model pile types are listed below.

with bending reinforcement:

- Conventional reinforced concrete model pile (*rc*)
- Concrete with bending reinforcement and steel fiber model pile (*ws-sfrc*)
- Concrete with only bending reinforcement model pile (*ws-rc*)

without bending reinforcement:

- Steel fiber reinforced concrete model pile (*sfrc*)
- Concrete model pile (*c*)

In this study, a total of twelve piles were tested. Lateral load tests were conducted under different rate of loading. Seven tests were performed under lateral loading and five tests were performed under lateral-axial loading. Pile head displacements and bending moment variations along the pile length were measured and recorded during the tests. Heave of the sand surface in front of the model pile and depression behind the pile were measured after the tests. Deformed shapes and cracks of model piles were measured along the depth after the tests. The effect loading rate on the soil-structure interaction was evaluated for the same loading types and the effects of axial load on soil-pile response were evaluated. Results are presented and compared in the following paragraphs.

5.3.1 Lateral Loading Tests

5.3.1.1 Rate of Loading: 4mm/min

Five types of model piles were tested under 4mm/min rate of loading. The results can be evaluated and compared in terms of pile head displacement, bending moment, crack pattern, deformed shape and condition of the sand surface around the pile after the tests. Pile head load-displacement curves for all model piles are presented in Figures 5.27. Pile head load-displacement curves of up to first crack detailed in Figure 5.28. Pile behaviors are compared in the initial stage and post crack stage. Initial stage and post crack stage can be defined as the loading stage up to the first crack and the loading stage after first crack, respectively. The first crack load–displacement level of the pile can be clearly seen in Figure 5.27. Load-displacement curves indicated that piles exhibited nonlinear behavior in the initial stage. After the initial stage the slope of the load-displacement curve varied suddenly. After the first crack, crack propagation took place on the bending reinforced piles. The irregular saw teeth in the post crack stage verify the crack propagation response. It should be noted that the line of *ws-sfrc* in this part continue smoothly due to the contribution of steel fibers.

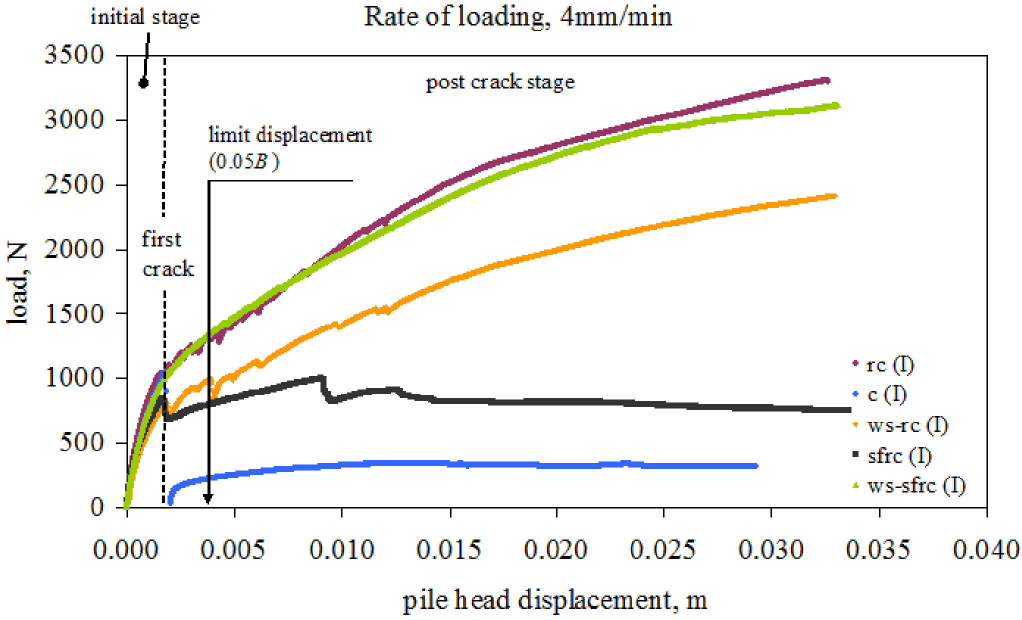

Figure 5.27 Pile head load-displacement relationship for all types of model piles

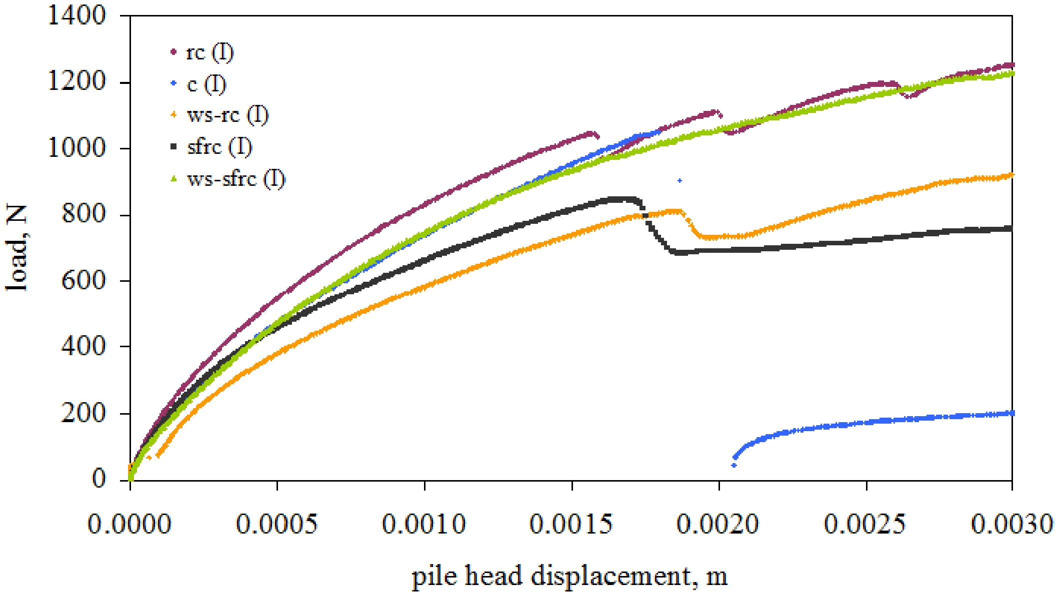

Figure 5.28 Pile head load-displacement relationship in the initial stage (rate of loading 4mm/min)

First crack load and displacements are listed in Table 5.3 with normalized values according to rc pile. It can be seen from the table that the head displacement readings were very close to each other when the first crack took place. This result proves the well repeatability of the tests and the test system stability. Comparison of bending reinforced model piles; *rc*, *ws-rc* and, *ws-sfrc* load-deformation relationships demonstrate that the performance of rc is better than *ws-rc* due to the presence of conventional shear reinforcement. The first crack load in model pile rc occurred 32% larger than that of the model pile *ws-rc*. However, without shear reinforcement, but with steel fiber %1 by volume content model pile, *ws-sfrc*, exhibited almost similar behavior with the conventional shear reinforced model pile, rc, under lateral loading. In addition, pile head displacement at first crack took place in *ws-sfrc* model pile 6% larger than that of model pile, *rc*. These results show that in the initial loading stage *ws-sfrc* model pile exhibited slightly more ductile behavior than *rc* model pile as can also be seen in Figure 5.28.

Table 5.3 First crack-pile head displacement for lateral loading (4 mm/min)

Model pile	First crack load, N	Normalized first crack	Pile head displacement, m	Normalized pile head displacement
rc	1034.81	1	0.00175	1
ws-sfrc	1027.28	0.99	0.00185	1.06
ws-rc	785.508	0.76	0.00189	1.08
sfrc	843.35	0.81	0.00172	0.98
c	1049.81	1.01	0.00180	1.03

The behavior of concrete (*c*) model pile and steel fiber reinforced concrete model pile (*sfrc*) were observed quite different. The number and location of hinges varied depending on the pile material. Concrete (*c*) model pile failed with single hinge, whereas sfrc model pile failed with double hinges. Double hinge occurrence can be seen in Figure 5.29. Although the first crack load capacity of the concrete model pile was found higher than the steel fiber reinforced concrete model pile (Table 5.3), the post crack behavior of *sfrc* model pile is better than *c* model pile. Concrete model pile cracked in a brittle manner and pile lost its load carrying capacity after first hinge happened. On the other hand, steel fiber reinforced concrete pile was able to carry additional load increments after excess deformations due to steel fiber bridging response. The upper portion of the *sfrc* model pile above the first hinge sustained imposed lateral loads up to ultimate load took place after the development of second hinge. Confinement effect of the surrounding soil is another cause of double hinge behavior. The load-displacement portion after single hinge for the concrete model pile represents only the soil resistance.

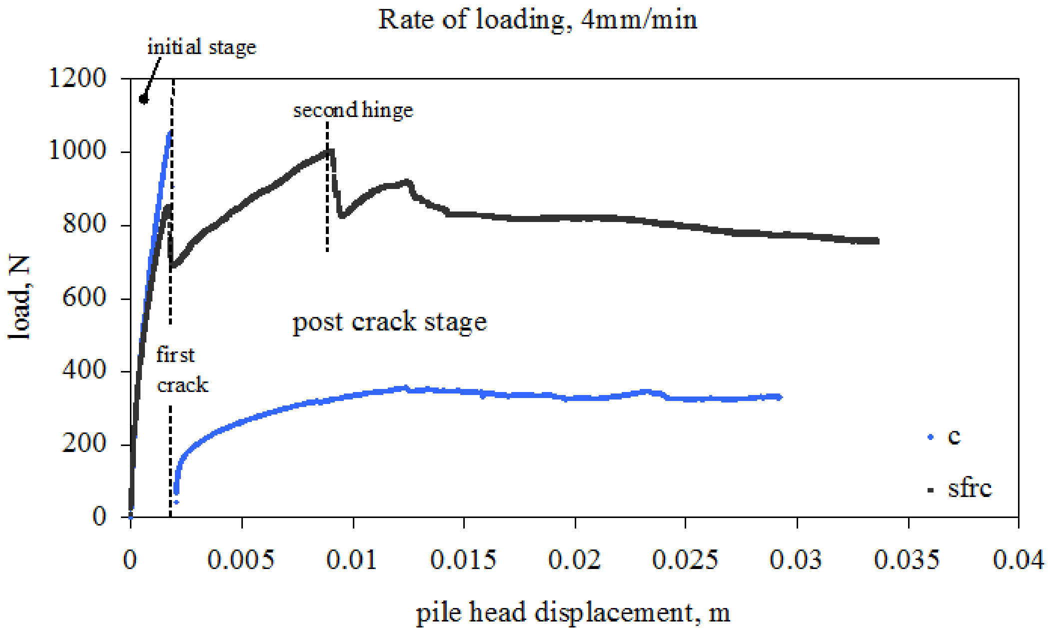

Figure 5.29 Pile head load-displacement relationship for without conventional reinforcement model piles

During the pile tests, strains were recorded from the tension side and compression side strain gauges along the pile. Moment-strain calibration curves which were presented in *Chapter 4, section 4.7* were used to obtain bending moments along the pile length. It was not possible to get data from strain gauges on the tension side after first crack took place. However, the strain values must be the same (±) for both sides up to the first crack. After verifying this issue with the recorded data, compression side strain-moment calibration relationships were used to obtain bending moments after first crack.

Moment distributions of model piles are presented in Figure 5.30. In moment distribution figures, “H” symbolize the normalized lateral load according to maximum reaction, H=1 equal to 3040 N, where the reaction recorded from the lateral tests (4mm/min & 0.85mm/min). In the initial stage (H=0.26), before first crack, bending moments of *rc* and *ws-sfrc* are similar and lower than the *ws-rc* and concrete piles. In the initial stage bending moments of *ws-rc* and concrete are also similar. Bending moments of *sfrc* occurred higher than the all other model piles. The maximum moments developed nearly at the same depth, ~ 60cm. In the post crack stage (H=0.65) maximum bending moment depth of reinforced concrete shifted upper part of the pile and focused on a single cross section. Besides, in the post crack stage the maximum moments in test *ws-rc* are also focused in a certain depth or cross section. On the other hand, in the post crack stage the bending moment distribution of the pile *ws-sfrc* is clearly different. Large bending moments distributed on a wide portion of the pile due to the contribution of steel fiber. In the post crack stage, bending moments of *ws-sfrc* model pile occurred higher than the *rc* model pile at some depths at the lateral load level H=0.65 and maximum lateral load level (H=1).

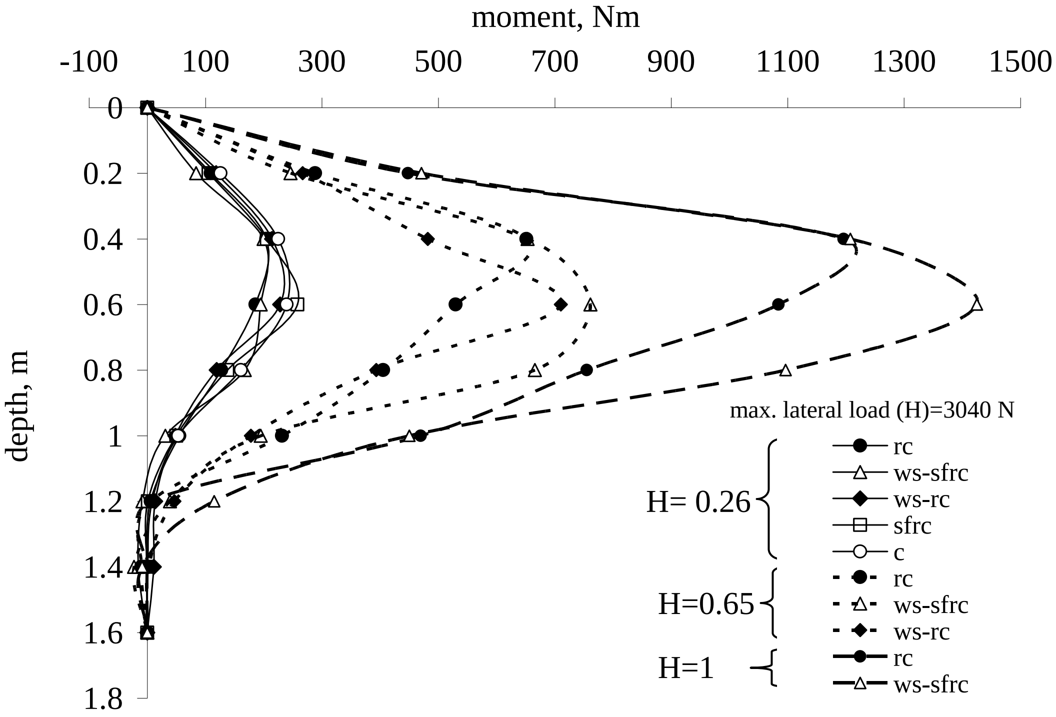

Figure 5.30 Comparison of bending moments of model piles under 4mm/min lateral loading rate

Cracking moments (M_{cr}) were obtained by taking into consideration the moment readings and obtained values were compared and checked with moment-curvature results (Figure 5.31). Cracking moment values of model piles with normalized values are presented in Table 5.4. The cracking moments of the *ws-sfrc* model pile is found to be 10% larger than that of the model pile rc.

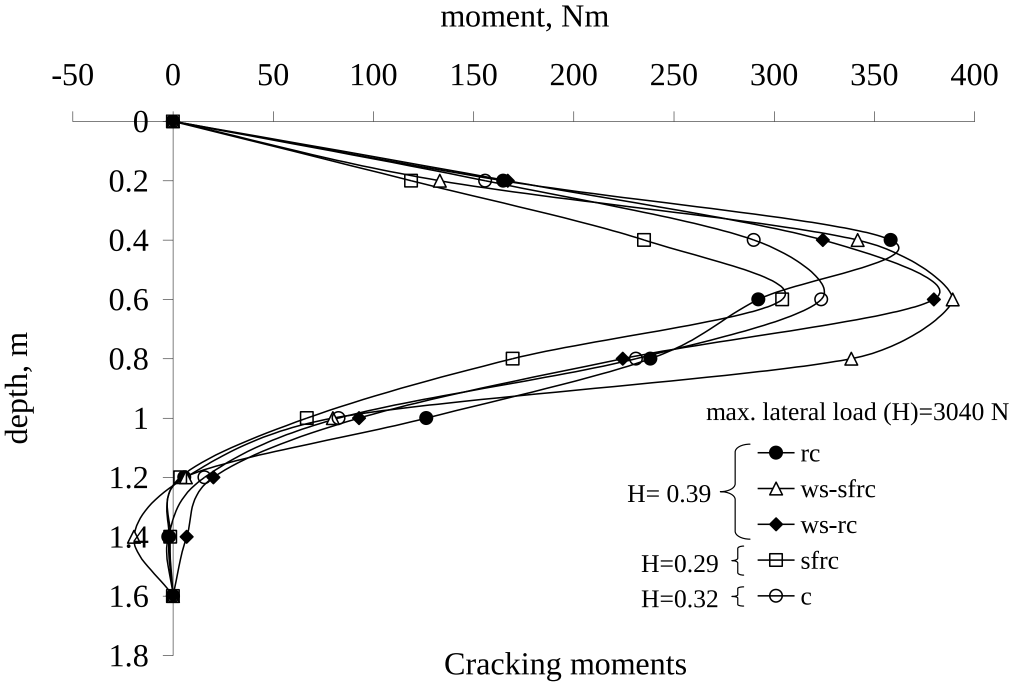

Figure 5.31 Cracking moments (M_{cr}) of model piles under 4mm/min lateral loading rate

Table 5.4 Cracking moments of the model piles under lateral loading (4mm/min)

Model pile	Cracking moment M_{cr} ,Nm	Normalized cracking moment
rc	354.14	1
ws-sfrc	389.02	1.10
ws-rc	379.66	1.07
sfrc	304.06	0.86
c	323.54	0.91

Variations of recorded bending moments without conventional reinforcement are presented in Figure 5.32 in order to understand hinge occurrence in detail and steel fiber contribution. Bending moment distribution of *c* and *sfrc* are close to each other. Maximum bending moments were recorded at the same depth for the *c* and *sfrc* concrete model piles. In addition, they occurred larger in *sfrc* model pile than concrete model pile. Moment cracking capacity of *sfrc* model pile was recorded %6 less than the concrete model pile. On the other hand, concrete model pile failed in single hinge and after first crack no more bending moments were recorded due to the cracked upper portion of the model pile separated from the lower part. However, double hinge developed in the test of *sfrc* model pile. After the first hinge, the pile continued to carry bending moment. At the cracking moment, fiber bridging became active and the pile has maintained the integrity. It is thought that steel fibers at the location of the first hinge were able to hold the pile entire due to the reestablished interlock with the concrete matrix. The soil zone around the pile is thought to have some contributions to the response of the pile. The upper portion of the pile above the first hinge starts to act as a shorter pile. Bending moments increased around the first hinge location and as a result of this, moment development second hinge took place over the first hinge. After the second hinge occurrence the pile failed under ultimate moment. It is noteworthy that *sfrc* pile can stand for higher moments. The moment in the second hinge was recorded 25 % and ultimate moment was recorded 55 % higher than the failure moment of the concrete pile.

The tested piles were also pictured together to show the differences and similarities between crack distribution along the pile (Figure 5.33). Crack depths for the piles are given in Table 5.5. Cracked patterns of the tested piles are illustrated with crack depths and deformation along the depth in Figure 5.34.

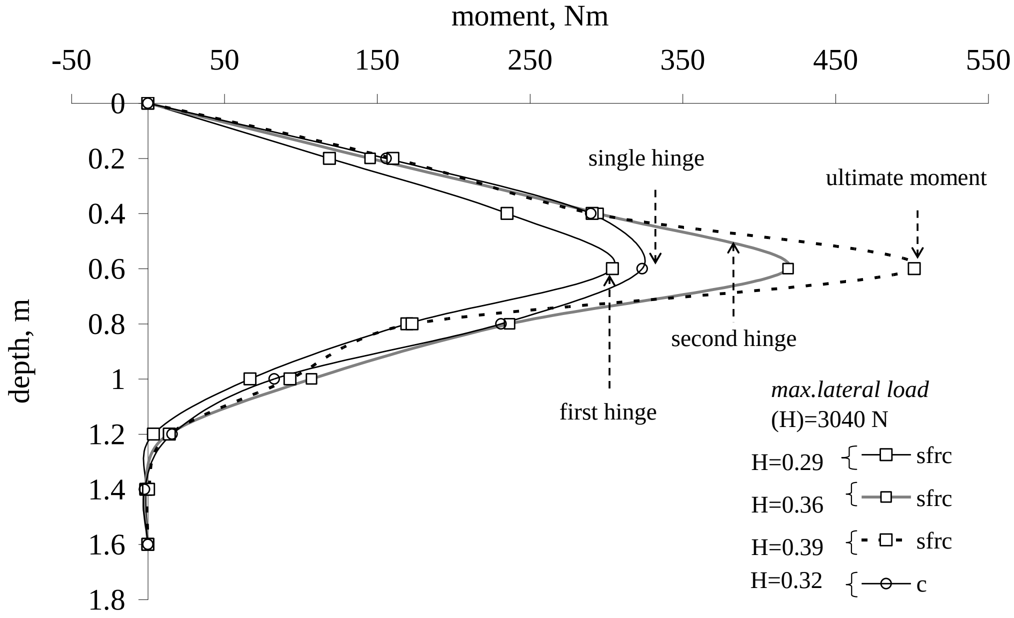

Figure 5.32 Critical bending moments of steel fiber reinforced concrete and concrete model piles

Figure 5.33 Damaged model piles after the tests, 4mm/min

Table 5.5 Crack depths of the piles under lateral loading, 4 mm/min

Model pile	Depth, cm										
rc	31	40	47.5	53	58	64					
ws-sfrc	30	43	54	62	72.2						
ws-rc	29	32.9	39.5	45	48.5	57.5	64.3	69	79.7	92.7	112.2
sfrc	50	66.5									
c	48.05										

The crack pattern of the *ws-rc* demonstrates the contribution of the longitudinal reinforcement when compared with concrete model piles crack pattern. Single crack occurred in the test of the concrete model pile and pile failed brittle. The crack pattern of *sfrc* and concrete model pile are dissimilar. Notice that the first crack took place at depth 66.5 cm in the *sfrc* model pile test and 48.5 cm in concrete model pile test. Steel fiber addition to the concrete matrix prevents the failure in the first crack depth and due to further loading second crack occurred at 50 cm depth. Concrete with only bending reinforcement model pile exhibited also more flexible response than that of the concrete model pile. Bending reinforcement has prevented the model pile from single hinge failure. On the other hand, in the test of *ws-rc* model pile, quite a number of cracks occurred along the pile. If carefully looked at the picture of the damaged piles (Figure 5.33), it can be seen that the lengths of the crack are shorter. There were only two cracks occurred along the pile at 57.5 and 64.3 cm depths. Remaining cracks along the pile are short cracks. Cracks extended below one meter corresponding to 2/3 of the pile length due to deficiency of shear reinforcement.

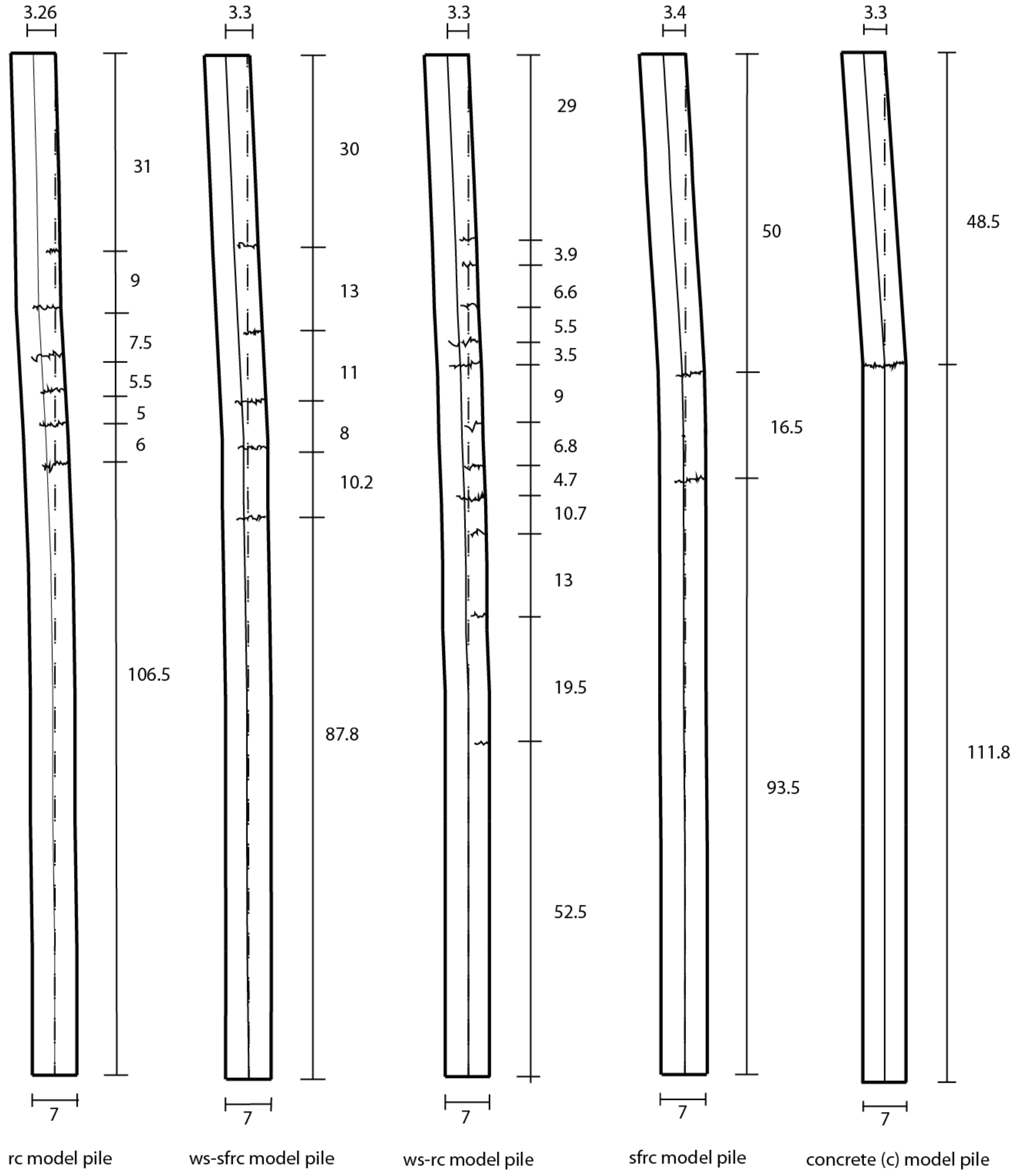

Figure 5.34 Crack patterns of model piles under lateral loading with 4mm/min rate of loading

Although *ws-sfrc* had only longitudinal reinforcement, crack propagation in the test of *ws-sfrc* is quite better than the crack propagation of *ws-rc*. In the test of *ws-sfrc* model pile, cracks took place on the upper part of the pile less than half of it as illustrated in Figure 5.34 and shown in Table 5.5. This revealed the contribution of the steel fiber addition without shear reinforcement. Moreover, crack propagation of the conventional reinforced concrete model pile (*rc*) is similar to the model pile (*ws-sfrc*) concrete with bending reinforcement and with steel fiber. Crack characterization of these piles is also similar considering the length of the cracks along the cross section, which can be observed in Figure 5.33. The main cracks occurred between 50 and 65 cm depths from the pile head in all of the model pile tests.

Sand was removed from the container after pile tests and the deformed shape of the pile was measured before disassembling and taking out the damaged pile from the container (Figure 5.35). Deformation-depth relations of laterally loaded piles under 4mm/min rate of loading are presented in Figure 5.36. Deformations along the depth of concrete model pile were not measured after the test due to single hinge occurrence. In the initial loads pile cracked suddenly and upper part of the pile above the hinge separated from the lower part of the pile.

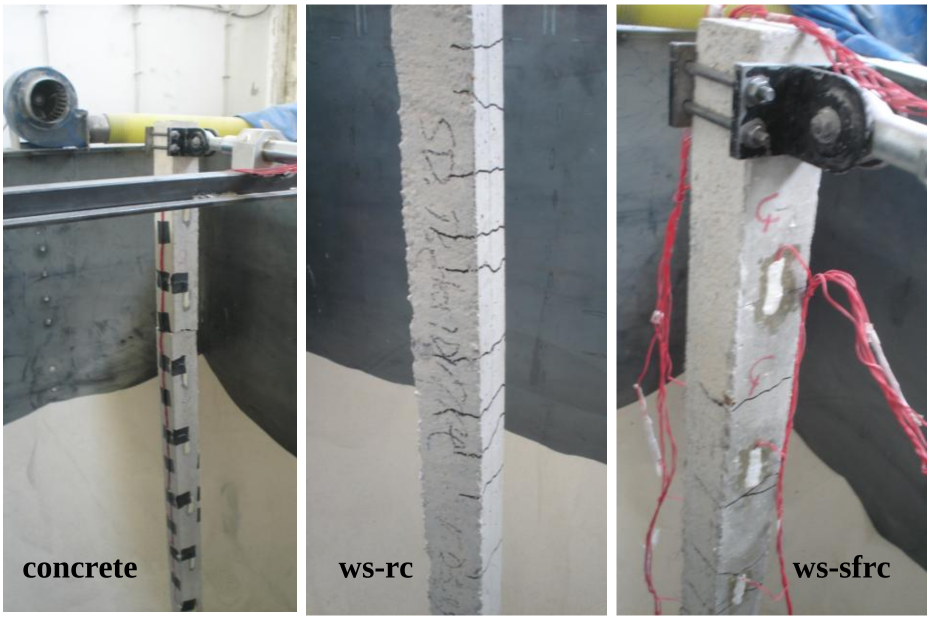

Figure 5.35 Damaged model piles after the test

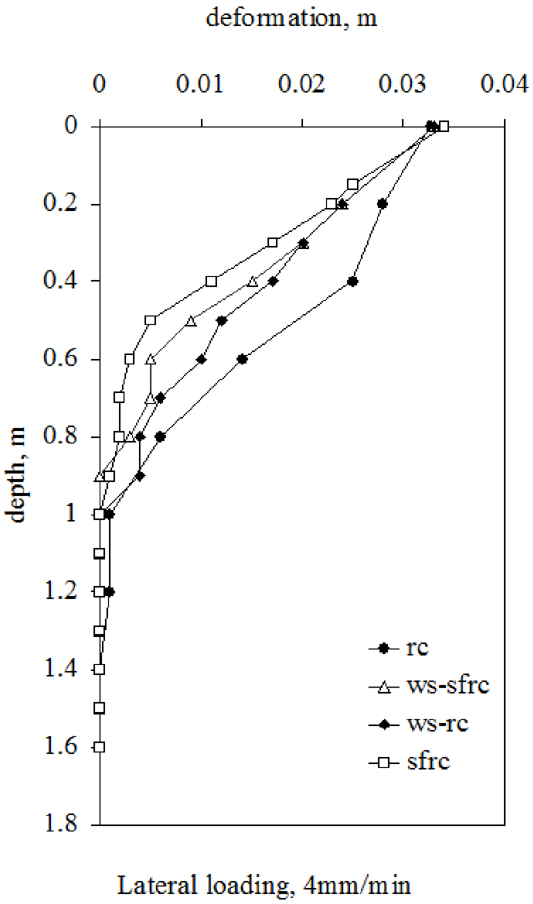

Figure 5.36 Variation of pile deformations with depth under lateral loading, 4mm/min

After the tests, condition of the sand surface was observed and required measurements were made. The movement of sand surface is shown and illustrated in Figure 5.37 and Figure 5.38. The contour in front of the pile is due to heaving and the contours behind the model pile represent the depressing. General dimension of heave and depression is given in Table 5.6.

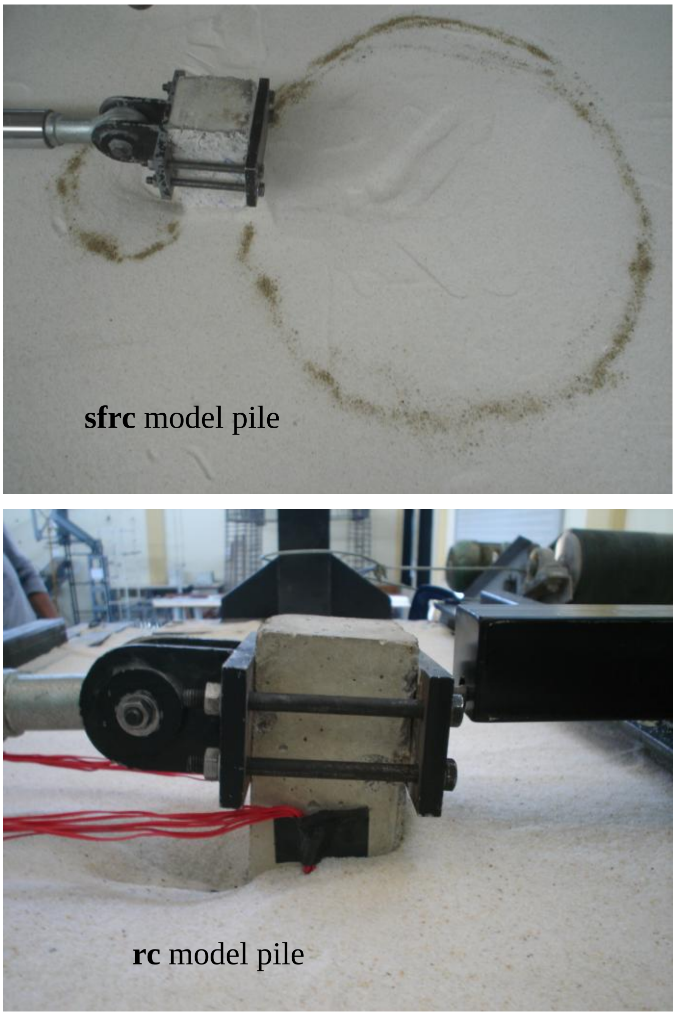

Figure 5.37 Sand surface conditions after the lateral load tests (4mm/min)

Table 5.6 General plan dimensions of moved soil at the sand surface (Lateral loading , 4mm/min)

Model pile	AB cm	CD cm	A’B’ cm	C’D’ cm
rc	42	42	15.5	12.5
ws-sfrc	46	38.5	19	13
ws-rc	50	43	17.5	13.5
sfrc	54	43	18	13.5
c	44	35	10	8.5

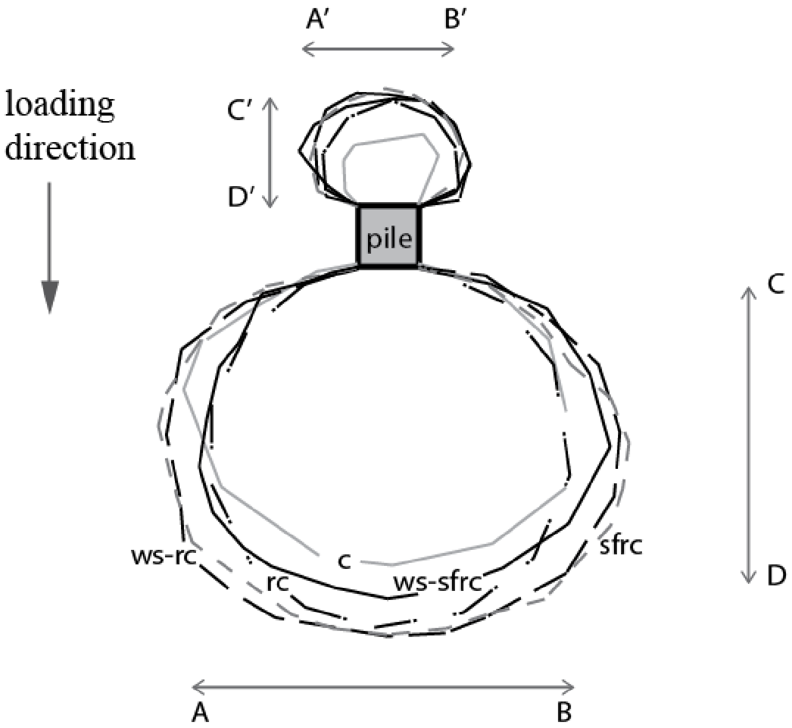

Figure 5.38 Sketches of heave and depression of sand surface due to lateral loading (4mm/min)

5.3.1.2 Rate of Loading: 0.85 mm/min

Concrete with bending reinforcement and steel fiber (*ws-sfrc*) and conventional reinforced concrete model pile (*rc*) were tested laterally under 0.85 mm/min rate of loading. Recorded load-pile head displacement relation is given in Figure 5.39 and Figure 5.40. The load-displacement curves achieved quite similar in the initial stage and post crack stage for the tested model piles, *ws-sfrc* and *rc*. In addition, first crack lateral load of *ws-sfrc* pile was determined to be 11% larger than that of model pile *rc* which is given in Table 5.7.

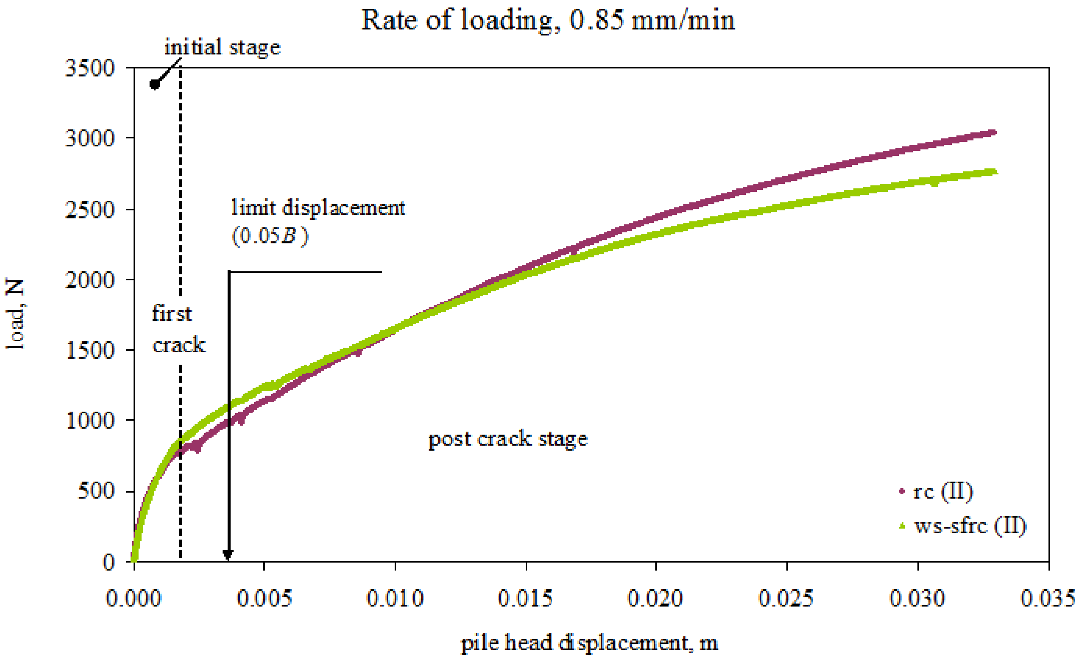

Figure 5.39 Pile head load-displacement relationship for *ws-sfrc* and *rc* model piles 085 mm/min

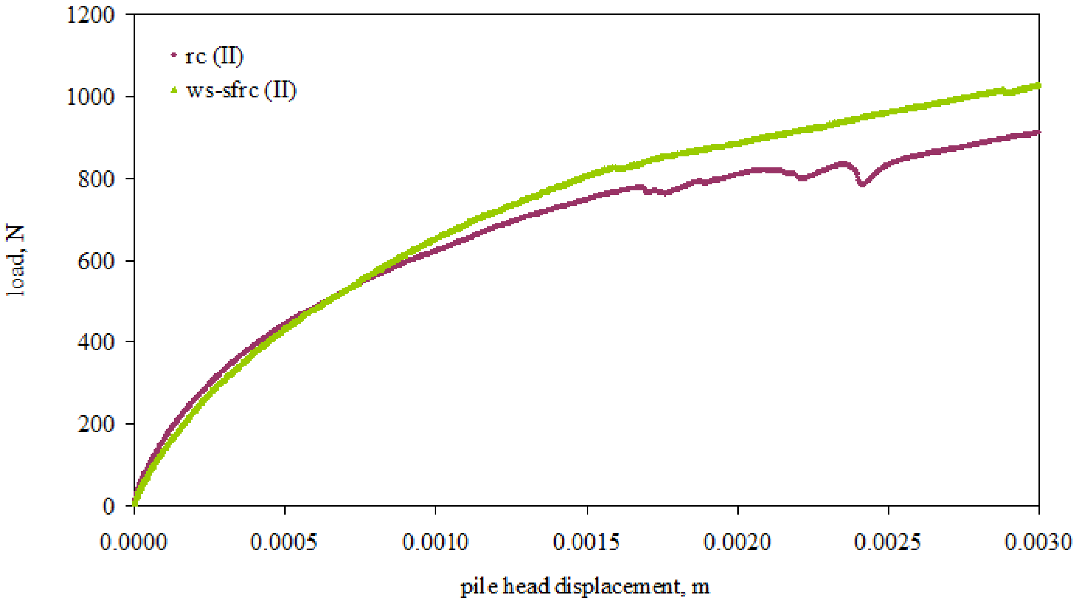

Figure 5.40 Pile head load-displacement relationship in the initial stage, rate of loading 0.85 mm/min

Table 5.7 First crack-pile head displacement for lateral loading (0.85mm/min)

Model pile	First crack load, N	Normalized first crack	Pile head displacement, m	Normalized pile head displacement
rc	788.87	1.00	0.00185	1.00
ws-sfrc	872.26	1.11	0.00188	1.02

Distributions of recorded bending moments along the pile depth are given in the Figures 5.41. It can be seen in Figure 5.41 that bending moments of *ws-sfrc* in the initial stage (H=0.19) are slightly lower than the model pile *rc*. In the post cracking stage (H=0.42) bending moment distribution occurred quite different. In the *rc* pile test, in the post crack stage (H=0.42), just after the first crack load level, maximum bending moment depth shifted above. At this stage maximum moment took place at the first strain gauge depth, 20 cm. Bending moment locations were focused at a certain depth in the test *rc* pile. A crack was observed at 29 cm depth on the rc pile after the test as can be seen in Figure 5.44. In contrast, maximum bending moments propagated on a large portion on the tested pile *ws-sfrc* at the same lateral load level (H=0.42). Subsequent loadings (H=0.77), maximum bending moment depth took place again at the lower depth of the tested *rc* pile as can be seen in Figure 5.41. At the maximum load (H=0.90) bending moments of *ws-sfrc* were recorded higher than that of the pile *rc*.

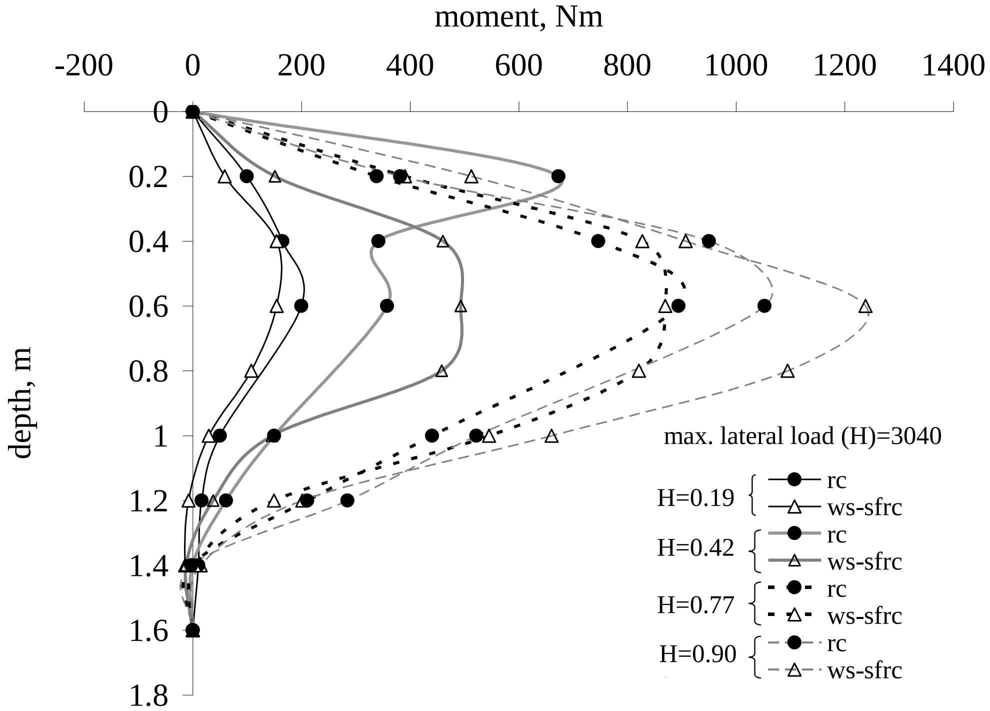

Figure 5.41 Comparison of bending moments *ws-sfrc* and *rc*

Cracking moment (M_{cr}) capacity of *ws-sfrc* pile was determined 17 % higher than the model pile *rc* (Table 5.8 & Figure 5.42).

Table 5.8 Cracking moments of the model piles under lateral loading (0.85 mm/min)

Model pile	Cracking moment M_{cr} ,Nm	Normalized cracking moment
rc	330.97	1.00
ws-sfrc	386.72	1.17

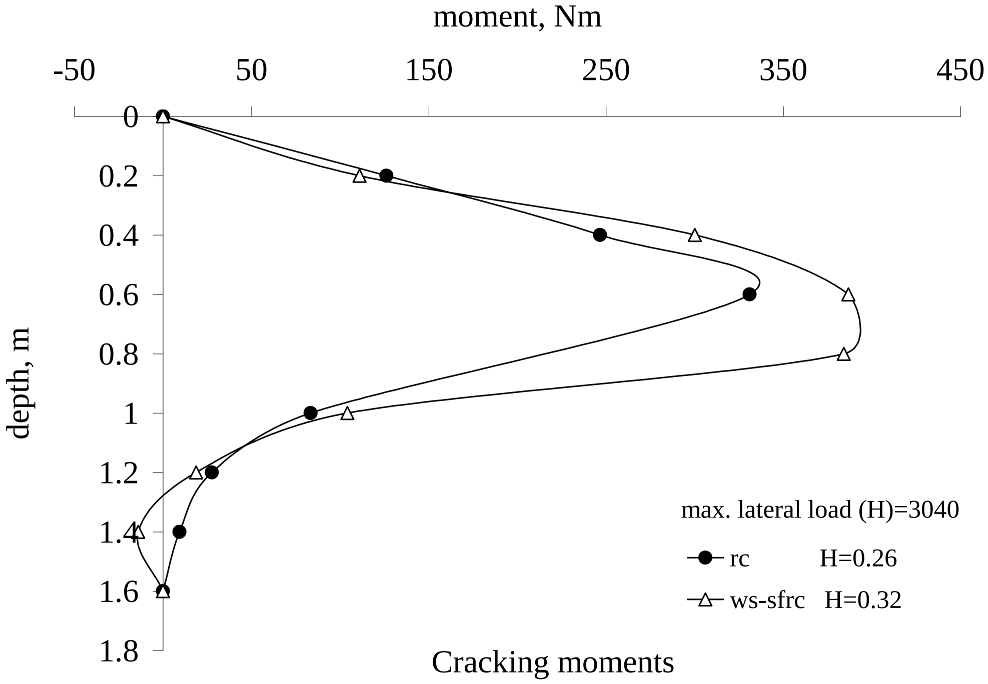

Figure 5.42 Cracking moments (M_{cr}) of model piles under 0.85mm/min lateral loading rate

The crack propagation of the tested piles are illustrated in Figure 5.43 and showed in Figure 5.44 with deformed shape. Crack depths of the piles are given in Table 5.9. Cracks occurred up to 75 % length of the rc pile whereas in the *ws-sfrc* model pile test cracks took place up to half the pile. In addition, the number of the cracks of *rc* pile was more than the *ws-sfrc* pile, although *ws-sfrc* was reinforced without stirrups. Deformed shape of rc pile is compatible with the crack pattern. Deformed shapes of the piles are quite similar up to 1 m depth (Figure 5.43). Small deformations were measured at the lower parts of the *rc* pile. This result reveals the contribution of the steel fiber on the behavior of the pile. The surrounding soil at the lower depths did not prevent cracks in the test of *rc* pile, although the shear reinforcement confinement effect contribution in that pile. On the other hand, at the same lower depths and at the same lateral load levels bending moments occurred less than the *rc* pile due to contribution of steel fibers. Steel fibers and subgrade soil were active together and prevented the crack occurrence on pile *ws-sfrc*.

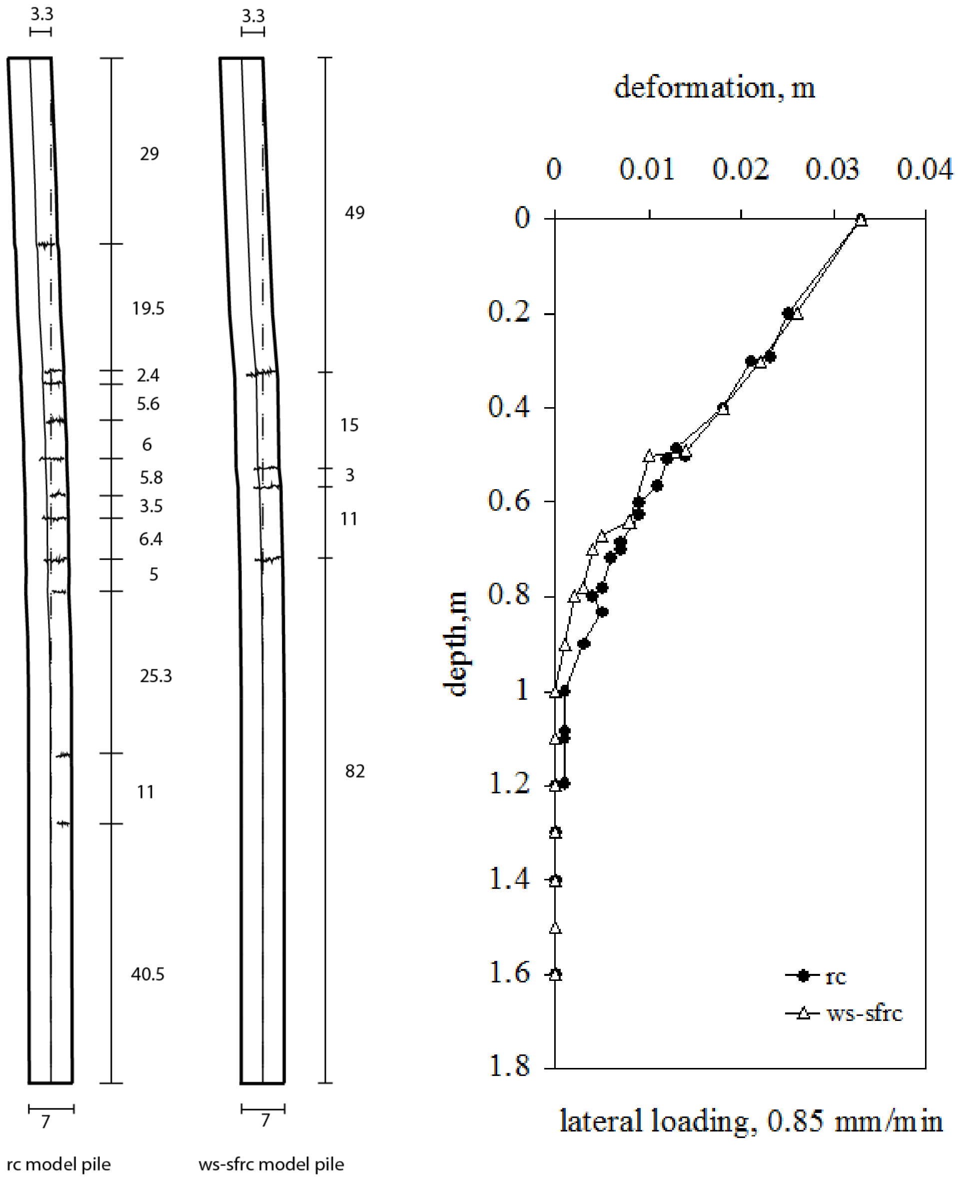

Figure 5.43 Crack patterns and variation of pile deformations with depth of model piles under lateral loading with 0.85mm/min rate of loading

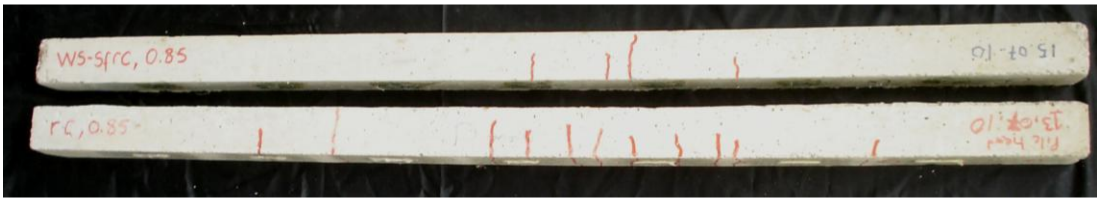

Figure 5.44 Damaged model piles after the test, 0.85 mm/min

Table 5.9 Crack depths of the piles under lateral loading (0.85 mm/min)

Model pile	Depth, cm										
rc	29	48.5	50.9	56.5	62.5	68.3	71.8	78.2	83.2	108.5	119.5
ws-sfrc	49	64	67	78							

The soil surface condition was measured and illustrated in Figure 5.45. General plan dimensions were given in Table 5.10.

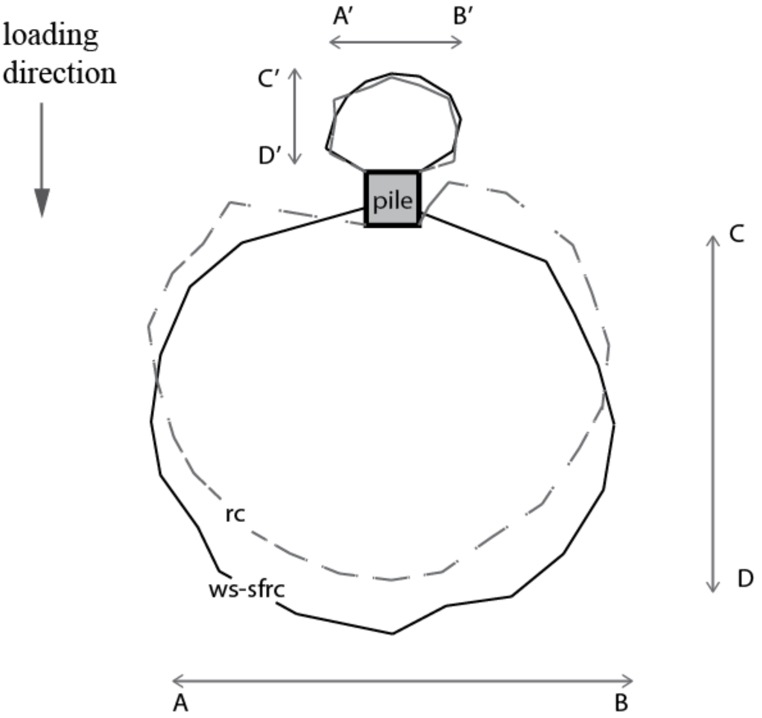

Figure 5.45 Sketches of heave and depression of sand surface due to lateral loading (0.85 mm/min)

Table 5.10 General plan dimensions of moved soil at the sand surface (Lateral loading, 0.85 mm/min)

Model pile	AB cm	CD cm	A’B’ cm	C’D’ cm
rc	60	48	16	13
ws-sfrc	60	54	17	13

5.3.2 Lateral-Axial Loading Tests

Five types of model piles were tested under lateral-axial loading condition and under 0.85 mm/min rate of loading. Constant axial load was applied as 5400 N on average at the pile head. Pile head load-displacement curves for all model piles are presented in Figures 5.46 and Figure 5.47. The first crack load and displacement values can be seen clearly from the load-displacement relationship. In the initial stage load-pile head displacements exhibited nonlinear behavior and after the initial stage the slope of the load-displacement curve varied abruptly. After the first crack, crack propagation took place on the bending reinforced piles. The broken lines in the post crack stage verify the crack propagation response. Load-displacement performance of the pile (*ws-sfrc*) is better than the pile conventional shear reinforced pile, *rc*. First crack load and displacement values are listed with normalized values according to *rc* pile in Table 5.11. The fist crack load capacity of *ws-sfrc* was obtained 26% higher than the *rc* pile. Although first crack load capacity of rc, *ws-rc*, c and sfrc pile founded similar, deformation capacity of *ws-rc*, c and *sfrc* were obtained nearly 20% less than the rc and *ws-sfrc* pile.

Table 5.11 First crack-pile head displacement for lateral-axial loading (0.85mm/min)

Model pile	First crack load, N	Normalized first crack	Pile head displacement, m	Normalized pile head displacement
rc	1158.76	1.00	0.00351	1.00
ws-sfrc	1465.77	1.26	0.00340	0.97
ws-rc	1159.76	1.00	0.00258	0.74
sfrc	1195.75	1.03	0.00302	0.86
c	1202.47	1.04	0.00288	0.82

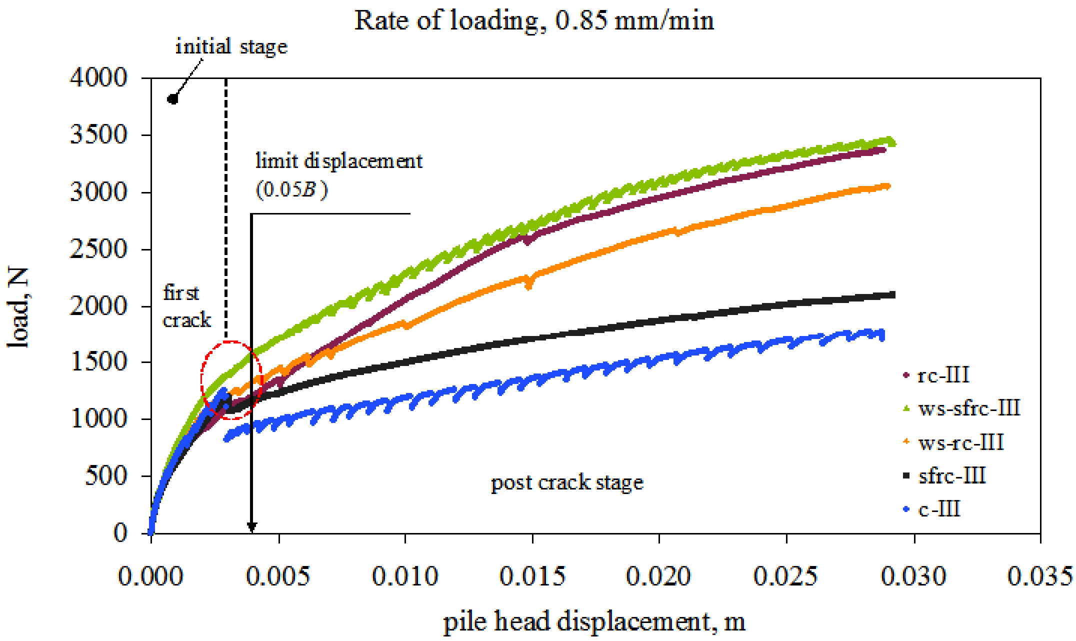

Figure 5.46 Pile head load-displacement relationship for all types of model piles, 0.85 mm/min

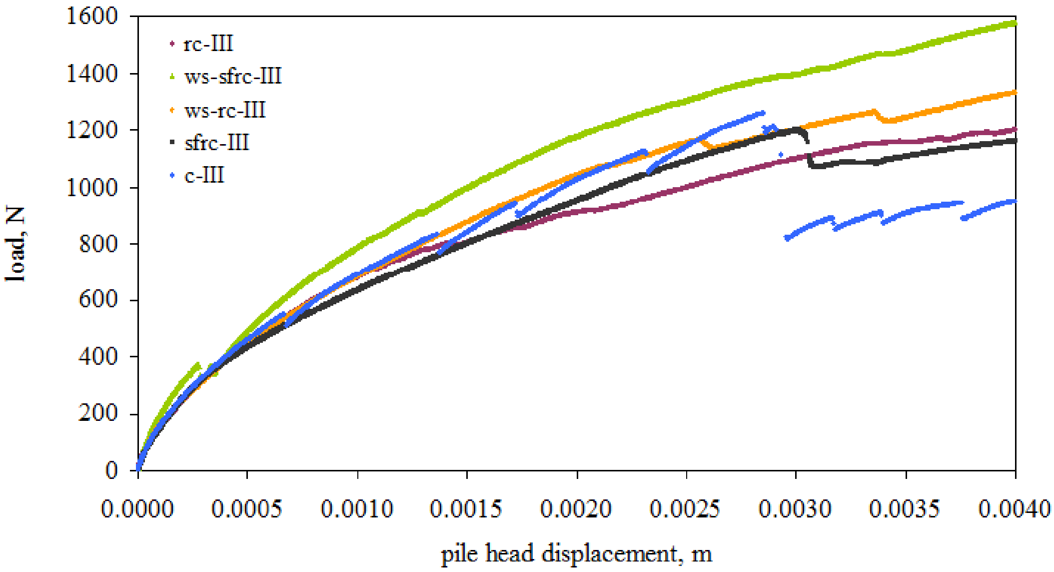

Figure 5.47 Pile head load-displacement relationship in the initial stage, rate of loading 4 mm/min

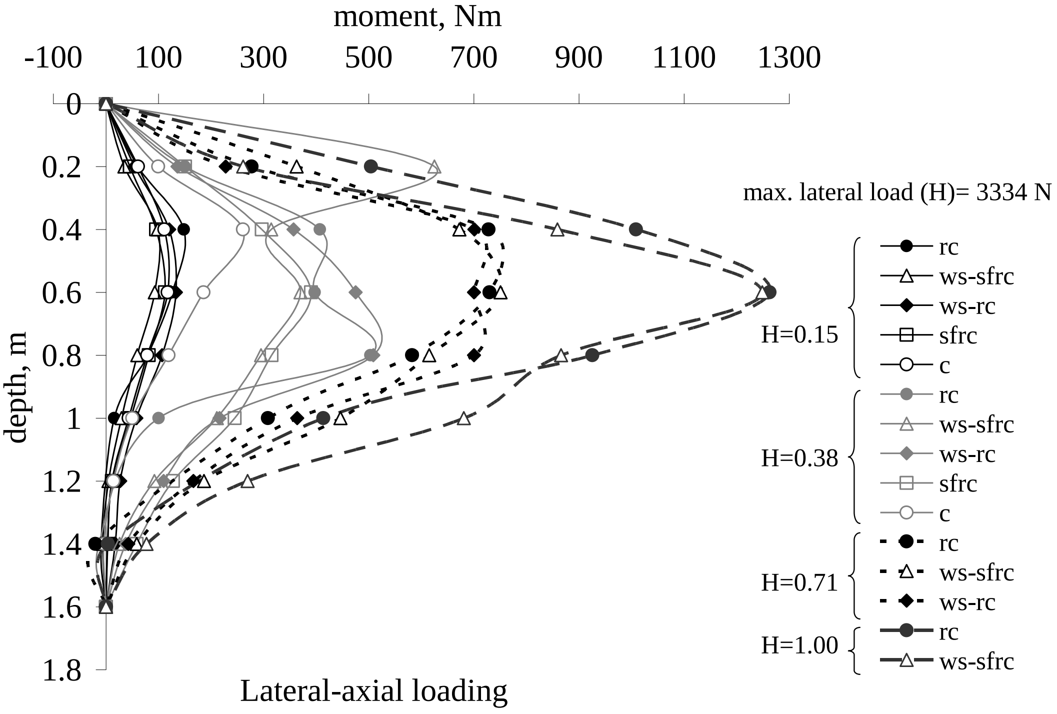

Figure 5.48 Comparison of bending moments of model piles under lateral-axial loading 0.85 mm/min

Variations of the recorded bending moments along the pile length are given in the initial stage and in the post crack stage in Figure 5.48. In the figures “H” symbolize the normalized lateral load according to maximum reaction obtained from the lateral-axial load tests (H=1.00 equal to 3334 N). In the initial stage (H=0.15) bending moment distribution characteristics were obtained similar. Their maximum bending moment generation depths were nearly equal. In this stage bending moments in *ws-sfrc* were recorded less than the other model piles. The highest bending moments took place in the *rc* pile at H=0.15. After cracking (H=0.38), moments decreased rapidly in the concrete model pile due to single hinge occurrence. Therefore at H=0.38 bending moment distribution of *c* pile was obtained less than the other piles. An interesting finding in this load level is about the behavior of *ws-sfrc*. At H=0.38 load level maximum bending moment depth of *ws-sfrc* shifted above. Although the maximum bending moment at that level was higher than the cracking moment value of *ws-sfrc* model pile, there wasn’t some macro crack observed on the pile after the test around that depth. Besides, moment distribution of *ws-sfrc* model pile was generally recorded less than rc model pile at H=0.38. The fact that recorded bending moments were less in test *ws-sfrc* pile is an indication to more flexible response when compared with the *rc* model pile in the initial stage. At the load level stage H=0.71 it can be noticed in Figure 5.48 that bending moment response is similar and bending moments are not focused at a certain depth due to axial loading. However, at the maximum load, H=1.00, it can be seen that maximum bending moments of the *ws-sfrc* and *rc* are quite similar and focused at a certain depth, ~ 0.60 m but the moments for the other depths were dissimilar. The cracking moment distribution of the piles under lateral-axial loading is given in Figure 5.49. Cracking moment capacities of model piles are obtained quite similar.

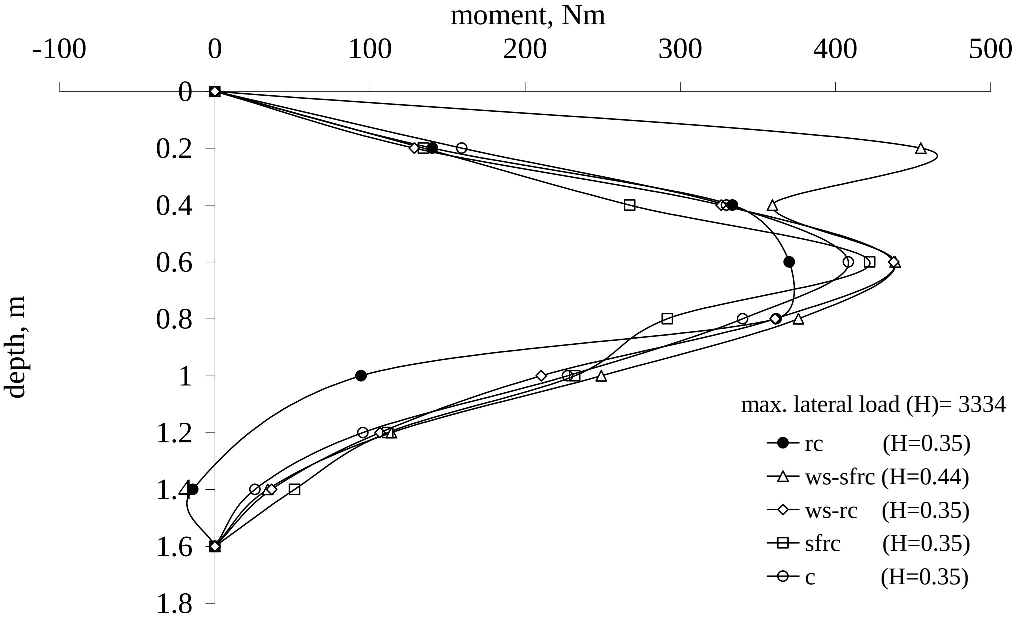

Figure 5.49 Cracking moments (M_{cr}) of model piles under lateral-axial loading

Table 5.12 Cracking moments of the model piles under lateral-axial loading (0.85 mm/min)

Model pile	Cracking moment M_{cr} ,Nm	Normalized cracking moment
rc	425.03	1.00
ws-sfrc	438.52	1.03
ws-rc	437.66	1.03
sfrc	422.15	0.99
c	408.45	0.96

Damaged piles under lateral-axial loading were pictured together to show the differences and similarities between pile responses (Figure 5.50). Crack depths are presented in Table 5.13. Crack pattern shows that the concrete and *sfrc* model piles cracked with single hinge. Hinges located approximately at the same depth for *c* and *sfrc* piles. However, in the test of c pile, upper part of the pile separated immediately from the lower part and recorded moments were abruptly decreased after hinge took place on the pile. In contrast *sfrc* model pile continued to carry bending moments after hinge took place due to presence of steel fibers. Although cracking moment capacity of the *sfrc* pile was obtained slightly (3%) larger than the concrete pile, moment carrying capacity of *sfrc* was attained 40% higher than the *c* pile. Under lateral-axial loading, crack distributions show that the behavior of *ws-sfrc* (concrete with bending reinforcement and steel fiber) is better than the pile reinforced conventional, *rc*. There were only two cracks that took place in the test of *ws-sfrc* whereas six crack occurred in the test of *rc* pile.

Figure 5.50 Damaged model piles after the test of lateral-axial loading

Table 5.13 Crack depths of the piles under lateral-axial loading, 0.85 mm/min

Model pile	Depth, cm					
rc	48	51.2	57	62.5	68.5	75.4
ws-sfrc	59	67.5				
ws-rc	30	58	66	75	80	91
sfrc	63.8					
c	65.5					

Crack patterns are illustrated in Figure 5.51 and deformed shape after the test is presented in Figure 5.52 and Figure 5.53. Deformed shape demonstrates that brittle failure occurred in the test of concrete pile. In that test, after single hinge occurrence whole pile body imposed to move laterally due to axial load and rotated from the base support as illustrated in Figure 5.51. On the other hand, *sfrc* pile shows more flexible behavior as can be seen in the deformed shape (Figure 5.53). Small deformations took place at the same depths even though its moment capacity is larger than the concrete model pile. Notice that deformations along the depth in *ws-sfrc* pile occurred higher than the *rc* pile along the pile depth. This result reveals that *ws-sfrc* model pile responds more flexible than the model pile *rc* under lateral loading while the pile is axially loaded. It can be concluded that deformation capacity of the *ws-sfrc* pile is better than the *rc* pile under lateral-axial loading.

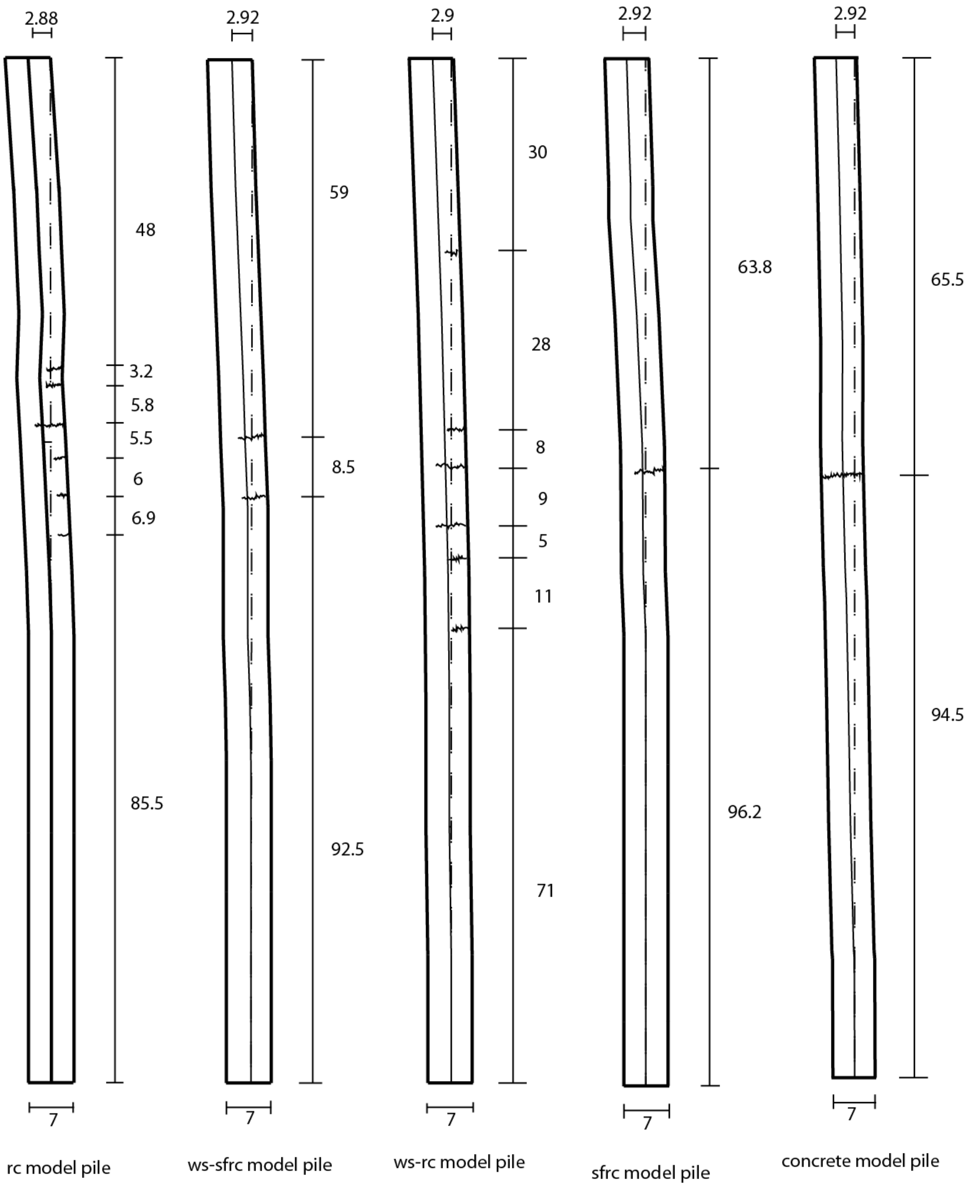

Figure 5.51 Crack patterns of model piles under lateral-axial loading with 0.85 mm/min rate of loading

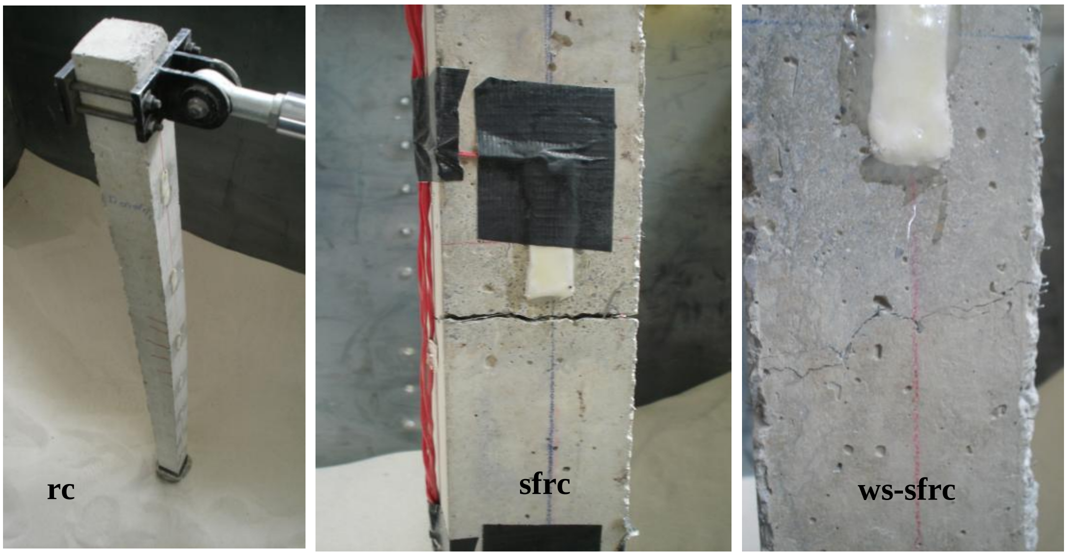

Figure 5.52 Damaged model piles after the test

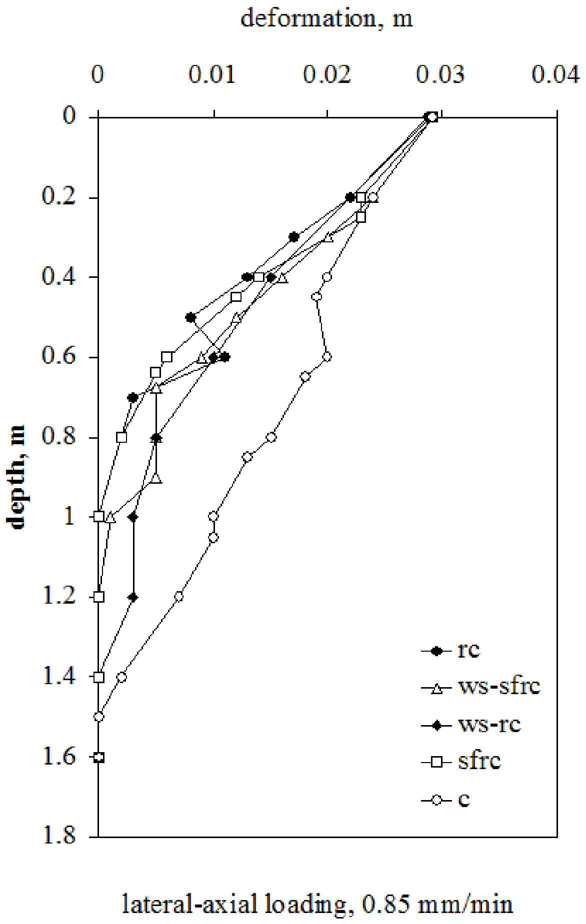

Figure 5.53 Variation of pile deformations with depth under lateral-axial loading

The soil condition of the sand surface was measured (Figure 5.54) and illustrated in Figure 5.55 and measured dimensions are given in Table 5.14.

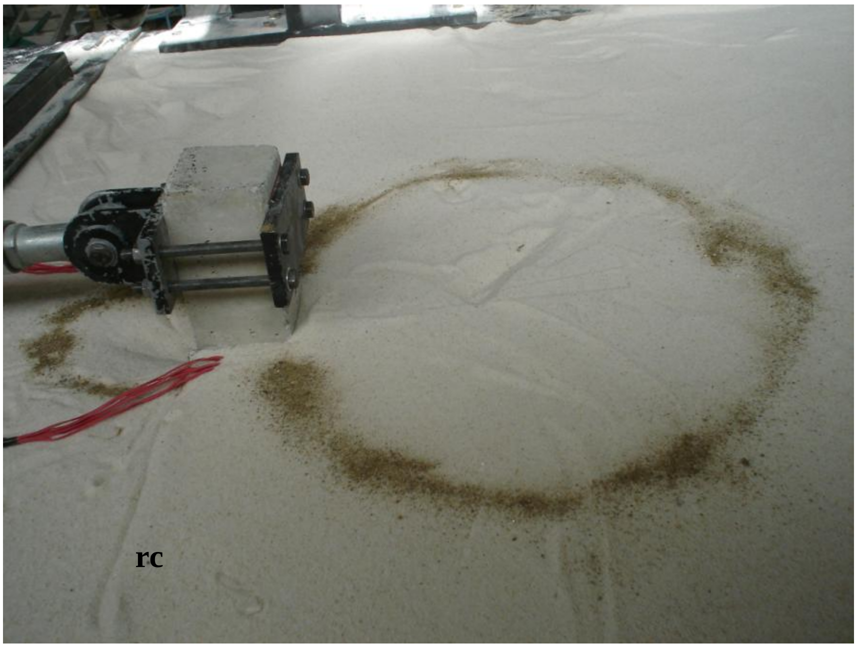

Figure 5.54 Sand surface after the lateral-axial load tests (0.85mm/min)

Table 5.14 General plan dimensions of moved soil at the sand surface-lateral-axial loading (0.85 mm/min)

Model pile	AB cm	CD cm	A'B' cm	C'D' cm
rc	43	39	13	10
ws-sfrc	64	54	19	11
ws-rc	46	40	19	10
sfrc	45	40	17	12
c	65	65	13	12

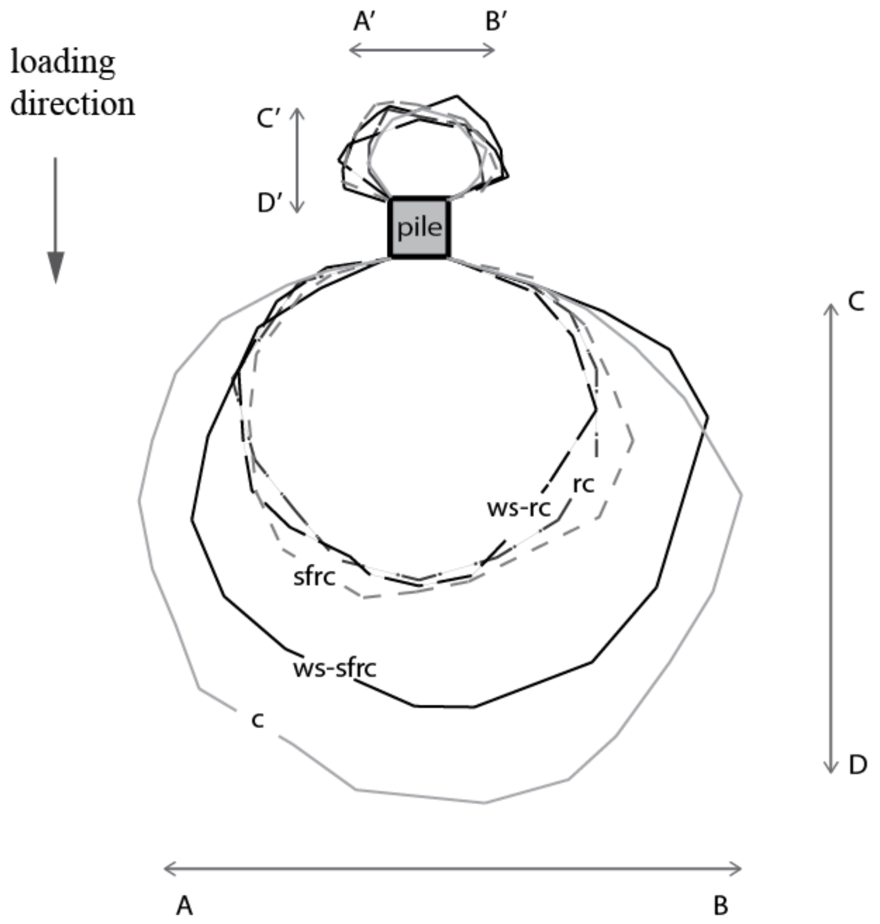

Figure 5.55 Sketches of heave and depression of sand surface due to lateral-axial loading (0.85 mm/min)

It is concluded that the behavior of fiber reinforced concrete model pile with bending reinforcement and steel fiber, *ws-sfrc*, is superior to conventional reinforced model piles. Under lateral-axial loading case less moments developed along the pile in the initial stage in *ws-sfrc* model pile, cracking moment capacities are nearly equal, crack pattern is better and deformation capacity is improved when compared with the rc pile. Laterally loaded *ws-sfrc* pile performance is better than the *rc* pile under axial loading. It shows that piles without stirrups exhibited improvement under lateral-constant axial loading due to presence of the steel fibers.

5.3.3 Effect of Axial Loading on the Behavior of Pile

In the following paragraphs the effect of axial loading on the behavior of pile was evaluated according to results of tests under lateral loading and lateral-axial loading. Loading rate of the tests was 0.85 mm/min. For this purpose, the test results of the conventional reinforced concrete model pile *rc* and concrete with bending reinforcement and steel fiber, *ws-sfrc*, were evaluated. Comparison of load-pile head displacement curves and moment distribution of rc pile presented in Figure 5.56 and Figure 5.57. Notice in Figure 5.56 that axial load increased the pile resistance especially after first crack. In other words displacements decreased under lateral-axial case. Application of the axial load improved; the horizontal load carrying capacity by 25% in *rc* pile at 0.01 m pile head displacement.

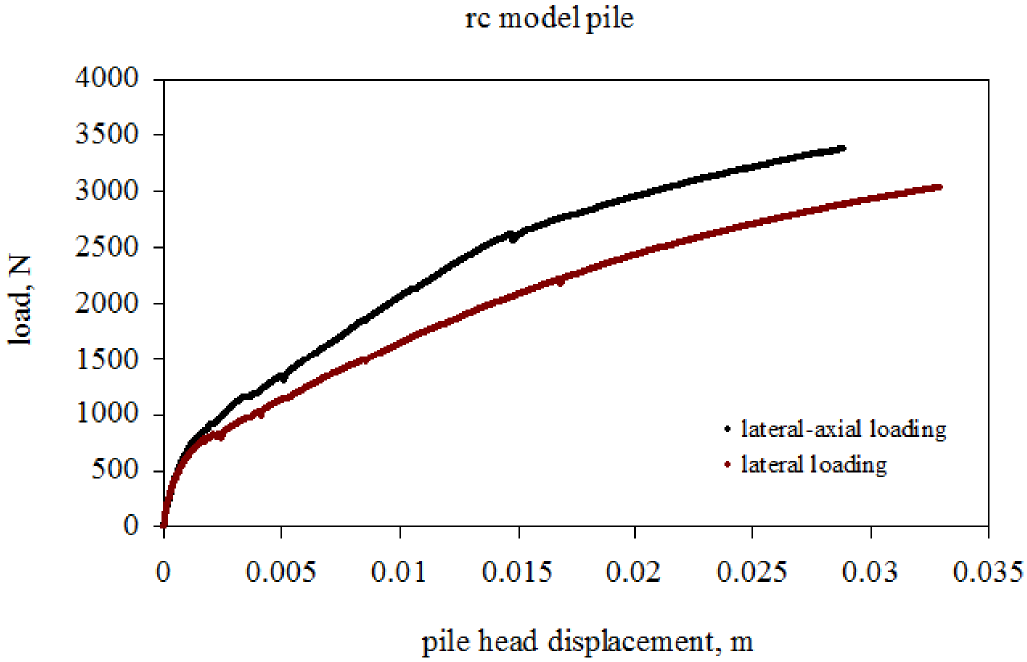

Figure 5.56 Comparison of pile head load-displacement of *rc* model pile

Moment distributions of *rc* pile under lateral loading case are compared with lateral-axial loading case (Figure 5.57). Maximum bending moment depths were obtained nearly at the same depths in two loading cases. In the lateral-axial loading test, moments were generally developed less than the lateral tests. Especially, in the initial stage (H=0.24) moments under lateral-axial loading were recorded visibly smaller than the test of *rc* pile under lateral loading. Small moment development at the subsequent loadings can be seen in Figure 5.57 particularly at the lower parts of the pile. Cracking moment capacity of *rc* pile in the test with axial loading was obtained 28% larger than the *rc* pile under lateral loading.

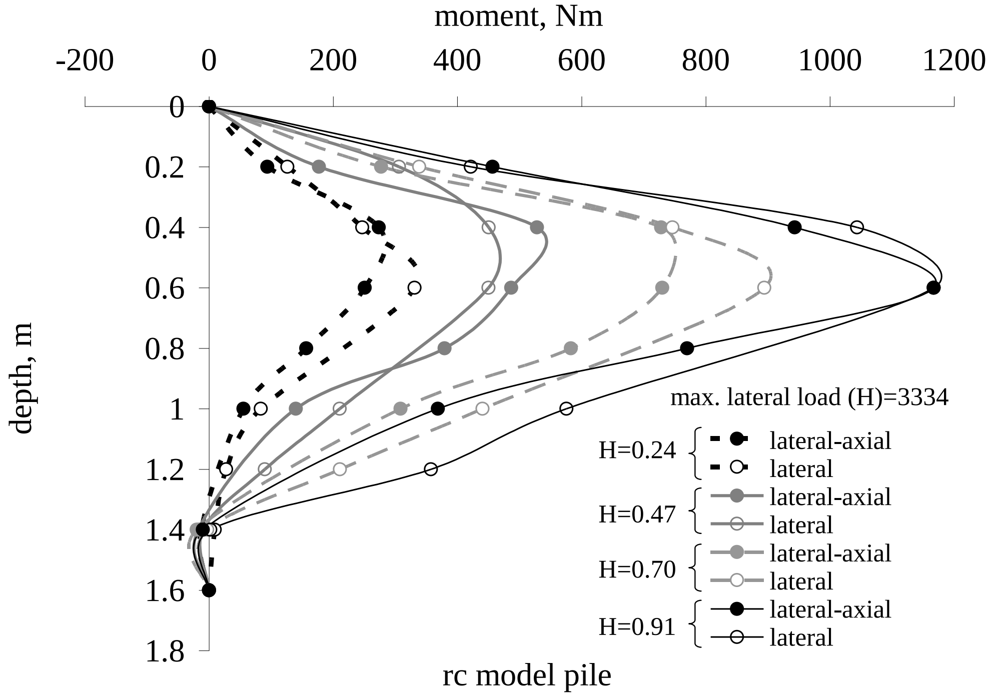

Figure 5.57 Comparison of moments of *rc* model piles under lateral and lateral-axial loading

Crack propagation of *rc* pile in lateral-axial load test was better than the test under lateral loading. Comparison of the damaged piles (Figure 5.43 and Figure 5.51) show that without axial load cracks reached the lower parts of the pile. All these results indicate that axial loading improve the performance of laterally loaded *rc* pile.

The contribution of axial loading can be obviously noticed from the test results comparison of *ws-sfrc* model pile. Axial loading altered the load–pile head displacement response of the *ws-sfrc* pile considerably (Figure 5.58). Under lateral-axial loading condition, *ws-sfrc* exhibit more resistance when compared with the lateral loading condition. Application of the axial load improved; the horizontal load carrying capacity by 39% in *ws-sfrc* pile at 0.01 m pile head displacement and the first crack load capacity of the pile by 35% in *ws-sfrc* pile.

Moment distributions of *ws-sfrc* were compared in Figure 5.59. Recorded moments show that in the case of lateral-axial load, moment development is apparently less than the moments of lateral loading case at the same load levels. Axial load improve the cracking moment (M_{cr}) capacity of *ws-sfrc*. Cracking moment was obtained 13% large with the presence of axial load. Crack depths and soil surface movement dimensions were obtained similar. In addition, only two cracks occurred in the test of lateral-axial loading whereas four cracks occurred in the lateral load case.

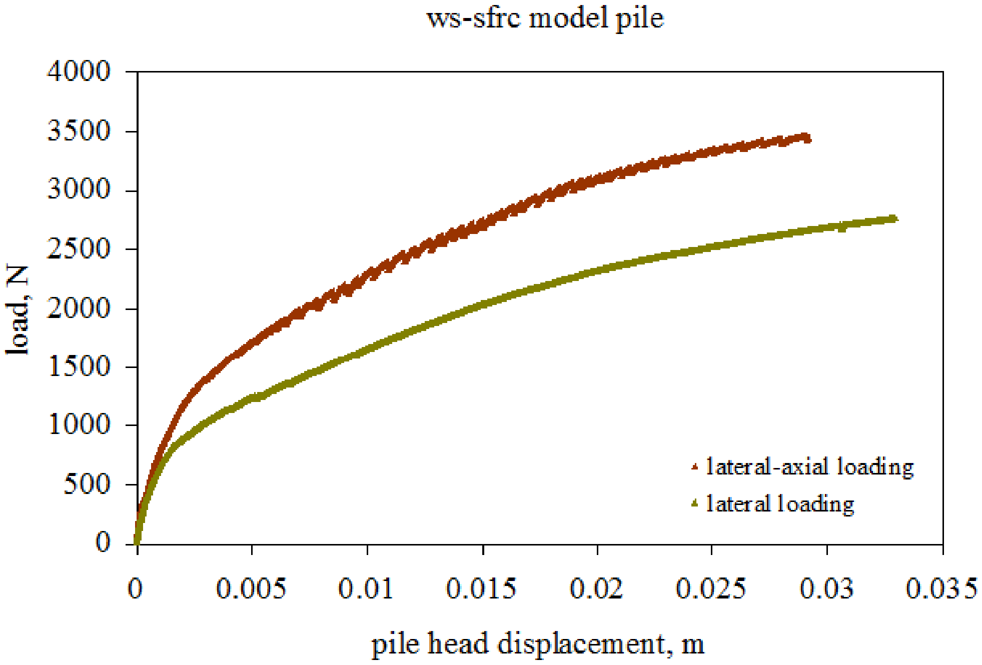

Figure 5.58 Comparison of pile head load-displacement of *ws-sfrc* model pile

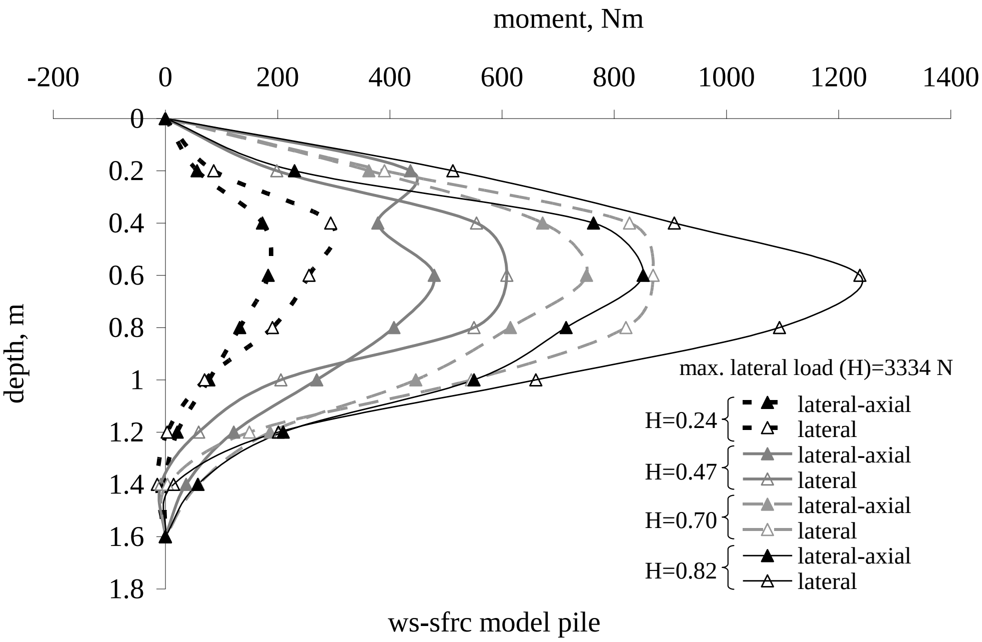

Figure 5.59 Comparison of moments of *ws-sfrc* model piles under lateral and lateral-axial loading

The results demonstrate that axial load improves the performance of the rc and *ws-sfrc* piles significantly. Cracking moment capacity and pile head load measurements increase considerably with the presence of axial load in *ws-sfrc* and *rc* model pile tests. Less moment occurrence along the *ws-sfrc* pile in the lateral-axial loading case is an indication to more flexible response when compared with the lateral loading case. In the literature, there are some studies about the effect of axial load on conventional reinforced concrete piles with steel fiber (Bodin & Madhkhan, 2002). It is emphasized that steel fiber reinforced concrete is more efficient in terms of dissipation of energy. Flexural tests were done on large scale steel fiber reinforced RC piles with and without axial load. The results of this study show that the increase in the moment capacity of the *rc* pile with 45kg/m^3 ~0.6% fiber content under axial loading was obtained 100%.

5.3.4 Effect of Loading Rate on the Behavior of Pile

The effect of loading rate on the behavior of piles has been investigated by researchers (Briaud & Garland, 1985); Al-Mhaidib, 2001; Dijkstra, 2004; Kong & Zhang, 2006). The effect of loading rate on pile groups in medium dense sand was investigated by model test method under axial load in the study of Al-Mhaidib (2004). The researcher indicated that the axial compressive capacity of pile group embedded in sand increases as the loading rate increases (Figure 5.60). Smooth steel piles having a diameter 25 mm and a length of 550 mm were used in the referred study. Researchers indicated that loading rate has a significant effect on the bending moment distribution of laterally loaded pile in sand (Kong & Zhang, 2006).

Piles were laterally loaded under two various rates, 4mm/min (I) and 0.85 mm/min (II), in order to evaluate the effect of loading rate on the response of piles. In this respect, the behavior of *ws-sfrc* and rc model piles were considered. Pile head deformation, moment distribution and deformed shapes of rc pile are given from Figures 5.61 to 5.63.

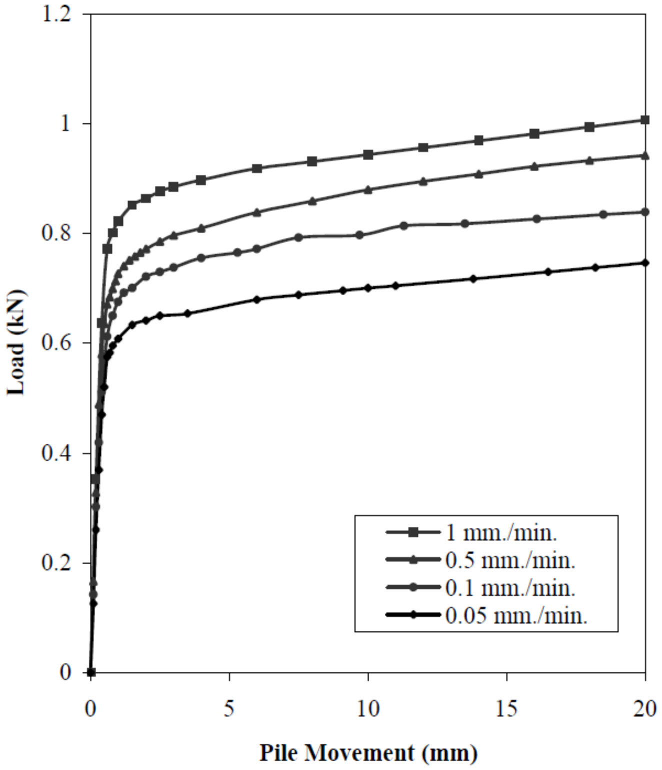

Figure 5.60 Load-displacement curves for model piles (Al-Mhaidib, 2004)

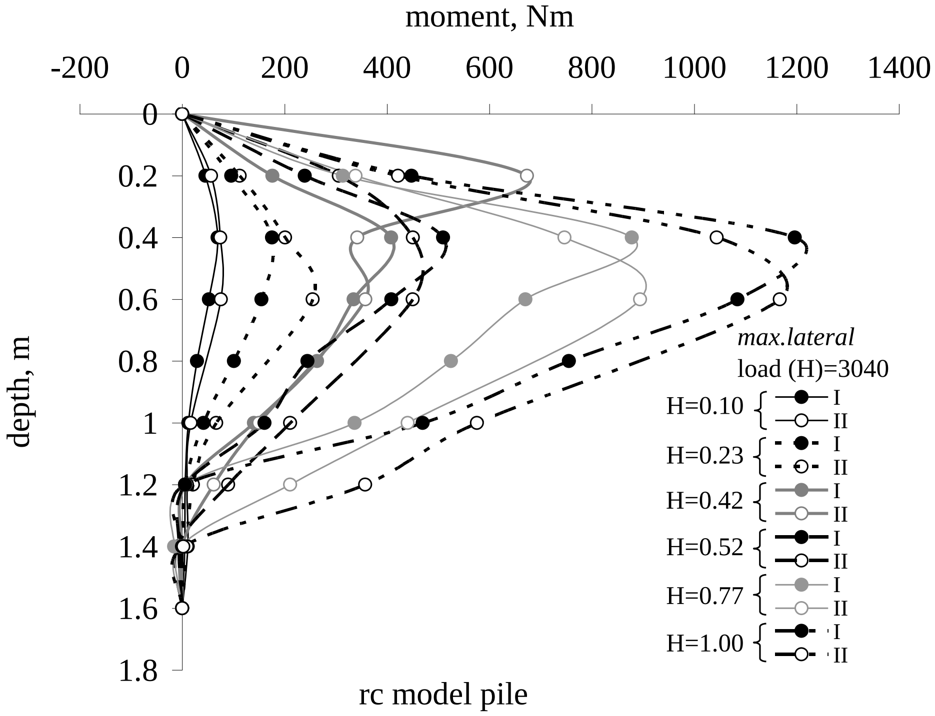

Figure 5.61 Comparison of moments of *rc* model piles at various rate of loading

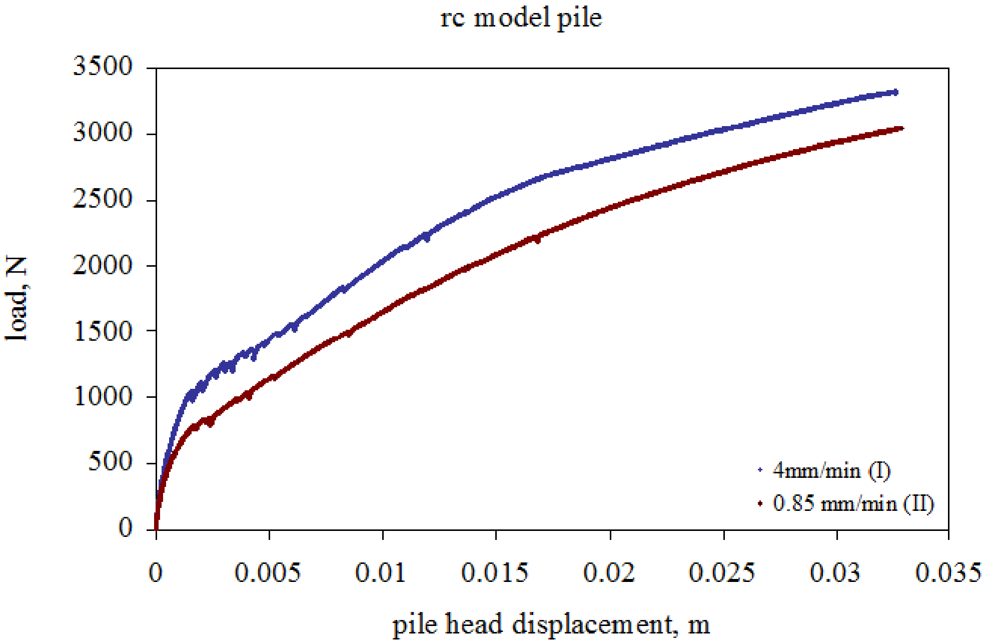

Figure 5.62 Pile head load-displacement relation of *rc* pile at various rate of loading

Rate of loading changes the bending moment distribution and load-head displacement response of rc pile as can be seen in Figure 5.61 and 5.62. The horizontal load carried by the rc pile was determined 24% higher than that of the test with 0.85 mm/min loading rate 0.01m pile head displacement.

In the initial stage (H=0.1) moments distribution are obtained similar. Subsequent stage (H=0.23) moment generation changed and lower moments took place on the pile at the same load levels in the rapid loading case. This behavior is compatible with the load deflection graphic (Figure 5.62). The reaction of the pile head and soil generated higher in the 4mm/min test than the slow test. In other words displacements were obtained less in rapid test. In the initial stage (H=0.1) load-displacement response were obtained similar. The rc pile head reaction was determined in the test 4mm/min 25% higher (H=0.23 to h=0.77) and 10% higher at the further loadings (H>0.77) than the test 0.85mm/min after the first crack. Cracking moment was determined 7% large in rapid test of rc pile. The further loading stage just after cracking (H=0.42), moment characteristic is quite different in the slow test. Maximum bending moment shifted above at H=0.42. Crack pattern in the test of 0.85mm/min also well-matched with the moment response. A crack was observed at 29 cm depth corresponding to close the recorded bending moment at 20 cm. It is interesting that in the rapid test a crack was occurred at 31 cm depth, but maximum bending moment location was not shifted. Notice that bending moments in the slow test (II) developed larger than the rapid test (I) under the maximum moment depths for all of the loading stages. The pile head measurements decreased or deformations increased and moments on the pile increased when the pile slowly loaded. Cracks propagated along the pile up to %75 of the pile depth due to large moment generation in slow test (Figure 5.43 and Table 5.9). Cracks took place only at the upper part of the pile up to 40% under 4mm/min (rapid) loading rate (Figure 5.34 and Table 5.5).

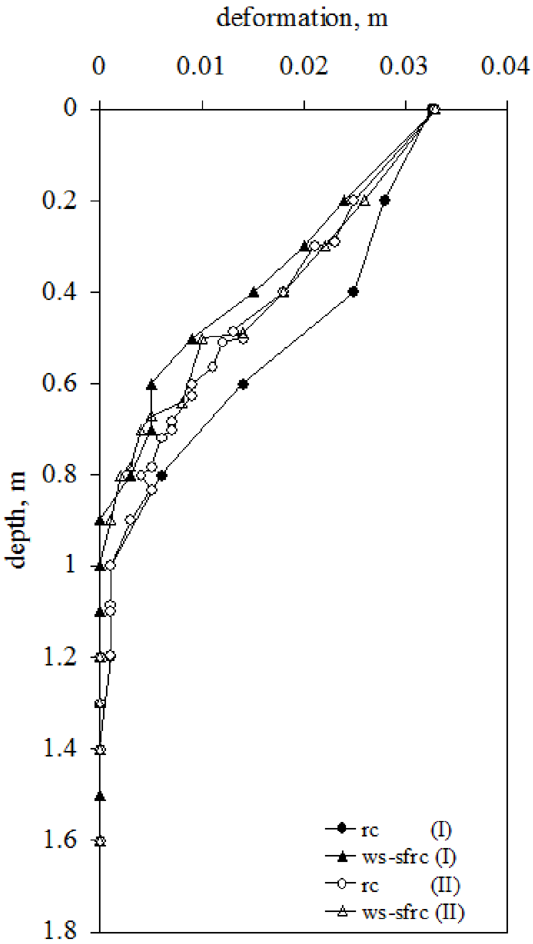

Figure 5.63 Variation of pile deformations with depth under different rate of loading

Observations and measurements at the sand surface show that rate of loading changes the movement of the sand especially in front of the pile. Comparison of the Figure 5.38; Table 5.6 and Figure 5.45; Table 5.10 demonstrate that movement of the sand surface occurred in the slow test significantly larger than in the rapid test. That result also verifies that pile head reaction occurred low in the slow test. In addition, deformation capacity of the *rc* pile decreased in the test II (0.85 mm/min) due to large moment occurrence as can be seen in 5.63. All these results express that the performance of *rc* pile under rapid loading better than the slow loading.

The effect of loading rate was also evaluated for the model pile with bending reinforcement and steel fiber, *ws-sfrc*, in terms of moment development, load-pile head displacement relation, crack propagation, deformed shape and condition of the soil surface. Moment and load-head displacement compared in the Figures 5.64 and 5.65.

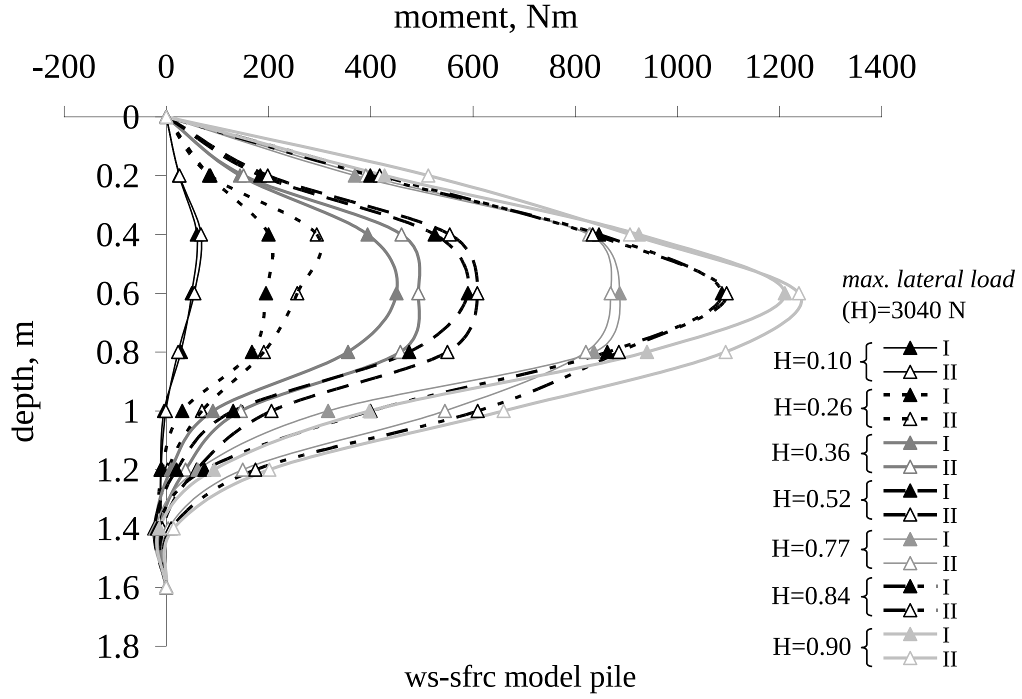

Figure 5.64 Comparison of moments of *ws-sfrc* model piles at various rate of loading

The tests result of *ws-sfrc* and *rc* piles show that there are some differences and similarities in the meaning of loading rate effects. In the initial loading stage (H=0.1) moment variations achieved quite similar in *ws-sfrc* tests. Load-pile head displacement relationships were obtained also similar in the initial stage. In the loading stages (H=0.26 and H=0.36) the moments in the rapid test were recorded less than the moments in slow test. However cracking moment values obtained almost the same value (Table 5.4 and Table 5.8). In the loading stage H=0.36 maximum moment depth shifted above part of the pile in the slow test as it happened in the rc pile test. Note that after the loading stage (H=0.36) all moments were developed quite similar especially at the above part of the pile in two loading cases. In the further loading stages and under the maximum moment depths, the recorded moments in the slow test were generally higher than the recorded moments in rapid test. On the other hand, these large moments did not cause cracks at the lower part of the pile. The crack propagation of the *ws-sfrc* piles under rapid and slow tests were obtained similar. That similarity can be seen by comparing the pictured crack pattern

(Figure 5.33 and Figure 5.44) and the crack depths values which are listed in Table 5.5 and Table 5.9.

Although crack patterns were achieved similar in the different loading rate tests, load-pile head displacement relations were obtained different. The horizontal load carried by the *ws-sfrc* pile was determined 20% higher than that of the test with 0.85 mm/min loading rate 0.01m pile head displacement. Pile head reaction decreases or deformation increases with the decrease of loading rate.

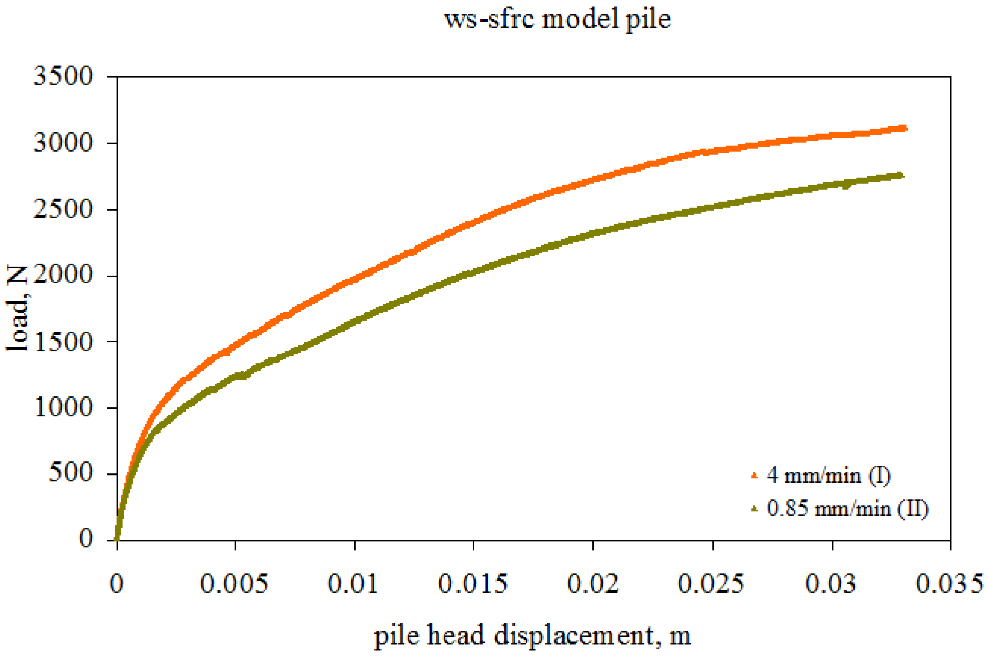

Figure 5.65 Pile head load-displacement relation of *ws-sfrc* pile at various rate of loading

Loading rate also effected the movement of the soil surface especially in front of the pile in the tests of *ws-sfrc*. The soil heave dimensions measured in the slow test were larger than the heave in the rapid test due to low pile head reaction. However, deformation shape were measured nearly same for the *ws-sfrc* pile as can be seen in Figure 5.64.

The results show that loading rate changed the behavior in terms of load-head displacement and moment distribution. It also changed movement of the soil at the surface in the *ws-sfrc* pile tests. However, the crack propagation, deformed shape, cracking moment and moment distribution after the first crack were obtained quite similar in the rapid and slow tests in *ws-sfrc*. The effect of loading rate was not enough to change pile behavior totally. On the other hand, the rate of the loading affected the behavior of the conventional concrete pile completely. Although *ws-sfrc* reinforced without shear reinforced, pile behavior is partially affected by the different rate of loading. It was stated in the literature that steel-fibers significantly improves many of the engineering properties of mortar and concrete, notably impact strength and energy absorption capacity (ACI, 1996). The rate of loading affected slightly the behavior of *ws-sfrc* due to energy were absorbed by the steel fiber reinforced concrete. It is concluded that under different loading rates the behavior of *ws-sfrc* is superior to *rc* piles in cohesionless soil.

5.4 Summary

In this section of the chapter a summary of the test results and discussions are made. It is aimed to provide the reader with a concise presentation of the model tests. Firstly, the tests on the concrete and *sfrc* model piles are summarized. These tests were made as supplementary to the tests given in the third chapter. Besides, the results obtained in these tests were compared with those of the flexible reinforced concrete piles (i.e. *rc*, *ws-rc* and *ws-sfrc*).

Moment cracking capacity of the *sfrc* model pile was recorded 6% less than the concrete model pile. However, concrete model pile was not able to carry further loads after the occurrence of the hinge. Concrete model pile failed with a single hinge whereas the *sfrc* model pile failed with double hinges. Concrete model pile cracked in a brittle manner and the pile lost its load carrying capacity after first hinge occurrence. On the other hand, steel fiber reinforced concrete pile was able to carry additional load increments with excessive deformations due to steel fiber bridging mechanism explained in the third chapter. After the first hinge occurrence the *sfrc* pile continued to carry bending moment. The moment in the second hinge was recorded as 25% higher than the failure moment of the concrete pile. The ultimate moment of the *sfrc* was also 55% larger than that of the concrete pile. In the lateral load test with a loading rate of 0.85 mm/min where axial load was also applied the moment carrying capacity of *sfrc* was 40% higher than that of the concrete pile although cracking moment capacity of the *sfrc* pile was obtained slightly more (3%) than the concrete pile.

The steel fiber ratio by volume was kept constant as 1% throughout the study since past experience and the literature showed that 1% steel fiber by volume was the most efficient amount in improving concrete behavior. The flexural element bending and lateral loading pile tests showed that addition of steel fibers could enable the engineer to avoid shear reinforcement (i.e. stirrups) in RC design.

The *ws-sfrc* pile exhibited approximately similar pile head load-deformation behavior to the conventional reinforced model pile, *rc*, including stirrups in the cage. First crack pile head load capacity is obtained also nearly equal in tests with a lateral loading rate of 4 mm/min. The *ws-sfrc* pile, on the other hand, exhibited a better response in the test with a slower rate (0.85 mm/min). The pile head first crack load of the *ws-sfrc* pile increased by 11% as compared with the *rc* pile in the slow rate test. The *ws-rc* pile (i.e. reinforced concrete pile without stirrups and steel fibers) did not behave well when compared with the *rc* and *ws-sfrc* piles. The first crack load in model *rc* and *ws-sfrc* piles happened to be 30% larger than *ws-rc* model pile. The first crack load capacity of the *ws-sfrc* pile increased more notably when it was also axially loaded. The increase in first crack load was 26% higher as compared with the *rc* pile.

Addition of steel fibers improved the cracking moment capacity of the *ws-sfrc* model pile by 10% as compared with the *rc* model pile under 4 mm/min lateral loading rate. The increase in cracking moment capacity of the ws-sfrc pile under a slower rate (i.e. 0.85 mm/min) was even 9% larger than the cracking moment capacity of *rc* pile under 4mm/min lateral loading rate. The rate of loading effected slightly the behavior of *ws-sfrc* due to energy were absorbed by the steel fiber reinforced concrete. It is concluded that under different loading rates the behavior of *ws-sfrc* is superior to *rc* piles in cohesionless soil.

The cracking moment of the *ws-sfrc* pile was 17% larger than that of the *rc* pile in slow rate case. The applied axial load, however, masked influence of pile material type on the cracking moment. One should note that the axial load level was decided in such a manner that the N-M pairs would remain within the effective concrete section. Care was spend so that the axial load was large enough to observe its effect on a particular material and small enough not to require high lateral loads that were beyond the capacity of the testing system. Effect of the axial load on pile response is discussed for each pile type is summarized in the following paragraph.

Applied axial load improved the cracking moment (M_{cr}) capacity of the *rc* pile by 28%. The first crack load was 47% higher and pile head displacements were considerably reduced beyond the first crack load. For instance 20% larger lateral load is necessary to reach the same displacement for *rc* pile. The axial load changed the response of the *ws-sfrc* pile remarkably. The cracking moment (M_{cr}) of *ws-sfrc* pile increased by 13% with the application of axial load. The first crack load of this pile increased by 68%. The shift between the pile head displacement curves was 35% (i.e. lateral load for same pile head displacement was 35% larger for the axial loading case).

Crack propagation along the model *ws-sfrc* pile is similar to the conventional reinforced concrete model pile (*rc*) in the test with a loading rate of 4 mm/min (i.e. fast loading). The crack propagation along the *ws-sfrc* pile, on the other hand, is quite better than the crack propagation of *ws-rc*. Positive influence of steel fiber in reducing crack formation is more noticeable in slow loading test where the *rc* pile was damaged more heavily as compared with the *ws-sfrc* pile. Moreover, tests under axial load clearly demonstrated steel fiber influence on crack formation. This fact proved the positive contribution of steel fiber on the behavior reinforced concrete piles. It seems possible to avoid shear stirrups from the reinforcement cage provided that large scale field tests are performed on prototype piles.

One should notice that values of pile response parameters generally have an increasing trend with the rate of loading. It was found that rate of loading considerably altered the bending moment distribution and load-head displacement response of the *rc* pile. Bending moments in the slow test (i.e. 0.85 mm/min) were larger than those of the rapid test (i.e. 4 mm/min) at elevations that were deeper than the depth of the maximum moment. The pile attained larger displacement for a particular measured lateral load thereby developing higher bending moments during the test with a loading rate of 0.85 mm/min. The pile head displacement-measured pile load curve belonging to the rapid rate test of the *rc* pile has load levels 25% larger than the slow rate test for a particular displacement. The shift is 20% for the *ws-sfrc* pile. Cracking moment is also 7% larger for the rapid rate test of the *rc* pile. Observations and measurements at the sand surface show that rate of loading changes the amount of the displaced sand mass especially in front of the pile. Movement of the sand surface is significantly larger in the slow test than in the rapid test for the *rc* and *ws-sfrc* pile.

CHAPTER SIX

NONLINEAR SOIL REACTION-DEFORMATION (p-y) RELATIONSHIPS

6.1 Introduction

In this chapter, experimentally derived p-y curves are compared with the currently available industry standard API recommended p-y curves. Effects of nonlinear behavior of steel fiber reinforced concrete and reinforced concrete pile on soil-pile interaction were investigated. The response of *ws-sfrc* pile is compared with that of the *rc* pile by defining p-y curves for each. Influence of loading rate and axial load on the nonlinear p-y curve is also assessed. The current API procedure for sandy soils is improved by incorporating the nonlinear dependence of empirical adjustment factor “A” on the cracking moment.

6.2 Nonlinearity of Pile Stiffness

As detailed before, nonlinear bending stiffness-moment relationship of the piles were obtained from the bending test results. Bending stiffness *EI* is constant until the occurrence of the first crack and the relation between the moment and curvature is still linear up to this stage. After the initial stage (i.e. post crack stage) *EI* decreases and the relation between the moment and curvature becomes nonlinear. Experimental moment-curvature (M-Φ) relation of the reference pile (decided as *rc* pile in this thesis) is compared with output of the nonlinear RC section analysis program XTRACT (Chadwell & Imbsen, 2004). As can be seen from Figure 6.1, the test data is in good agreement with XTRACT analysis up to the yield moment for the case where axial load is not taken into consideration (V=0). The bending reinforcement showed strain-hardening behavior after the yield point during the tests, a fact that cannot be taken into consideration in numerical analysis. A moment-curvature relation was also obtained in XTRACT analysis for the case where the axial load is equal to V=5400N. As one can notice in Figure 6.1, the bending stiffness of the pile in the test where V=5400 N is 30% and 5% larger than that of the V=0 case in the linear (i.e. before the cracking moment) and nonlinear (i.e. beyond the cracking moment) stages, respectively.

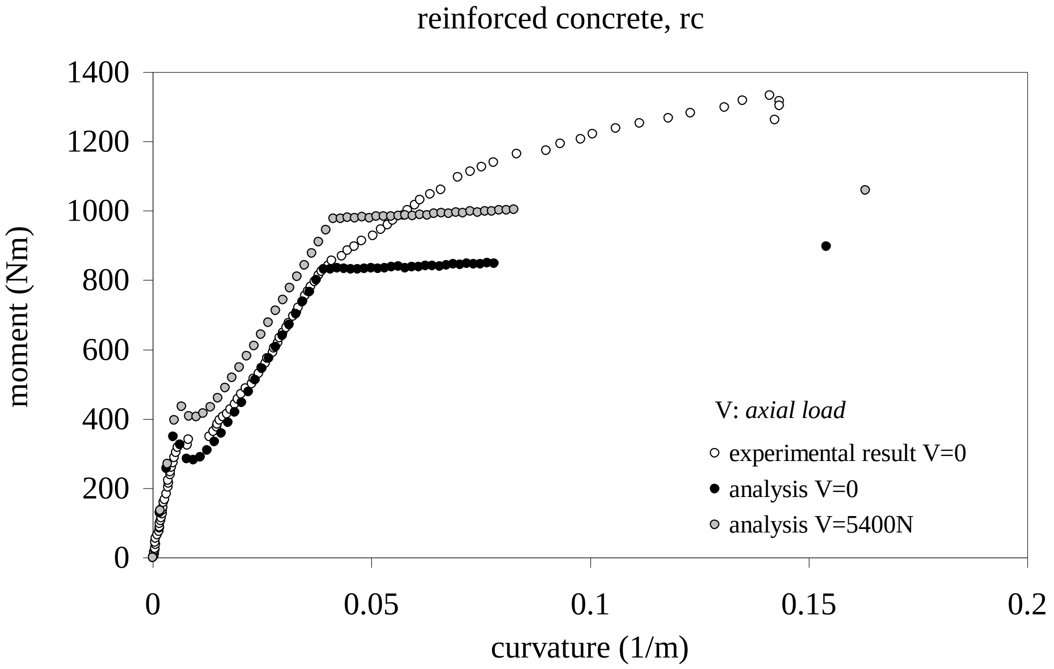

Figure 6.1 Comparison of moment-curvature curves

6.3 Soil Reaction-Deformation (p-y) Curves

The p-y curves were obtained by analyzing the experimental data. Distribution of shear force *(V)*, soil resistance *(p)*, slope *(s)*, and pile deformation *(y)* with depth were obtained by successive integration and differentiation of the recorded bending moment *(M)* data. The cubic spline interpolation technique was utilized during the analyses. Nonlinearity of the bending stiffness, *EI*, as a result of bending moment development along the pile due to lateral loading was taken into account in stepwise manner where decrements of *EI* were considered in numerical analyses.

$$M(x) = EI\,\frac{d^2y}{dx^2} \qquad 6.1$$

Shear force, *(V),* is obtained by single derivation of the fitted cubic spline between the successive moment data points. Lateral soil-pile reaction, *(p),* per unit length was obtained by double differentiation of the bending moment data along the pile.

$$V = EI\frac{d^3y}{dx^3} \qquad 6.2$$

$$p(x) = EI\frac{d^4y}{dx^4} \qquad 6.3$$

The slope *(s)* was obtained by integrating the cubic spline once then dividing the obtained results to *EI*. The deformation *(y)* was obtained after the second step integration of the cubic spline.

$$S = \frac{dy}{dx} \qquad 6.4$$

Bending stiffness reduction taking place along the pile during lateral loading was defined based on the developed moment (Figure 5.26). This is done at each strain gage location on the pile since soil-pile reaction (*p)* and deflection (*y)* were computed at these locations. The moment data were evaluated in increments resembling the nonlinear static pushover technique so that nonlinear nature of the moment development can be traced. This numerical solution technique allows tracing of the entire nonlinear moment-curvature path in incremental steps. The p-y curves were also obtained assuming constant *EI* and bilinear *EI* along the pile. These curves were compared with the curves of the push-over technique. In the bilinear analysis, EI was taken as 70% of the initial *EI* in the post crack stage. Analyses results show that the soil-pile reaction (*p)* is not significantly dependent on *EI* whereas the deflection (*y)* appears to depend on the bending stiffness variation. In the push-over analysis, deformation values were found as larger than the constant and bilinear analysis. Comparison of the p-y curves (at 0.1 m depth) obtained according to different analysis methods is presented in Figure 6.2 for the *rc* pile. Pile head deformations of the push-over analysis were compared with the measured pile head deformations and it is concluded that the push-over analysis technique is more reliable. The flowchart presented in Figure 6.3 briefly describes the procedure employed in this study.

During the tests hinges occurred intensively between 0.4 m and 0.55 m below the sand surface. Below 0.55 m *(~8B)* and especially 0.7 m where hinges were relatively scarce the soil resistance to the pile was significantly small. Therefore, nonlinear p-y curves were obtained up to 0.7 m depth corresponding to *10B* where *B* is the pile width.

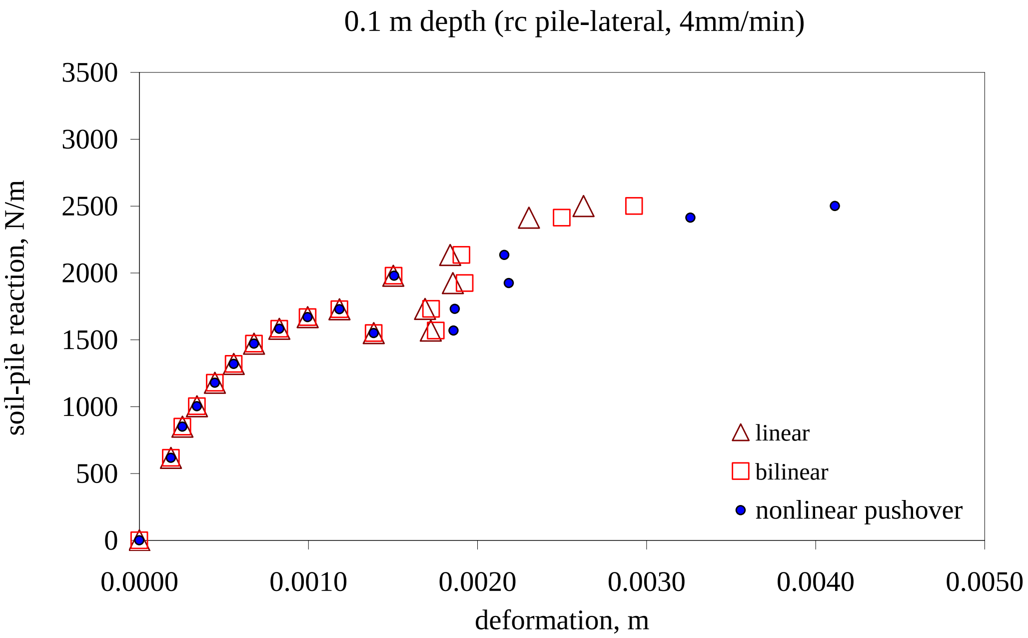

Figure 6.2 Comparison of analysis methods for p-y curves

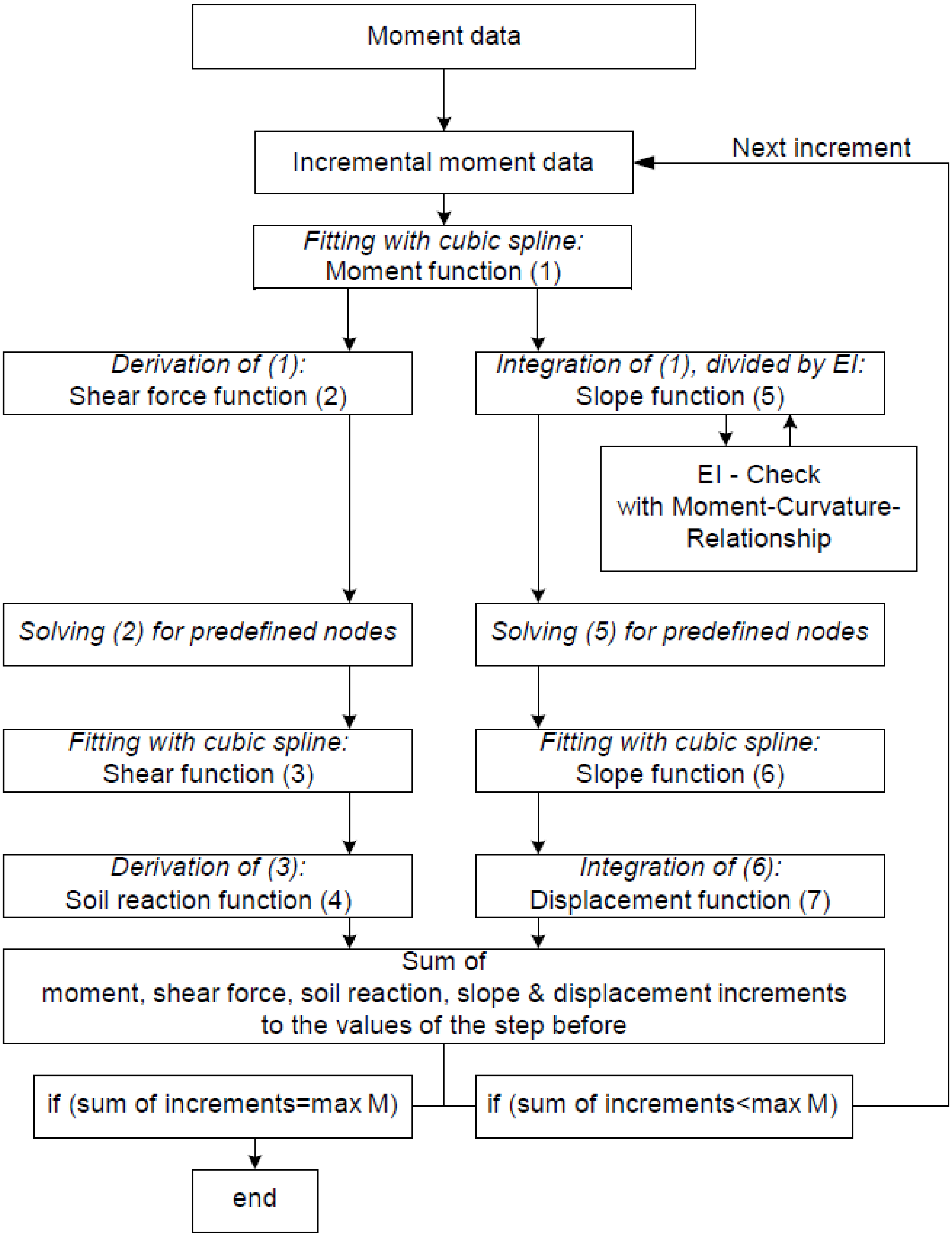

Figure 6.3 Flowchart for analysis of laterally loaded piles

6.3.1 Soil Reaction-Deformation (p-y) Curves under Lateral Loading

The p-y curves based on test data of laterally loaded piles under 4mm/min loading rate are given and compared with p-y curves of API-2000 (Figure 6.4). The recommended API curve equation and definition of the *A* coefficient can be seen in Equations 6.5 and 6.6. The *ws-rc* and *c* piles seems to be in good agreement with the API p-y curve at 0.1 m depth. On the other hand, at this shallow depth *rc* and *ws-sfrc* piles provides considerably higher soil-pile reaction compared to API p-y curves. At 0.3 m depth only *rc* pile is in better agreement with the API p-y curve. The piles *ws-sfrc*, *c* and *sfrc* yielded lower soil-pile reactions than the API curve. The agreement is even worse at 0.5 m depth.

$$p = A \times p_u \times \tanh\left[\frac{k \times H}{A \times p_u} \times y\right] \qquad 6.5$$

$$A = \left(3.0 - 0.8\frac{H}{D}\right) \geq 0.9 \text{ for static loading} \qquad 6.6$$

where

A= an adjustment factor to account for cyclic or static loading condition

p_u=ultimate bearing capacity at depth H, (kN/m)

k= initial modulus of subgrade reaction, (kN/m^3)

It should be noted in Figure 6.4 that once first crack took place on the pile, soil-pile reaction increased abruptly in the *rc* and *ws-sfrc*, piles. Cracking moments (at first hinge) corresponding to lateral load levels were given in the fifth chapter. It is concluded that the portion of the pile above the hinge that took place at the cracking moment responded as a shorter rigid pile and loaded the soil resulting in larger soil resistance values. Therefore, the data acquired until the occurrence of the cracking moment were regarded as the base data for the development of p-y curves.

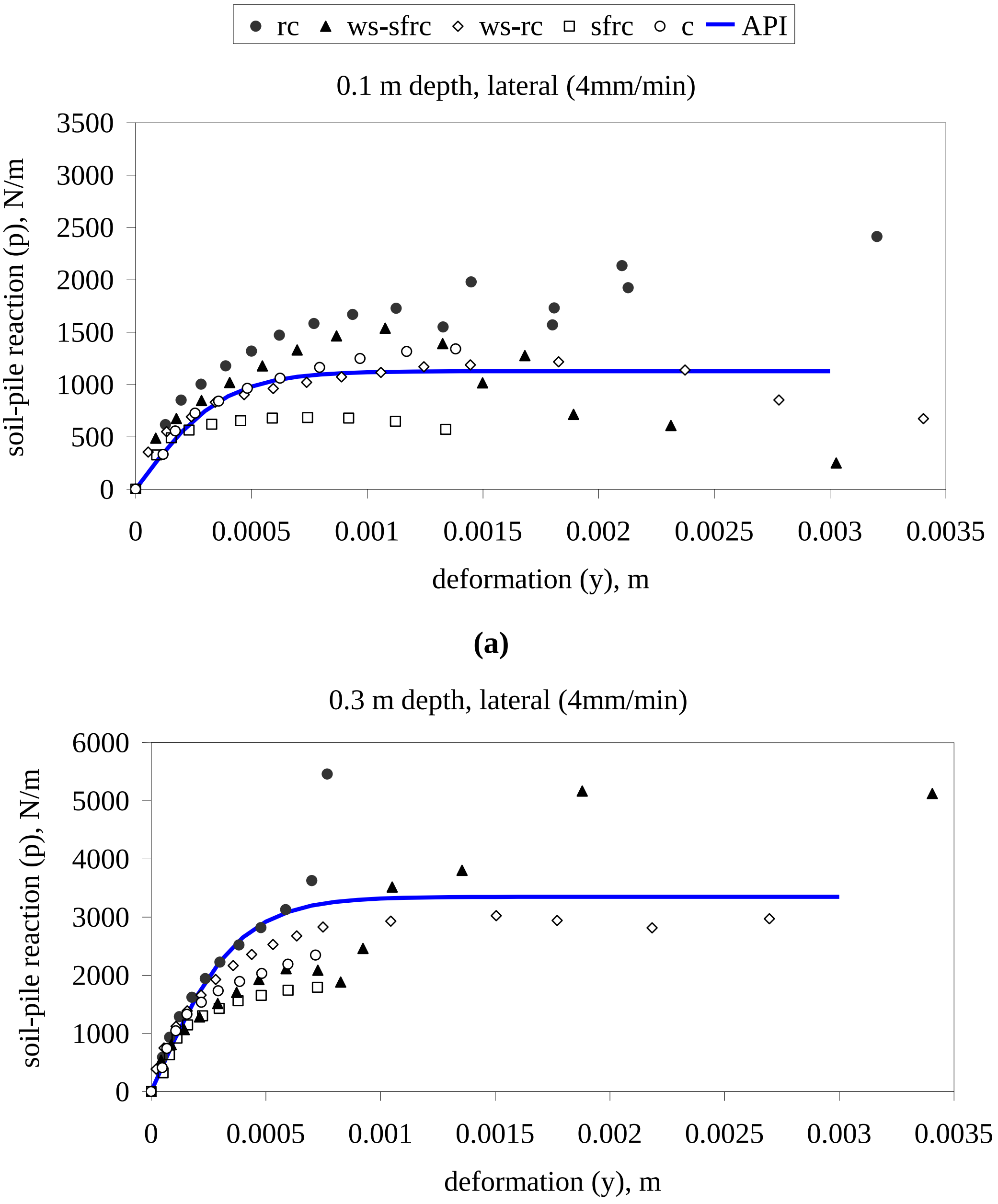

(a)

(b)

Figure 6.4 Comparison of p-y curves for the laterally loaded piles (4mm/min)
(a) 0.1 m (b) 0.3 m depths

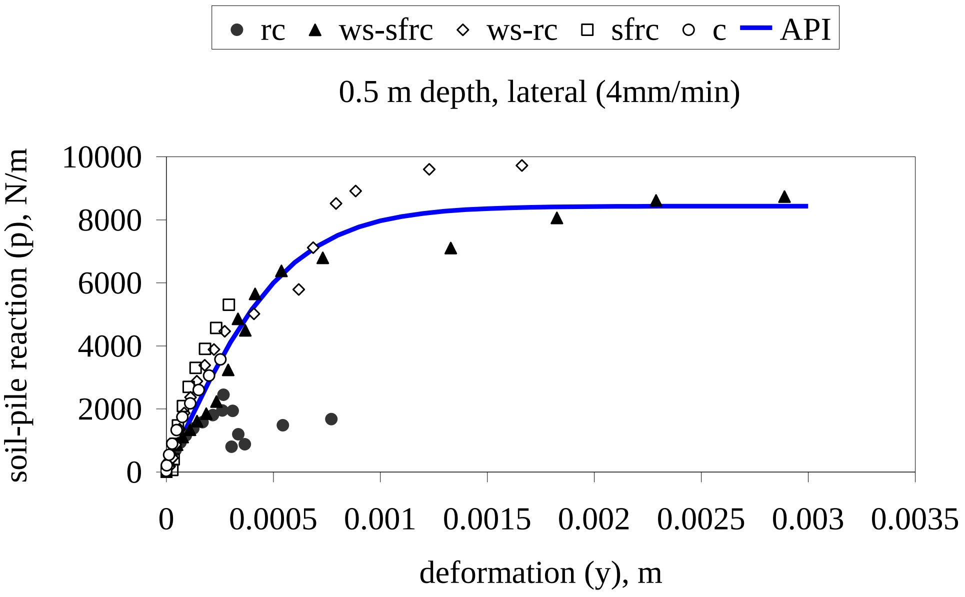

(c)

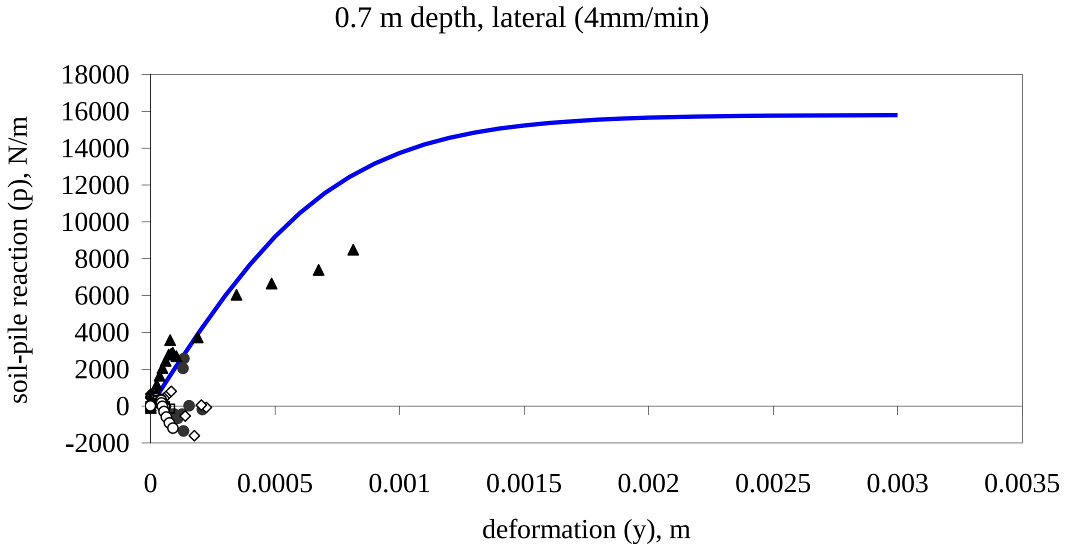

(d)

Figure 6.4 (c) 0.5 m (d) 0.7 m depths -*continued*

Most probably, the correction factor *A* in the proposed API load-deflection (p-y) approximation is not sufficient in taking care of the response of reinforced concrete piles. Model of p-y curve for sand (API) were emprically derived based on full-scale steel pile tests under lateral loading such as Mustang Island (Cox, Reese, & Grubbs, 1974), Sabine River (Matlock, 1970) and Houston (Reese & Welch, 1975). In some recent studies, this issue is also considered by the researchers. Juirnarongrit &

Ashford (2005) emphasized that the experimental adjustment factor *A* for the static load test was simplified using a linear equation; therefore, resulted in a difference in the ultimate soil resistance. In the referred study, back calculated p-y curves were obtained based on the full scale laterally loaded reinforced concrete piles (Figure 6.5). Researchers compared the back calculated p-y curves with API p-y curves. The results of the comparison of referred study are similar with the results of the comparison this dissertation. Janoyan (2001) stated that the API and SWM (strain wedge model) curves would be appropriate for rigid piles, but are clearly not appropriate for nonlinearly behaving piles (i.e. flexible piles with respect to the soil). The author added that those so called "standard" p-y curves were derived assuming linear EI.

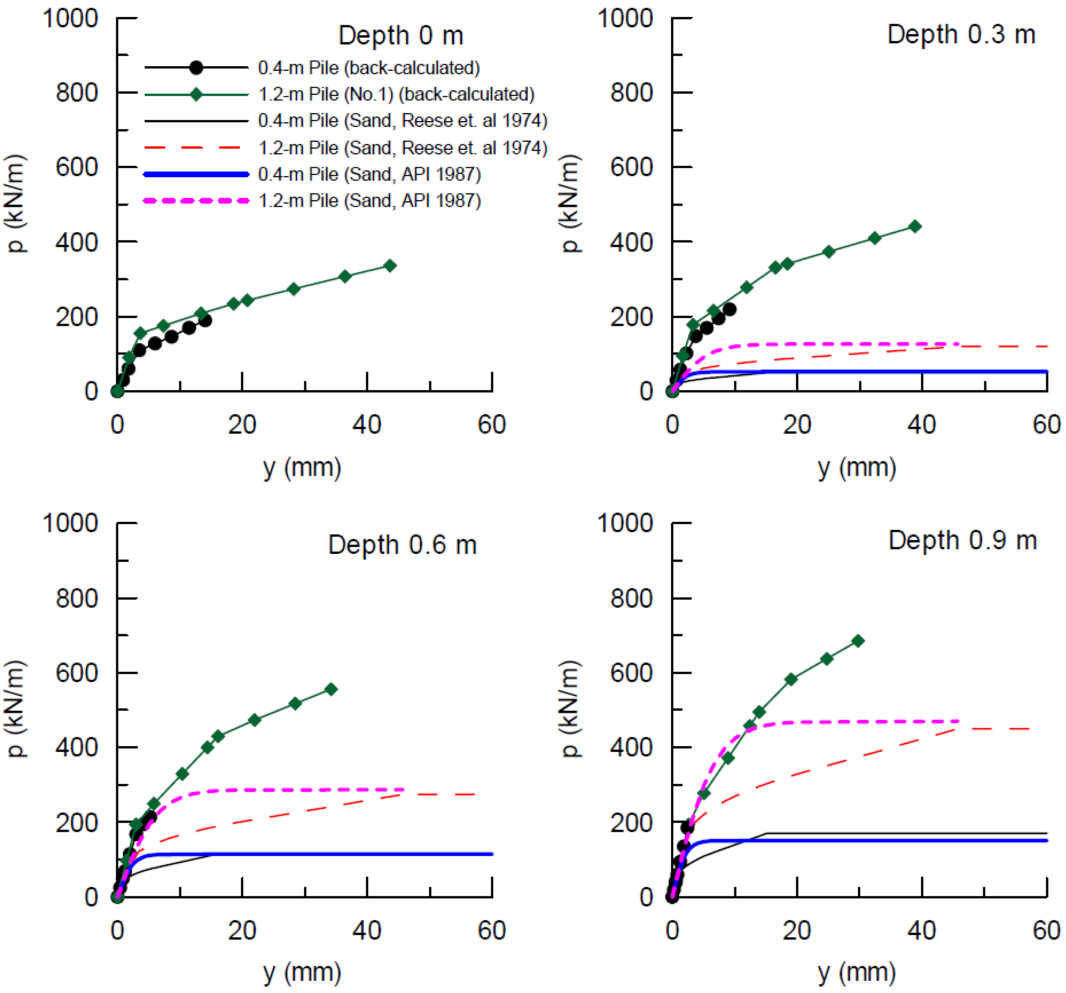

Figure 6.5 Comparison of p-y curves at soil surface, 0.3 m depth, 0.6 m depth, 0.9 m depth (Juirnarongrit & Ashford, 2005)

6.3.2 Soil Reaction-Deformation (p-y) Curves under Lateral-Axial Loading

As noted in the fifth chapter, piles were also laterally loaded under constant axial load (V=5400 N). It is a known fact that axial load has a major impact on the stiffness of the structural members. Therefore, nonlinear analysis was made in order to get the moment-curvature relation of the axially loaded pile as can be seen in Figure 6.1. The cracking moment and yield moment increased 17% due to axial load application. Such effects observed in terms of increases in *EI* and cracking moment were taken into consideration during p-y curve analyses of the lateral-axial load tests.

The p-y curves based on lateral-axial loading test data are given and compared with the API p-y curve in Figure 6.6. It can be seen that the API curve can trace the general trend of the experimentally derived curves at 0.1 m depth. However, the API curve overestimates the soil reaction at depths 0.3 m and 0.5 m. One should be aware of the fact that the data of the lateral load tests and lateral-axial load tests are not comparable since the rate of loading in the lateral-axial tests are much smaller being 0.85 mm/min as compared with 4 mm/min of the lateral load tests. It is considered that slower loading rate resulted in softer soil-pile interaction with consequent smaller soil reactions. Test data at same loading rates are compared and discussed in proceeding sections.

It should be noted in Figure 6.6 that a hinge occurred on the pile at deflection y= 0.0012 m at 0.1 m depth. At 0.3 m and 0.5 m it can be seen in Figure 6.6 that first crack occurred on the pile at smaller deformations. In lateral-axial loading case hinges intensively took place between 0.4 m and 0.65 m depths. Therefore, soil reactions computed at the depth of 0.7 m were much smaller since the transfer of the applied lateral head load was significantly interrupted by the formation of the hinge.

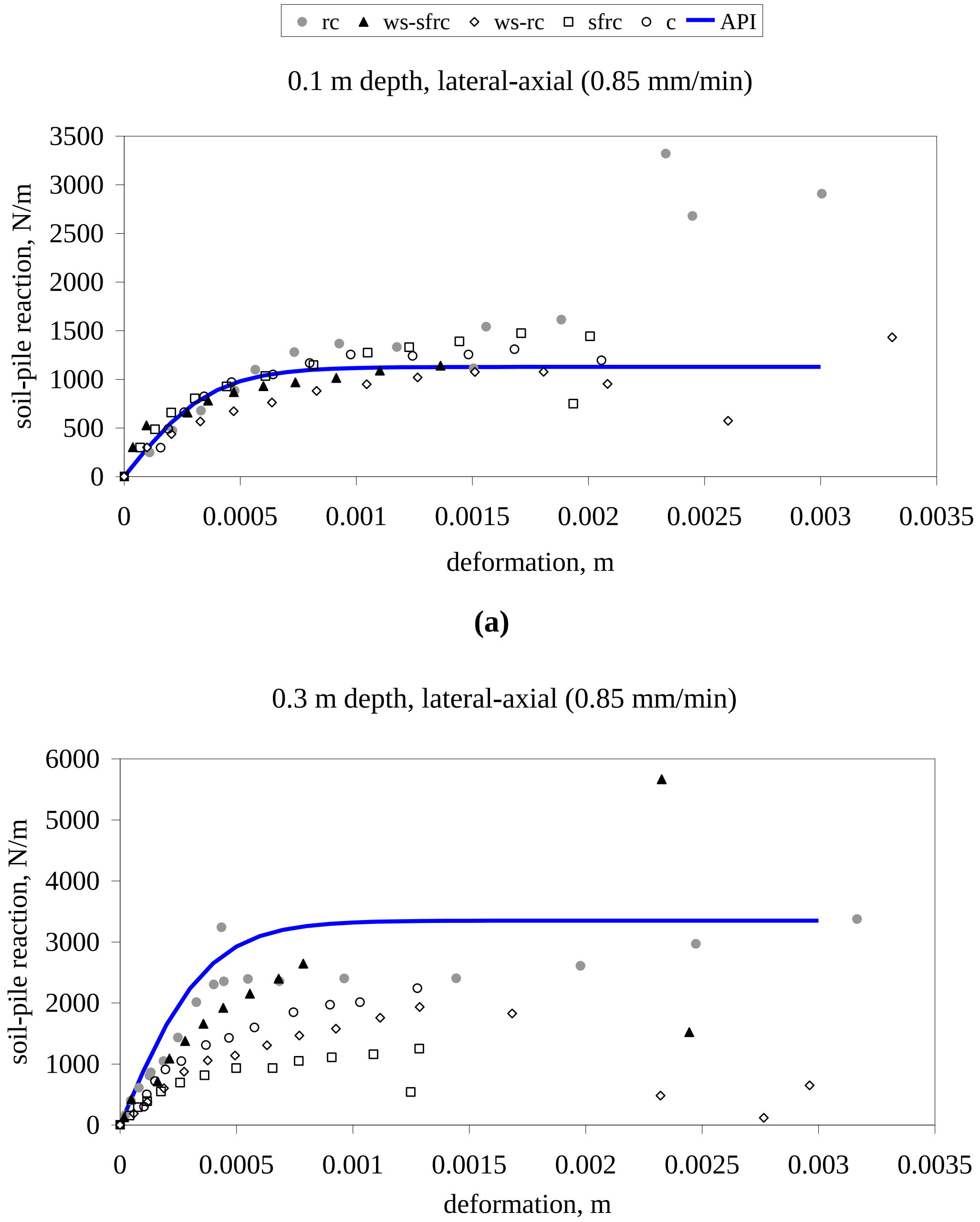

(b)

Figure 6.6 Comparison of p-y curves for the lateral-axial loaded piles (0.85 mm/min)
(a) 0.1 m (b) 0.3 m depths

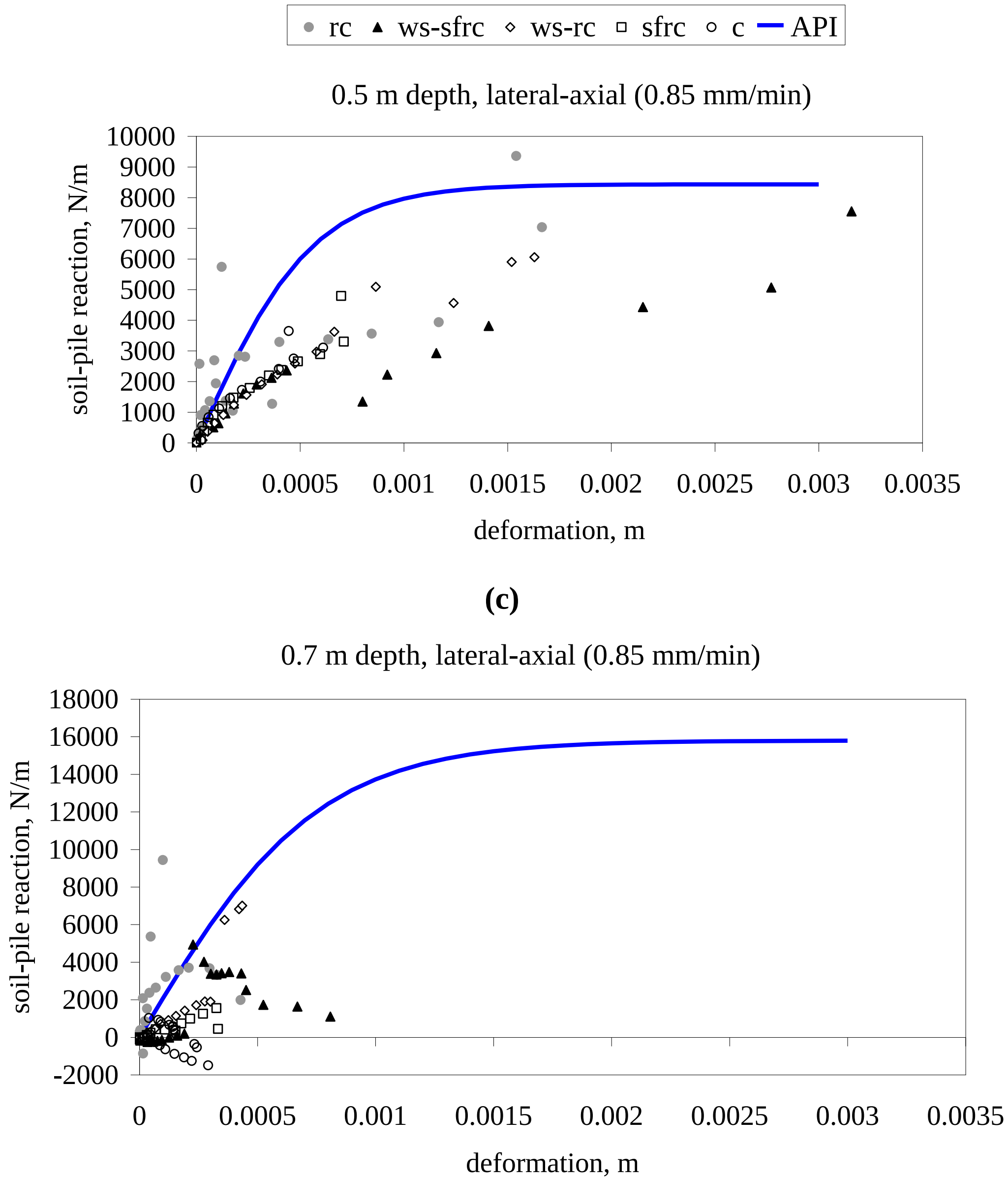

(c)

(d)

Figure 6.6 (c) 0.5 m (d) 0.7 m depths - *continued*

6.3.3 Effect of Axial Loading on p-y Curves

In this section, experimentally derived p-y curves under lateral loading rate of 0.85 mm/min with and without axial loading are compared. The effect of axial load on p-y curves of *rc* and *ws-sfrc* piles are reviewed and compared with the API p-y curves. The effect of axial load on the behavior of the pile has been evaluated in terms of pile head displacement, moment distribution and crack propagation in the *Chapter 5, Section 5.3.3.* In that section, it is concluded that axial load improves the performance of laterally loaded *rc* and *ws-sfrc* piles. Mostafa & El Naggar (2006), showed that existence of the pile cap and axial loading significantly decreases the lateral pile head displacement. A similar finding was achieved in this dissertation as one can see in Figures 5.57 and 5.59. Researchers indicated that axial loading substantially would alter the shear force distribution along the pile. It is stated that ignoring the axial loading at the pile head significantly overestimates the bending moment along the pile shaft.

The p-y curves for two cases are presented in Figure 6.7 and 6.8 for the *rc* and *ws-sfrc* piles respectively. It is found that derived and API p-y curves are quite similar in the initial stage at 0.1 m depth. However, in further stages of the p-y curves based on data behaved differently from API curves. The cracking moment capacity of the lateral-axial loaded *rc* and *ws-sfrc* pile is approximately 28% and 13% higher than the pile tested under only lateral load. As a consequence of this, the *rc* and *ws-sfrc* piles developed plastic hinges early in the test where the piles were loaded only laterally.

The API curve is stiffer than the *rc* pile under only lateral loading condition at 0.3 m depth. The soil-pile reaction at first crack was obtained very low under lateral loading case. In the lateral-axial loading case, the slope of the API curved is in good agreement at 0.3 m depth with the experimental curve of the *rc* pile test. However, *rc* pile cracked before reaching the ultimate soil-pile reaction defined according to the API procedure. The API curve is slightly stiffer than the *ws-sfrc* p-y curve under lateral-axial loading at 0.3 m depth. The first crack took place just before the ultimate soil-pile reaction of the API curve.

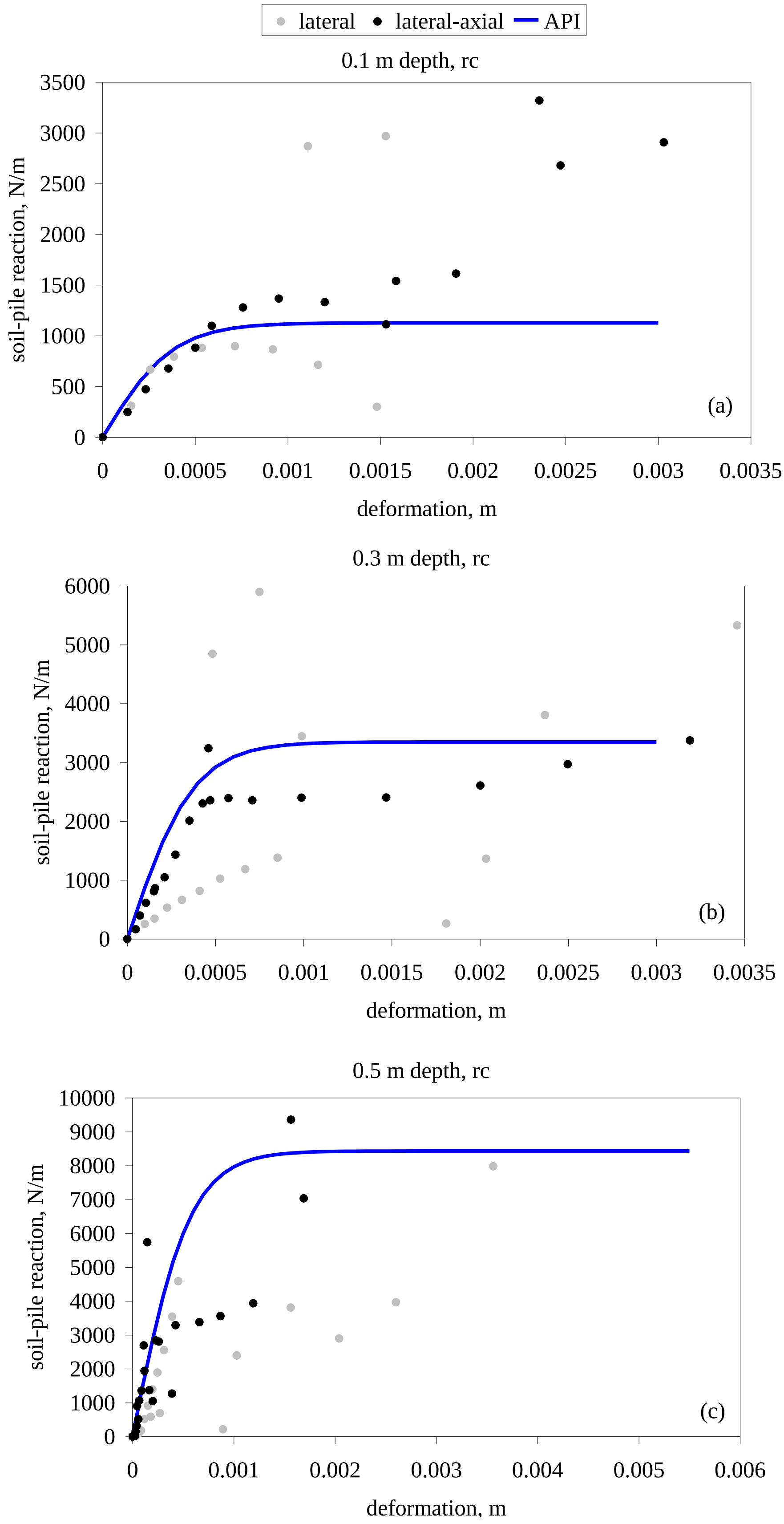

Figure 6.7 Effect of axial loading on p-y curves of *rc* pile (0.85 mm/min)

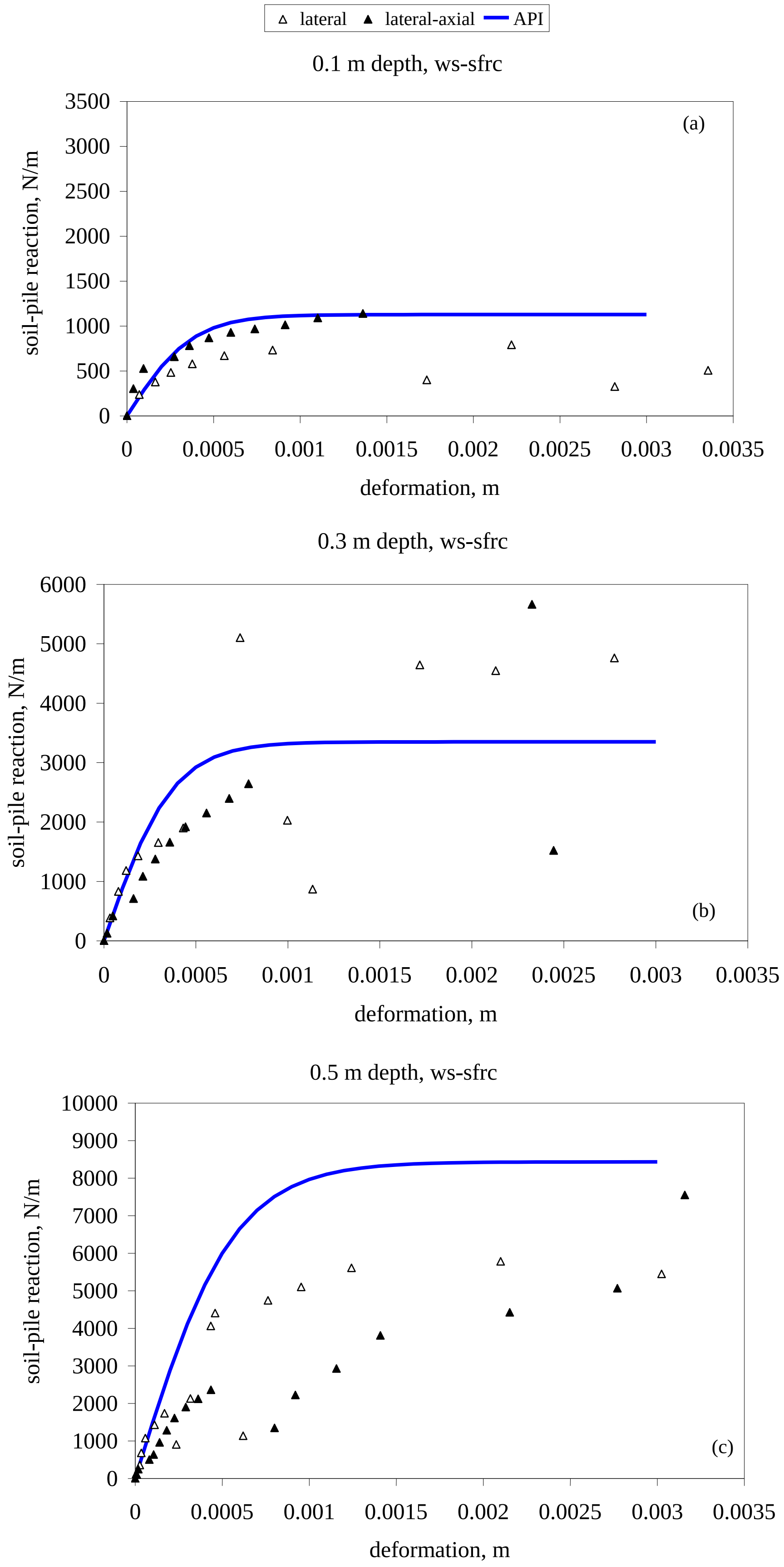

Figure 6.8 Effect of axial loading on p-y curves of *ws-sfrc* pile (0.85 mm/min)

6.3.4 Effect of Loading Rate on p-y Curves

As noted previously in *Section 5.3.4 of Chapter 5,* effect of loading rate on the behavior of the pile was investigated by several researchers. Kraft, Cox, & Verner (1981) studied the effect of the loading rate on the capacity of the vertically loaded single pile in clay. Tests were conducted on full scale piles. Kraft et. al. (1981) indicated that the pile capacity increased with an increase in the loading rate. Researchers stated that higher soil-pile stiffness observed for the faster tests. Al-Mhaidib's (2001; 2004) studies were based on model pile tests in sand and clay under different axial loading rates. Pile head load-deformation curves show that the pile capacity increases with the increase of loading rate in clayey soil (Al-Mhaidib, 2001). Kong & Zhang, (2006) stated that according to model pile lateral loading tests in sand loading rate had a minor effect on the lateral pile resistance at specified displacements, but had a considerable effect on the bending moment distributions and soil reaction distributions. The researchers added that the locations of the maximum bending moment shifted upwards and the reaction at shallow depths increased as the loading rate became higher. It should be noted that these studies were based on the test data of steel model piles or aluminum tubes. In these studies the loading rate effect on pile material and its reflections on p-y curves were not directly investigated. In this respect, this study provides a test data about loading rate effect on pile material and its consequences on the p-y curves for reinforced concrete piles.

Piles were laterally loaded under two different loading rates, 4mm/min and 0.85 mm/min, in order to review the effect of loading rate on the p-y curves. In this respect, the p-y curves of *ws-sfrc* and *rc* model piles were considered. The experimentally derived p-y curves for two cases are presented and compared with the API p-y curves in Figure 6.9 and 6.10.

The p-y curves of conventional reinforced concrete pile under different loading rates show that loading rate has a substantial effect on the p-y curve as can be seen from Figure 6.9. The p-y curves at 0.1 m and 0.3 m depths under loading rate of

4mm/min are stiffer than the p-y curves at 0.85 mm/min loading rate. This trend indicates that soil-pile reaction and soil-pile stiffness considerably increase with an increase in loading rate. The comparison of hinge numbers along the pile show that two times as much hinges took place on the pile at slow loading rate. This is better observed if one compares Figure 5.34 with Figure 5.44.

On the other hand, the p-y curve of the *ws-sfrc* pile indicates that p-y curves are slightly affected from rate of loading (Figure 6.10). The p-y curves of *ws-sfrc* at 0.1 m depth under loading rate of 4mm/min are stiffer than the p-y curves at 0.85 mm/min loading rate. Stiffness of the p-y curve and ultimate soil-pile reaction are close at different loading rates for the depths of 0.3 m and 0.5 m up to first crack moment. It should be noted that at 0.7 m depth soil-pile reaction could be recorded in the test of *ws-sfrc* pile. Although the soil-pile reaction in the initial stage of the p-y curve obtained similar, the soil-pile reaction at first crack under rapid test achieved larger than that obtained in the slow test.

As noted in *Section 5.3.4* of the previous chapter that steel-fiber addition considerably improves impact strength and energy absorption capacity. This is because the p-y curves were obtained quite similar under different loading rates in *ws-sfrc* pile test. It is considered that under different loading rates the behavior of the *ws-sfrc* pile is better than that of the *rc* pile.

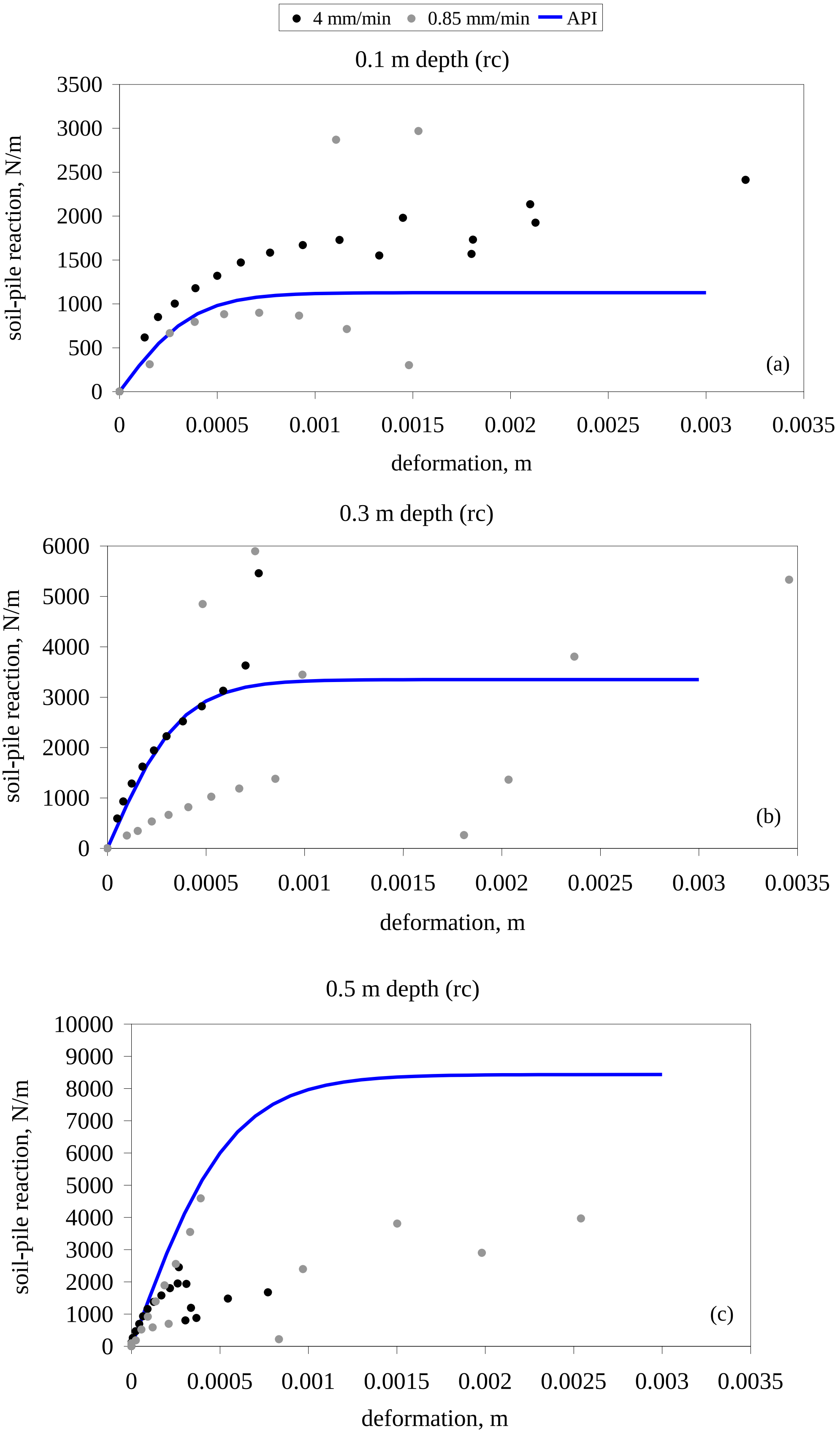

Figure 6.9 Effect of loading rate on p-y curves (a) 0.1 m (b) 0.3 m (c) 0.5 m depths (*rc* pile)

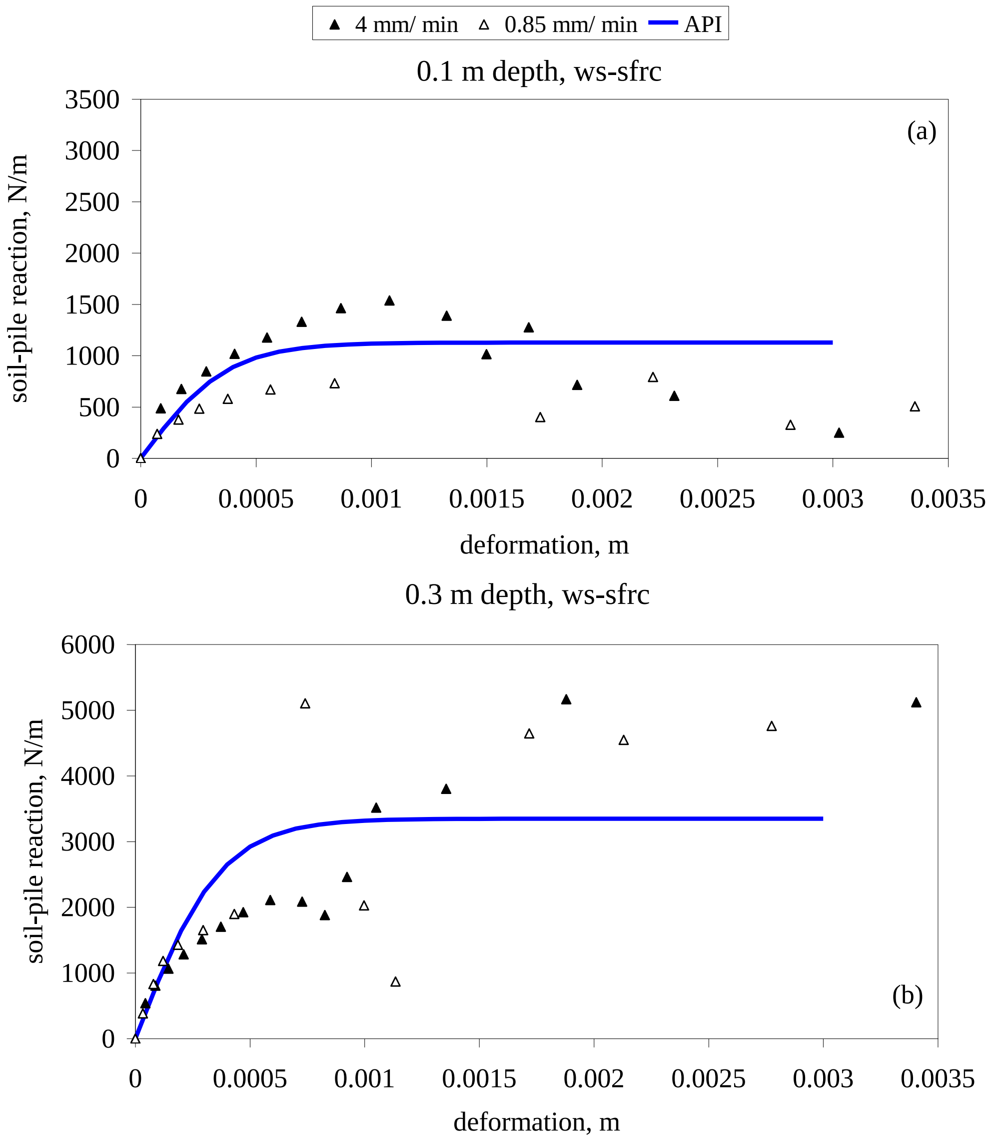

Figure 6.10 Effect of loading rate on p-y curves (a) 0.1 m (b) 0.3 m depths (*ws-sfrc* pile)

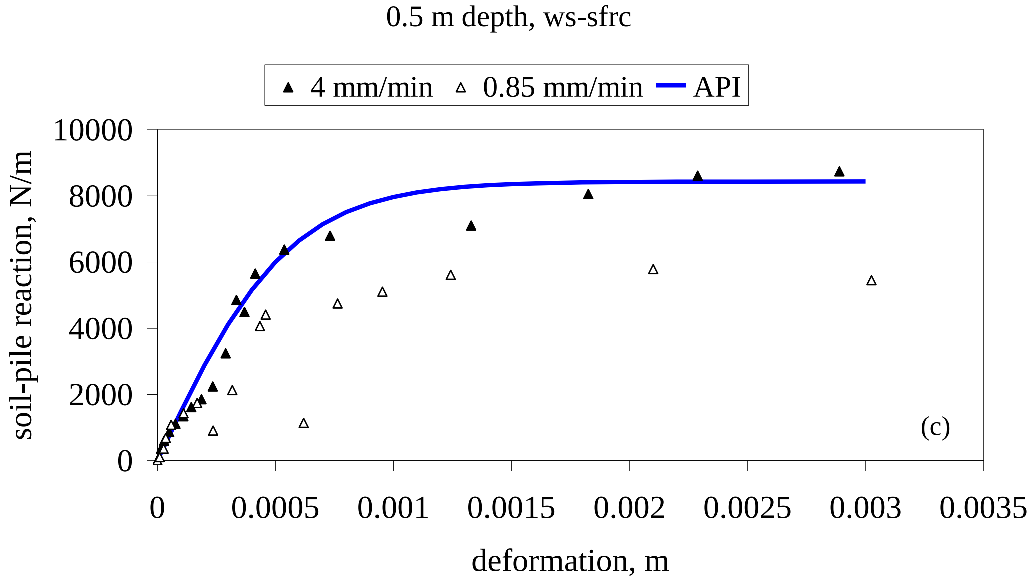

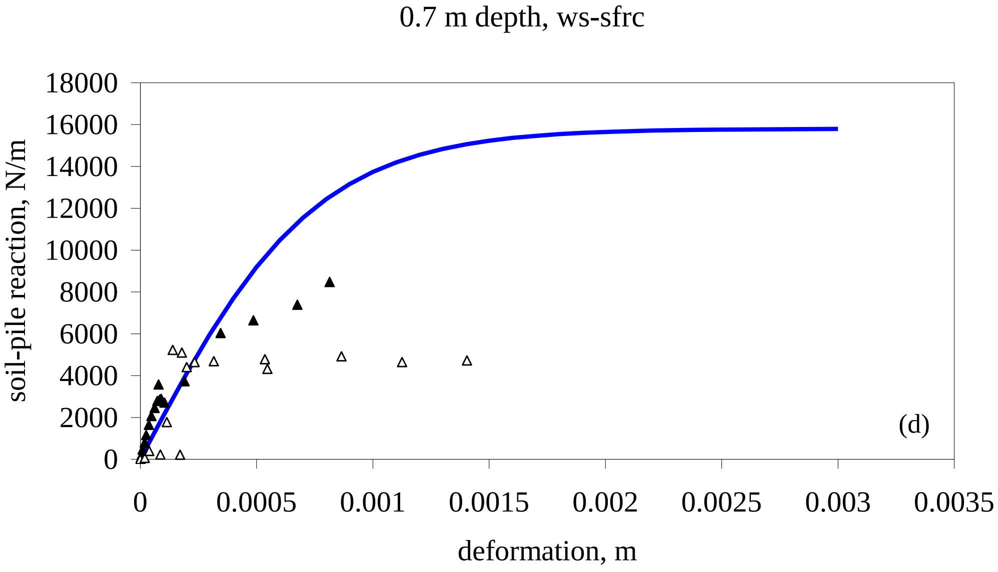

Figure 6.10 (c) 0.5 m (d) 0.7 m depths- *continued*

6.3.5 Recommended p-y Curves for Flexible RC Piles in Medium Dense Sand

It should be noted that agreement between the p-y curves based on test data and p-y curves based on API happened to be quite random. This may be attributed to the fact that the ultimate soil resistance as utilized in the standard p-y models is based on limited field data where steel pipe piles were tested. Similar findings were also reported in the past for laterally loaded model piles where API based p-y curves yielded soil resistance values that were considerably different than those of the experimental curves (Kong & Zhang, 2006; Yan & Bryne, 1992). Effect of pile rigidity on p-y curves are presented in *Chapter 2, Section 2.3.2.* The study of Ashour & Norris (2000) showed that effect of pile material on p-y curve was significant. Hinge development mechanism is an important issue in order to understand the behavior of p-y response of reinforced concrete pile.

The experimental p-y curves reveal that hinge generation has an important role on the soil-pile reaction and pile deformation relationship. Hinge generation mechanism can be expressed as a function of pile and soil properties. Pile width, *B,* and cracking moment, M_{cr}, are the essential pile properties that affect the p-y curves. Angle of internal friction, ϕ, and unit weight of soil, γ, are essential soil properties.

As mentioned *in Section 6.3.1* the correction factor *A* in the proposed API p-y curve establishment procedure fails to capture the ultimate soil resistance and slope of the curve for reinforced concrete piles. It appears that a new approximation is necessary for the adjustment factor *A*. One also needs to incorporate M_{cr} (the cracking moment) into the p-y equation since it was found that test piles structurally failed before the soil reached its ultimate shear strength. Besides, soil-pile interaction was in effect for the model pile tests where flexible piles were tested in medium dense sand. One might expect that the limit state soil parameters would not be sufficient in defining the ultimate soil resistance since the bending stiffness would highly affect the soil reaction against the pile, a fact long been noticed for the distribution of contact pressure beneath spread foundations.

For this purpose, back calculation method was used to estimate the factor *A* from the experimentally derived p-y curves of piles. A relation was developed between the factor *A* and *z/B*, where *z* denotes the depth from the soil surface (Figure 6.11 to Figure 6.15). After the development of the new *A* factor, M_{cr} is incorporated into the p-y curve formulation.

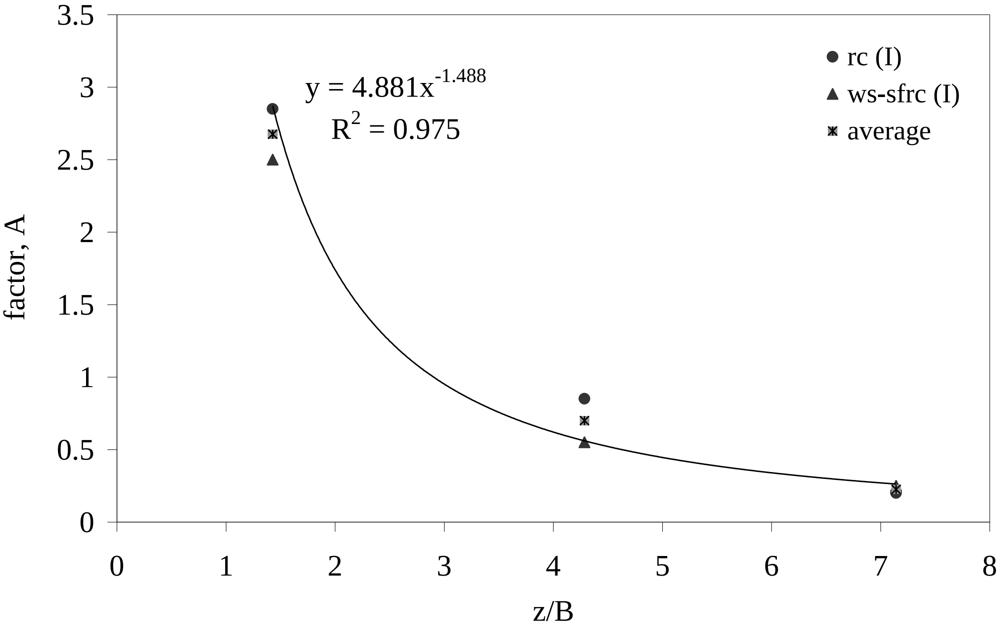

Figure 6.11 Factor *A* and z/B relation, (I): lateral loading, 4mm/min, rc and ws-sfrc piles

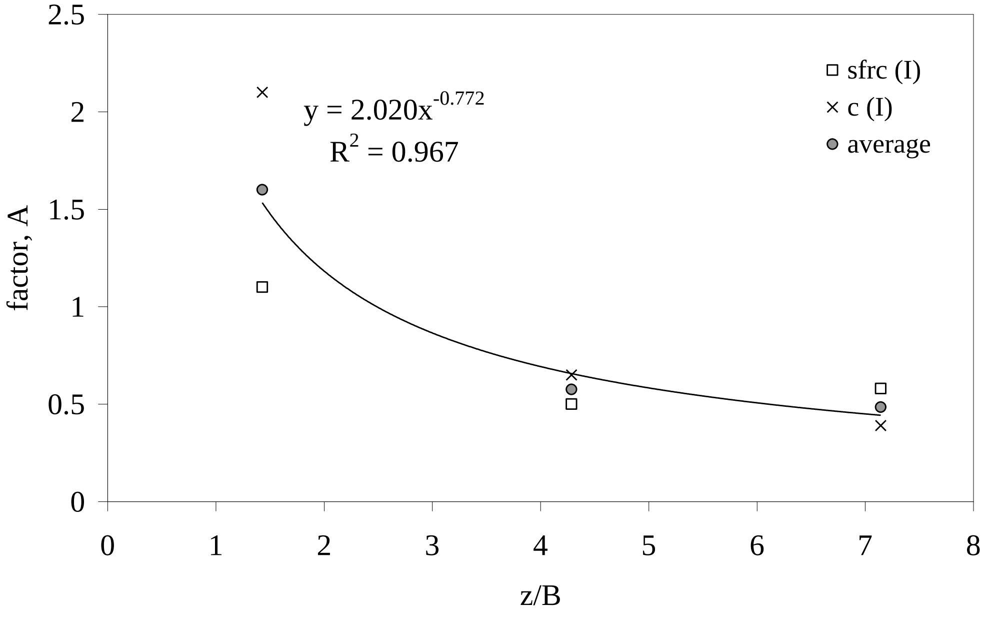

Figure 6.12 Factor *A* and z/B relation, (I): lateral loading, 4mm/min, *sfrc* and *c* piles

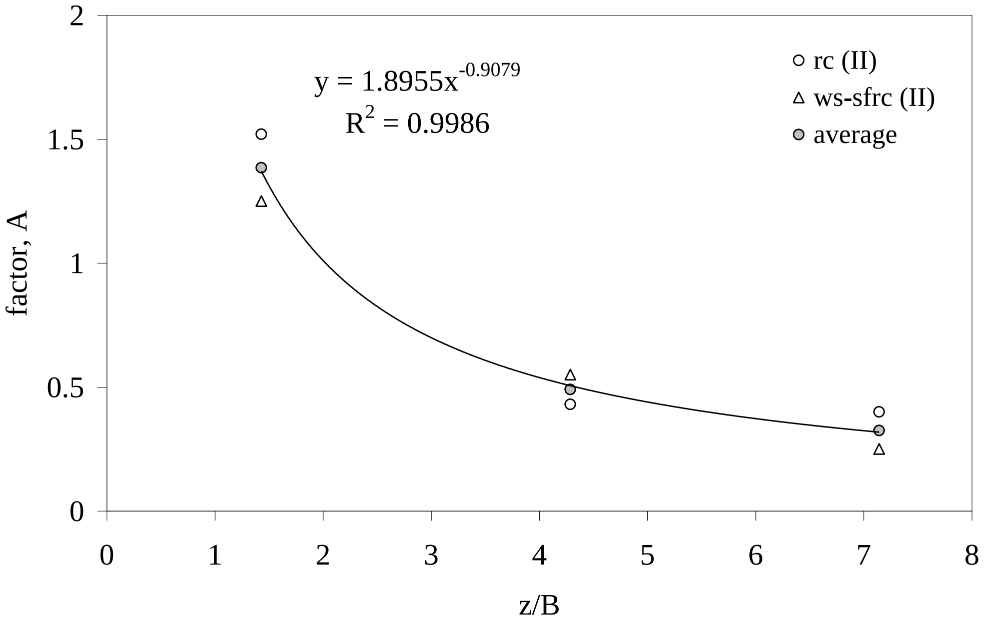

Figure 6.13 Factor *A* and z/B relation (II): lateral loading, 0.85 mm/min, *rc* and *ws-sfrc* piles

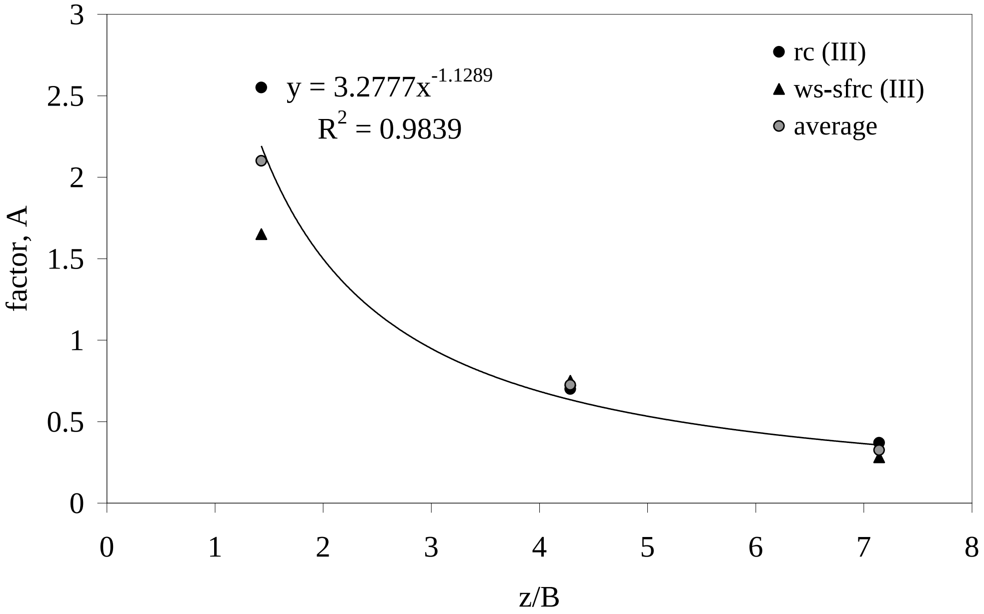

Figure 6.14 Factor *A* and z/B relation, (III): lateral-axial loading, 0.85 mm/min, *rc* and *ws-sfrc* piles

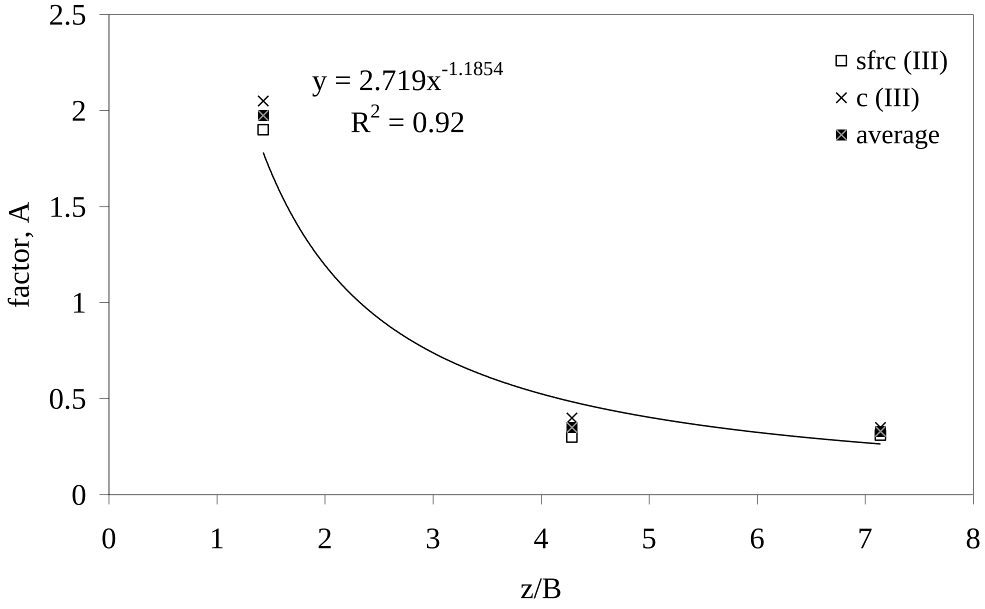

Figure 6.15 Factor *A* and z/B relation, (III): lateral-axial loading, 0.85 mm/min, *c* and *sfrc* piles

In the second step a relationship was developed between the ultimate bearing capacity, p_u, and the cracking moment, M_{cr}. Ultimate bearing capacity was obtained for the specific depths, 0.1 m, 0.3 m, and 0.5 m, according to API recommendation. The ultimate lateral bearing capacity for sand is obtained at shallow depths according to Equation 6.7.

$$p_u = (C_1 \cdot z + C_2 \cdot B) \cdot \gamma \cdot z \qquad 6.7$$

where

p_u = ultimate bearing capacity (force/ unit length), (N/m),

γ = unit weight of soil (N/m^3),

z = depth, (m)

φ = angle of internal friction of sand, in degrees

C_1, C_2= coefficients determined from Figure 6.16 as a function of ϕ,

B = pile width (m)

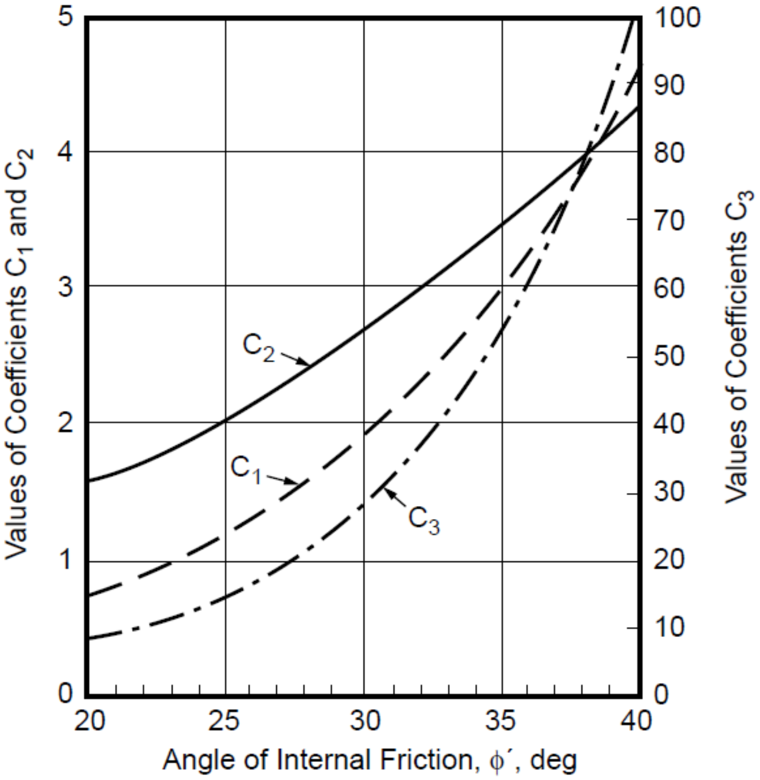

Figure 6.16 Coefficient as function of angle of internal friction (API, 2000)

A relation was developed between p_u/M_{cr} and z/B as for two different loading conditions shown in Figure 6.17 and Figure 6.18.

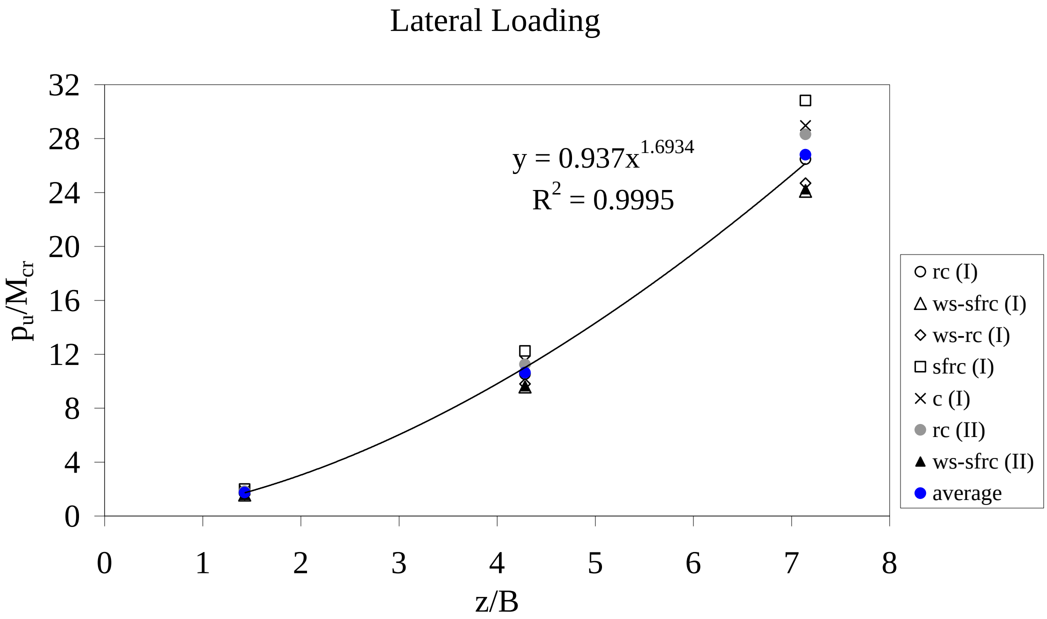

Figure 6.17 p_u/M_{cr} and z/B relation under lateral loading

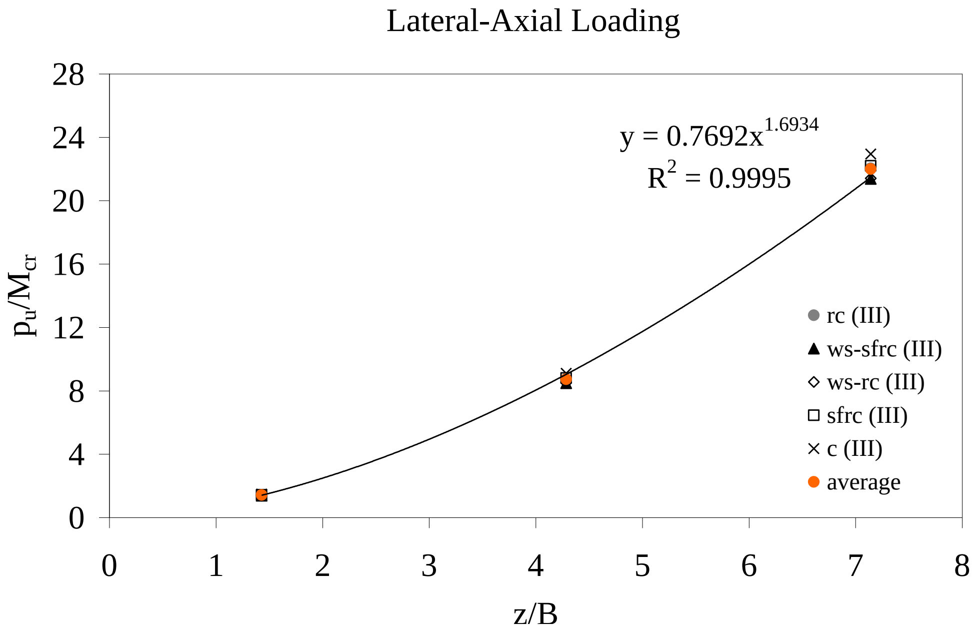

Figure 6.18 p_u/M_{cr} and z/B relation under lateral-axial loading

The obtained relationships of *A* and p_u parameters are presented in Table 6.1. The lateral soil/pile reaction-deformation (p-y) relationships of reinforced concrete piles in medium sand can be approximated at any specific depth z, by the following expression;

$$P = A \cdot p_u \cdot \tanh\left[\frac{k \cdot z}{A \cdot p_u} \cdot y\right] \quad 6.8$$

Where

A= factor to account for cyclic or static loading condition,

k= initial modulus of subgrade reaction determined from Figure 6.19 (N/m^3),

y = lateral deformation (m)

M_{cr} = cracking moment (Nm)

The p-y curves of *ws-sfrc* and *rc* piles under lateral loading (4mm/min) based on the above proposed model are compared with the curves based on test data as can be seen in the following Figure 6.20 to Figure 6.27. The remaining curves are shown in Appendix-C. The p-y curves established with respect to the recommended model are found as satisfactory in representing experimental p-y curves up to M_{cr}.

Table 6.1 The relationships of A and p_u parameters

Loading Condition	Loading Rate	Model pile	Adjustment factor, A	Ultimate soil-pile resistance, p_u
Lateral loading	*Rapid* *(4mm/min)*	**rc & ws-sfrc**	$A = 4.881 \cdot \left(\frac{B}{z}\right)^{1.488}$	$p_u = 0.937 \cdot \left(\frac{z}{B}\right)^{1.6934} \cdot M_{cr}$
		c & sfrc	$A = 2.020 \cdot \left(\frac{B}{z}\right)^{0.772}$	
	Slow *(0.85mm/min)*	**rc & ws-sfrc**	$A = 1.896 \cdot \left(\frac{B}{z}\right)^{0.9079}$	
Lateral-Axial loading	*Slow* *(0.85mm/min)*	**rc & ws-sfrc**	$A = 3.278 \cdot \left(\frac{B}{z}\right)^{1.1289}$	$p_u = 0.769 \cdot \left(\frac{z}{B}\right)^{1.6934} \cdot M_{cr}$
		c & sfrc	$A = 2.719 \cdot \left(\frac{B}{z}\right)^{1.1854}$	

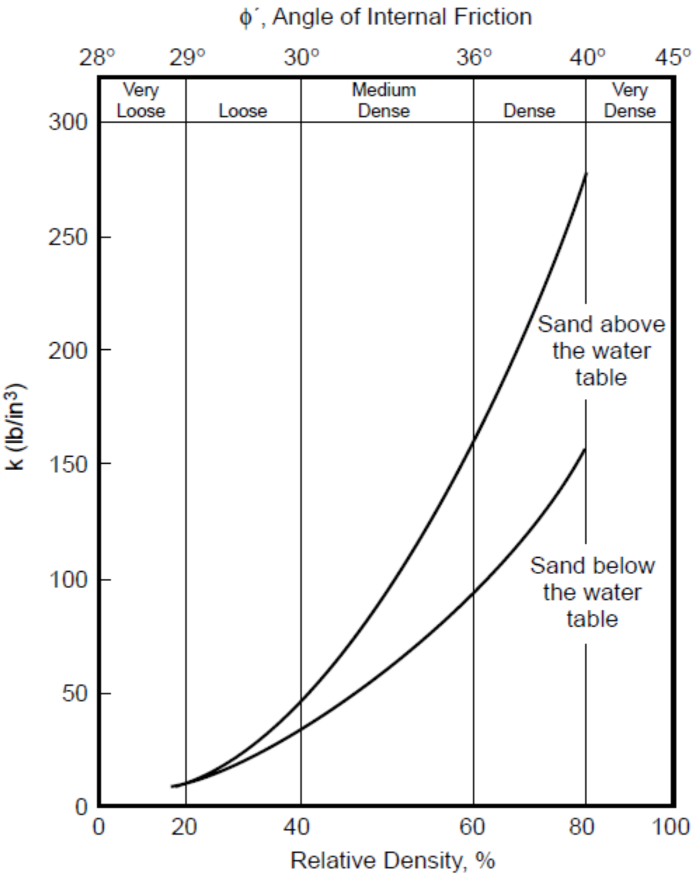

Figure 6.19 Initial modulus of subgrade reaction (API, 2000)

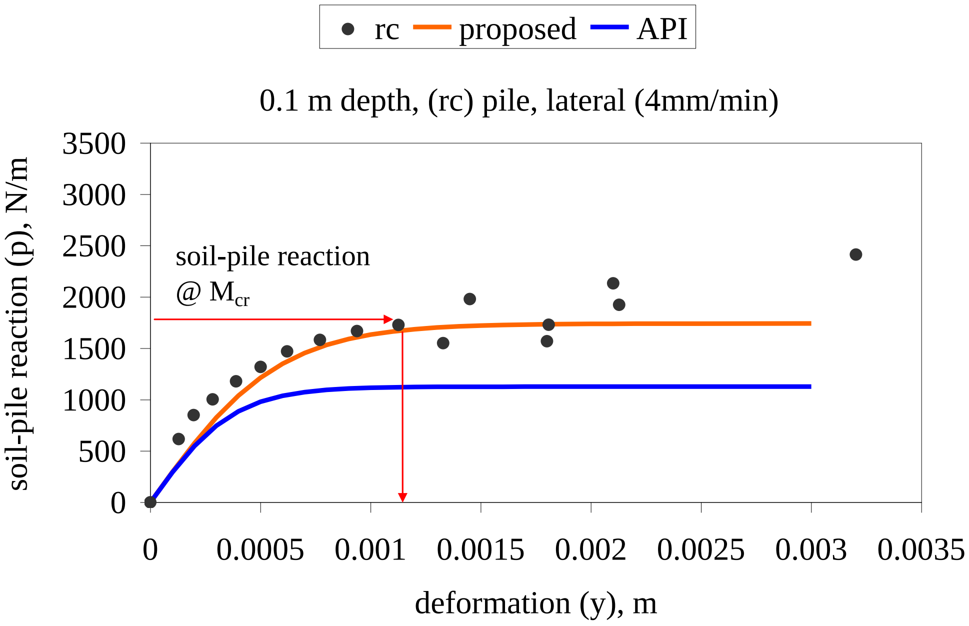

Figure 6.20 Comparison of proposed and experimental p-y curves, rc pile, 4mm/min at 0.1 m depth

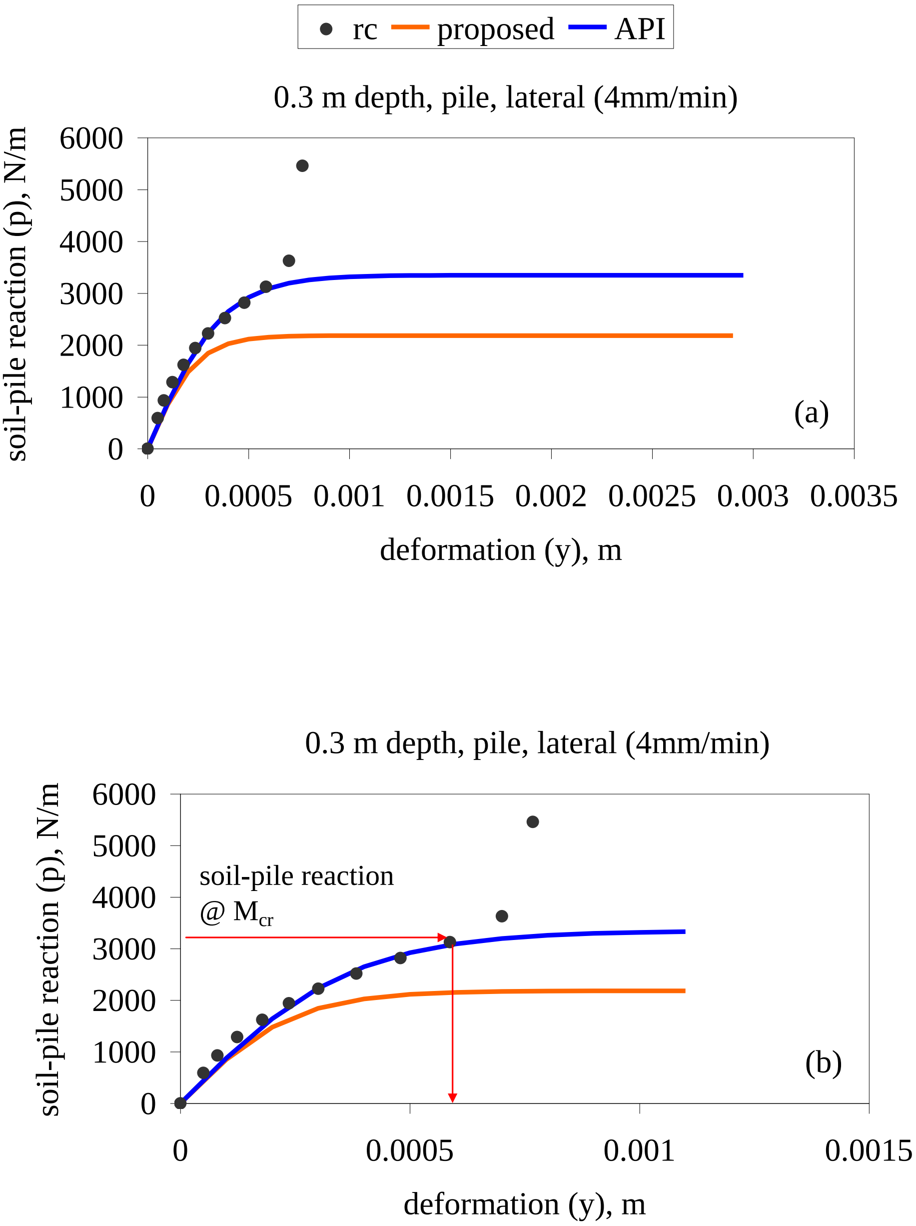

Figure 6.21 Comparison of proposed and experimental p-y curves, *rc* pile, 4mm/min at 0.3 m depth (a) over-all p-y (b) p-y between 0-0.0015 m

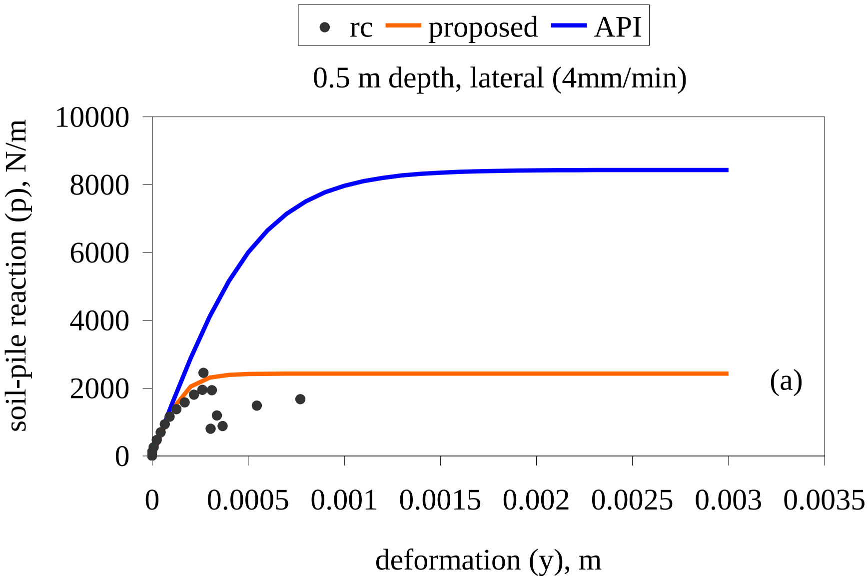

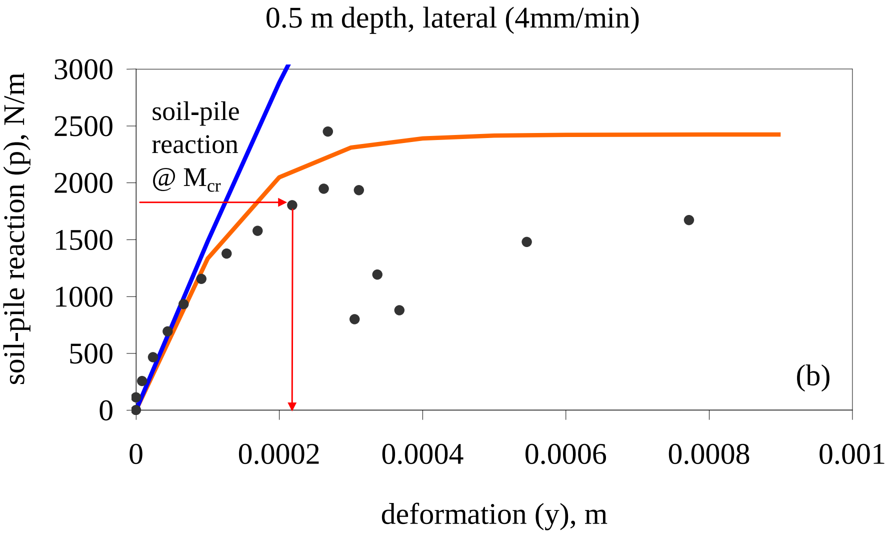

Figure 6.22 Comparison of proposed and experimental p-y curves, *rc* pile, 4mm/min at 0.5 m depth (a) over-all p-y (b) p-y between 0-0.001 m

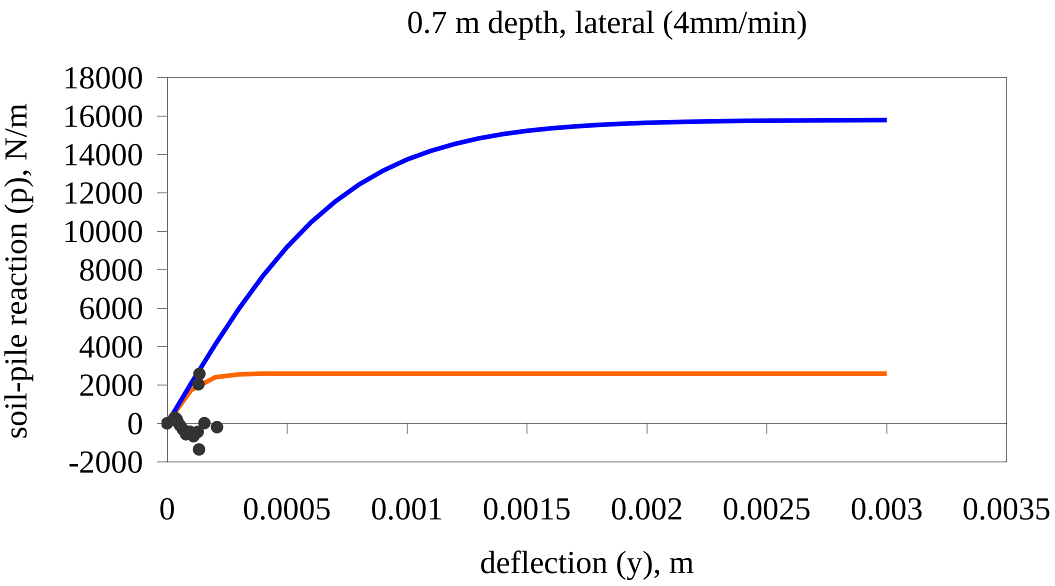

Figure 6.23 Comparison of proposed and experimental p-y curves, *rc* pile, 4mm/min at 0.7 m depth

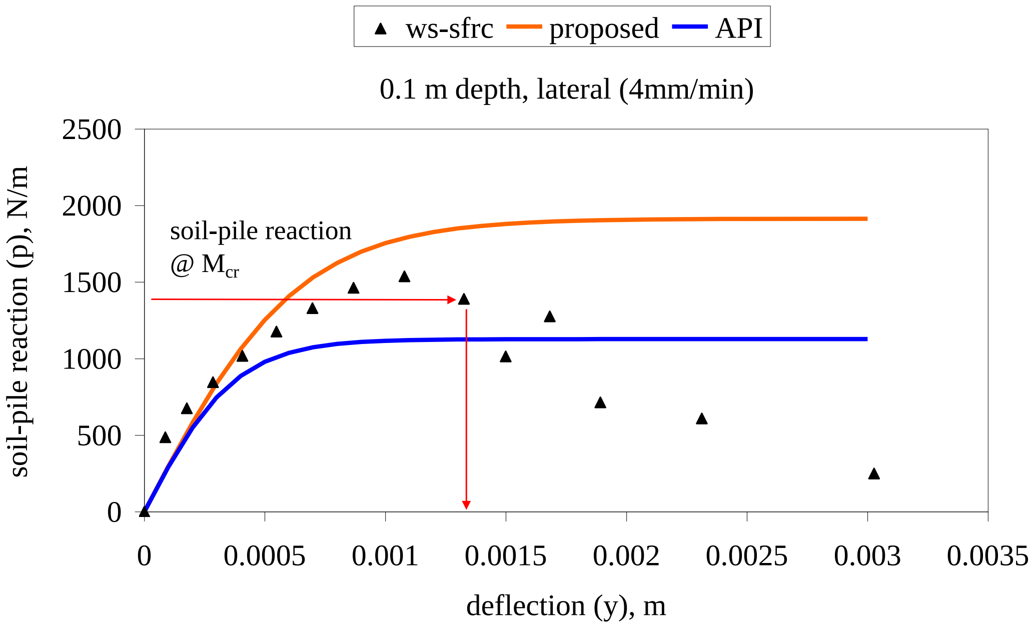

Figure 6.24 Comparison of proposed and experimental p-y curves, *ws-sfrc* pile, 4mm/min at 0.1 m depth

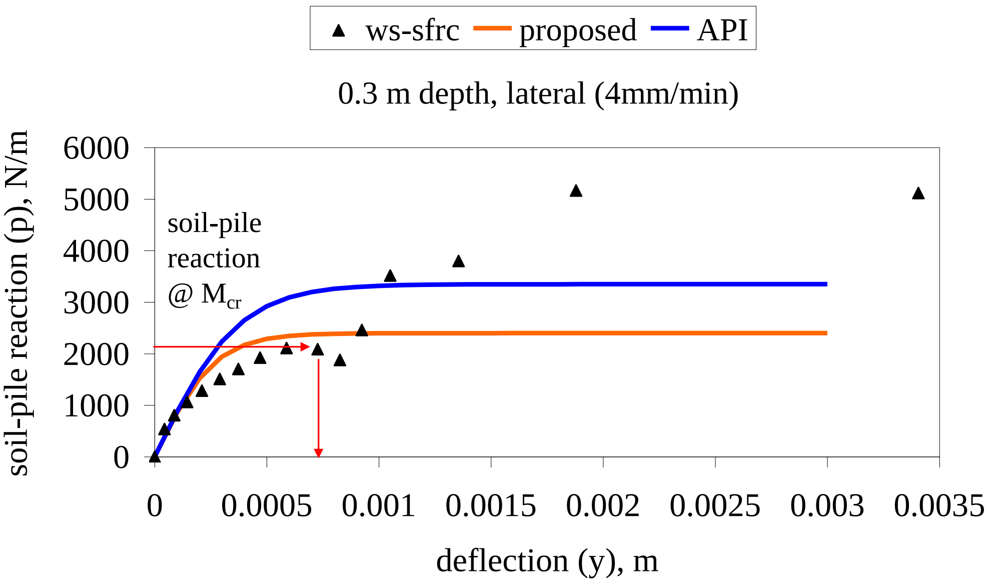

Figure 6.25 Comparison of proposed and experimental p-y curves, *ws-sfrc* pile, 4mm/min at 0.3 m depth

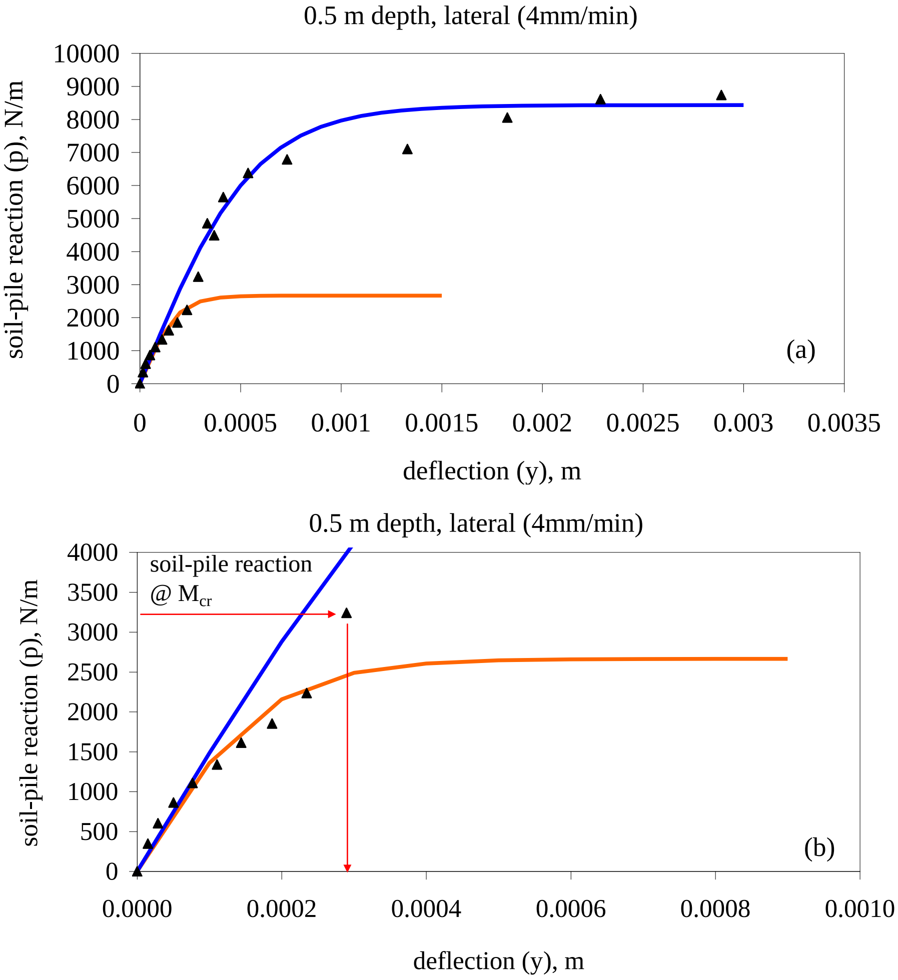

Figure 6.26 Comparison of proposed and experimental p-y curves, *rc* pile, 4mm/min at 0.5 m depth (a) over-all p-y (b) p-y between 0-0.001 m

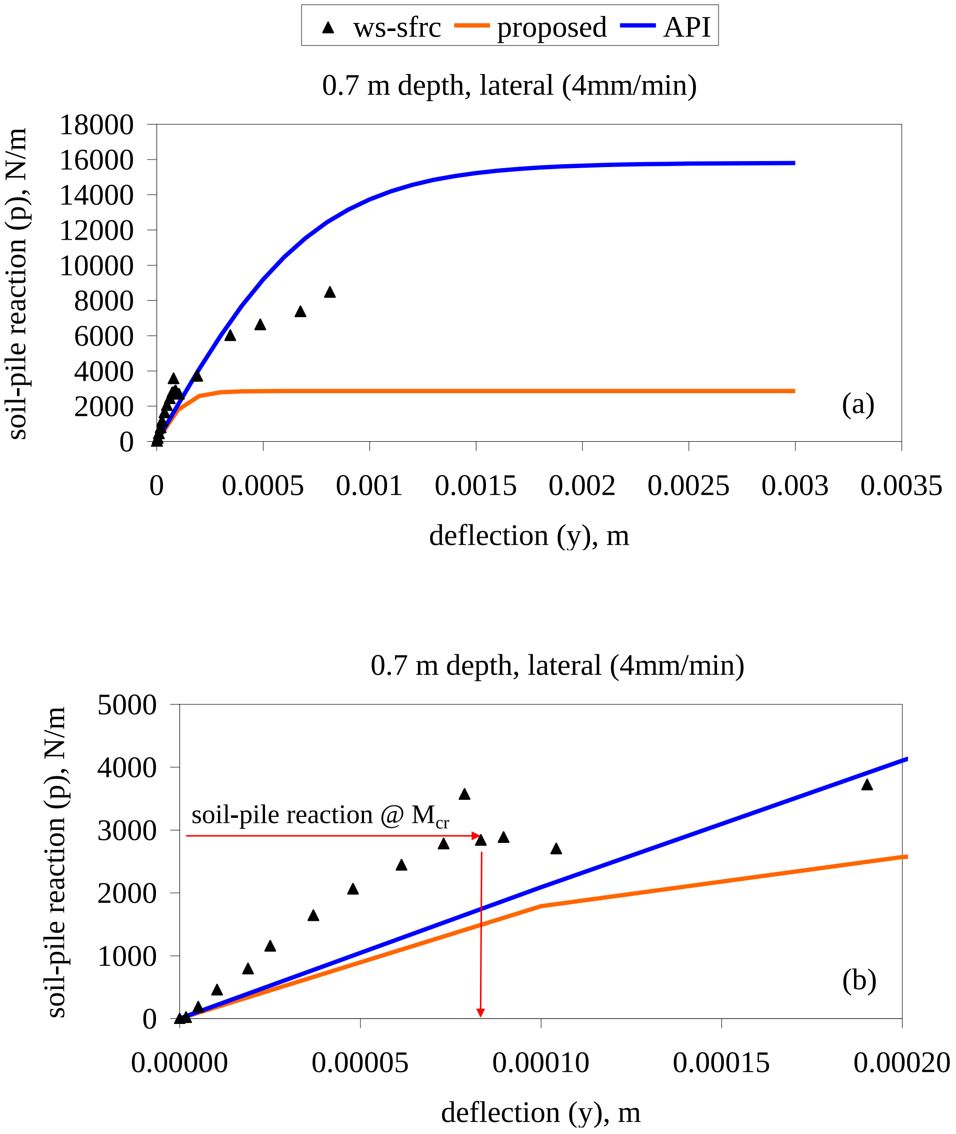

Figure 6.27 Comparison of proposed and experimental p-y curves, *rc* pile, 4mm/min at 0.7 m depth (a) over-all p-y (b) p-y between 0-0.0002 m

CHAPTER SEVEN

CONCLUSIONS AND RECOMMENDATIONS

Behavior of laterally loaded reinforced concrete model piles in medium dense sand was investigated in this study. Emphasis was given to the soil-pile interaction aspects of RC piles with steel fibers. Experimental data were acquired on nonlinear behavior of model RC piles. Influence of steel fibers on pile response was especially studied. The study enabled observation of loading rate effects and influence of axial load and steel fiber on soil-pile interaction. A new methodology to improve the industry standard American Petroleum Institute (API) load-deformation (p-y) curve establishment method is suggested to incorporate influence of nonlinear material behavior on p-y curves. Findings of this dissertation study are summarized and conclusions are made along with the recommendations for future studies in below paragraphs:

Several model piles made of conventional reinforced concrete (“*rc*”), reinforced concrete with only bending reinforcement and steel fibers (“*ws-sfrc*”), reinforced concrete with only bending reinforcement (“*ws-rc*”), concrete (“*c*”) and steel fiber reinforced concrete (“*sfrc*”) were tested. The following factors were investigated while studying lateral load response of the model piles:

- Pile head load-deformation relation and first crack load capacity
- Moment distribution along the pile and cracking moment capacity
- Crack distribution and hinge development
- Lateral load-deformation (p-y) curves
- Effect of axial load on the behavior of laterally loaded pile
- Effect of loading rate on the response of laterally loaded pile

Comparison of different types of model piles on the basis of above given factors resulted in the following conclusions:

- It is determined in the bending test of the flexural elements that the ductility factor of the *ws-sfrc* specimen is 100% higher than that of the *rc* beam.

- It is concluded that under different lateral loading rates the behavior of the *ws-sfrc* pile is better than that of the *rc* pile. The *ws-sfrc* pile was not negatively affected by the loading rate whereas the *rc* pile was intensely cracked especially in the slow rate test.

- In all loading conditions cracking moment capacity of the *ws-sfrc* pile was obtained higher than the *rc* pile and *ws-rc* pile.

- In all loading conditions the *ws-sfrc* pile head load-deformation relation was obtained quite similar to the *rc* pile.

- The *ws-sfrc* pile behavior is superior to the *rc* pile under axial loading.

- Ultimate moment capacity of the *sfrc* pile is considerably higher than the concrete pile.

- The *sfrc* pile demonstrated higher energy absorbing capacity with respect to the concrete pile under lateral and lateral-axial loading cases.

- The test results demonstrate that axial load improves significantly the performance of the *rc* and *ws-sfrc* piles. Axial loading considerably alters the moment distribution, pile head lateral load reaction, cracking moment and crack propagation for these piles.

- It was noticed while deriving experimental p-y curves that application of the recorded bending moment data in incremental steps, a technique similar to the so-called pushover analysis methodology, enabled a closer approximation to the nonlinear moment-curvature of the tested piles. This was reflected in better representation of the recorded pile head displacements. It is concluded that nonlinear pushover technique is more reliable than linear and bilinear analyses where bending stiffness of the pile is either kept constant or arbitrarily reduced to a pre-assumed value in the nonlinear pile behavior region.

- It is concluded that axial load significantly increases the soil-pile stiffness of the *rc* pile.

- It is also obtained that rate of loading significantly alters the p-y curve of the *rc* pile whereas it slightly influences the p-y curve of *ws-sfrc*.

- The test results of the *ws-sfrc* pile show that loading rate changed the behavior of the pile in terms of pile head load-displacement and moment distribution. It also changed movement of the soil mass at the surface in the *ws-sfrc* pile tests. However, the crack propagation, deformed shape after the test, cracking moment and moment distribution after the first crack were obtained quite similar in the rapid and slow tests for the *ws-sfrc* model pile. It is considered that steel fibers improved pile response by means of crack arresting mechanism. Although confinement effect of the shear reinforcement is not pronounced for steel fibers, their rather homogenous distribution inside the concrete matrix is thought to act against shear and bending forces.

- The *ws-sfrc* pile is more flexible as compared with *ws-rc* piles since they can exhibit smaller displacements at the same measured load with fewer disturbances. It is considered that reinforced concrete pile without shear stirrups would only be possible by the use of steel fibers.

- Test results of *c* and *sfrc* model piles verified that steel fiber addition affected hinge occurrence and p-y curve response.

- The *sfrc* piles with 1.0% and 1.5% steel fiber failed with double hinges. The soil–pile interaction affected *sfrc* model pile response by means of side friction stresses acting along the pile surface thereby reducing pull-out stresses on steel fibers.

- Positive influence of soil side friction on fiber pull-out stresses has resulted in the occurrence of a second hinge on the remaining portion of the pile above the first hinge for piles with steel fiber content 1% and 1.5%.

- It can be noticed in the *sfrc* pile tests that the slope of the experimental p–y curves belonging to the short pile segment above the first hinge location remarkably increased indicating rigid pile behavior.

- The p-y curve obtained by means of 3D finite element analyses of the concrete model test was found to be in good agreement with experimental p-y curves. One should note API method does not simulate observed pile behavior.

- The p-y curves of conventional reinforced concrete pile under different loading rates show that loading rate has a substantial effect on the p-y curve.

- Experimental p-y curves demonstrate double peaks as if they consist of two distinct curves especially for depths 0.3 m and 0.5 m below the sand surface. This is not valid for 0.1 m depth where a single traditional p-y curve exists. It is considered that at shallow depths the sand failed whereas at deeper depths the pile cracked and loaded the soil in a different manner as described in the below paragraphs.

- The flexibility of the reinforced concrete pile has a substantial influence on soil-pile interaction. It is considered that the cracking moment and M-EI relationship dictate first peak of a p-y curve rather than the ultimate soil resistance for flexible RC piles. The p-y curves established with respect to the API (American Petroleum Institute) procedure are found as usually unsatisfactory in representing experimental p-y curves. It is found that API method fits well to the experimental data near sand surface where effective stress is low enough resulting in the failure of the sand. However, API methodology is usually not capable of representing the data at deeper depths where there are two peaks in p-y data.

- A new methodology to improve the industry standard API procedure is suggested to incorporate pile flexibility parameters into the p-y curve formulation. The traditionally defined ultimate soil resistance of the API procedure is adjusted as a function of soil depth, pile width and cracking moment. The p-y curves generated according to the suggested procedure successfully produced the experimental curves until the first peak beyond which the pile behaves as a shorter pile segment generating a stiffer portion in the p-y curve. It appears that multiple hinge formation is influential on load-deformation response.

- Further research including large scale lateral load tests on prototype piles is necessary in order to test applicability of the proposed p-y curve generation methodology.

- There is a need for a comprehensive structural testing program to develop axial load-moment interaction (N-M) diagrams for reinforced concrete structural piles with steel fibers.

REFERENCES

Abendroth, E.R., & Greimann, L.F. (1990) Pile Behavior Established From Model Tests. *Journal of Geotechnical Engineering, ASCE,* 116, 571-588.

Adhikary, B. B., & Mutsuyoshi, H. (2006). Prediction of Shear Strength of Steel Fiber RC Beams Using Neural Networks. *Construction and Building Materials, 20,* 801-811.

Akdağ, C.T. (2004). *A Modeling Study on the Lateral Load Capacity of Steel-Fiber Concrete Piles*. M.Sc Thesis. İzmir, Dokuz Eylül University.

Al-Mhaidib, A. I. (2001). Loading Rate Effect on Piles in Clay from Laboratory Model Tests. *Journal of King Saud University (Engineering Sciences),* 13, 39-55.

Al-Mhaidib, A. I. (2004). Effect of Loading Rate on Pile Groups in Sand. *In Proceedings of International Conference on Geotechnical Engineering*, Sharjah, Uniated Arap Emirates (UAE).

American Concrete Institute Committee (ACI). (1996). *State of the Art Report on Fiber Reinforced Concrete, ACI 544.1R-96*. United States of America: American Concrete Institute.

American Petroleum Institute (API). (2000) *Recommended Practice for Planning, Desingning and Constructing Fixed Offshore Platforms,* API-RP2A-WSD (21th Edition). Washington, D.C.: American Petroleum Institute.

American Society for Testing and Materials. (1997). ASTM C1018, Standard Test Method for Flexural Toughness and First-Crack Strength of Fiber-Reinforced Concrete_Using Beam with Third-Point Loading. *Annual Book of ASTM Standards*, West Conshohocken, PA: ASTM International.

Ashour, M., & Norris, G.M. (1998). Lateral Loading of a Pile in Layered Soil using the Strain Wedge Model. *Journal of Geotechnical and Geoenvironmental Engineering, ASCE, 124*, 303-315.

Ashour, M., & Norris, G.M. (2000). Modeling Lateral Soil-Pile Response Based on Soil-Pile Interaction. *Journal of Geotechnical and Geoenvironmental* Engineering, ASCE, 126, 420-428.

Ashour, S. A. (2000) Effect of Compressive Strength and Tensile Reinforcement Ratio on Flexural Behavior of High-Strength Concrete *Beams. Engineering Structures, 22,* 413-423.

Ashour, M., Norris, G., & Pilling,P. (2002) Strain Wedge Capability of Analyzing Behavior of Laterally Loaded Isolated Piles, Drilled Shafts, and Pile Groups. *Journal of Bridge* Engineering, ASCE, 7, 245-256.

Ashour, M., Norris, G.M., & Shamsabadi, A. (2001) Effect of the Non-Linear Behavior of Pile Material on the Response of Laterally Loaded Piles. *Proceeding, 4th International Conference on Recent Advances in Geotechnical Earthquake Engineering and Soil Dynamics* (Paper 6.10). Calfornia.

Ashour, S. A., Wafa, F. F., & Kamal, M. I. (2000). Effect of the Concrete Compressive Strength and Tensile Reinforcement Ratio on the Flexural Behavior of Fibrous Concrete Beams. *Engineering Structures, 22*, 1145-1158.

Ashour, M., Pilling P., & Norris, G. (2004) Lateral Behavior of Pile Groups in Layered Soils. *Journal of Geotechnical and Geoenvironmental Engineering, 130,* 580-592.

Baguelin, F., Frank,R., & Said, Y.H., (1977). Theoretical Study of Lateral Reaction Mechanism of Piles. *Géotechnique, 27*, 405-434.

Banthia, N.,Yan,C, & Bindiganavile. (2000). Development and Application of High Performance Hybrid Fiber Reinforced Concrete. In Rossi, P., & Chanvillard, G. (Eds.). *Fibre-Reinforced Concretes (FRC) Proceedings of the Fifth RILEM Symposium* (471-480). Lyon: RILEM Publications.

Barakat, S.A., & Altoubat, S. (2010) Concrete Welding Using Steel Fibers. *Engineering Structures, 32*, 2065-2073.

Barros, J. A. O., & Figueiras, J. A. (1999). Flexural Behavior of SFRC: Testing and Modelling. *Journal of Materials in Civil Engineering*, *11*, 331-339.

Bayasi, Z., & Downey, K., (1995). Steel Fiber Reinforced Piles at Horse Mesa Dam. *Concrete International, 17*, 32-36.

Bayasi, Z., & Zeng, J. (1997) Flexural Behavior of Slurry Infiltrated Mat Concrete (SIMCON). *Journal of Materials in Civil Engineering*, *9* (4), 194-199.

Bransby, M. F. (1999). Selection of p-y Curves for the Design of Single Laterally Loaded Piles. *International Journal for Numerical and Analytical Methods in Geomechanics,* 23(15), 1909-1926.

Briaud, J.L., & Garland, E. (1985). Loading Rate Method for Pile Response in Clay. *Journal of Geotechnical Engineering, ASCE,* 111, 319-335.

Brodbaek, K. T., Moller, M., Sorensen S. P. H., & Augustesen A. H. (2009). *Review of p-y Relationships in Cohesionless Soil. DCE Technical Report*. Denmark: Aalborg University.

Broms, B.B. (1964-a). Lateral Resistance of Piles in Cohesive Soils. *Journal of the Soil Mechanics and Foundations Division, ASCE, 90,* 26-63.

Broms, B.B. (1964-b). Lateral Resistance of Piles in Cohesionless Soils. *Journal of the Soil Mechanics and Foundations Division, ASCE, 90*, 123-156.

Brown, D. A., Morrison, C., & Reese, L.C. (1989). Lateral Load Behavior of Pile Group in Sand. *Journal of Geotechnical Engineering, 114*, 1261-1277.

Brown, D., Shie, C., & Kumar, M. (1989). P-Y Curves for Laterally Loaded Piles Derived from Three Dimensional Finite Element Model. S. Pietruszczazk & N. Pande, (Eds.). *Proceedings of the Third International Symposium on Numerical Models in Geomechanics (NUMOG III), Niagara Falls,* (683-690). Canada: Elsevier Applied Science.

Buyle-Bodin, F., & Madhkhan, M., (2002). Performance and Modelling of Steel Fibre Reinforced Piles Under Seismic Loading. *Engineering Structures, 24*, 1049-1056.

Campione, G., & Mangiavillano, M. L. (2008). Fibrous Reinforced Concrete Beams in Flexure: Experimental Investigation, Analytical Modelling and Design Considerations. *Engineering Structures, 30,* 2970-2980.

Chadwell, C. B., & Imbsen, R.A., (2004). XTRACT- *Cross Section Analysis Software for Structural and Earthquake Engineering*. 15 October 2010 http:// www.imbsen.com/xtract.htm.

Chai, Y. H., & Hutchinson, T. C. (2002) Flexural Strength and Ductility of Extended Pile-Shafts. II: Experimental Study. *Journal of Structural Engineering, 128,* 595-602.

Choi, O. C., & Lee, C. (2002). Flexural Performance of Ring-Type Steel Fiber-Reinforced Concrete. *Cement & Concrete Research, 33,* 841-849.

Chunxiang, Q., & Patnaikuni, I. (1999). Properties of High-Strength Steel Fiber-Reinforced Concrete Beams in Bending. *Cement and Concrete Composites, 21,* 73-81.

Cox, W. R., Reese, L. C., & Grubbs, B. R. (1974). Field Testing of Laterally Loaded Piles in Sand. *Proceedings of the Offshore Technology Conference* (459-472) Houston, Texas.

Cucchiara, C., La Mendola, L., & Papia M. (2004). Effectiveness of Stirrups and Steel Fibres as Shear Reinforcement. *Cement and Concrete Composites, 26*, 777-786.

Dancygier, A. N., & Savir, Z. (2006). Flexural Behavior of HSFRC with Low Reinforcement Ratios. *Engineering Structures, 28,* 1503-1512.

Dickin, A.E., & Nazir, R. (1999) Moment-Carrying Capacity of Short Pile Foundations in Cohesionless Soil. *Journal of Geotechnical and Geoenvironmental Engineering*, 125, (1), 1–10.

Dijkstra, J. (2004). Influence of Loading Rate on Pile Capacity in Unsaturated Sand. MSc Thesis. Nederland, Delph University of Technology.

Dry, C., & Corsaw, M. (2003). A Comparison of Bending Strength Between Adhesive and Steel Reinforced Concrete with Steel Only Reinforced. *Concrete. Cement & Concrete Research*, *33*, 1723-1727.

Devlet Su İşleri (DSİ). (1994) *Çelik Liflerle Güçlendirilmiş Beton*, *Yayın No: MLZ-878.* Ankara, Türkiye: Bayındırlık ve İskan Bakanlığı Devlet Su İşleri Genel Müdürlüğü Teknik Araştırma ve Kalite Kontrol Dairesi Başkanlığı.

Ellis, E. A., & Springman, S.M. (2001) Modelling of Soil-Structure Interaction for a Piled Bridge Abutment in Plane Strain FEM Analyses. Computers and Geotechnics, 28, 79-98.

Eren, Ö., & Çelik, T. (1997) Effect of Silica Fume and Steel Fibers on Some Properties of High-Strength Concrete, *Construction and Building Materials*, *11*, 373-382.

Ezeldin, A. S., & Balaguru, P. N. (1992). Normal- and High-Strength Fiber-Reinforced Concrete Under Compression. *Journal of Materials in Civil Engineering*, *4*, 415-429.

Fan, C., & Long, J. H. (2005) Assessment of Existing Methods for Predicting Soil Response of Laterally Loaded Piles in Sand. *Computers and Geotechnics,32*, 274-289.

Fanella, D. A., & Naaman, A. (1985). Stress-Strain Properties of Fiber Reinforced Mortar in Compression. *American Concrete Institute Journal, Proceedings*, *82*, 475-483.

Fischer G, & Li, V. C. (2002). Effect of Matrix Ductility on Deformation Behavior of Steel-Reinforced ECC Flexural Members under Reversed Cyclic Loading Conditions. *American Concrete Institute Structural Journal*, *99*, 781-790.

Fujii S, Cubrinovski M, Tokimatsu K, & Hayashi T. (1998) Analyses of damaged and undamaged pile foundations in liquefied soils during the 1995 Kobe earthquake. In *Proceedings of the Geotechnical Earthquake Engineering and Soil Dynamics II* (1187–1198). Seattle, USA: American Society of Civil Engineering (ASCE).

Gazetas G, & Mylonakis G. (1998). Seismic Soil-Structure Interaction: New Evidence and Emerging Issues. *In Proceedings of the Geotechnical Earthquake*

Engineering and Soil Dynamics III. (1119–1174) Seattle, USA: American Society of Civil Engineering (ASCE).

Gerolymos, N., Escoffier, S., Gazetas, G., & Garnier, J. (2009). Numerical Modeling of Centrifuge Cyclic Lateral Pile Load Experiments. *Earthquake Engineering and Engineering Vibration, 8*, 61-76.

Hansen, B. J. (1961). The Ultimate Resistance of Rijid PİIes Against Transversal Forces. *Danish Geotechnical Institute Bulletin*, 12, 5-9.

Hutchinson, T. C., Chai Y. H., Boulanger, R. W., & Idriss, I. M. (2004). Inelastic Seismic Response of Extended Pile-Shaft-Supported Bridge Structures. *Earthquake Spectra*, 20, 1057–1080.

Hutchinson T. C., Chai Y. H., & Ross W. B. (2005). Simulation of Full-Scale Cyclic Lateral Load Tests on Piles. Journal of Geotechnical and Geoenvironmental Engineering, 131, 1172-1175.

Imam, M., Vandewalle, L., Mortelmans, F, & Van Gemert D. (1997). Shear domain of Fibre-Reinforced High-Strength Concrete Beams. *Engineering Structures*, *19*, 738-747.

Janoyan, K.D. (2001). *Interaction between Soil and Full Scale Drilled Shaft under Cyclic Lateral Load.* Ph.D. Dissertation. Los Angeles: University of California.

Johnston, C. D. (1974). Steel Fiber Reinforced Mortar and Concrete- A Rewiev of Mechanical Properties. In *Fiber Reinforced Concrete* (127-142). Detroit, Michigan: ACI, American Concrete Institute SP-44.

Junior, S. F, & de Hanai, J. B. (1997). Shear Behaviour of Fiber Reinforced Beams. *Cement and Concrete Composites, 19*, 359-366.

Junior, S. F, & de Hanai, J. B. (1999). Prestressed Fiber Reinforced Concrete Beams with Reduced Ratios of Shear Reinforcement. *Cement and Concrete Composites, 21*, 213-221.

Juirnarongrit, T., & Ashford, S. (2003). Evaluation of Pile Diameter Effect on Initial Modulus of Subgrade Reaction. *Journal of Geotechnical and Geoenvironmental Engineering*, *129*, 234-242.

Kagawa T, & Kraft ML. (1981). Lateral pile response during earthquakes. *Journal of the Geotechnical Engineering*, *107*, 1713–1731.

Khodair, A. Y., & Hassiotis, S. (2005) Analysis od Soil-Pile Interaction in Integral Abuntment. *Computers and Geotechnics, 32*, 201–209.

Kong, L.G., & Zhang, L.M. (2006). Rate-controlled Lateral-load Pile Tests Using a Robotic Manipulator in Centrifuge. Geotechnical Testing Journal, ASTM,192-201.

Kosmatka, S. H., & Panarese, W. C. (1994). *Design and Control of Concrete Mixtures*. United States of America: Portland Cement Association.

Kraft, L.M., Cox, W.R., & Verner, E.A. (1981). Pile Load Tests: Cyclic Loads and Varying Load Rates. *Journal of Geotechnical Engineering, ASCE*, 107, 1-19.

Krumbach, R., Seyfarth, K., Erfurt, W., & Friedemann, K. (1998). High Strength Concrete-Durability Investigations by Using the CDF-Test-First Results. *Annual Civil Engineering Report (LACER), 3*, 57-72.

Kwak, Y., Eberhard, M. O., Kim, W., & Kim, J. (2002). Shear Strength of Fiber-Reinforced Concrete Beams without Stirrups. *American Concrete Institute Materials Journal*, *99*, 530-538.

Kwak, H.G., & Kim, S.P. (2002). Nonlinear Analysis of RC Beams Based on Moment-Curvature Relation. *Computer & Structures, 80,* 615-628.

Li, F., & Li, Z. (2001). Continuum Damage Mechanics Based Modeling of Fiber Reinforced Concrete in Tension. *International Journal of Solids and Structures, 38, 777-793.*

Li, V. C. (2002). Large Volume, High- Performance Applications of Fibers in Civil Engineering. *Journal of Applied Polymer Science, 83*, 660-686.

Li, V. C., Wang, S., & Wu, C. (2001). Tensile Strain- Hardening Behavior of Polyvinyl Alcohol Engineered Cementitious Composite (PVA-ECC). *American Concrete Institute Materials Journal*, *98,* 483-492

Li, V. C., Ward, R., & Hamza, A. M. (1992). Steel and Synthetic Fibers as Shear Reinforcement. *American Concrete Institute Materials Journal, 89*, 499-508.

Lim, D. H., & Oh, B. H. (1999). Experimental and Theoretical Investigation on the Shear of Steel Fibre Reinforced Concrete Beams. *Engineering Structures, 21*, 937–944.

Limkatanyu, S., Kuntiyawichai, K., Spacone, E., & Kwan, M. (2008). Response of Reinforced Concrete Piles Including Soil-Pile Interaction Effects. *The 14Th World Conference On Earthquake Engineering*. Beijing, China.

Long, J. H., & Reese, L.C. (1984). Testing and Analysis of Two Offshore Drilled Shafts Subjected to Lateral Loads. In Langer, Mosley, Thompson (Eds.). *Laterally Loaded Deep Foundations: Analysis and Performance* (214-228). Philadelphia: American Society for Testing and Materials, ASTM.

Mailhot, T., Bissonnete, F., & Pigeon, M. (2001). Flexural Fatigue Behavior of Steel Fiber Reinforced Concrete Before and After Cracking. *Materials and Structures, 34* (6), 351-359.

Mansur, M. A., Chin, M. S., & Wee, T. H. (1999). Stress-Strain Relationship of High-Strength Fiber Concrete in Compression. *Journal of Materials in Civil Engineering, 11*, 21-29.

Matlock, H. (1970) Correlations for Design Laterally Loaded Piles in Soft Clay. *Proceedings of the Second Annual Offshore Technology Conference*, (577-607). Houston, Texas.

Meda, A., Minelli, F., Plizzari, G.A., & Riva, P. (2005). Shear Behaviour of Steel Fibre Reinforced Concrete Beams. *Materials and Structures, 38*, 343-351.

Murchison, J. M., & O'Neill, M. W. (1984). Evaluation of p-y Relationships in Cohesionless Soils. In *Proceedings, Symposium of Analysis and Design of Pile Foundations* (174-191). San Francisco, CA: American Society of Civil Engineering (ASCE).

Mizuno H. (1987). Pile damage during earthquakes in Japan (1923–1983). In *Proceedings of Response of Pile Foundations During Earthquakes* (53–78). Atlantic City, USA: American Society of Civil Engineering (ASCE).

Mylonakis G, Nikolaou AS, & Gazetas G. (1997). Soil–Pile-Bridge Seismic Interaction: Kinematic and Inertial Effects. Part I: Soft Soil. *Earthquake Engineering & Structural Dynamic*s, *26*, 337–359.

Naaman, A. E. (2003). Engineered Steel Fibers with Optimal Properties for Reinforcement of Cement Composites. *Journal of Advanced Concrete Technology*, *1* (3), 241-252.

Nataraja, M.C., Dhang, N., & Gupta, A. P. (1999). Stress-strain Curves for Steel-Fiber Reinforced Concrete under Compression. *Cement & Concrete Composites, 21,* 383-390.

Nikolaou S, Mylonakis G, Gazetas G, & Tazoh T. (2001). Kinematic Pile Bending During Earthquakes: Analysis and Field Measurements. *Geotechnique, 51,*425–40.

Nilson, H. A., (1997). *Design of Concrete Structures*. United States of America: McGraw-Hill.

Nip, D. C. N., & Ng, C. W. W. (2004). Back-Analysis of Laterally Loaded Bored Piles. *Proceedings of the Institution of Civil Engineers Geotechnical Engineering, 158,* 63-73.

Nunez, I. L. (1988). Driving and Tension Loading of Piles in Sand on a Centrifuge. *Proceedings International Conference Centrifuge Paris, France,* (353–362). Rotterdam: Balkema.

Oh, B. H., Park, D. G., Kim, C. J., & Choi, C. Y. (2005) Experimental and Theoretical Investigation on The Postcracking Inelastic Behavior of Synthetic Fiber Reinforced Concrete Beams. *Cement and Concrete Research, 35,* 384-392.

Özcan , M. D., Bayraktar, B., Şahin, A., Haktanır, T., & Türker, T. (2009). Experimental and Finite Element Analysis on the Steel Fiber-Reinforced concrete (SFRC) Beams Ultimate Behavior. *Construction and Building Materials, 23,* 1064-1077.

Özden, G., & Akdağ, C.T. (2009). Lateral Load Response of Steel Fiber Reinforced Concrete Model Piles in Cohesionless Soil. *Construction and Building Materials, 23,* 785–794.

Padmarajaiah, S. K. & Ramaswamy, A. (2004) Flexural Strength Predictions of Steel Fiber Reinforced High-Strength Concrete in Fully/Partially Prestressed Beam Specimens. *Cement and Concrete Composites, 26,* 275-290.

Patra N. R., & Pise J. P. (2001) Ultimate Lateral Resistance of Pile Groups in Sand. *Journal of Geotechnical and Geoenvironmental Engineering, 127,* 481–487.

Peng, J., Clarke B. G., & M. Rouainia. (2006) A Device to Cyclic Lateral Loaded Model Piles. *Geotechnical Testing Journal*, 29, 1-7.

Poulos, H.G. (1971 a). Behavior of Laterally Loaded Piles. I: Single piles. *Journal of the Soil Mechanics and Foundations Division, ASCE, 97*, 711-731.

Poulos, H.G. (1971 b). Behavior of Laterally Loaded Piles. II: Pile groups. *Journal of the Soil Mechanics and Foundations Division*, *ASCE, 97*, 733-751.

Poulos, H.G., & Davis, E. H. (1980). *Pile Foundation Analysis and Design.* Canada: John Wiley & Sons.

Prakash S., & Kumar S. (1996). Nonlinear Lateral Pile Deflection Prediction in Sands. *Journal of Geotechnical Engineering, ASCE, 122*, 130-138.

Reese, L. C. (1977). Laterally Loaded Piles: Program Documentation. *Journal of Geotechnical Engineering, 103,* 287-305.

Reese, L. C. (1984). Behavior under Lateral Loading of Piles Supporting Offshore Structures. In J.F, Wilson,(Ed.), *Dynamics of Offshore Structures* (399-448). New York: John Wiley and Sons.

Reese, L.C., Cox, W., & Koop, F. (1974). Analysis of Laterally Loaded Piles in Sand. *Proceedings, 6th Offshore Technology Conference* (473-483).Houston, Texas.

Reese, L. C., & Van Impe, W. F. (2001). *Single piles and pile groups under lateral loading*. Rotterdam: A.A. Balkema.

Reese, L.C., & Welch, R.C. (1975). Lateral Loading of Deep Foundations in Stiff Clay. *Journal of Geotechnical Engineering, ASCE, 101*, 633-649.

Remaud D. (1999). *Pieux sous charges latérales: Etude expérimentale de l'effet de Groupe*. Thése de Doctorat de l' Université de Nantes.

Robins, P., Austin, S., Chandler, J., & Jones, P. (2001). Flexural Strain and Crack Width Measurement of Steel-Fibre-Reinforced Concrete by Optical grid and Electrical Gauge Methods. *Cement and Concrete Research, 31*, 719-729.

Rollins, K. M., Lane, J. D., & Gerber T. M. (2005). Measured and Computed Lateral Response of a Pile Group in Sand. *Journal of Geotechnical and Geoenvironmental Engineering, 131*, 103-114.

Romualdi, J. P., & Batson, G.B. (1963). Mechanics of Crack Arrest in Concrete. Journal of the Engineering Mechanics , 89, 147-168.

Rossi, P. (2000). Ultra-High Performance Fibre Reinforced Concretes (UHPFRC): An overview. In Rossi, P.& Chanvillard, G. (Eds.). *Fibre-Reinforced Concretes (FRC) Proceedings of the Fifth RILEM Symposium.* (87-100). Lyon: RILEM Publications.

Seed, H. B., & Reese, L.C. (1955). The Action of Soft Clay Along Friction Piles. *American Society of Civil Engineers, ASCE, 122*, 731-765.

Shah, S.P., & Rangan,R.V. (1971). Fiber Reinforced Concrete Properties. *American Concrete Institute Journal, Proceedings*, 68, 126-135.

Simon, A., Hazar, Z., Lecointre, D., & Petitjean. (2002). Realization of two road bridges with Ultra-High-Performance Fibre-Reinforced Concrete. In *J.6th International Symposium on High Strength / High Performance Concrete*. Leipzig Germany, June.

Singh, A., & Prakash, S. (1971). Model Pile Group Subjected to Cyclic Lateral Load. *Soils and Foundations*, *11*, 51-60.

Soranakom, C., & Mobasher, B. (2007) Closed-Form Moment-Curvature Expressions for Homogenized Fiber-Reinforced Concrete. *American Concrete Institute Materials Journal*, *ACI*, *104*, 351-359.

Soranakom, C., & Mobasher, B. (2008). Correlation of Tensile and Flexural Responses of Strain Softening and Strain Hardening Cement Composites. *Cement and Concrete Composites*, *30*, 465-477.

Tao X, Kagawa T, Minowa C, & Abe A. (1998). Verification of dynamic soil-pile interaction (1199–210). In *Proceedings of the Geotechnical Earthquake Engineering and Soil Dynamics III*, Seattle, USA: American Society of Civil engineering (ASCE).

Tokyo Sokki Kenkyujo Co. Ltd. (2010). *Strain Gauges.* Retrieved November 06, 2010, from http:/ www.tml.jp/e/download/catalogdownload.htlm.

Wang, S. (1986). *Analysis of Drilled Shafts Employed in Earth-Retaining Structures*. Ph.D. Dissertation. The University of Texas at Austin.

Wood, D.M. (2004). *Geotechnical Modelling*. United States of America: Spon Press.

Yan, L., & Bryne P.M. (1992). Lateral Pile Response to Monotonic Pile Head Loading. *Canadian Geotechnical Journal*, *29*, 955-970.

Yang, E. H., Wang, S., Yang, S., & Li, V. C. (2008). Fiber-Bridging Constitutive Law of Engineered Cementitious Composites. *Journal of Advanced Concrete Technology*, *6* , 181-193.

Zhang, L. (2009) Nonlinear analysis of laterally loaded rigid piles in cohesionless soil. *Computers and Geotechnics*, *36*, 718–724.

Zhang, J., Stang, H., & Li, V. C. (1999). Fatigue Life Prediction of Fiber Reinforced Concrete under Flexural Load. *International Journal of Fatigue*, *21*, 1033-1049.

APPENDİX-A

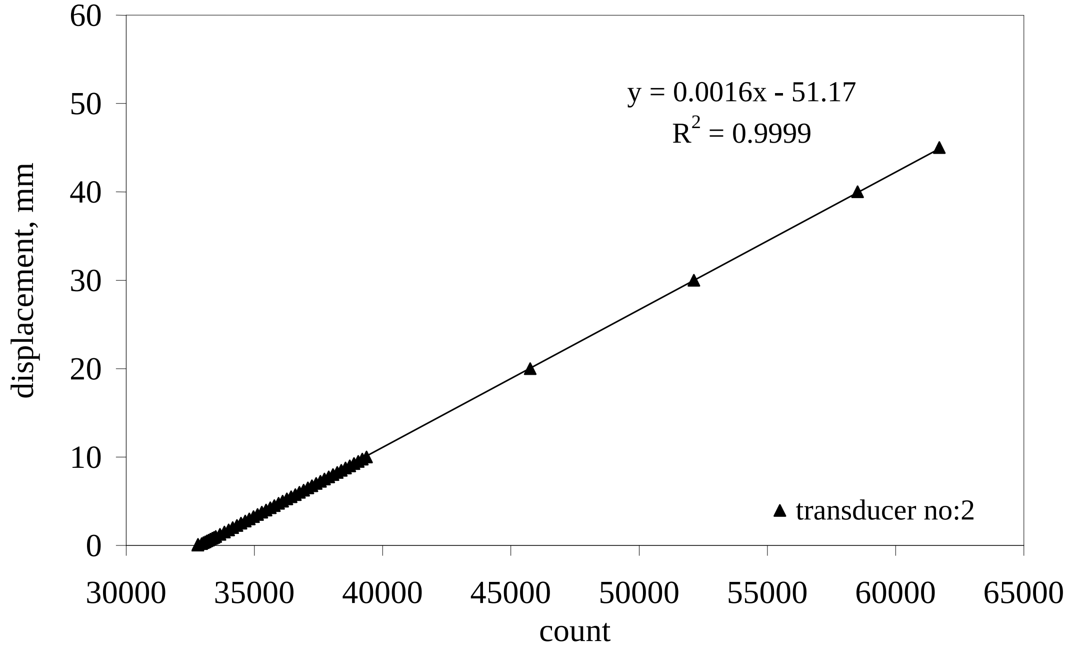

Figure A-1 Calibration result of transducer no: 2

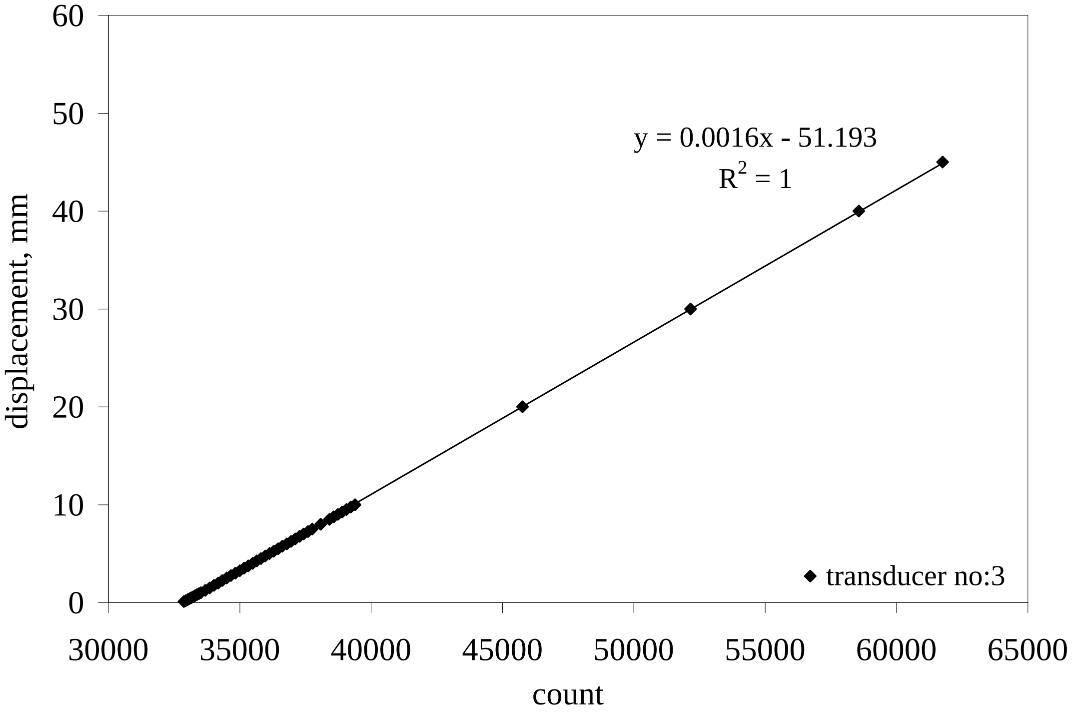

Figure A-2 Calibration result of transducer no:3

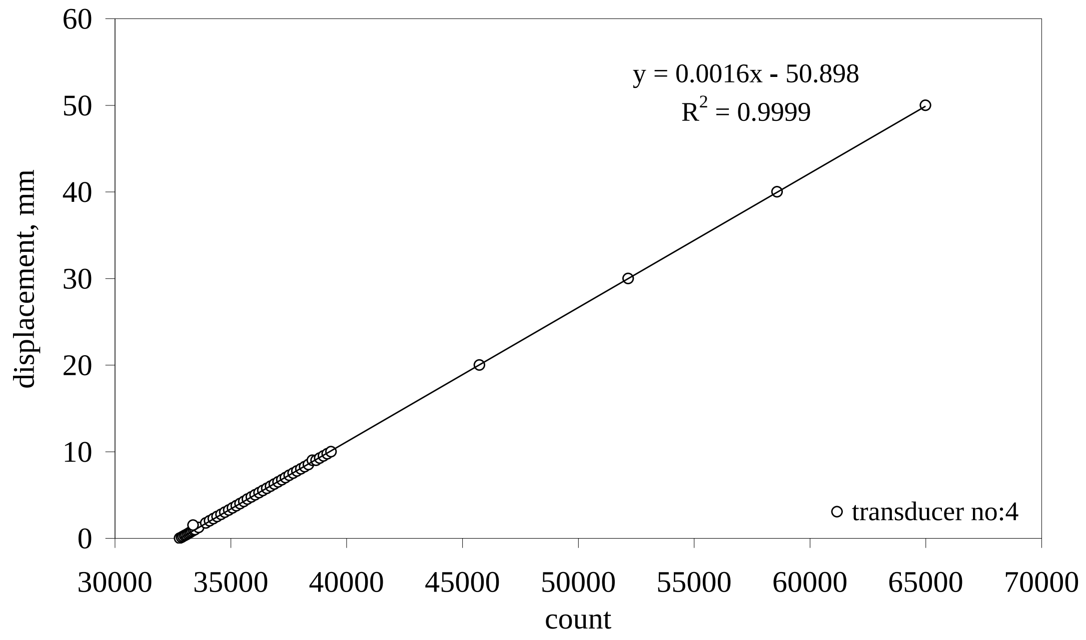

Figure A-3 Calibration result of transducer no:4

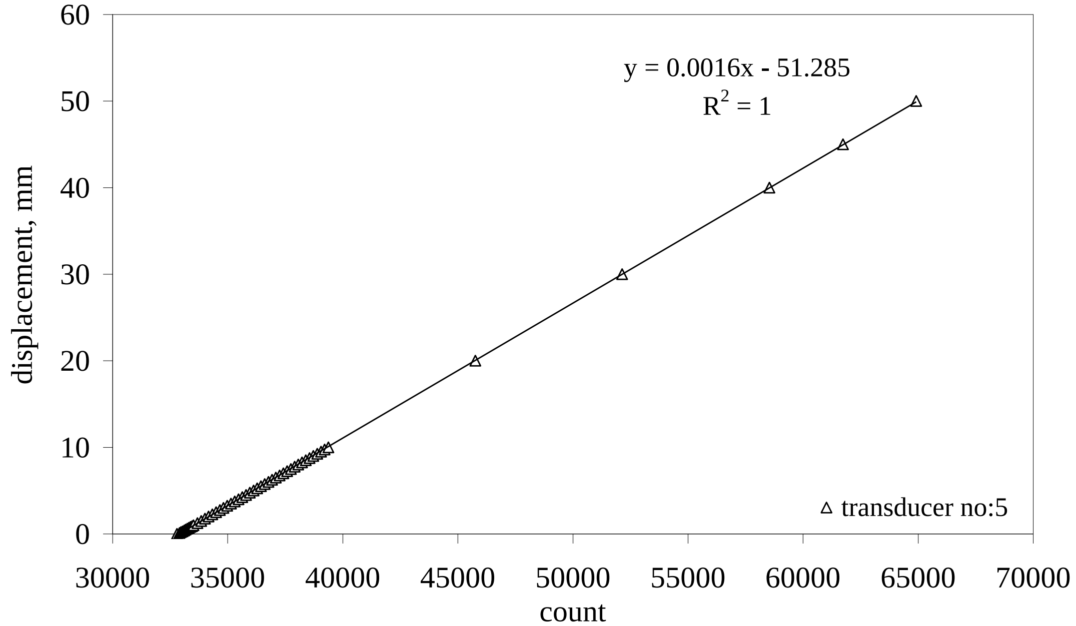

Figure A-4 Calibration result of transducer no:5

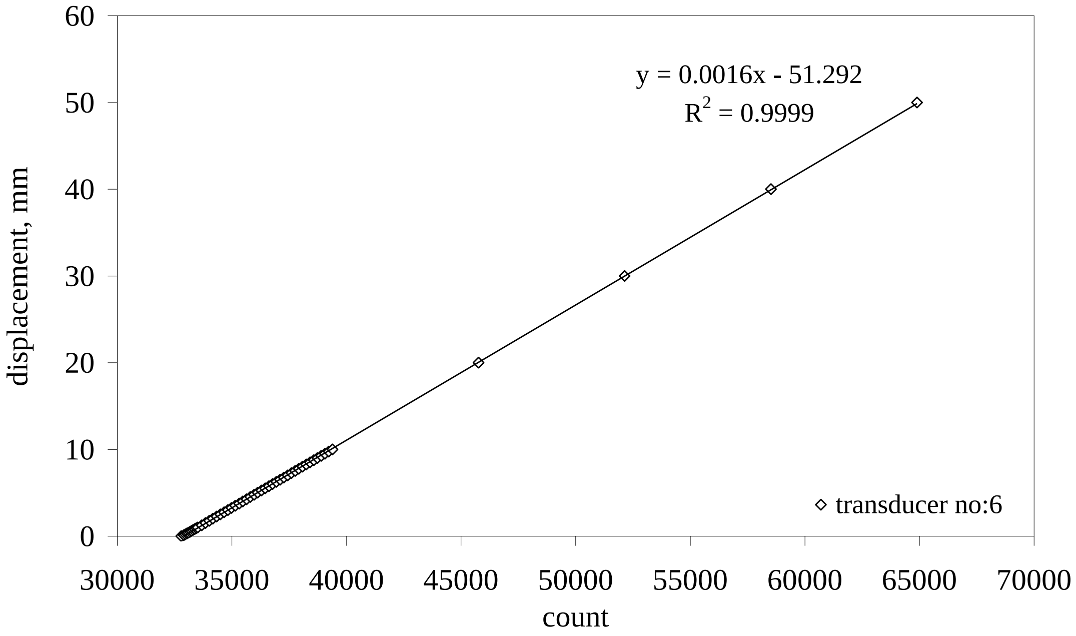

Figure A-5 Calibration result of transducer no:6

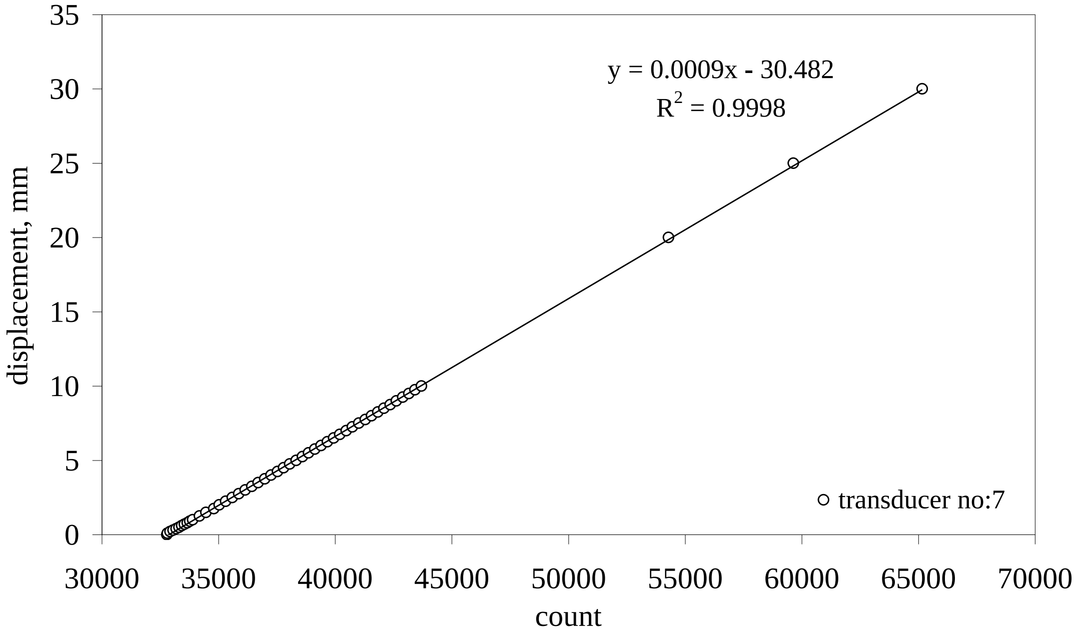

Figure A-6 Calibration result of transducer no:7

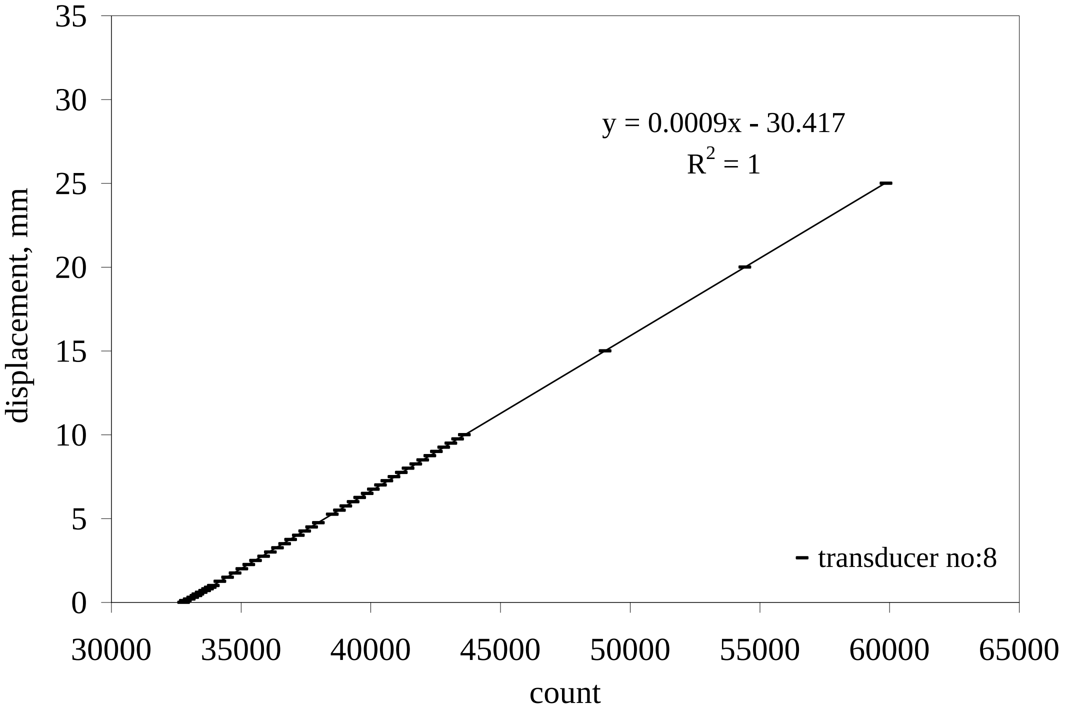

Figure A-7 Calibration result of transducer no:8

APPENDİX-B

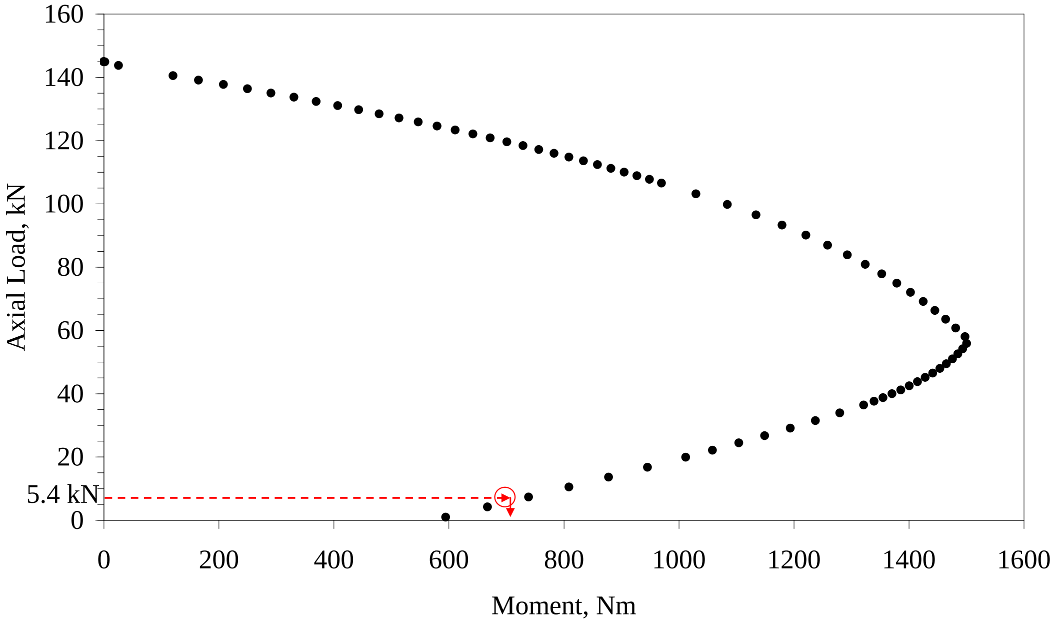

Figure B-1 The N-M interaction diagram of the RC section

APPENDİX-C

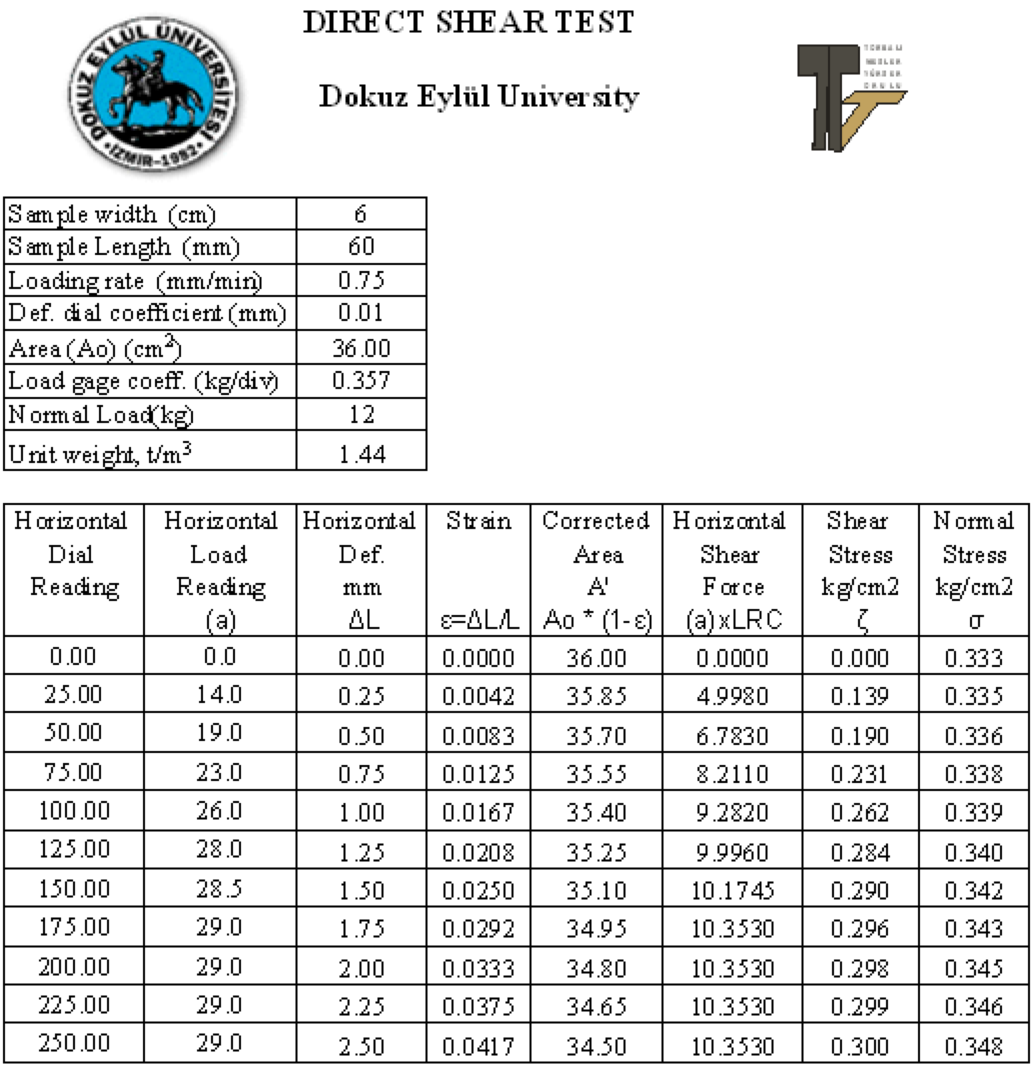

DIRECT SHEAR TEST

Dokuz Eylül University

Sample width (cm)	6
Sample Length (mm)	60
Loading rate (mm/min)	0.75
Def. dial coefficient (mm)	0.01
Area (Ao) (cm^2)	36.00
Load gage coeff. (kg/div)	0.357
Normal Load(kg)	12
Unit weight, t/m^3	1.44

Horizontal Dial Reading	Horizontal Load Reading (a)	Horizontal Def. mm ΔL	Strain ε=ΔL/L	Corrected Area A' Ao * (1-ε)	Horizontal Shear Force (a)xLRC	Shear Stress kg/cm2 ζ	Normal Stress kg/cm2 σ
0.00	0.0	0.00	0.0000	36.00	0.0000	0.000	0.333
25.00	14.0	0.25	0.0042	35.85	4.9980	0.139	0.335
50.00	19.0	0.50	0.0083	35.70	6.7830	0.190	0.336
75.00	23.0	0.75	0.0125	35.55	8.2110	0.231	0.338
100.00	26.0	1.00	0.0167	35.40	9.2820	0.262	0.339
125.00	28.0	1.25	0.0208	35.25	9.9960	0.284	0.340
150.00	28.5	1.50	0.0250	35.10	10.1745	0.290	0.342
175.00	29.0	1.75	0.0292	34.95	10.3530	0.296	0.343
200.00	29.0	2.00	0.0333	34.80	10.3530	0.298	0.345
225.00	29.0	2.25	0.0375	34.65	10.3530	0.299	0.346
250.00	29.0	2.50	0.0417	34.50	10.3530	0.300	0.348

Figure C-1 Direct Shear Test, normal load: 12 kg

DIRECT SHEAR TEST

Dokuz Eylül University

Sample width (cm)	6
Sample Length (mm)	60
Loading rate (mm/min)	0.75
Def. dial coefficient (mm)	0.01
Area (Ao) (cm^2)	36.00
Load gage coeff.(kg/div)	0.357
Normal Load(kg)	24
Unit weight, t/m^3	1.44

Horizontal Dial Reading	Horizontal Load Reading (a)	Horizontal Def. mm ΔL	Strain $\varepsilon=\Delta L/L$	Corrected Area A' Ao *(1-ε)	Horizontal Shear Force (a)xLRC	Shear Stress kg/cm^2 ζ	Normal Stress kg/cm^2 σ
0.00	0.0	0.00	0.0000	36.00	0.0000	0.000	0.667
25.00	14.0	0.25	0.0042	35.85	4.9980	0.139	0.669
50.00	18.0	0.50	0.0083	35.70	6.4260	0.180	0.672
75.00	19.5	0.75	0.0125	35.55	6.9615	0.196	0.675
100.00	20.0	1.00	0.0167	35.40	7.1400	0.202	0.678
125.00	20.0	1.25	0.0208	35.25	7.1400	0.203	0.681
150.00	22.0	1.50	0.0250	35.10	7.8540	0.224	0.684
175.00	24.0	1.75	0.0292	34.95	8.5680	0.245	0.687
200.00	28.0	2.00	0.0333	34.80	9.9960	0.287	0.690
225.00	30.0	2.25	0.0375	34.65	10.7100	0.309	0.693
250.00	34.0	2.50	0.0417	34.50	12.1380	0.352	0.696
275.00	39	2.75	0.0458	34.35	13.9230	0.405	0.699
300.00	43	3.00	0.0500	34.20	15.3510	0.449	0.702
325.00	47	3.25	0.0542	34.05	16.7790	0.493	0.705
350.00	49.5	3.50	0.0583	33.90	17.6715	0.521	0.708
375.00	50	3.75	0.0625	33.75	17.8500	0.529	0.711
400.00	50	4.00	0.0667	33.60	17.8500	0.531	0.714
425.00	50	4.25	0.0708	33.45	17.8500	0.534	0.717
450.00	50	4.50	0.0750	33.30	17.8500	0.536	0.721

Figure C-2 Direct Shear Test, normal load: 24 kg

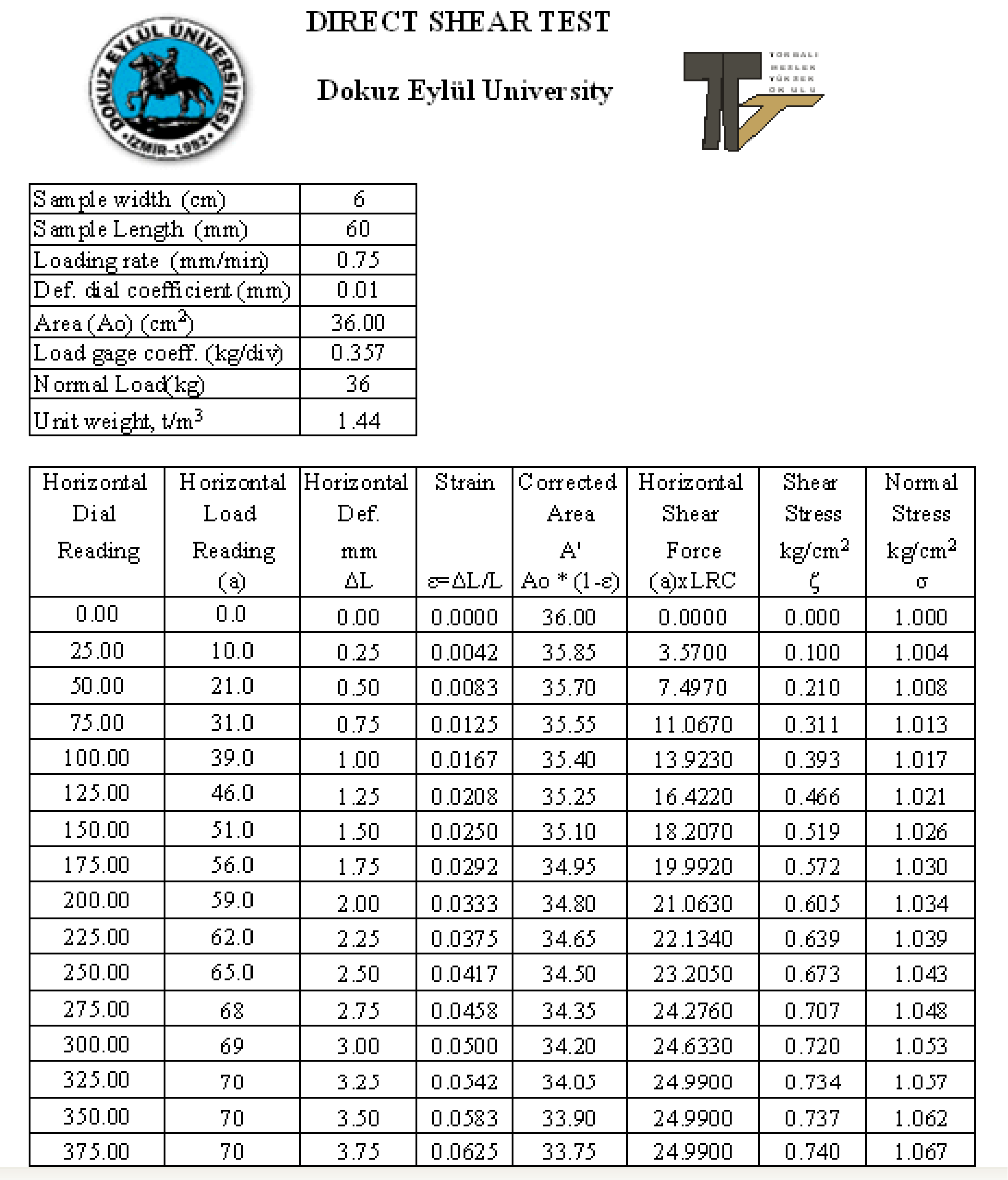

DIRECT SHEAR TEST

Dokuz Eylül University

Sample width (cm)	6
Sample Length (mm)	60
Loading rate (mm/min)	0.75
Def. dial coefficient (mm)	0.01
Area (Ao) (cm^2)	36.00
Load gage coeff. (kg/div)	0.357
Normal Load(kg)	36
Unit weight, t/m^3	1.44

Horizontal Dial Reading	Horizontal Load Reading (a)	Horizontal Def. mm ΔL	Strain ε=ΔL/L	Corrected Area A' Ao * (1-ε)	Horizontal Shear Force (a)xLRC	Shear Stress kg/cm^2 ζ	Normal Stress kg/cm^2 σ
0.00	0.0	0.00	0.0000	36.00	0.0000	0.000	1.000
25.00	10.0	0.25	0.0042	35.85	3.5700	0.100	1.004
50.00	21.0	0.50	0.0083	35.70	7.4970	0.210	1.008
75.00	31.0	0.75	0.0125	35.55	11.0670	0.311	1.013
100.00	39.0	1.00	0.0167	35.40	13.9230	0.393	1.017
125.00	46.0	1.25	0.0208	35.25	16.4220	0.466	1.021
150.00	51.0	1.50	0.0250	35.10	18.2070	0.519	1.026
175.00	56.0	1.75	0.0292	34.95	19.9920	0.572	1.030
200.00	59.0	2.00	0.0333	34.80	21.0630	0.605	1.034
225.00	62.0	2.25	0.0375	34.65	22.1340	0.639	1.039
250.00	65.0	2.50	0.0417	34.50	23.2050	0.673	1.043
275.00	68	2.75	0.0458	34.35	24.2760	0.707	1.048
300.00	69	3.00	0.0500	34.20	24.6330	0.720	1.053
325.00	70	3.25	0.0542	34.05	24.9900	0.734	1.057
350.00	70	3.50	0.0583	33.90	24.9900	0.737	1.062
375.00	70	3.75	0.0625	33.75	24.9900	0.740	1.067

Figure C-3 Direct Shear Test, normal load: 36 kg

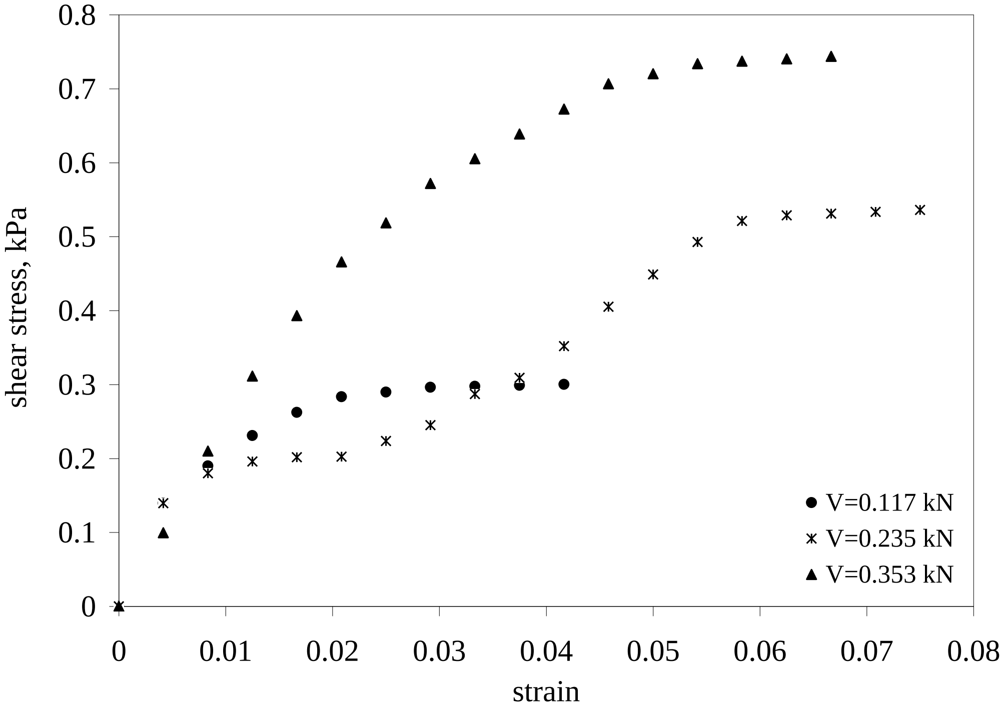

Figure C-4 Shear stress-strain relationship

APPENDİX-D

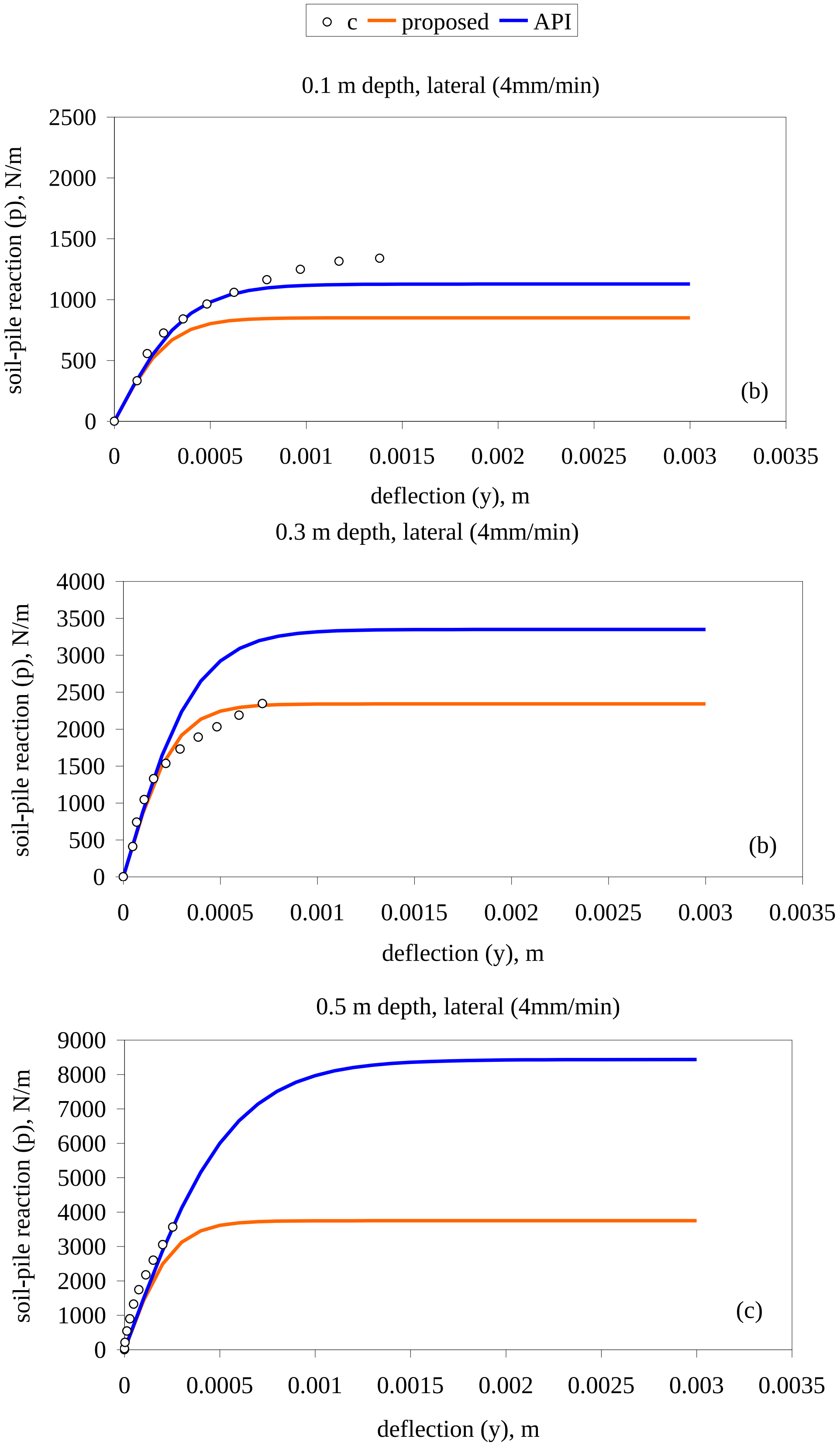

Figure D-1 Comparison of proposed and experimental p-y curves, *c* pile, 4mm/min (a) 0.1 m (b) 0.3 m (c) 0.5 m depths

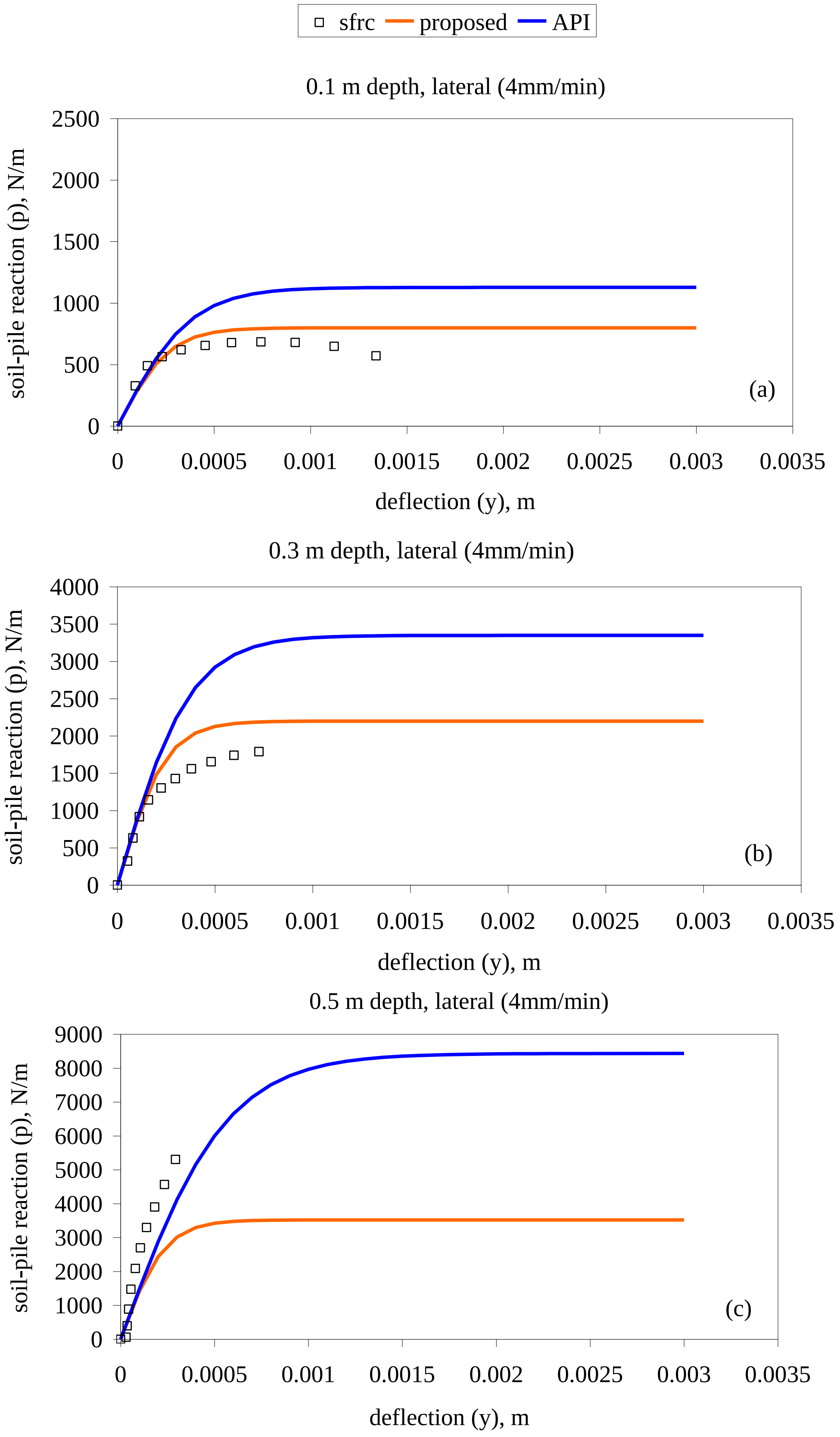

Figure D-2 Comparison of proposed and experimental p-y curves, *sfrc* pile, 4mm/min (a) 0.1 m (b) 0.3 m (c) 0.5 m depths

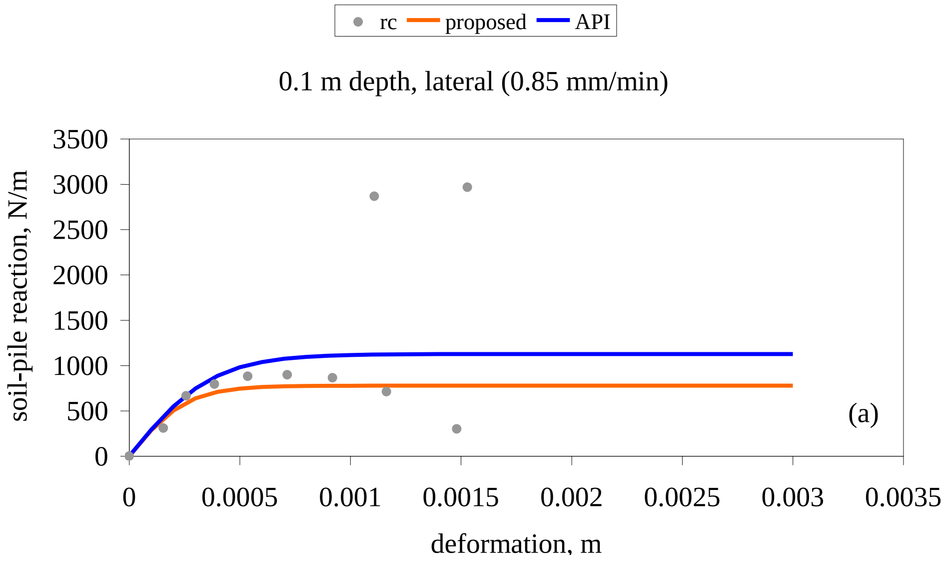

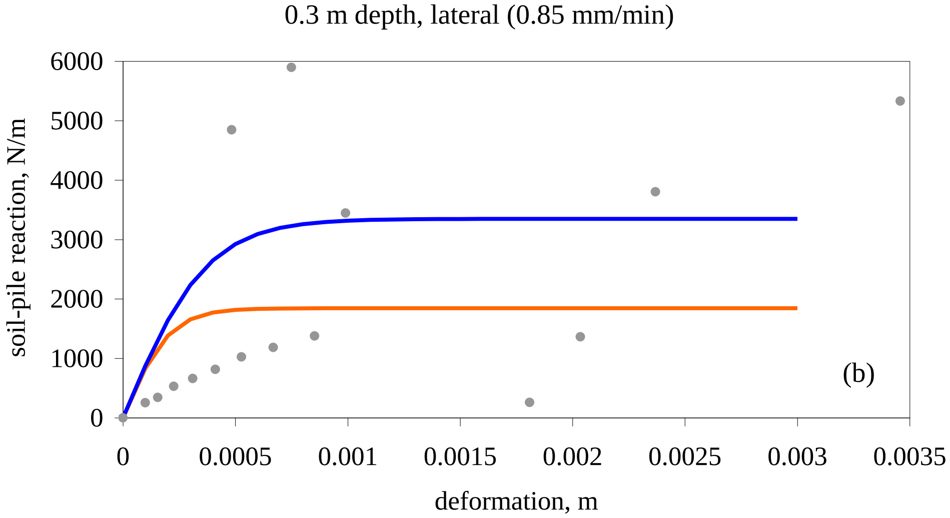

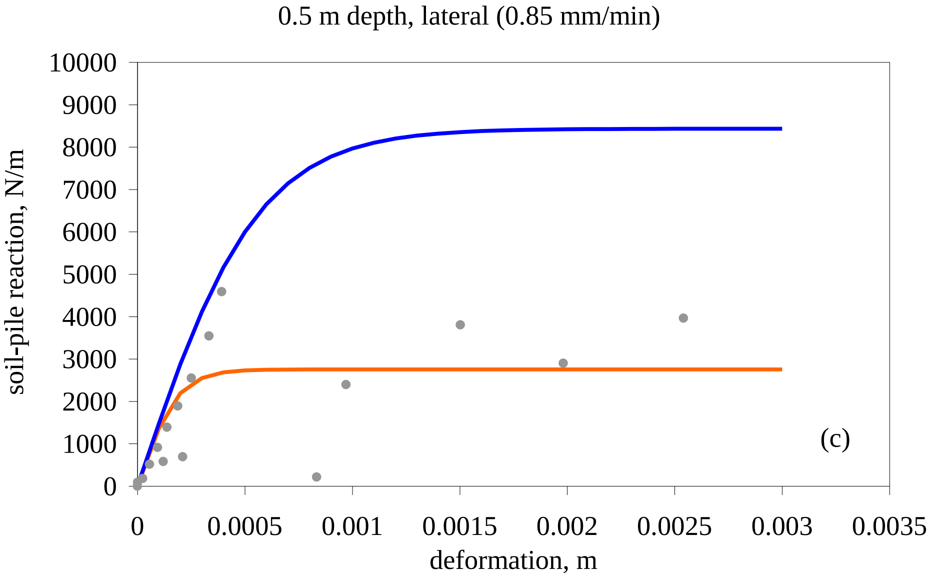

Figure D-3 Comparison of proposed and experimental p-y curves, *rc* pile, 0.85mm/min (a) 0.1 m (b) 0.3 m (c) 0.5 m depths

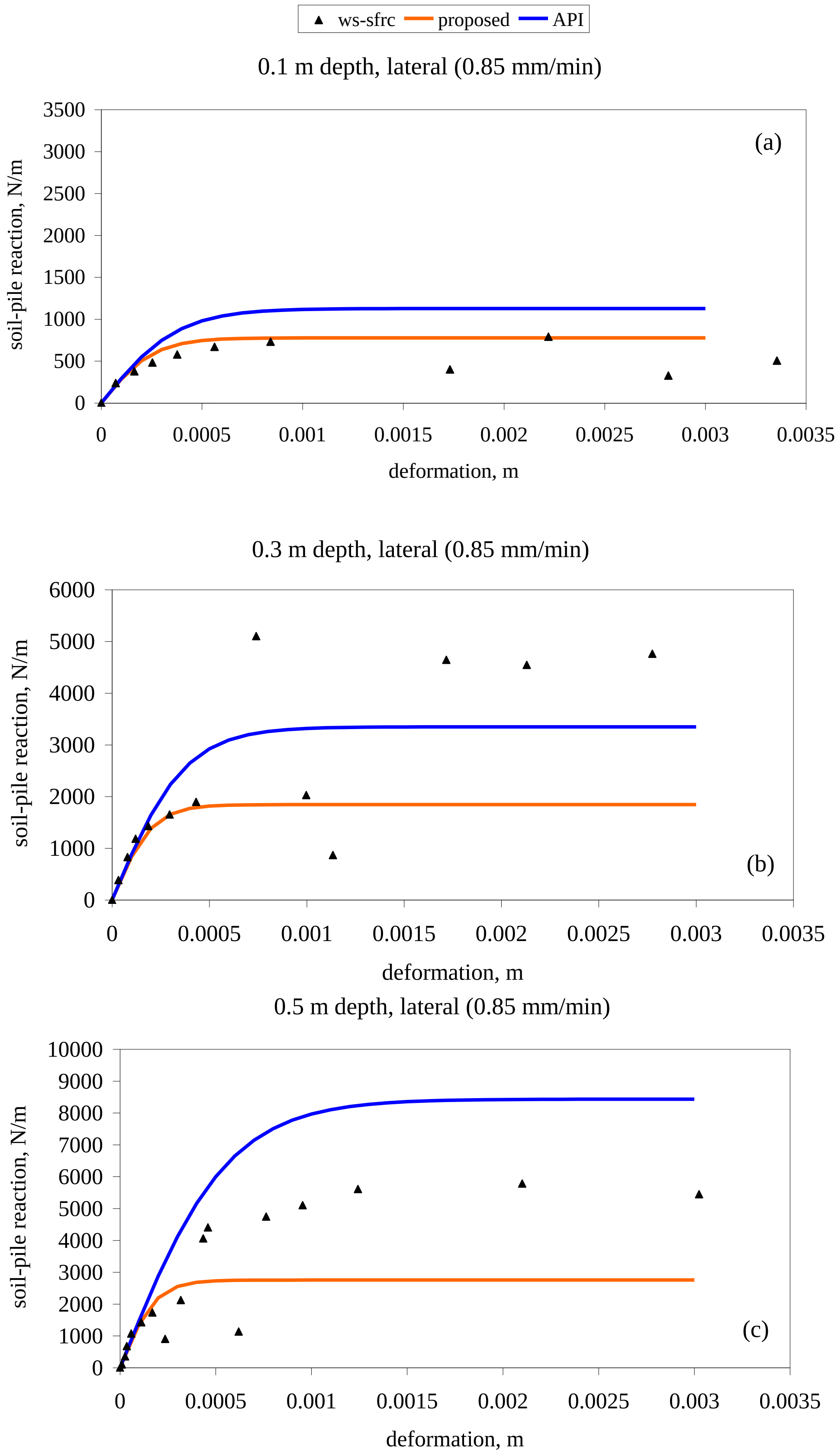

Figure D-4 Comparison of proposed and experimental p-y curves, *ws-sfrc* pile, 0.85mm/min (a) 0.1 m (b) 0.3 m (c) 0.5 m depths

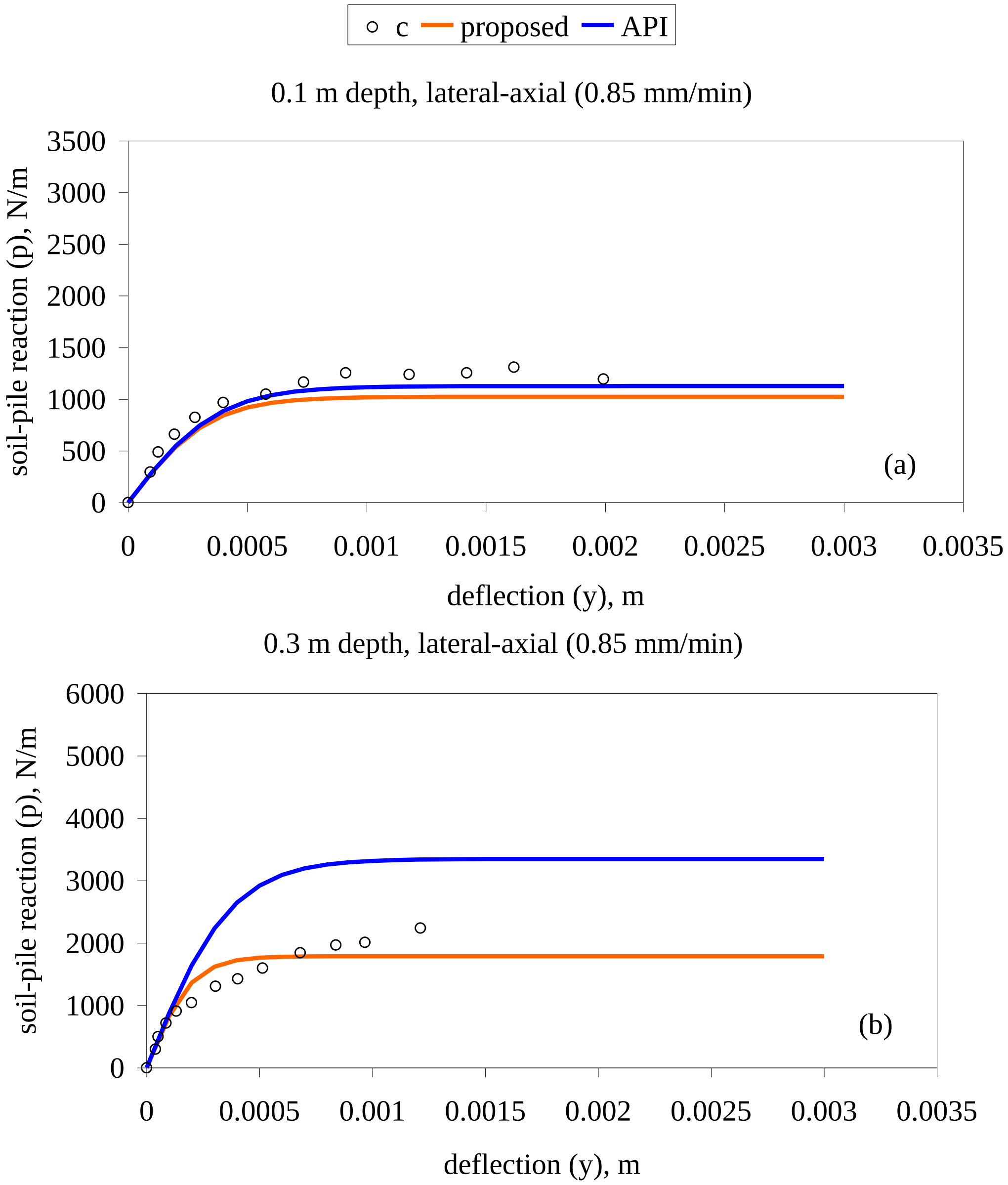

Figure D-5 Comparison of proposed and experimental p-y curves, *c* pile, lateral-axial loading 0.85mm/min (a) 0.1 m (b) 0.3 m depths

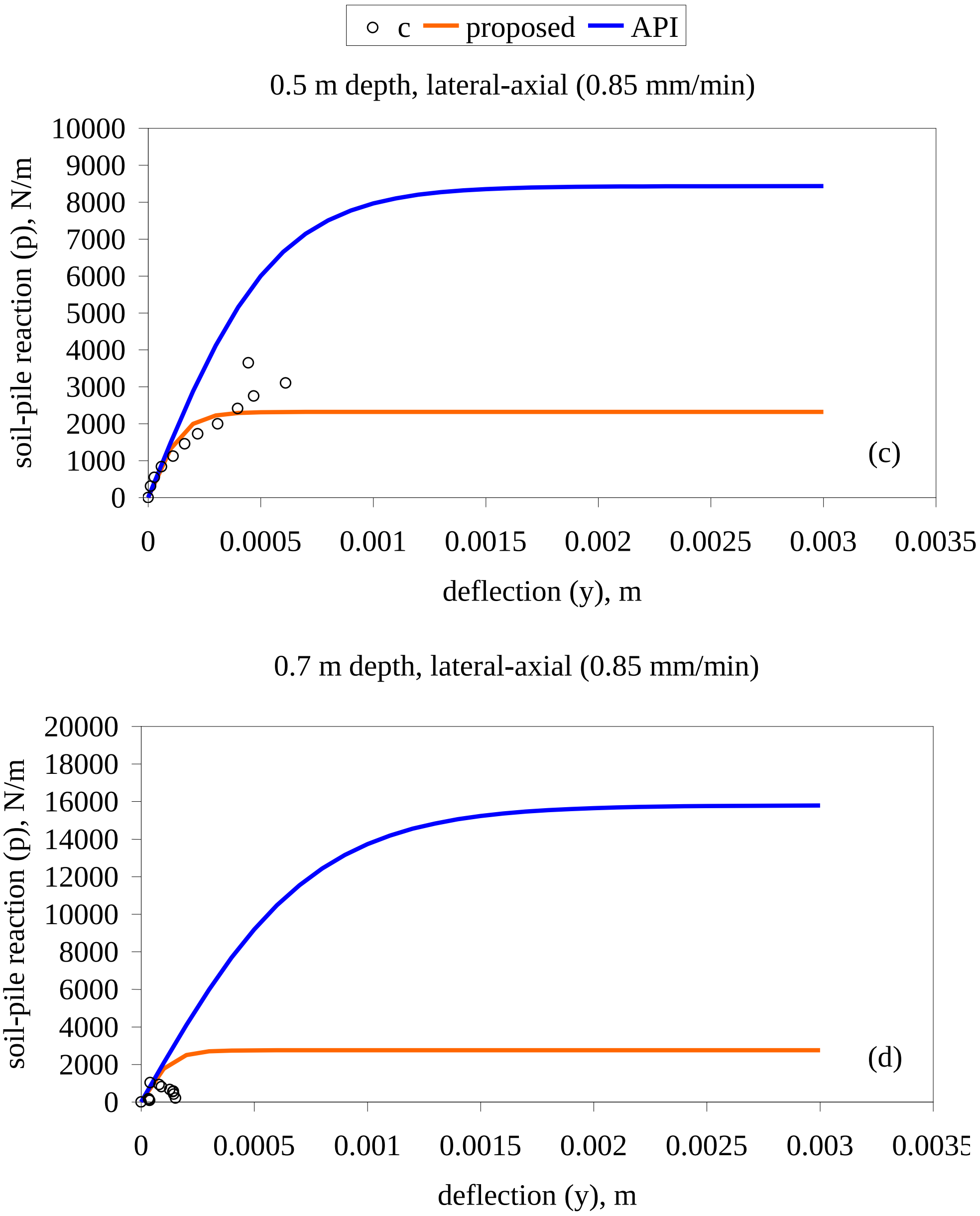

Figure D-5 (a) 0.5 m (b) 0.7 m depths - *continued*

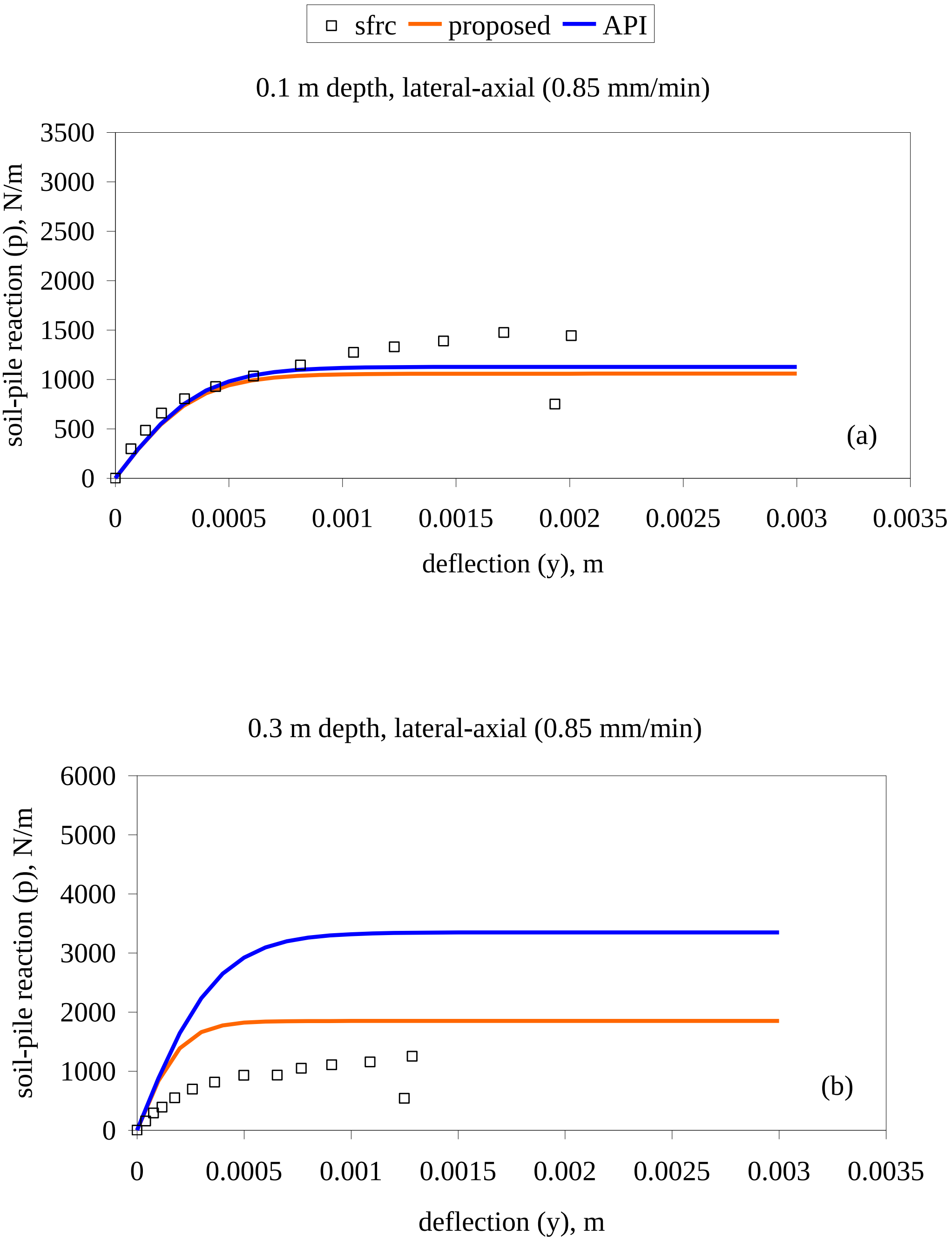

Figure D-6 Comparison of proposed and experimental p-y curves, *sfrc* pile, lateral-axial loading 0.85mm/min (a) 0.1 m (b) 0.3 m depths

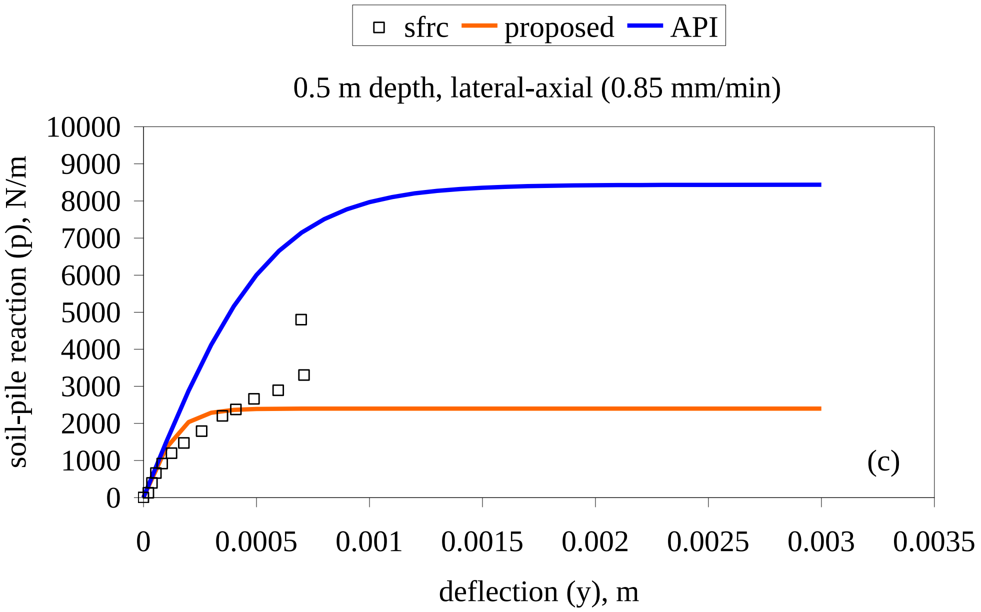

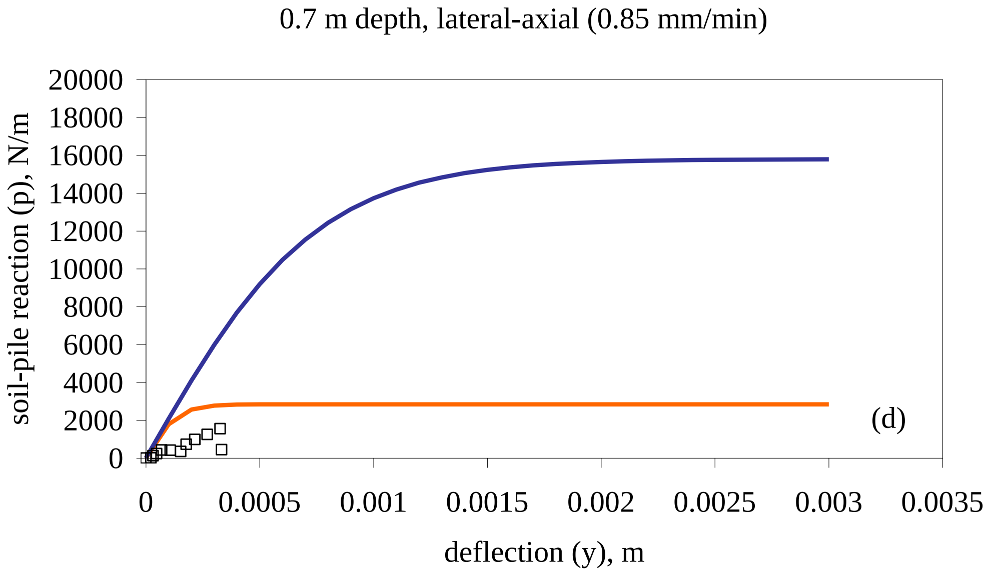

Figure D-6 (c) 0.5 m (d) 0.7 m depths -*continued*

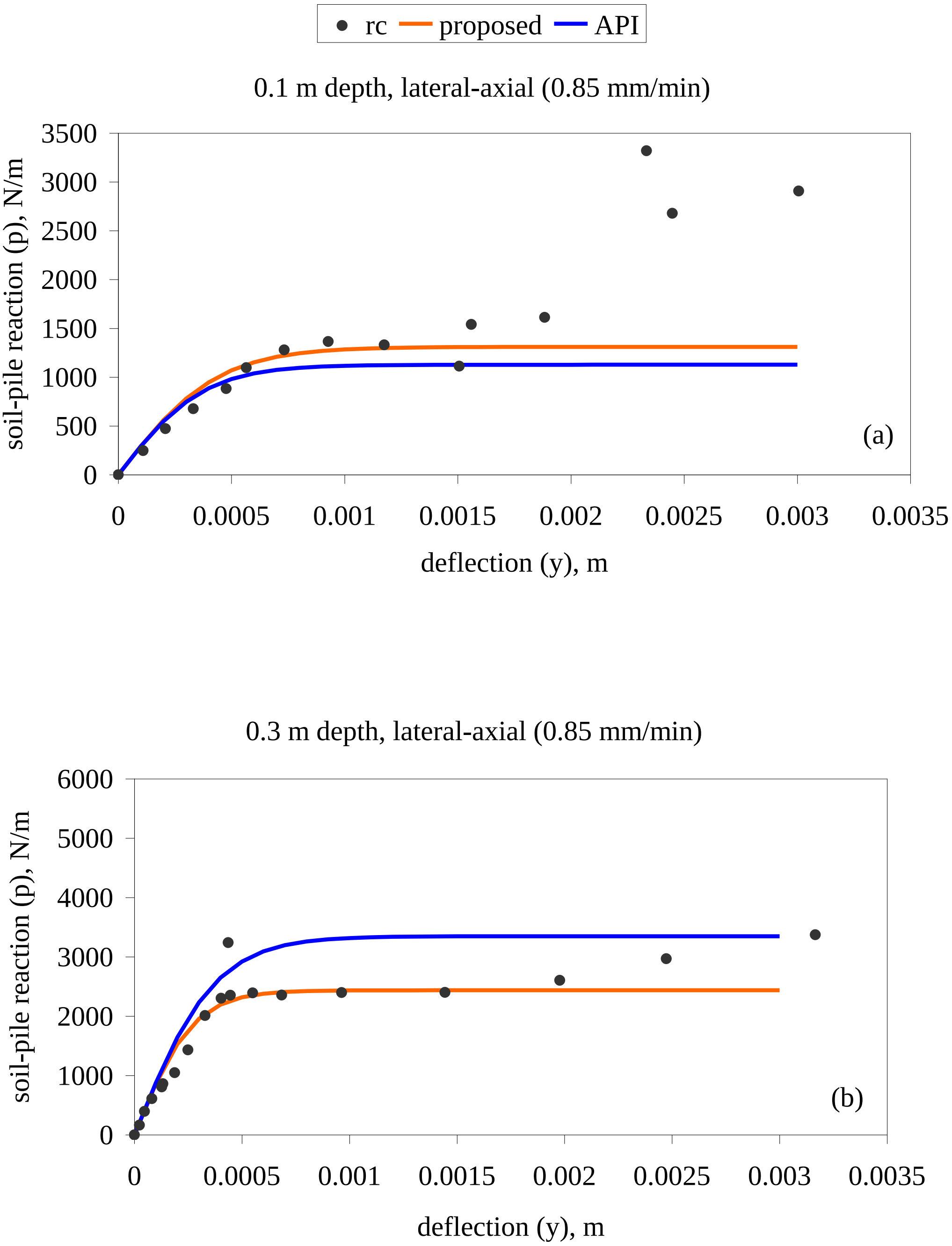

Figure D-7 Comparison of proposed and experimental p-y curves, *rc* pile, lateral-axial loading 0.85mm/min (a) 0.1 m (b) 0.3 m depths

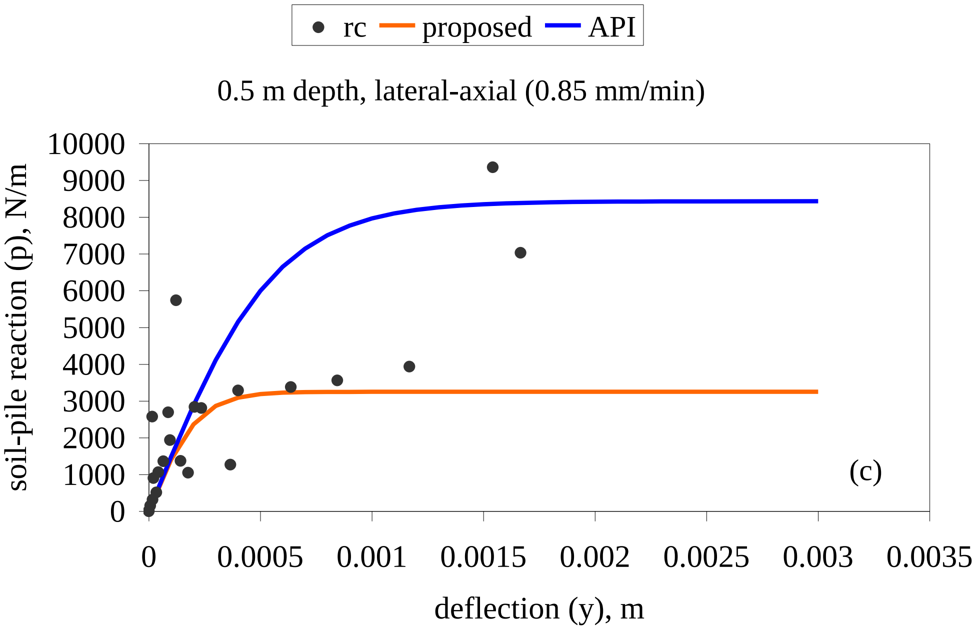
0.5 m depth, lateral-axial (0.85 mm/min)

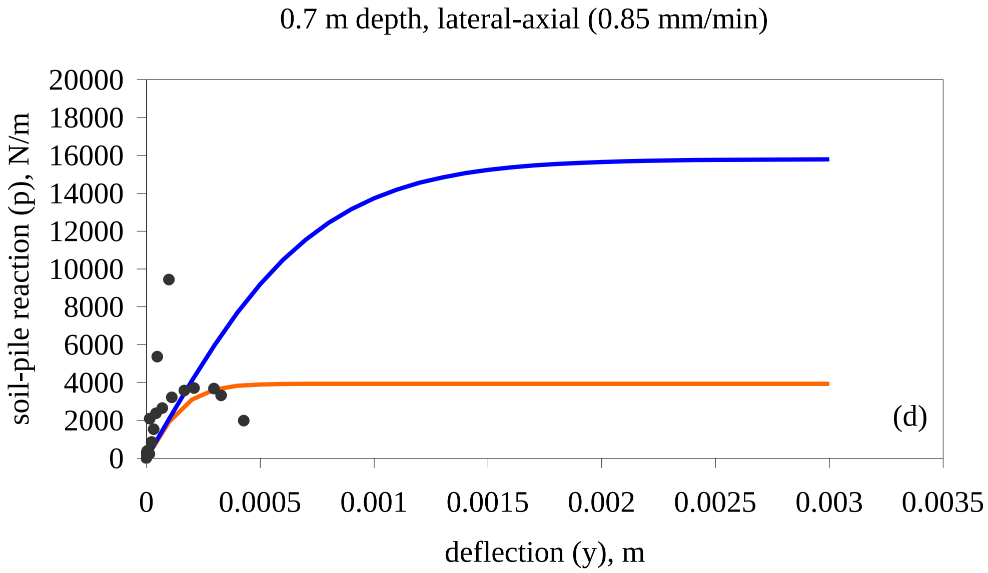
0.7 m depth, lateral-axial (0.85 mm/min)

Figure D-7 (a) 0.5 m (b) 0.7 m depths- *continued*

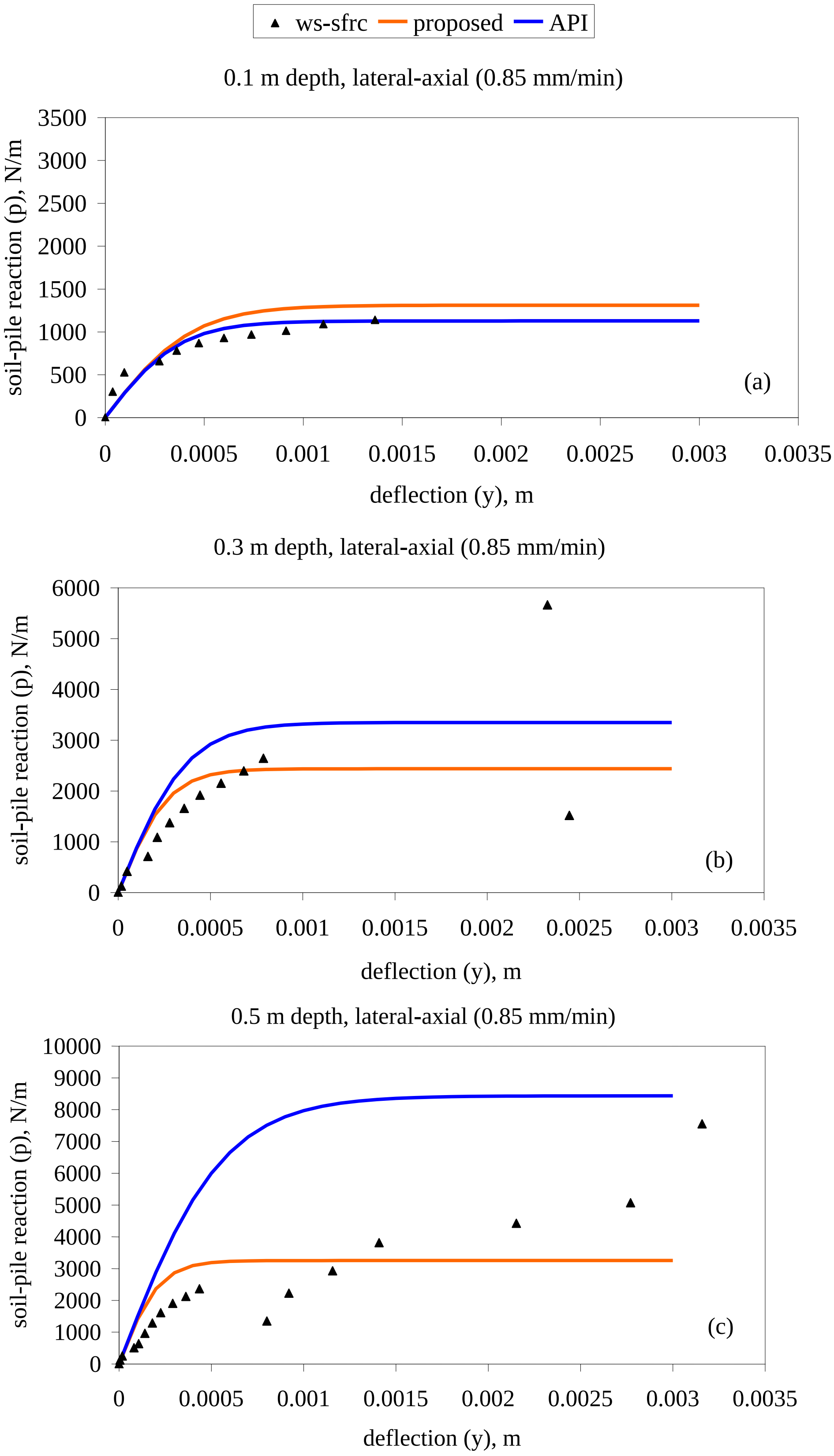

Figure D-8 Comparison of proposed and experimental p-y curves, *ws-sfrc* pile, lateral-axial loading 0.85mm/min (a) 0.1 m (b) 0.3 m (c) 0.5 m depths

APPENDİX-E

LIST OF FIGURES

APPENDİX-E

TABLES